Department
Chemie und Pharmazie

FRIEDRICH-ALEXANDER
UNIVERSITÄT
ERLANGEN-NÜRNBERG
NATURWISSENSCHAFTLICHE
FAKULTÄT

Approaching the pressure and materials gap – impact on model systems and surface reactions

Auswirkung der Pressure und Materials Gap auf Modellsysteme und Oberflächenreaktionen

Der Naturwissenschaftlichen Fakultät
der Friedrich-Alexander-Universität Erlangen-Nürnberg

zur Erlangung des Doktorgrades Dr. rer. nat.
vorgelegt von

Sandra Krick Calderón

aus Erlangen

Als Dissertation genehmigt
von der Naturwissenschaftliche Fakultät
der Friedrich-Alexander-Universität Erlangen-Nürnberg

Tag der mündlichen Prüfung: 09.12.2016

Vorsitzende/r des Promotionsorgans: Prof. Dr. Georg Kreimer
Gutachter/in: Prof. Dr. Hans-Peter Steinrück
Prof. Dr. Jörg Libuda

„Man sollte alles so einfach wie möglich machen
- aber auch nicht einfacher.“

– *nach Albert Einstein*

Contents

1. Introduction 1

1.1 Catalysis 1
1.2 Surface science approach and the pressure and materials gap 4

2. Fundamentals and techniques 11

2.1 X-ray Photoelectron Spectroscopy 11
  2.1.1 Basics 11
  2.1.2 Near-ambient pressure XPS 15
  2.1.3 Impurities 18

2.2 “GAP” NAP-XPS setup 19
  2.2.1 Setup 19
  2.2.2 Quantification of XPS 22

2.3 Online gas analysis 24
  2.3.1 Fundamentals 24
  2.3.2 Quantification of the online gas analysis and TPD measurements 25

2.4 Low Energy Electron Diffraction 26
2.5 Experimental remarks 27
  2.5.1 Sample preparation 27
  2.5.2 Gases 29

3. Investigated reactions 31

3.1 The CO oxidation reaction on platinum 31
  3.1.1 Carbon monoxide on Pt(111) 32
  3.1.2 Oxygen on Pt(111) 34
  3.1.3 Reaction of co-adsorbed carbon monoxide and oxygen 34
  3.1.4 CO_2 on Pt(111) 36

3.2 Intercalation and reactions under 2D systems 37
3.3 Ethanol steam reforming 39

4. Oxidation of Pt(111) at near-ambient pressures 41

  4.1 General 41
  4.2 Experimental aspects and methods 43
  4.3 NAP-XPS and ReaxFF GCMC results on the time-dependent growth of platinum oxide 43
  4.4 Comparison of experiment und theory 51
  4.5 Conclusion 54

5. CO oxidation on Pt(111) at near-ambient pressures 57

  5.1 General 57
  5.2 Experimental aspects 59
  5.3 Temperature programmed measurements 59

5.4 Isothermal Reaction 70
5.5 Growth and Poisoning with ”non-platinum”-oxides 73
5.6 Conclusion 74

6. Reactivity of TiO_2 nanotube-supported Pt particles in the CO oxidation reaction 77

6.1 General 77
6.2 Experimental aspects 79
6.3 Investigated Pt/TiO_2NT samples and active sites determination 79
6.4 Reactivity of different Pt-containing samples 82
6.5 Oxidation states and surface species 86
6.6 Diffusion and mass transfer limitations 92
6.7 Conclusion 94

7. Intercalation of CO and O_2 at the graphene/Rh(111) interface 97

7.1 General 97
7.2 Experimental aspects 98
7.3 Growth of graphene on Rh(111) 98
7.4 Intercalation of CO 100
7.5 Intercalation of O_2 105
7.6 Conclusions 110

8. Near ambient pressure XPS investigation of the interaction of ethanol with Co/CeO_2(111) 113

8.1 General 113
8.2 Experimental aspects 115
8.3 XPS characterization of CeO_2(111) on Cu(111) 115
8.4 Adsorption and decomposition of ethanol on CeO_2(111) at different pressures at 300 K 117
8.5 Reactions of 0.1 mbar C_2H_5OH on CeO_2(111) film at different temperatures 121
8.6 Interaction of C_2H_5OH with Co/CeO_2(111) 122
8.7 Conclusions 126

9. Summary and Outlook 129
10. Zusammenfassung und Ausblick 133
11. Appendix 139

11.1 Appendix to Chapter 4 139
  11.1.1 Details on the ReaxFF GCMC simulations 139
  11.1.2 GCMC simulations 140

11.2 Appendix to Chapter 5 143
  11.2.1 Fitting procedure 143

11.3 Appendix to Chapter 6 144
  11.3.1 LEED picture of the 1x1 reconstruction of TiO_2(110) 144
  11.3.2 Changes in the film for the $Pt_{5nm}TiO_2$(110) sample before and after the reaction ramp 144

11.3.3 SE micrographs of the $Pt_{5nm}TiO_2NT$ and the $Pt_{5nm}TiO_2(110)$ samples after use in reaction experiments 145

11.4 Appendix to Chapter 7 146
11.4.1 Unprocessed TPD spectra for CO intercalation 146

12. Literature 147
13. Acknowledgements 155
14. Curriculum Vitae 156
15. List of Publications 157

1. Introduction

1.1 Catalysis

In 1836 BERZELIUS created the term “catalysis” and described catalysts as materials which have a “catalytic force” and therefore “the property of exerting on other bodies an action which is very different from chemical affinity. By means of this action, they produce decomposition in bodies, and form new compounds into the composition of which they do not enter”.[1] At this early stage BERZELIUS already correctly described a catalyst being able to decompose and form new compounds while it is not consumed during this reaction. Later, in 1895 OSTWALD defined that a catalyst accelerates a reaction rate without influencing the position of the chemical equilibrium, which is still the accepted definition.

Quickly the high potential of catalysis was realized and systematic research followed; the importance of this field is reflected by the fact that nowadays 90 % of all chemicals in industry are produced with the aid of catalysts.[2, 3] Besides the lower energy need for the catalysed reaction, also, the selectivity of reactions can be changed, i.e. certain reaction pathways are favoured by a catalyst. An additional driving force for research in catalysis and screening of catalysts is the request to increase the activity, which denotes the production rate of a specific catalyst in a reaction. Furthermore, a catalyst should also exhibit a high stability to be suitable for large-scale processes, or in other words, the deactivation of the catalyst should only occur very slowly. Typical deactivation processes are poisoning of the catalyst and therefore inhibition of the reaction and decomposition of the catalyst. Usually, the target quantities for the optimization of a catalyst are given in the following order: selectivity > stability > activity. In this context, the main goal is the efficient use of raw materials and often the optimization of an existing process is favoured over the development of completely new systems.[2, 4]

Generally, it is differentiated between homogeneous and heterogeneous catalysis. Whereas in a homogeneous system the catalyst and reactants are in the same phase, mostly in a liquid in which the catalyst is dissolved, in heterogeneous catalysis the catalyst is not in the same phase as the reactants and/or products. Here, the catalyst often is solid and the reactants/products may be gaseous or liquid. Heterogeneous catalysts are by far more important in industrial catalysis as the market share of homogeneous catalysts is estimated to be only ~10-15%. One advantage of heterogeneous compared to homogeneous catalysis is that the product phase may easily be separated from the catalyst, saving costly separation steps. A very important group in the field of heterogeneous catalysts are supported catalysts, where the catalytically active substance (often a metal) is dispersed on a support material with a large surface area (often metal oxide surfaces).[2]

The first stage of industrial catalysis at the start of the 19th century, unfortunately, was motivated and dominated by the development of explosives and weapons based on ammonia. Initially, the HABER-BOSCH process for ammonia synthesis was developed in order to provide a fertilizer to prevent a famine in Europe. This greatly changed when Europe entered the Great War and ammonia ended up as a bulk chemical in the synthesis of nitrogen-based explosives. Nowadays, the focus in catalysis shifted from war-based materials mainly to petrochemistry, pharmaceutical chemistry and environmental catalysis, where especially the latter caused another boost in research from 1970 to the present day. This field of catalysis is inspired by the growing awareness of the impacts that industry has on the environment and deals with the reduction of emission and use of harmful substances in industrial processes, many of them being under debate to be connected to the climate change.[3]

Despite the vast number of applications of catalysts, the fundamental processes taking place during a catalytic reaction like individual reaction steps, distinct reaction intermediates and oxidation states of the catalyst are often not sufficiently understood.[4] Here, the challenge lies in the vast number of different catalysts as they are often specific to one particular reaction.

In 2007, the Nobel Prize in chemistry was awarded to ERTL[5] for his pioneering work in the field of surface chemistry used for describing heterogeneously catalysed processes. In his work, he revealed fundamental processes and reaction steps taking place at the surfaces of catalysts used in prominent applications like in automobiles or the electrodes of fuel cells.[4-7]

The motivation of such work lies in the implementation of heterogeneously catalysed reactions in industry as well as in daily life. An example for the latter is the car's catalytic converter, where harmful gases like CO, NO and hydrocarbons are converted to non-toxic products, namely CO_2 and N_2, which is possibly the most wide-spread application of a heterogeneous catalyst. The understanding of the surface chemistry is also extraordinarily important for processes used in industrial-scale, prominent examples being the HABER-BOSCH process and the FISCHER-TROPSCH reaction for hydrocarbon synthesis.[2, 8] All reactions named have in common, that the activation of small molecules like CO, N_2 or NO at the catalyst surface plays a major role for the outcome of the reaction. Of high importance in this context is the breaking of bonds in very stable molecules like N_2 in order to enable further reactions, which is not easily possible in the absence of a catalyst. Another important field recently attracting increasing attention is electrochemistry, as for example, fuel cells are interesting devices for conversion of chemical energy to electrical energy. Such techniques based on catalysed reactions are under debate to solve the energy storage/transport challenge.

In his work, ERTL used simple, defined catalysts in order to understand independent reaction steps. Only by understanding the fundamental reaction steps taking place at the catalyst surface at an *atomic* scale, site and size-specific reaction rates or effects like poisoning of the catalyst may be understood. This knowledge again may be used to improve catalysts in terms of activity, selectivity and life time.

1.2 Surface science approach and the pressure and materials gap

Investigation of catalytically important interfaces, whether being liquid-solid, gas-solid or solid-solid, are part of surface science, and lead to the development of several surface-sensitive techniques.[9-12] In heterogeneous catalysis, mostly the gas-solid interface is of fundamental interest, which is located at the catalyst surface. Many conventionally used techniques within this field, like photoelectron or Auger electron spectroscopy, temperature-programmed desorption (TPD) and low energy electron diffraction (LEED) work at ultra-high vacuum (UHV), which denotes pressures between 10^{-7} and 10^{-10} mbar. There are two major reasons for this requirement: on one hand, charged particles like electrons used as probes in electron spectroscopies have a limited mean free path of only several nanometers and therefore demand the absence of a gas phase between sample and detector.[13] The mean free path is a measure of how long a particle travels in average before losing energy by collision with another particle. On the other hand, investigating the samples in an UHV environment provides the opportunity to investigate a *clean* surface. Contaminations mainly result from residual gases present in the environment of the samples and may drastically alter and even hinder the reaction progress. The degree of contamination of the sample is an interplay of the adsorption rates r_{ads} of the different gases present and is dependent on particle flux F to the surface, given by HERTZ-KNUDSEN equation (I) and therefore the respective partial pressure p, particle mass and gas temperature T, and the respective sticking probability S at a certain temperature.[12]

$$F = \frac{p}{(2\pi mkT)^{1/2}} \qquad \text{(I)}$$

$$r_{ads} = F \times S\,. \qquad \text{(II)}$$

In practice, time constants for clean (adsorbate-free) surfaces of ~10-10^3 s are achieved in UHV, which makes surface investigations possible.

It was shown that surface science under UHV conditions is a convenient tool in order to identify individual reaction steps and fully describe reactions on surfaces.[4, 10-12] Starting from the adsorption, different steps like diffusion of the reactants and reaction on the surface take place; also, the desorption of the products is important in order to prevent blocking of the active reaction sites after the first turnover. Therefore, it is important to understand each individual step in order to be able to improve a catalyst. To enable such detailed investigations, usually well-defined surfaces are used, which are provided by single crystals. Techniques like x-ray photoelectron spectroscopy (XPS) and scanning tunneling microscopy (STM) are able to discriminate between different sites and adsorbates. This combination of very clean UHV conditions and well-defined surfaces is known as “surface science approach”, which offers the opportunity to investigate a system under very controlled conditions. Often this approach includes theoretical methodology in order to reveal the energetics of each reaction step.[9] Undoubtedly, this fundamental research is of great importance. However, the simplified picture of a single crystal under ultraclean vacuum conditions in many cases does not describe the state of the catalyst and therefore also the kinetics and thermodynamics of the specific reaction under realistic reaction conditions. Here, the terms of the pressure and materials gap have been created in order to describe the challenge to simply extrapolate results obtained from surface science to reactions performed under realistic conditions.[14, 15]

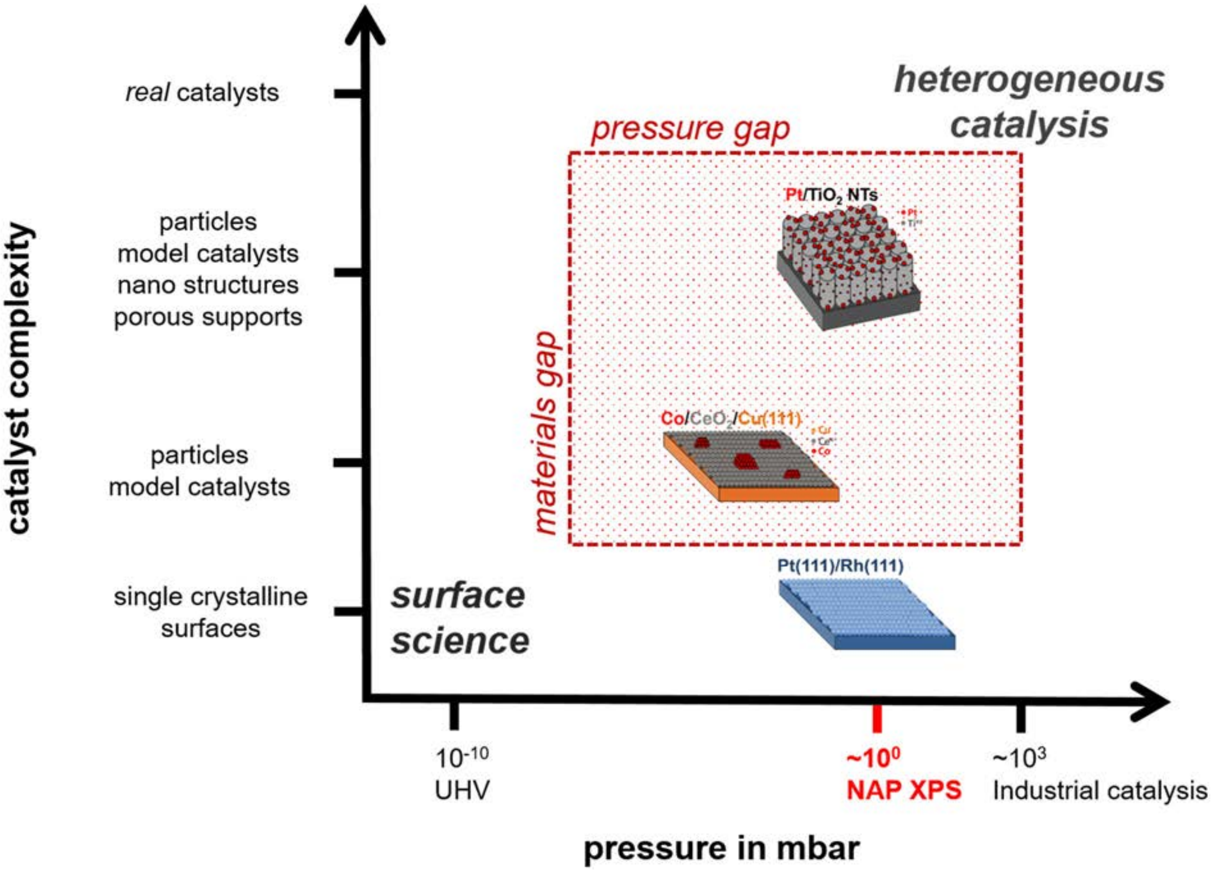
real catalysts
particles
model catalysts
nano structures
porous supports
particles
model catalysts
single crystalline
surfaces
catalyst complexity
heterogeneous
catalysis
pressure gap
materials gap
Pt/TiO2 NTs
Pt
Co/CeO2/Cu(111)
Cu
Co
Pt(111)/Rh(111)
surface
science
10-10
UHV
~100
NAP XPS
~103
Industrial catalysis
pressure in mbar

Figure 1.1: Systems investigated throughout this work in the pressure and materials gap. Investigations, which advance into both pressure and materials gap are shaded in red.

The term pressure gap describes the difference in pressure between the UHV used in surface science and the high pressures up to several bars in industrially applied heterogeneous catalysis as schematically shown in Figure 1.1 (x-axis). There are different effects the increased pressure may have on the reaction, one being certainly the crossover of several flow regimes by changing the total pressure. In UHV, the molecular flow regime is dominating, where the mean free path of the gas molecule is larger than the dimensions of the reaction chamber, which is described by the Knudsen number

$$K_n = \frac{l}{d} > 0.5 \qquad \text{(III)}$$

with l being the mean free path of the gas particles and d the dimension of the chamber component.[16] In this flow regime, the gas flow is described by the kinetic gas theory; here, reactions can be “collision-limited”, that means, the reaction rate is limited by the impingement of the reactants on the surface.[17] By increasing the total pressure, the flow regime changes to Knudsen and laminar flow regimes, where Knudsen numbers below 0.5 are found, meaning that the inelastic mean free path of the gas particles is equal or smaller than the chamber dimensions. The exact description of such flow regimes is not trivial as other effects like heat effects, for example the heat up of the gas stream at the catalyst surface, might play a role when considering catalytic reactions at elevated pressures and considerably influence the gas flow within the chamber.[4, 18] In contrast to the molecular flow regime, in the laminar flow regime, mass transfer may become rate-determining as diffusion limitations of reactants and products can dominate. At very high conversions, reactions may become mass-transfer- rather than collision-limited, where the reaction rate is only dependent on the diffusion of the reactants to the surface. This might pose a problem when determining conversions and reaction rates.

The second major challenge in terms of pressure difference is the emergence of new phases at elevated pressures. On one hand, phases which are not formed in UHV due to thermodynamic barriers might be found in the mbar range already. If these phases alter the reactivity of the catalyst, extrapolation from UHV work is not possible.[14, 19] A famous example is the CO oxidation reaction on platinum group metals. For some metals like for example platinum, it is still under debate, whether the metallic or the oxidised surface is the more reactive phase.[20, 21] Using molecular oxygen, in UHV no platinum oxides are formed under reaction conditions, while the formation might be possible under elevated pressures, see also Chapter 4.[22, 23] On the other hand, the failure of extrapolation could also be of kinetic nature; reaction steps, which are kinetically hindered at low pressures, might become possible and even dominant at high pressures.[14]

In addition, a materials gap exists between well-ordered surfaces conventionally used in surface science and catalysts on porous supports used in industry. Surface science investigations are traditionally conducted on low-index surfaces, which are the simplest models of a heterogeneous catalyst. These surfaces are often the thermodynamically most stable phases[24], but do not always resemble the active phases found on “real” catalysts. The reason for the discrepancy is that “real” catalysts usually consist of metal particles, which are supported on porous materials.[25] By using stepped surfaces as a subsequent step, it was found that often kink and step sites are more reactive due to the different bonding situation at the undercoordinated metal atoms. In many cases, the bond dissociation in molecules is facilitated at these sites, which is important when considering oxidation processes or reactions that require e.g. the splitting of a C-C bond. The specific nature of the site may not only influence the reactivity, but also the selectivity of the reaction.[22, 26, 27] This, at least partly, explains the different reactivity and selectivity of metal particles in many reactions, as many undercoordinated sites are found, depending on the size of the particle. Therefore, in a third step, surface science investigations were extended to model catalysts consisting of particles supported on oxidic surfaces, which resemble real catalysts much better. Usually, oxidic materials like ceria, titania and alumina are used as support.

But also when using metal particles, which exhibit different adsorption sites at different facettes, kinks and step sites, there is a huge difference between the idealised particles present in UHV and catalyst particles under reaction conditions. It was shown that a catalyst “at work” is far from being a static system; on the contrary, a catalyst is a highly dynamic system, which is changing during reaction.[28-30] First, effects like particle sintering and coalescence might change the particle density and size during reaction and therefore change the reactivity of the catalyst with time.[31] Also, changes in the oxidation state of the catalyst during the reaction and under different reactant conditions might occur. Finally, also the porous support material might change during reaction progress. The reason for using materials with high porosity is the increased specific surface area and therefore higher metal loading of the catalyst compared to flat supports. Another benefit is that by using particle-support materials the total need of the often very costly catalytically active metal is reduced.[25, 32] Depending on the reaction, the support may be inert, that means, it does not influence the reaction, or it might electronically or even chemically participate in the reaction.[33, 34] For example, titania is known for its strong metal-support interaction (SMSI) in combination with platinum group metal particles. As a result, the electronic structure of the particles is changed and influences adsorption probabilities for gases like CO or the support might even “creep” onto the particles and block reaction sites.[35-37] For ceria, a chemical change is observed in many reactions, as it is known as an oxygen buffer system.[38, 39] Effects like (reverse) spill-over of oxygen species from the ceria support to the particles were observed in many catalysed reactions and indicate a participation of the support in the reaction.[40] Additionally, for porous materials, effects like pore diffusion may also influence the reaction.[41-43]

But particles may also change reversibly due to a change in their environment during reaction. It was shown that Rh-Pd and Pd-Pt core-shell particles restructured reversibly by changing the elemental composition at the surface depending on the gas environment.[29] For nanometer-scaled platinum particles even a reversible restructuring of the facettes was observed during the CO oxidation reaction.[30] Both phenomena are explained by a change in surface free energy as a result of the change of the gas environment. In case of the bimetallic particles, different gases were applied to the particles; depending on the oxidising (O_2, NO) or reducing (CO, H_2) nature of the respective gas, new (more stable) phases like oxides may arise and cover the surface. In case of the platinum particles, the CO partial pressure in the reaction mixture (CO or O_2) determined the shape of the particles.[29, 30] These examples show to what great extent the catalyst changes *during* reaction, although it might be in the same state before and after the reaction experiment. This clearly shows the importance of *in situ* measurements, which imposes high challenges on some conventional surface science techniques.

Many of the techniques available today are also employed at elevated pressures. Amongst them are x-ray absorption techniques like near-edge x-ray absorption fine structure (NEXAFS) or extended x-ray absorption fine structure (EXAFS), x-ray scattering methods like x-ray diffraction (XRD), x-ray reflectivity (XRR), infrared techniques like Fourier transform infrared spectroscopy (FT-IR) and diffuse reflectance infrared Fourier transform spectroscopy (DRIFTS), and sum frequency generation (SFG). All these techniques have in common, that they use photons as a probe instead of charged particles; the former have a much smaller cross section with matter. Unfortunately, when detecting photons, the smaller cross section and therefore much higher mean free path also results in a loss of surface sensitivity when probing the surface. Furthermore, conventional infrared techniques lack direct information on the oxidation state of the surface.

For this reason, in the recent years many groups tackled the challenge of refining techniques, which are using electrons as a probe for *in situ* reaction experiments at elevated pressures. The most prominent examples are “high pressure” STM and XPS setups, which put special requirements on the reactor design and volume.[44, 45] As the term high pressure is misleading when not referred to UHV pressures, but to conditions used in industrial processes, the term near-ambient (NAP) or ambient pressure (AP) XPS were established for XPS setups working in the mbar regime. In this work a NAP-XPS setup was used, which enables measurements at pressures of up 1 mbar, taking a step into the pressure gap. With this technique, the surface species and oxidation states of catalysts and support were investigated *in situ* in a quantitative way. NAP-XPS was combined with simultaneous online gas analysis by using a quadrupole mass spectrometer (QMS). This allows to determine conversions and turnover frequencies (TOFs) of reactions. These techniques are explained in Chapters 2.1.2, 2.2 and 2.3.

The materials gap was approached by using catalysts of different complexity, as schematically shown in Fig. 1 (y-axis). The main reaction in focus of the investigations is the CO oxidation reaction, which is known to be catalysed by platinum group metals.[46-48] The fundamentals of this historically and practically very important reaction are reviewed in Chapter 3.1.

The first and most simple catalyst used was a Pt(111) single crystal. Although the reaction and the oxidation state of this crystal are well-known in UHV, the reaction in the near-ambient pressure regime is still under debate.[17, 21, 49] In Chapter 4 the oxidation of the Pt(111) single crystal by molecular oxygen was investigated in the temperature range relevant for the reaction (300 - 700 K) as the oxidation state of the platinum in a so-called “highly active reaction regime” is still not fully understood. Also, oxidation of platinum at elevated pressures is not yet thoroughly investigated, despite being a well-established catalyst in heterogeneous catalysis. The results were combined with ReaxFF grand canonical Monte Carlo (ReaxFF-GCMC) calculations performed in the work group of Prof. Dr. Timo Jacob of the “Institut für Elektrochemie” at the University of Ulm to elucidate the formation and the structures of the found oxides.

Following the experiments of the oxidation of Pt(111), in Chapter 5 the CO oxidation reaction on the Pt(111) single crystal was investigated at different CO:O_2 ratios and total pressures of up to 1 mbar. The insights into new effects like MTLs which were gained by this investigation acted as a basis in order to interpret the CO oxidation reaction on more complex systems.

In Chapter 6, the reaction was investigated on platinum particles supported on titania nanotube arrays under similar conditions, which were prepared in the work group of Prof. Dr. Patrik Schmuki in the Chair of Surface Science and Corrosion of the Department of Materials Science and Engineering of the University Erlangen-Nürnberg. Three different samples containing differently sized particles decorated on upright standing titania nanotube arrays were examined with regard to reactivity, oxidation states of catalyst and support and surface species at different temperatures in comparison to the Pt(111) single crystal. This system was chosen in order to compare the results to catalysts used for example in automobiles, where Pt particles supported on porous materials are used.

A possibility to tune and confine the CO oxidation reaction is to perform the reaction at the interface of graphene grown on a metal substrate. In Chapter 7 preliminary results are discussed, showing NAP-XPS investigations of the intercalation of CO and O_2 at 1 mbar and 300 K under a closed graphene sheet on Rh(111). These results show that, in theory, CO oxidation experiments confined in 2D are possible at mbar pressures.

Changing the topic, in the last chapter of the experimental chapter, in Chapter 8, the results obtained for the adsorption of ethanol on a model catalyst, namely ceria supported cobalt particles at near-ambient pressures are shown. These results give insights into the steam reforming of ethanol, which is industrially very important as the energy carrier hydrogen is produced from ethanol. As ethanol is readily available from fermentation of agricultural wastes, this reaction could be, if further improved and understood, pioneering in addressing the world energy problem.

In the last chapter of this thesis (Chapter 9), the investigations are summarised and an outlook is given.

2. Fundamentals and techniques

In this chapter, the fundamentals of the techniques, namely XPS, online gas analysis and LEED used for the reaction experiments performed during this work and the analysis of the obtained data are explained. Also, a description of the set-up of the NAP-XPS chamber used is included. Furthermore, the preparation of the different samples is described and remarks on the experimental conditions are provided.

2.1 X-ray Photoelectron Spectroscopy

2.1.1 Basics

In photoelectron emission, electrons are emitted upon irradiation of a surface with photons of sufficient energy. This process is based on the outer photoelectric effect, which was first described by HERTZ in 1884, followed by a quantum mechanical description by EINSTEIN in 1905.[50, 51] In photoelectron spectroscopy, these electrons are sorted by their kinetic energy and detected. Generally, photoelectron spectroscopy is divided into x-ray photoelectron spectroscopy (XPS) and ultraviolet electron spectroscopy (UPS) by the energy of the photons used for excitation. As a result, electrons of different levels are probed: while in XPS energetically deeper lying core levels are probed, in UPS less tightly bound valence levels are accessed.

XPS is one of the most popular techniques used in surface science. One major reason is the intrinsic surface sensitivity of this technique: as the electrons used as a probe have a limited inelastic mean free path of only several nm in condensed matter, only information from the outmost layers of a compound is collected. Usually, a core level of an element gives rise to a signal of a specific binding energy as is seen in Figure 2.1, which is the origin of the name "ESCA" (electron spectroscopy for chemical analysis) for XPS. On the way through matter, photoelectrons are undergoing inelastic scattering processes like electronic excitations or excitation of electron-hole pairs at the Fermi level of metals, which change their kinetic energy. All electrons that experience scattering events ("secondary electrons") contribute to the background increase at low kinetic energies (high binding energies) measured in XPS.

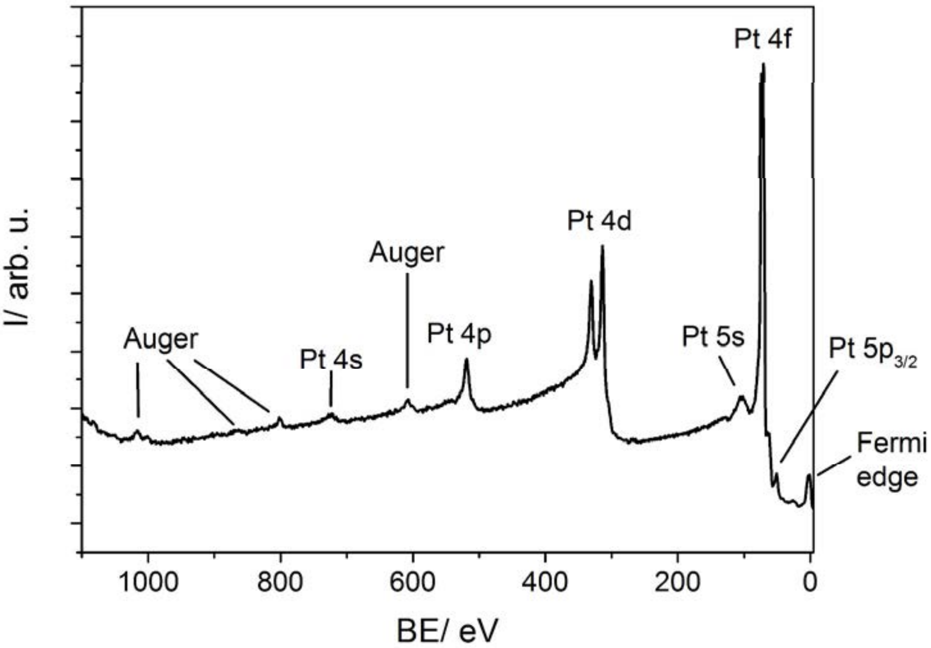

Figure 2.1: Survey spectrum of a Pt(111) single crystal.

This is observed in Figure 2.1, which shows a typical survey spectrum of a Pt(111) single crystal. All signals that are not related to primary photoelectrons are Auger signals, created by decay processes of core holes. These core holes are filled by electrons of outer shells and on account of the energy conservation, either a photon or an Auger electron can be emitted, which then is also detected in the spectrum. The photo- and Auger effect are shown in Figure 2.2. An easy way to discriminate Auger electrons from photoelectrons is changing the excitation energy, as signals from Auger processes change the position in the XP spectrum, while photoelectrons emerge at the same binding energy.

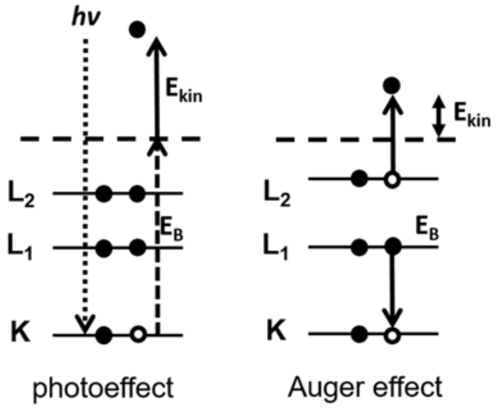

Figure 2.2: Schematic drawing of the photo- and the Auger effect.

Another advantage is that XPS allows for a quantitative analysis. This means the XP signal is proportional to the number of excited core levels, taking into account element-specific cross sections.

Upon irradiation, photoelectrons are emitted on condition that the work function Φ is overcome by the energy of the photons.[13] As the kinetic energy E_{kin} of the electrons can be measured, the binding energy E_B can be easily calculated as follows:

$$E_B = h\nu - E_{kin}\,. \qquad \text{(IV)}$$

This equation is valid for free atoms and molecules in the gas phase; here the vacuum level (E_{vac}) is used as energy reference, where the electron has no interaction with the core hole state. The binding energy E_B is considered as the difference between the ionized final state E_f^{N-1} containing *N-1* electrons and the neutral initial state E_i^N containing *N* electrons:

$$E_B(k) = E_f^{(N-1)} - E_i^N\,. \qquad \text{(V)}$$

Equation (IV) describes the frozen orbital approximation, which is neglecting any rearrangement of the orbitals as a result of photoemission. In this case, the binding energy E_B exactly equals the negative of the Hartree-Fock orbital energy of the initial state of the electron $-\varepsilon_k$:

$$E_B(k) = -\varepsilon_k. \qquad \text{(VI)}$$

This approximation is known as the Koopman’s theorem.[12]

In practice, such calculated binding energies often are only estimates. The photoionization process is influenced by initial as well as final state effects, contributing both to the measured binding energy and thus to the chemical shift. Firstly, the electrons are not frozen but relax in response to the core hole creation and therefore lower the energy of the final state (final state effect). Atomic relaxation might occur in any phase (solid, liquid, gas) but in case of solids even an electronic relaxation in neighbouring atoms can contribute, which is called extraatomic relaxation. Also, excitation of additional electrons into unbound states (shake-off) or unoccupied valence band states (shake-up) might occur, resulting in satellites. Nevertheless, although core levels are probed, which are not directly involved in chemical bonds, an element might exhibit a typical shift in XP binding energy depending on the chemical surrounding. The shift is dependent on the electronegativity of the neighbouring atom and can be used in order to obtain a better understanding of the bonding situation of the compound under investigation. For example, metal oxides often exhibit binding energy shifts of several eVs due to the oxygen environment, making the estimation of oxidation states possible.[13] But not only atoms attached to a different chemical surrounding exhibit a shift, even different binding motifs might give distinguishable XP signals. Here, a good example is CO on Pt(111), where the signal of CO adsorbed in on-top sites emerges at 532.7 eV and the signal adsorbed in bridge sites at 531.0 eV in the O 1s due to different environment of the adsorbed CO molecules.[52, 53]

These effects can be used in order to determine oxidation and binding states in chemical reactions.

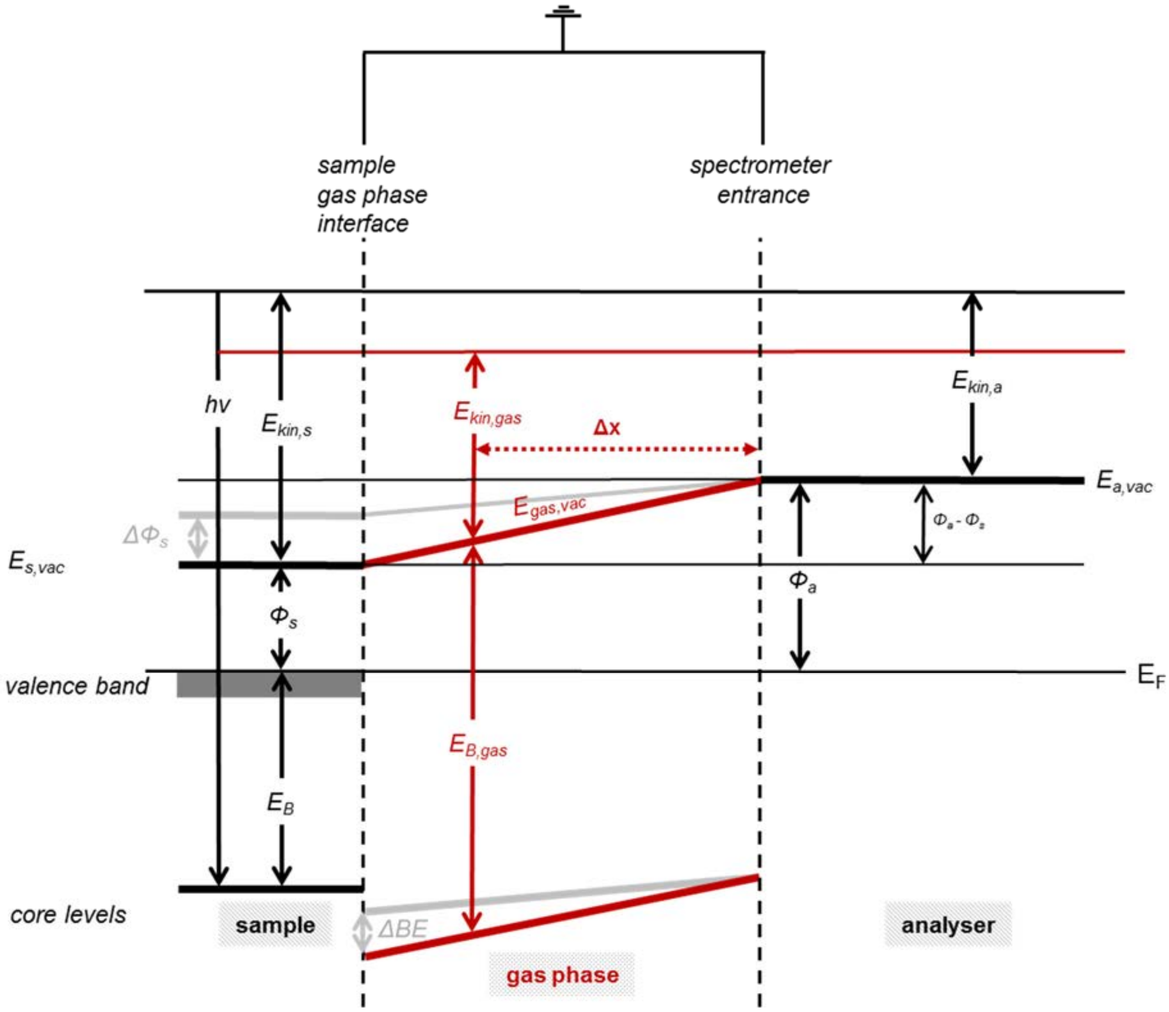
sample gas phase interface
spectrometer entrance
hv
$E_{kin,s}$
$E_{kin,gas}$
Δx
$E_{kin,a}$
$E_{a,vac}$
$E_{gas,vac}$
$\Delta\Phi_s$
$E_{s,vac}$
$\Phi_a - \Phi_s$
Φ_s
Φ_a
valence band
E_F
$E_{B,gas}$
E_B
core levels
sample
ΔBE
gas phase
analyser

Figure 2.3: Schematic diagram for emission and detection of photoelectrons without (black) and with gas phase over the sample (red).[10, 54, 55]

Additionally, being an initial state effect, spin-orbit coupling is neglected as both E_i^N and E_f^{N-1} are single-valued and therefore predict only one peak in the photoelectron spectrum. In reality, the energy of the electronic states does not solely depend on the electronic configuration, but also on angular momentum coupling. As a result of photoexcitation, an unpaired spin is left which can be oriented up or down. Therefore, any state with $l > 0$ (= s levels) can couple with both spin states observed as a doublet in the XP spectrum, with the total angular momentum $j = l \pm 1/2$.[12] Depending of the probed core level (p, d, f…) the doublet has a specific area ratio.

Usually, solid metallic samples are investigated with XPS, where the Fermi level is used as energy reference. As analyser and sample are conductively connected and grounded, their Fermi levels are aligned. The work functions of sample Φ_s and analyser Φ_a are not equal, resulting in a contact potential $V_{a\text{-}s}$ due to the work function difference Φ_a - Φ_s, which has to be considered. In order to correct equation (VII), the work function Φ_a has to be subtracted[10, 12, 13]:

$$E_B = h\nu - E_{kin} - \Phi_a \ . \qquad \text{(VII)}$$

The energy diagram for XPS in UHV is schematically shown in Figure 2.3 in black; the red and grey lines are not yet discussed as there is no gas phase contribution in UHV.

2.1.2 Near-ambient pressure XPS

During the last decades, XPS has been refined in order to be used at higher pressure up to several mbar.[45, 56-59] Near-ambient pressure XPS (NAP-XPS) techniques are based on a system of differentially pumped stages in combination with small apertures, lowering the pressure from mbar pressures to high vacuum between the measurement chamber and the analyser. As both analyser and x-ray gun require high vacuum conditions, additionally, the x-ray source has to be sealed against the high pressure of the measurement chamber. This is often realized by introduction of a Si_3N_4 window between x-ray source and sample. In more advanced systems, electron optics are implemented, which focus the electrons on the apertures and therefore increase the transmission of the electrons through the differential pumping system.[56] The major challenge in using XPS at high pressures lies in the loss of signal intensity due to scattering of the photoelectrons coming from the sample with the gas phase. As the electrons are traveling through the gas phase, they may undergo elastic or inelastic collisions with the gas particles, whereas the mean free path depends on the kinetic energy of the electrons, the gas pressure and the nature of the gas.[45] For the herein used NAP-XPS chamber a first order exponential decay of the sample signal was found for increasing sample-aperture distance (= larger gas phase) following:

$$\ln \mathrm{I}/\mathrm{I}_0 = -(\sigma_e \cdot d_{\mathrm{eff}} \cdot p)/(k \cdot T) \qquad \text{(VIII)}$$

where σ_e denotes the cross section for electron scattering, d_{eff} the sample-aperture distance, p the partial pressure of the gas, k the Boltzmann constant and T the gas temperature. This behaviour illustrates the need to lower the sample-aperture distance and it was found that at 1 mbar the effective distance should be around 1 mm.[58] Furthermore, the pressure drops considerably through the first aperture. Unfortunately, the pressure gradient also expands over the aperture into the measurement chamber, and hence a critical distance between first aperture and sample should be maintained in order to have the background pressure on the sample. This is especially important if a strong pressure-dependence is observed in the investigated system, as different phases could be influenced by a pressure drop. In this context, Bluhm *et. al* found a necessary minimal distance of 2·z, where z is the diameter of the first aperture, in order to obtain 95 % of the nominal background pressure over the sample at their NAP-XPS machine at the synchrotron facility BESSY II.[56] In practice, the loss in intensity due to scattering of the photoelectrons with the gas phase still either needs to be compensated by longer acquisition times or the use of x-ray sources with high fluxes, as available in synchrotron facilities.

In contrast to UHV work, in NAP-XPS also gas phase signals are detected, usually occurring at higher binding energies than the signals resulting from surface signals. Figure 2.4 shows selected O 1s spectra recorded during growth of platinum oxide on Pt(111) at 1 mbar O_2 and a sample temperature of 300 K. The signal at higher binding energies stems from the O_2 gas phase, whereas the growing signal at lower binding energy is a result of platinum oxide growth.

A shift of the gas phase signal with time is observed; this can in principle have different reasons as explained in the following.

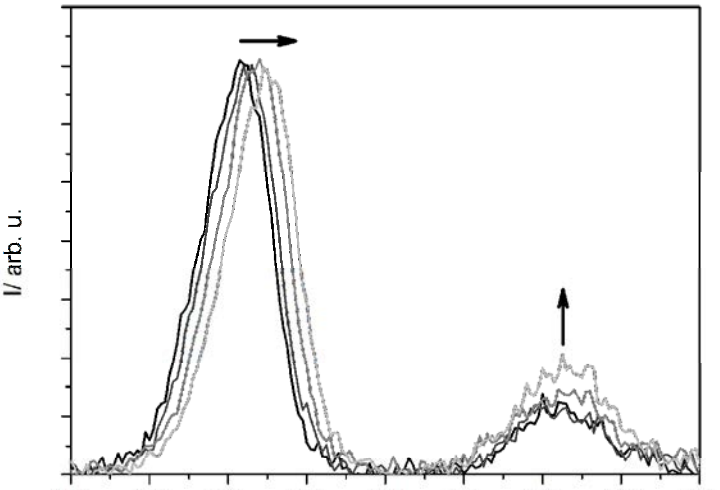

Figure 2.4: Selected O 1s spectra during platinum oxide growth on Pt(111) at 300 K and 1 mbar O_2.

The gas phase contribution to the energy level diagram for XPS measurements is shown in red in Figure 2.3. As already explained, all photoelectrons are influenced by the contact potential $V_{a\text{-}s}$ (please see also Figure 2.5) resulting from the work function difference Φ_a - Φ_s between sample and analyser. In Figure 2.3 the first aperture denotes the analyser entrance, while the contributions of all other apertures are neglected and the work function of the analyser is assumed to be constant.

Firstly, in contrast to photoelectrons originating from the sample, the gas phase molecules do not have the same position within the chamber, or in other words, the molecule-aperture distance is not the same for different molecules. This is schematically depicted in Figure 2.3 and 2.5 as the distance Δx. Therefore, photoelectrons originating from different places between sample and analyser entrance are influenced by a different potential, unlike the sample, as here Δx is constant and the potential is the same for all electrons. As a consequence, the gas phase signal is composed of an average of different kinetic energies due to the different position of the gas phase molecules within the probed volume and therefore the position-dependent potential $V(x)$. The probed volume is illustrated in Figure 2.5 as the overlap of incoming x-rays (yellow) and way to the analyser (blue) within the analyser focus. This is only a schematic drawing; the evaluation of the real probe volume is difficult as the volume where most of the signal originates from and hence the weighting of signal contribution from different positions within this volume is unknown. Shifts in the binding energy of the gas phase therefore may be observed if the sample-aperture distance is changed, which, within a certain range, always happens by introduction of a new sample into the chamber. Additionally, insufficient manipulator cooling at high heating temperatures may also lead to changes in the manipulator on account of thermal expansion and therefore to a changed aperture-sample distance.

Secondly, the gas phase signal can shift due to charging of the gas phase with time. This is especially observed in absence of a sample, as charge neutralization then is only possible at the chamber walls. When using metallic samples, usually, charge neutralization may also occur at the sample surface, therefore this effect is not as pronounced.

Another important reason for binding energy shifts of the gas phase signals is a change in the work function of the sample surface. This explains the shift of the gas phase observed in Figure 2.4. During the growth of platinum oxide at the surface, the work function of the surface changes, which in turn changes the measured binding energy $E_{B,gas}$ of the gas phase, as depicted in grey in Figure 2.3. This is rationalized by the gas phase being referenced to the vacuum level $E_{gas,vac}$. On the contrary, the surface signals do not experience any shifts due to a change in work function, as they are referenced to the Fermi level and therefore the binding energy E_B is not influenced.[54, 60] This effect can be employed for determining unknown work functions by comparison to reference samples with a known work function. For gas molecules in the very proximity to the sample surface, the value of the binding energy shift corresponds to the value of shift in work function.[54] This in turn means that for practical application, either very defined, narrow x-ray beams as available in synchrotron facilities, and/or grazing incidence is required to exclude the contribution of gas molecules in larger distance to the sample.

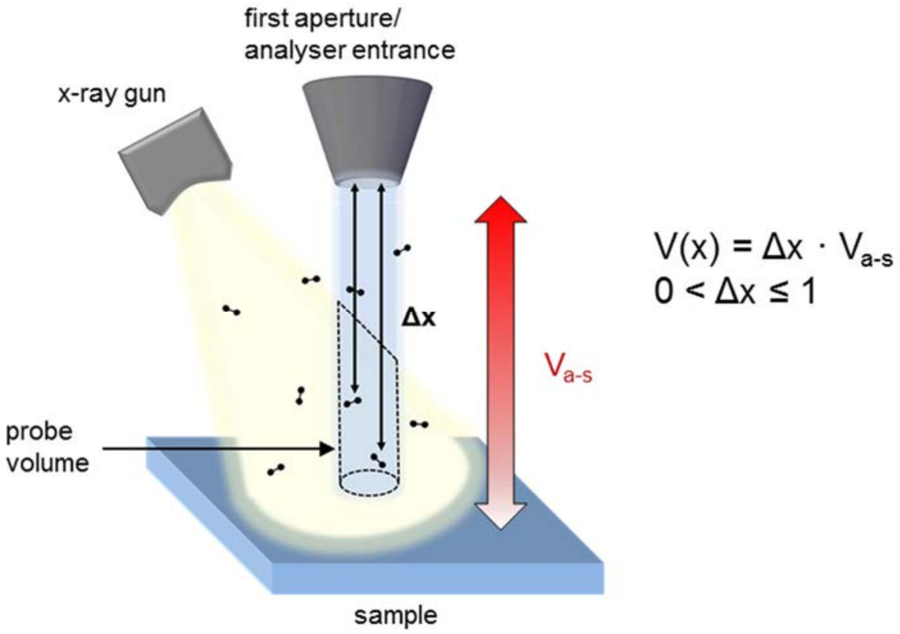

Figure 2.5: Schematic drawing of the probed volume and the molecule-aperture distance Δx within the contact potential $V_{a\text{-}s}$.

2.1.3 Impurities

One challenge emerging by applying surface techniques at higher pressures is the occurrence of impurities. One of the major reasons for the work under UHV conditions is the feasibility to work on clean surfaces. Most NAP-XPS systems are based on UHV chambers, in which one of the chambers is back-filled to mbar pressures. This theoretically gives the opportunity to probe the surface under clean UHV conditions before and after experiments. Unfortunately, practically, this is only partly true as pumping back down to UHV after a high pressure experiment might take several hours. Additionally, one has to be aware that gases used for experiments always contain small amounts of impurities. In high quality gases, these impurities are in the range of ppm, not causing surface contaminations in typical UHV experiments, albeit at pressures in the mbar range. For example, assuming a sticking coefficient of 1, at a pressure of 10^{-6} mbar, the partial pressure of the impurity gas corresponds to 10^{-12} for 1 ppm. This causes no significant contamination of the sample within the time scale of the experiment. On the contrary, at mbar pressures, the partial pressure of the impurity gas reaches 10^{-6} mbar, which could contaminate the surface within 1 second. This is especially challenging, as the acquisition times of near-ambient pressure experiments are usually higher due to the loss in signal based on damping of the photoelectrons in the gas phase, as explained in Chapter 2.1.2.

Another problem is the emergence of new impurity compounds at the surface based on the higher pressure. Throughout this thesis this has shown to be in particular an issue when using the Pt(111) single crystal at high oxygen partial pressures and elevated temperatures. It is known that platinum single crystals often contain bulk impurities such as Si and Ca.[61] When heated in oxygen, they form stable oxides, which poison the surface and sometimes are difficult to detect by conventional XPS. Therefore, thorough attention has to be paid to the nature of the detected surface phases as this effect is more pronounced at elevated pressures as compared to UHV and will be further discussed in Chapters 4 and 5. Interestingly, after exposure to air and reintroduction to the chamber, the amount of silicon found in the near-surface region is increased again and silicon oxide formation is enhanced compared to the state before exposure to air. This could be explained by a chemical potential and therefore higher diffusion/solubility of oxygen in the crystal at the higher oxygen partial pressure in air.

2.2 “GAP” NAP-XPS setup

2.2.1 Setup

The NAP-XPS setup used is home-built and was constructed within the scope of a PhD thesis.[58] The schematic drawing of the chamber is shown in Figure 2.6. In principle, it is composed of three separate UHV chambers: the measurement chamber, the preparation chamber and the transfer system, which enables transfer between the two UHV chambers as well as introduction of new samples through a load lock, which can be reversibly vented and pumped. All chambers are pumped by a combination of turbomolecular pumps (TPs) backed by roughing pumps, enabling UHV pressures. All sample holders are transferable through a system of transfer arms (TFS), heatable by resistive heating and the manipulators in measurement and preparation chamber can be cooled with liquid nitrogen. Temperature measurement is enabled by type K thermocouple (TC) connections through the manipulator to the sample. For all investigations, the TC was directly spot-welded onto the sample holders or the sample.

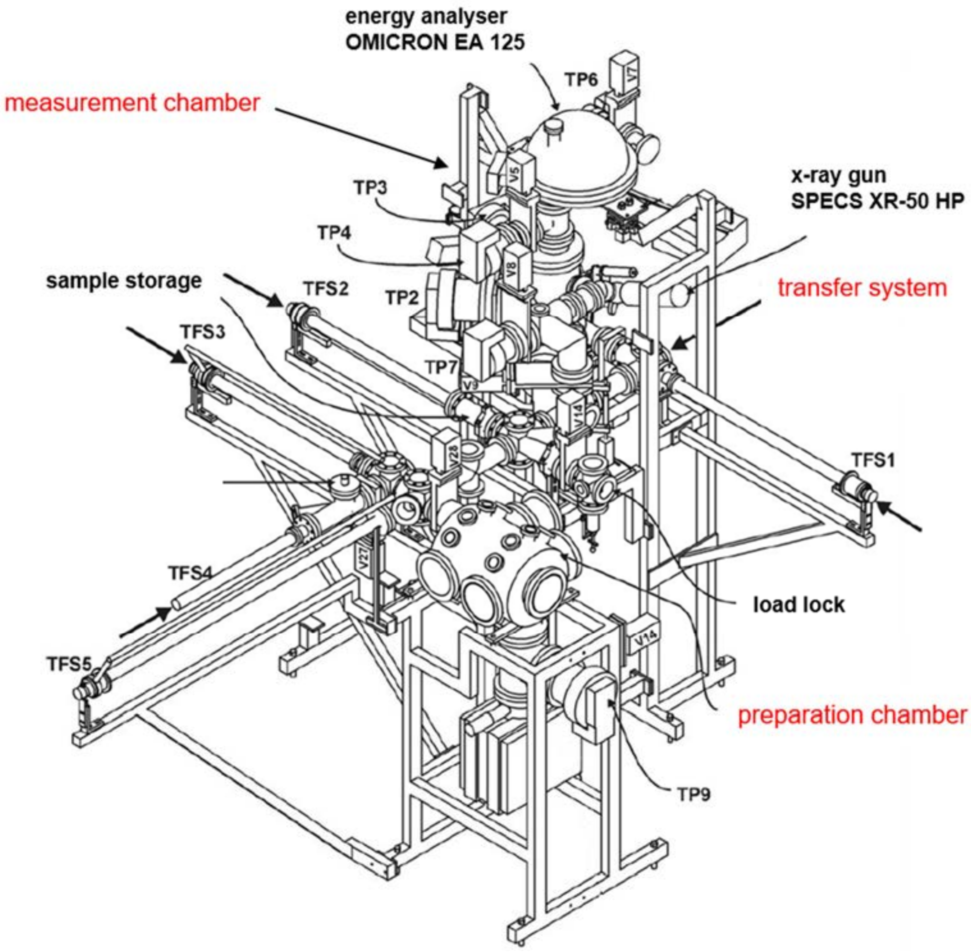
energy analyser
OMICRON EA 125
TP6
V7
measurement chamber
V5
TP3
x-ray gun
SPECS XR-50 HP
TP4
V8
transfer system
sample storage
TFS2
TP2
TFS3
TP7
V9
V14
TFS1
V28
V27
TFS4
load lock
TFS5
V14
preparation chamber
TP9

Figure 2.6: Schematic drawing of the GAP apparatus.[58]

The preparation chamber is equipped with a sputter gun and LEED optics to enable clean surface preparation and structure examination. Also, the UHV TPD experiments were conducted in this chamber using a QMS. The transfer system connects both chambers and has access to the load lock and a sample storage, which can store up to four samples.

The centrepiece of the apparatus is the measurement chamber. Here, XPS measurements in UHV as well as at near-ambient pressure up to ~1 mbar are possible. As excitation source a SPECS XR-50 HP x-ray gun is used, which was attached during this thesis and replaced the previous model. In contrast to the old x-ray gun which used a 3 µm thick Al window as a seal, the new model uses a 200 nm thick Si_3N_4 window, which is more stable and easier to handle and withstands pressures up to 20 mbar on the measurement side against the high pressure in the x-ray gun. Both Al and Mg K_α can be used for excitation and were used in this work. For electron detection a modified OMICRON EA 125 energy analyser with an increased working distance is used.

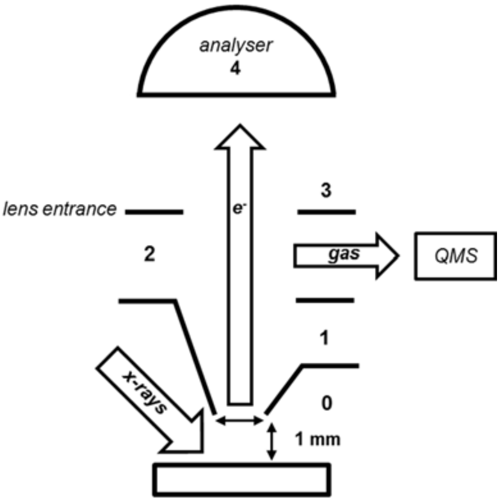

Figure 2.7: Schematic drawing of the differential pumping stages of the measurement chamber.

The basic principle of the NAP-XPS setup is based on four differentially pumped stages between sample and analyser, reducing the pressure from mbar to high vacuum. This is schematically depicted in Figure 2.7, where the numbers denote the respective differential pumping stage. The incidence angle of the x-rays is 65°, whereas detection takes place in 0° emission with respect to the surface normal. As already discussed in Chapter 2.1.2, during near-ambient pressure experiments, the sample is put in a distance of ~1 mm to the first aperture which has a diameter of 1.4 mm. For measurements at pressures higher than 10^{-3} mbar the gate valve in front of the TP of stage 0 is closed and pumping solely occurs through the first aperture.

During the CO oxidation experiments, a QMS was attached to the second differentially pumped stage to allow simultaneous online gas analysis. By introduction of a copper flange with a 1.5 mm pin hole in front of the QMS part, the pressure was reduced to ~10^{-7} – 10^{-6} mbar during experiments conducted at 1 mbar. Additionally, a TP was attached to the QMS part to maintain high vacuum.

Gas dosage was accomplished by background dosing through two separated leak valves. Therefore, simultaneous use of two different gases is possible. For pressure measurements in the UHV range hot cathodes were used, whereas at elevated pressure a MKS Barathron 121 pressure gauge was applied, which allows gas-type independent pressure measurement. Additionally, a Pfeiffer Vacuum PKR 251 full range gauge is attached to the chamber in order to bridge the pressure range from 10^{-6} – 10^{-3} mbar.

For further details of the setup please see Refs. [57] and [58].

2.2.2 Quantification of XPS

Throughout the work on the Pt(111) single crystal, the binding energies of the O 1s region were referenced to the CO bridge and on-top binding energies [53] and for the work on the Rh(111) to the binding energies of CO in three-fold hollow and bridge sites [62, 63], whereas all other spectra were referenced to the Fermi edge. Shifts in the gas phase were not considered, as they may arise due to different reasons as discussed in Chapter 2.1.2.

For the investigations on the platinum samples, all coverages given were obtained from a comparison to the c(2x4) CO superstructure with a coverage of 0.5 ML.[64] Thereby 1 ML corresponds to one adsorbate molecule or atom per surface atom on the Pt(111) surface

For the experiments on the Rh(111) crystal, the coverages were obtained from a comparison of the intensities to the (2x2)-3CO superstructure of CO on Rh(111) with a coverage of 0.75 ML.[62, 65]

It was found that the coverage determination is influenced by the sample position, due to the changing gas phase with changing sample-aperture distance. Therefore, a more accurate sample positioning was installed by means of a camera attached to a CF40 window flange in front of the measurement chamber.

For data evaluation, the spectra were first fitted using the CasaXPS Software Version 2.3.16Dev6. The processed data was exported and plotted using Origin. The Pt 4f spectra were fitted by an asymmetric pseudo-Voigt function after subtraction of a Shirley background. From the Ti 2p spectra, also a Shirley background was subtracted, but symmetric pseudo-Voigt functions were used for fitting. A linear background was subtracted from C 1s and O 1s core level spectra prior to fitting for Chapters 4-7. For the surface components, a symmetric function was used, which reproduces the data well, with the exception of the graphene C 1s signals in Chapter 7, where an asymmetric function was used according to [66]. The gas phase peaks in the presence of the sample were fitted with line shapes that were determined from reference measurements of the respective gas, obtained in absence of a sample. The O_2 gas phase was fitted with an asymmetric line shape, whereas the CO and CO_2 gas phase signals were fitted with symmetric functions. In Chapter 8, Tougaard (Ce 3d) or Shirley (O 1s, Co 2p) baselines were subtracted and symmetric line shapes were used.

CO conversions were always calculated as

$$1 - (CO/CO_0) = CO_2/(CO_0) \qquad \text{(IX)}$$

in percentage and to correct for changes in pressure during the experiment, CO_0 is calculated at time t as $CO(t)+CO_2(t)$.

Turnover frequencies (TOFs) were calculated from the conversions using the method described in [67]. The flux of CO molecules on the surface was calculated from the impingement rate of CO at the given partial pressure using the Hertz-Knudsen equation (I) (determined from XP gas phase signals) and a gas temperature of 300 K divided by the surface atom density of the respective sample. The flux was then multiplied with the CO conversion to obtain the TOF.

Table 2.1: Excitation sources for the respective chapters.

Chapter	Excitation source
4	Mg K_{α}
5	Al K_a: ramp 2 K/min Mg K_{α}: all other
6	Al K_a
7	Al K_a
8	Al K_a

For excitation either Mg or Al K_{α} was used with energies of 1253.6 eV and 1486.6 eV, respectively. The excitation sources for the investigations in the different chapters are given in Table 2.1. Further details on measurement parameters are given in the respective chapters.

2.3 Online gas analysis

2.3.1 Fundamentals

In heterogeneous catalysis, often devices such as mass spectrometers and gas chromatographs are used in order to measure gaseous reactants, products and their conversion. Often, these techniques are combined with other techniques, which are able to detect the reaction progress at the surface. By means of this combined approach, simultaneous identification of gas phase species and surface species as well as catalyst/ support oxidation states is possible.[4]

Throughout this thesis, NAP-XPS which gives information about catalyst, support and surface species was combined with simultaneous online gas analysis using a quadrupole mass spectrometer (QMS). In surface science, a QMS is commonly used in UHV for temperature-programmed desorption (TPD) experiments. A surface is covered with one or more species and heated with a linear heating ramp β ($T = T_0 + \beta t$), while detecting the desorbing atoms/molecules using a QMS. Here, it is utilised that the signal in the QMS is proportional to the partial pressure of the desorbing gas when neglecting readsorption and under the assumption of infinitely high pumping speed.[68] Using this approach, TPD often is used to determine activation energies applying the Polanyi-Wigner equation:

$$r_{des} = \nu_n \cdot e^{\frac{-Ea}{RT}} \cdot \Theta^n \qquad \text{(X)}$$

where r_{des} is the desorption rate, ν_n the frequency factor, E_a the desorption activation energy, R the ideal gas constant, Θ the surface coverage and n the desorption order.[4]

This procedure has also been applied at elevated pressures in order to obtain reaction rates and kinetics.[69] In many publications, mass spectroscopy has been used in order to link conversion to a certain surface state determined by different techniques and also for evaluation of activation energies.[17, 44, 49, 67, 70] Often, a major draw-back in this context is the distance of the QMS to the sample surface, as local probing is challenging. Therefore, in many cases only conversions, which are integrated over the chamber volume, are obtained, which renders the determination of real activation energies difficult. Another problem is that the gas detection cannot occur at high pressures, but the pressure in the QMS has to be reduced to high vacuum for many detectors. Therefore, often differentially pumped systems are used, which alter the gas composition as the pumping is gas-dependent.[17, 49, 67, 71-74] During the investigation of the CO oxidation reaction throughout this thesis, unfortunately, deriving any kinetic and thermodynamic parameters was not possible due to the strong mass transfer limitations observed and/or the influence of the pumping stages.

2.3.2 Quantification of the online gas analysis and TPD measurements

Usually, for the near-ambient pressure experiments the Faraday cup was used as detector. For measurements at 10^{-2} and 10^{-3} mbar, a secondary electron multiplier was used.

For both detectors, factors were evaluated for the correction of the mass spectra for contributions due to CO_2 decomposition at the QMS filament, the different QMS sensitivities and gas-dependent pumping of the differential pumping system.

CO conversions and TOFs using the QMS signals were calculated using the same procedure as explained for XPS in Chapter 2.2.2 using the surface atom density of the Pt(111) surface (1.5×10^{15} cm^{-2}) or particles (please see Figure 6.2).

The TPD measurements conducted in UHV in Chapter 7 were acquired in the preparation chamber using a secondary electron multiplier. The manipulator of the preparation chamber was cooled with liquid nitrogen for 1.5 h prior to the TPD experiment. CO and O_2 was intercalated in the measurement chamber at 1 mbar and after pump-down to UHV, the sample was transferred to the preparation chamber for the TPD experiment.

2.4 Low Energy Electron Diffraction

Low Energy Electron Diffraction (LEED) is a well-established method in order to determine the structure of well-ordered crystal surfaces and ordered adsorbate overlayers. Usually, electrons with kinetic energies of 10-500 eV are used, as their de-Broglie wavelength is in the order of 0.1 nm and therefore comparable to interatomic distances in crystals and molecules.[75, 76] This technique is especially well-suited in order to investigate surfaces, because of the small inelastic mean free path of these electrons of around 1 nm. Thus, in contrast to X-ray diffraction, LEED only gives information about the topmost atomic layers. A collimated, mono-energetic beam of electrons is directed onto a surface. Back-scattered electrons and their diffraction pattern are detected by a fluorescence screen. Therefore, the reciprocal space is directly recorded and gives insight into the periodicity of the surface. More detailed analysis in order to obtain quantitative information about atomic positions within the surface can only be obtained by an I-V (I(E)) analysis, where the energy-dependence of the LEED spot intensities has to be evaluated and solved in combination with computational simulations.[75, 77]

In this work LEED was used in order to verify the surface structure of clean single crystals as well as for coverage calibration by preparing ordered surface structures.

2.5 Experimental remarks

2.5.1 Sample preparation

Pt(111)

The purity of the Pt(111) crystals used was 99.999% and the accuracy of the polishing angle was <0.1° as denoted by the supplier (MaTecK). They were cleaned by cycles of Ar^+ sputtering at $2x10^{-5}$ mbar at room temperature (1 kV, 20 min, ~5 -10 μA) and annealing at 1100 K (3 min). The surface order was regularly checked by LEED. The Pt(111) single crystal were spot-welded directly to the sample holder using Ta wires. For temperature measurement a type K thermocouple was spot-welded on the crystal.

$Pt_{5nm}TiO_2NT$, $Pt_{15nm}TiO_2NT$ and $Pt_{ion-milled}TiO_2NT$ samples

The nanotube-supported Pt particles samples investigated in Chapter 6 were prepared by Jeong-Eun Yoo of the Chair of Surface Science and Corrosion (Prof. Patrik Schmuki) of the Department of Materials Science and Engineering of the University Erlangen-Nürnberg.

The TiO_2 nanotube arrays were prepared by anodization in an electrolyte based on *o*-H_3PO_4 with 3 M HF (Sigma-Aldrich). Prior to the anodization process, the Ti foils (0.125 mm thick, 99.7 % purity, Goodfellow) were degreased by sonication in acetone, ethanol and deionized water and dried in a N_2 stream. A two-electrode setup consisting of a Ti foil (15 x 15 mm^2, working electrode) and a Pt gauze (counter electrode) was used for the anodic growth, where a potential of 15 V was applied for 2 h (by a Voltcraft VLP 24 Pro DC power supply). The nanotube arrays were rinsed with ethanol and dried in N_2. The as-prepared films were coated with Pt of nominal coverages of either 5 nm ($Pt_{5nm}TiO_2NT$) or 15 nm ($Pt_{15nm}TiO_2NT$) using a high vacuum sputter coater (Leica – EM SCD500) and a 99.99 % Pt target (Hauner Metallische Werkstoffe). The Pt-coated samples were annealed in N_2 at 873 K for 1 h in order to form Pt particles (dewetting of Pt layers). After the dewetting process, the samples were heat-treated in air at 723 K for 1h for crystallization of TiO_2 NTs. For a detailed preparation procedure please see Ref. [78]. The anatase/rutile ratio was 0.6 after the preparation procedure.

For the preparations of the ion-milled sample ($Pt_{ion-milled}TiO_2NT$), after the preparation of $Pt_{15nm}TiO_2NT$, an IM 4000 (Hitachi) ion mill was used in order to remove the upper rim of the tube. Acceleration potential, discharge potential, discharge current, and ion beam current were 2 V, 1 V, 360 μA, and 110 μA, respectively. The flow rate of Ar gas was kept at 0.08 cm^{-3}/min, and the sample was rotated at 25 r/min (360˚).

Preparation of the $Pt_{5nm}TiO_2(110)$ sample

The accuracy of the polishing angle of the $TiO_2(110)$ single crystal used in Chapter 6 was < 0.5° as denoted by the supplier (CrysTec). It was cleaned by cycles of Ar^+ sputtering at $8x10^{-6}$ mbar (1 kV, 30 min, ~5 μA), annealing at 950 K in $5x10^{-6}$ mbar O_2 for 10 min, and cooling in oxygen to T<400 K. Cleanness was checked by XPS, and the structure of the 1x1 reconstruction[79] was confirmed by LEED before Pt sputtering and after Ar^+ sputtering used to remove the Pt from the surface after the reaction experiments (see Figure 11.3.1 of the Appendix). After the cleaning procedure, the crystal was exposed to ambient atmosphere and 5 nm Pt were sputtered onto it. In order to ensure identical preparation conditions as for the nanotube-supported samples, the sample was heated to 723 K in air for 1 h prior to use.

Cleaning of the TiO_2-supported samples

All TiO_2-supported samples contained carbon impurities from wet-chemical preparation and exposure to ambient conditions. Therefore, the samples were heated to 400 and 600 K in case of the $Pt_{5nm}TiO_2(110)$ in 1 mbar of O_2 until no further carbon was observed with XPS. Phosphorous was identified as impurity due to the preparation procedure, where H_3PO_4 was used.

The TiO_2 NT-supported samples were spot-welded directly to the sample holder using Ta wires; for accurate temperature measurements a type K thermocouple was directly attached to the samples. The $TiO_2(110)$ single crystal was attached to a Ta foil, and a type K thermocouple was spot-welded to this foil. All samples were heated by resistive heating. The maximum temperature deviation between the thermocouple and the $TiO_2(110)$ single crystal was ~25 K, as deduced from an independent measurement with a pyrometer.

The SE micrographs of the $Pt_{5nm}TiO_2(110)$ sample were acquired with a Zeiss EVO 40 SEM working with a thermionic tungsten emitter at a base pressure in the 10^{-6} mbar range. The morphology of the TiO_2NT-supported samples was determined by field-emission scanning electron microscopy (Hitachi FE-SEM S4800, Japan).

Rh(111)

The purity of the Rh(111) crystal used was 99.99% and an accuracy of the polishing angle of <0.4° was denoted by the supplier (MaTecK). The crystal was cleaned by Ar^+ sputtering at $8x10^{-6}$mbar at room temperature (1 kV, 30-45 min, ~5 μA) and flashing to 1100-1200 K. The surface order was regularly checked by LEED. The Rh(111) single crystal was spot-welded directly to the sample holder using Ta wires. For temperature measurement a type K thermocouple was spot-welded on the crystal. Prior to the first use in experiments, the crystal was heated to ~1500-1600 K once, leading to a sharp LEED pattern.

Graphene was grown by a CVD process dosing ~8x10^{-9} mbar propene at 920 K, until saturation was reached in the C 1s (please see Chapter 7.3 for details). After the experiments, graphene was removed either by sputtering or heating in 1x10^{-6} mbar O_2 at 900 K for 12 min.

Preparation of the Co/CeO_2 sample:

The Cu(111) crystal used in Chapter 8 was cleaned with cycles of Ar^+ sputtering (1 keV, 300 K, 45 min) and annealing at 873 K for 5 min, leading to a sharp hexagonal LEED pattern and a contamination level (typically C and O) below 1%, verified by XPS. The CeO_2(111) film was prepared on Cu(111) in a similar way as reported in literature[80-83]. Ce metal (Alfa Aesar, purity 99.9%) was evaporated with an e-beam evaporator from a Mo crucible with an evaporation rate of 0.15 Å/min in an O_2 background pressure of 1×10^{-6} mbar at a substrate temperature of 523 K for 100 min. O_2 was pumped down at the end of the growth, when the sample cooled down to 430 K. The Ce rate was set already in the absence of O_2 with a quartz crystal microbalance and it was stable during the film growth, as it was checked also at the end of Ce evaporation. The ceria film thickness obtained this way was 17.3 Å assuming CeO_2 stoichiometry, corresponding to 5.5 ML of CeO_2(111). Investigations of the film with LEED showed the characteristic (1.5 × 1.5) pattern of CeO_2 with the complete absence of the Cu(111) spots; the latter observation is attributed to the formation of a continuous ceria film. Additional treatments in 1x10^{-6} mbar of O_2 up to 673 K did not result in any appreciable changes in LEED, in the Cu/Ce XPS intensity ratios and in Ce 3d peak shapes. No dewetting of the ceria film was observed during the experiments, since no increase in the Cu $2p_{3/2}$ XPS intensity was observed. Cobalt was evaporated from a wire (99.99% purity, MaTecK GmbH). The cobalt deposition rate was calibrated by a quartz microbalance. The Cu(111) single crystal was attached to the sample holder with Ta wires; a type K thermocouple was attached to a hole drilled into the single crystal and therefore was in direct contact to the crystal.

2.5.2 Gases

The purity of the used gases was 4.7 for CO and 5.0 for O_2. The purity of propene was 2.5. Ethanol (cleanliness: 99.9%) was further purified with freeze-pump-thaw cycles prior to use.

3. Investigated reactions

In this chapter the fundamentals of the reactions that were investigated throughout this work are discussed. First, the adsorption of oxygen and CO on platinum is discussed, mainly focussing on UHV work, as the effect of increased pressure will be discussed first for O_2 adsorption and also co-exposure of O_2 and CO in Chapter 4, 5 and 6. Additionally, short introductions for intercalation of molecules under graphene and for ethanol steam reforming will be given, being in the focus of the Chapters 7 and 8 of this thesis.

3.1 The CO oxidation reaction on platinum

In the CO oxidation reaction, gaseous CO and O_2 are reacted, where the only product is CO_2:

$$2\,\mathrm{CO} + \mathrm{O_2} \rightleftharpoons 2\,\mathrm{CO_2}. \qquad \text{(XI)}$$

The reaction is exothermic and especially metals such as Pt and Pd were found to be highly active in catalysing this reaction. The investigation of this reaction has aroused tremendous interest among the scientific world during the last decades. There are two major reasons for this: first, the CO oxidation is a practically very important reaction, as nowadays every car contains a catalytic converter, which converts toxic gases including CO from the exhaust of the combustion engine. The need of the conversion of CO lies in its toxic nature; by oxidation of CO the atoxic CO_2 is formed. Not less important is the removal of CO from large gas streams, necessary due to the ongoing growth of petrochemistry.[47, 84]

The second reason lies in the simplicity of this reaction. As shown in equation XI, the reaction has only one product and the only conceivable side reaction is the deposition of carbon by decomposition of CO. Whereas CO adsorption on alkali metals and early transition metal surfaces usually is dissociative[85], on late transition metal surfaces adsorption is predominantly molecular and therefore usually no carbon deposition is observed.[86, 87] From UHV studies it was found, that the reaction follows a *Langmuir-Hinshelwood mechanism* on platinum [8, 23, 88, 89]:

$$\mathrm{CO} + * \rightleftharpoons \mathrm{CO_{ads}} \qquad (1)$$

$$\mathrm{O_2} + 2\,* \rightleftharpoons 2\,\mathrm{O_{ads}} \qquad (2)$$

$$\mathrm{CO_{ads}} + \mathrm{O_{ads}} \rightleftharpoons \mathrm{CO_{2ads}} \qquad (3)$$

$$CO_{2ads} \rightarrow CO_2 + * \qquad (4)$$

where the subscript “ads” denotes an adsorbed species and “*” a free adsorption site. The reaction can be divided into the adsorption of both reactants, reaction of the adsorbed species and desorption of the product.

The respective reaction steps are shown in Figure 3.1 and will be explained in detail in the following:

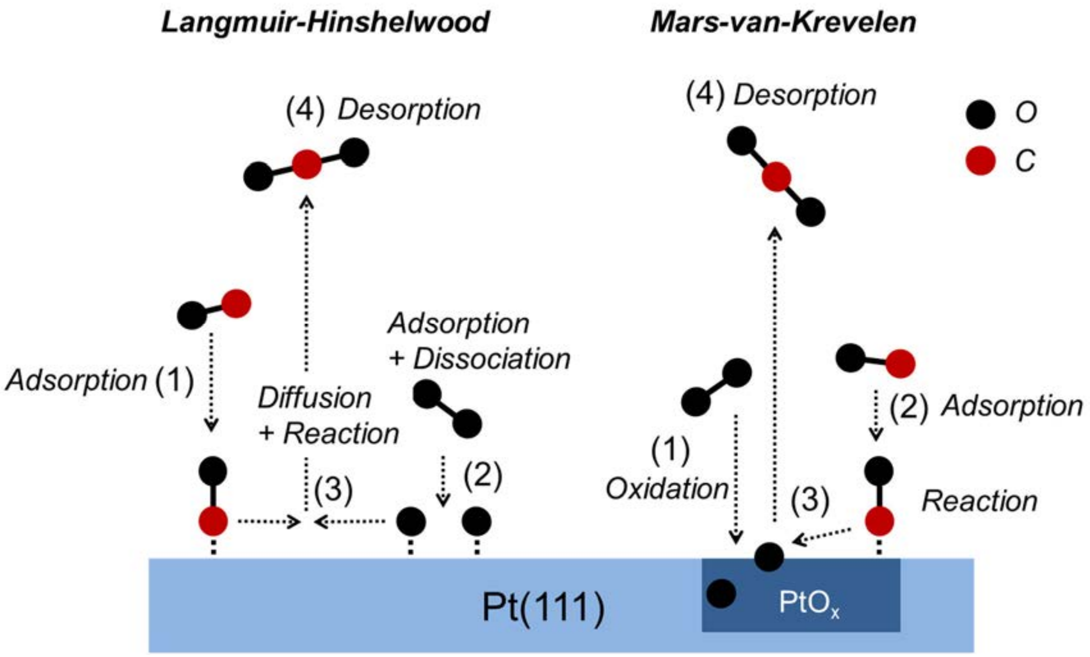
Langmuir-Hinshelwood
Mars-van-Krevelen
(4) Desorption
(4) Desorption
O
C
Adsorption (1)
Diffusion
+ Reaction
(3)
Adsorption
+ Dissociation
(2)
(1)
Oxidation
(3)
(2) Adsorption
Reaction
Pt(111)
PtO$_x$

Figure 3.1: Schematic illustration of the Langmuir-Hinshelwood and the Mars-van-Krevelen mechanism.

3.1.1 Carbon monoxide on Pt(111)

CO adsorption on platinum, and on other transition metal surfaces, is described by the Blyholder model. CO adsorbs molecularly, while the carbon 5σ lone pair interacts with the metal by donating electron density to the vacant metal conduction band. Additionally, there is a charge transfer from the d-band to the antibonding π* orbitals of the CO molecule[90, 91] as schematically illustrated in Figure 3.2a. As a consequence of this so-called backbonding to the CO molecule, the C-O bond is weakened which plays a crucial role in the reactivity of the molecule. On the other hand, backbonding results in a strong CO-metal bond. The actual bonding strength depends on the respective metal and hence on the d-electron density at the Fermi level. Therefore, the Blyholder model suggests a strong correlation of the CO chemisorption energy on a specific metal and the strength of the back bonding.[92]

On Pt(111), CO adsorbs molecularly on two different adsorption sites, as shown in top view in Figure 3.2b: for low coverages first “on-top” sites are populated (A), followed by a population of two-fold coordinated “bridge” sites (B) via the carbon atom. From UHV work, the binding energy difference was determined to be 95 meV [93] and the saturation coverage of CO on Pt(111) was found to be 0.5 ML at room temperature. This CO superstructure is usually described as a c(2x4)-CO overlayer and was first identified by low energy electron diffraction (LEED).[94] It is produced by CO exposure at 100 K but in order to obtain sharp reflexes, the sample was annealed to 260 K. After the annealing step, half of the CO molecules populate on-top and half bridge sites. Further increase of the CO coverage up to ~0.6-0.7 ML is only achieved after extensive exposure at temperatures below room temperature and is connected to compression effects of the CO adlayer.[64, 93, 94] By increasing the CO pressure into the mbar regime, a coverage of 0.6 ± 0.15 ML was obtained at ~370 K (Chapter 5). In temperature-programmed desorption (TPD) experiments, it was found that CO completely desorbs from Pt(111) at temperatures below 500 K in UHV.[64, 94] Nevertheless, when going to Pt particles also CO adsorption on step sites has to be considered, like previously observed on Pt particles prepared on a graphene/Rh(111) support. In temperature-programmed XPS (TPXPS) experiments it was found that CO adsorbed on step sites desorbed at higher temperatures than on bridge and on-top sites.[95] The possibility to discriminate between different CO adsorption sites of the surface is often used for surface site determination in catalysis with CO being a suitable probe molecule, as it only binds to one adsorption site at once and does not dissociate on many transition metals.

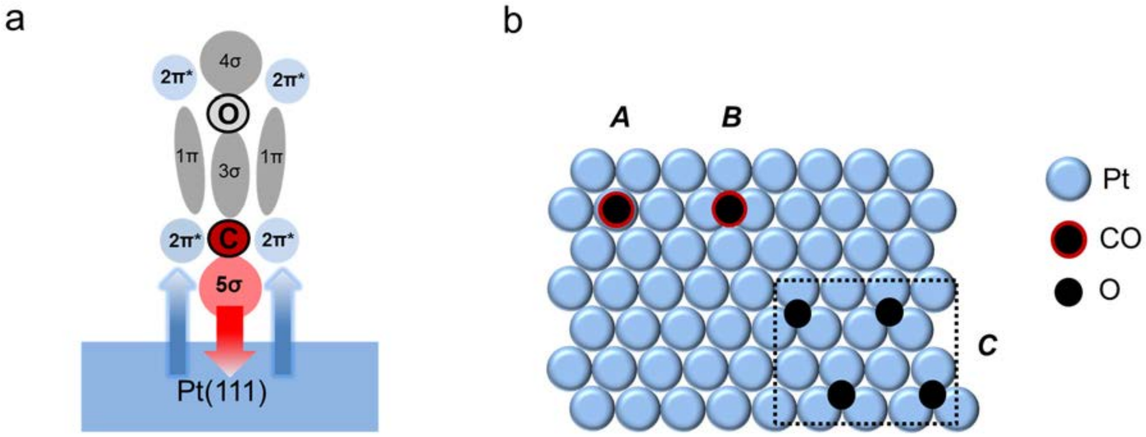

Figure 3.2: (a) Adsorption of CO on transition metals according to Blyholder and (b) top view of the CO adsorption on on-top sites A, on bridge sites B and O adsorption in three-fold hollow sites C in the p(2x2)-O superstructure (b).

3.1.2 Oxygen on Pt(111)

As for CO, O_2 adsorption on transition metal surfaces is explained by the Blyholder model shown for CO/Pt(111) in Figure 3.2a. In case of oxygen, there is a charge transfer from a filled 2π orbital to the metal d band. On the other hand, there is back bonding to the oxygen molecule as electron density is donated from the metal d band to the 2π* orbital. As the 2π* orbitals are antibonding, this again leads to a weakening of the oxygen-oxygen bond.[96] Whereas in case of CO, desorption is observed before dissociation of the C-O bond, O_2 is adsorbed molecularly only below 170 K on Pt(111) as a peroxo-like species. In TPD experiments it was found that by heating the surface to temperatures exceeding 170 K, molecularly adsorbed O_2 partly desorbs and partly dissociates forming a p(2x2)-O overlayer with a surface coverage of 0.25 ML.[97, 98] The respective structure of the overlayer was determined by LEED and EELS (electron energy loss spectroscopy)[99], where atomic oxygen is adsorbed in three-fold hollow sites as shown in Figure 3.2b in the dashed box labelled as c. This phase is fully desorbed at 1000 K as derived from TPD data.[98, 100] Oxygen coverages exceeding 0.25 ML are not found at room temperature in UHV and are only achieved by means of dosage of reactive oxygen species such as NO_2[101], O_3[102] or atomic oxygen[103] or at very high temperatures of T > 1073 K and T = 1300 K[61, 104]. Therefore, when using molecular oxygen, platinum oxides do not play a role in the CO oxidation reaction on Pt(111) in UHV. A difference in oxygen adsorption is found when using platinum particles as they are containing undercoordinated sites such as step and defect sites, which facilitate oxygen dissociation and oxide formation.[22, 105]

When increasing the pressure into the mbar regime, new oxygen phases are found. For example, by applying ~0.7 mbar O_2 to a single crystal at 420 K or higher, oxidation of Pt(111) was found to proceed via the formation of a PtO-like surface-oxide phase, later forming PtO_2 trilayers as deduced from NAP-XPS and x-ray absorption spectroscopy (XAS).[106] The formation of such new platinum oxide phases at higher pressures has to be considered when investigating the CO oxidation under these conditions, as such phases are potentially the active catalysts.

3.1.3 Reaction of co-adsorbed carbon monoxide and oxygen

Many UHV experiments were performed on the co-adsorption of CO on a p(2x2)-O precovered surface. In the co-adsorption situation with preadsorbed oxygen, oxygen atoms block the bridge adsorption sites and CO merely adsorbs on on-top sites.[23, 107] From TPD and STM work, it was found that in this case, the reaction takes place at immobile oxygen island edges, as CO and O do not form mixed phases. The activation energy of the reaction is highly dependent on the surface coverage of O, for high oxygen coverages, an activation energy around 50 kJ/mol was determined by different groups, whereas the activation energy increases to 100 kJ/mol for low oxygen coverages.[8, 23, 49] This effect is known as CO-poisoning, therefore, when starting out with a CO-precovered surface, the reaction is inhibited and no reaction occurs as long as no CO is desorbed from the surface and oxygen cannot adsorb and dissociate on the surface. This effect is especially pronounced, since for dissociation two surface sites are required. When starting out with a CO precovered surface, CO poisons the surface and oxygen adsorption is not observed for temperatures below CO desorption. CO poisoning was also found at higher pressures, where the reaction onset therefore is dependent on the CO coverage, which in turn depends on CO partial pressure.[17, 49]

An effect that has been often observed in a certain temperature window in UHV as well as at higher pressures is rate oscillations. Rate oscillations were thoroughly followed on the Pt(100) and Pt(110) surfaces by tracking work function changes and using photoemission electron microscopy (PEEM).[6, 108] It was shown that the oscillations found under stationary conditions were a result of a phase transition as a consequence of a change in reactant surface concentrations. In case of the Pt(100) surface, a transition between a quasihexagonal (5x20) clean surface to the unreconstructed (1x1) surface at high CO coverages was observed.[108] For Pt(110), it was traced to a change from the “missing row” (2x1) reconstruction in UHV to the (1x1) surface above a critical CO partial pressure. Description of the rate kinetics is complex and under certain conditions chaotic behaviour is found.[6] As the Pt(111) surface is structurally stable, no such effects are observed in UHV, however, at higher pressures, rate oscillations were observed also for this surface. Similar effects were found for supported Pt particles, and different explanations were given. Amongst them were reversible platinum oxidation-reduction cycles and in case of the particles, refacetting of crystalline planes. Additionally, the impact of bulk impurities such as silicon in the platinum single crystals was brought up.[30, 72, 109, 110]

In recent decades, the discussion arose, whether metallic platinum or platinum oxide is the better catalyst under realistic conditions. Here, the challenge lies in the determination of the phase present under reaction conditions, i.e. *in situ* or even in *operando* measurements are needed as certain phases potentially might only exist during reaction. Another issue is to find out whether the potentially most active phase actually is present during the reaction and under which conditions it exists. For example, in titration experiments the reactivity of different platinum phases was probed by exposure to CO. Here, a decrease in the reactivity with an increase in surface oxidation was found. Chemisorbed oxygen was most reactive, whereas a fully terminated surface comprised of α-PtO_2 trilayers was inert towards CO at 300 K and 10^{-5} mbar.[111] This order of reactivity in UHV does not necessarily mean that the most reactive phase is present under reaction conditions at higher pressures, nor is it clear whether only one phase exists or, for example, platinum oxides coexist with metallic platinum in the active catalyst. From high pressure STM work on Pt(110) at oxidising CO/O_2 mixtures in the bar regime, a Mars-van-Krevelen mechanism on platinum oxide was proposed, which is depicted on the right side of Figure 3.1.[21, 73] In contrast to the Langmuir-Hinshelwood mechanism, here, first a reaction of oxygen with the platinum to a platinum oxide (step 1 in Figure 3.1) occurs, which is the active catalyst. Following, CO is adsorbed (step 2) and subsequently, the surface is reduced by CO forming CO_2 (step 3). In a last step, the product is desorbed from the surface (step 4). This STM work indicates that a change in reaction conditions may even result in a change of reaction mechanism, once more underlining the importance of *in situ* measurements.

3.1.4 CO_2 on Pt(111)

CO_2 physisorbs on Pt(111) at temperatures below 95 K, which is the desorption temperature in UHV.[112] Chemisorption is only observed on transition metal surfaces exhibiting stabilising effects like atomically rough surfaces or alkali metal-modified surfaces.[113, 114] As a well-prepared Pt(111) single crystal was used throughout this work, immediate, irreversible desorption of CO_2 from the Pt(111) surface was observed. This is important as a possible back reaction, forming CO and O can be neglected and does not have to be considered throughout this work.

3.2 Intercalation and reactions under 2D systems

During the last decade, two-dimensional (2D) systems like graphene and boron nitride have been investigated with huge interest, which was triggered by the award of the Nobel prize in Physics to GEIM and NOVOSELOV for the “ground-breaking experiments” regarding the two-dimensional material graphene. This success has stimulated the research for other 2D systems like silicenes, phosphorenes and hexagonal boron nitride.[115-118] The reasons for the intense research are the interesting properties that graphene exhibits: amongst them are high mechanical strength, unique charge transport properties and exceptional thermal conductivity. These properties give rise to a huge amount of applications ranging from energy storage devices like batteries to single molecule gas sensors, as photocatalytic materials for environmental decontamination and transparent conducting electrodes.[118-120]

Also in surface science, graphene has been extensively studied. It is possible to grow graphene in UHV *in situ* on many hexagonal transition metal surfaces, such as Rh(111), Ir(111), Ru(0001), Pd(111) and Pt(111).[66, 121] Usually, graphene is grown in a chemical vapour deposition (CVD) process through cracking of alkenes like propene or butane on the substrate surface.[121] Graphene consists of carbon atoms attached to each other in a honey-comb like structure, linked by covalent bonds. In many cases the graphene layer is held only by weak van-der Waals interaction on the substrate, while a corrugation of the graphene sheet is observed through a lattice-mismatch on some of the transition metal surfaces, giving rise to a Moiré pattern visible in LEED.[121-123] The exact electronic structure and morphology of the graphene sheet depends on the chemical interaction with the substrate. It was found that with increasing interfacial orbital hybridization between the graphene and metal states the corrugation is increasing in the order Pt(111) < Ir(111) < Rh(111) < Ru(0001) due to higher interaction of the graphene layer with the substrate surface.[123]

Despite the intercalation of elements, e.g. Ba, Si, Ca, K, Ni, Pt, Au, Ce in the interface between graphene and substrate, which is known to be possible since years [124-126], more recently, also molecules, especially gases, have been intercalated.[127-133] Here, for example, CO, O_2, H_2 and H_2O have been studied so far. This effect is very fundamental, as intercalation of gases consequently always has to be considered when working at ambient atmosphere, as the found threshold pressures for intercalation are in the mbar range.[128-130, 134-136] The respective pressure, at which intercalation starts, is dependent on the graphene – metal interaction. In this respect, for example, intercalation of CO under Pt(111) is observed in the 10^{-4} mbar range for a closed graphene layer [135], whereas on a closed Ru(0001) surface the pressure has to be increased to ~13 mbar [129]. For graphene flakes ($\Theta < 1$ ML) on Pt(111) intercalation is already observed in the 10^{-6} mbar range, suggesting that intercalation occurs at island edges and defects (“defect-aided intercalation mechanism”) and not through penetration of the graphene lattice.[135]

The intercalation of gases like CO and O_2 has opened up the possibility to perform reaction in 2D space – namely at the interface between graphene and the metal substrate by intercalation of gas mixtures.[135, 137] Due to the confined reaction environment, the reaction might take place very differently than on a bare metal surface. For graphene/Pt(111) it was found from TPD experiments in combination with DFT calculation that the adsorption strength of molecules like CO is influenced by the graphene overlayer. More precisely, the interaction of CO with the Pt surface is weakened, therefore CO desorption is observed in a sharp transition at lower temperatures compared to the bare Pt(111) surface. For the CO oxidation reaction underneath the graphene sheet at mbar pressures, a lowering of the activation energy was found compared to the reaction at the same pressure on the bare Pt(111), which was attributed to the changed adsorption behaviour.[135] These findings are unexpected since graphitic overlayers commonly are considered to inhibit reaction and on this account, the term “2D nanoreactor” was created for such systems. Also, for hexagonal boron-nitride intercalation of CO [138] and O_2[139] has been tested and therefore expansion of reaction investigations to further 2D systems is likely to occur soon. Using different 2D materials may enable the specific tuning of reaction conditions by changing the adsorption behaviour of different reactants and therefore control reactions on a high level.

3.3 Ethanol steam reforming

The ever-increasing energy demand but limited availability of fossil fuels requires the implementation of alternative/renewable energy sources; amongst them are photovoltaics, wind power techniques and fuel cells. Furthermore, the rising public awareness and the need to protect the environment induce growing research in these fields. A technology which is often brought up in combination with production of electricity is fuel cells, where hydrogen is directly converted into electrical energy, which can be further used. The advantages of this technology lie in its high energy conversion efficiency, zero emission, scalability and quick installation.[140, 141] Particularly noteworthy from an environmental point of view is that the only byproduct is water.

A significant reaction for hydrogen production is steam reforming. Generally, the steam reforming reaction is an endothermic reaction where water vapour is reacted with hydrocarbons or alcohols mostly forming carbon monoxide as a byproduct, carbon dioxide and hydrogen. E.g., the steam reforming of ethanol is highly interesting as ethanol is readily available from fermentation of agricultural wastes. As plants in turn process the CO_2 formed during the steam reforming of ethanol, the carbon cycle is closed and the related CO_2 emission usually is not considered to contribute to global warming.[142] The desired reaction route is shown in equation (XII):

$$\mathrm{CH_3CH_2OH + 3\ H_2O \rightleftharpoons 6\ H_2 + 2\ CO_2}\ . \qquad \text{(XII)}$$

Despite the simple overall reaction scheme, ethanol steam reforming is a very complex reaction and reaction pathway and therefore intermediates and byproducts highly depend on the actual catalyst-support system used.[142, 143] Noble metals such as Rh, Pd and Pt are known for their high catalytic activity in this reaction, but exhibit one major drawback, which is their high cost. Therefore, other, low-cost transition metals like Co have been tested and found to be applicable as catalysts.[144] Highly favourable is the high selectivity for H_2 and CO_2 found for supported Co catalysts at relatively low temperatures.[145, 146] It was shown, that also the support material plays an important role for efficiency, reaction pathway and selectivity. Traditionally, often Al_2O_3 is used as a cheap support material, however, as it is an acidic support, dehydration and as a result coke formation is favoured, resulting in a poisoning of the catalyst.[147] To counteract coke formation, ceria was found to be a promising basic support material, which is known for its oxygen capacity properties and high redox activity. Another advantage is the promotion of the water-gas shift reaction found for ceria which shown in equation (XIII). In this reaction, in a second step CO, often a byproduct of the steam reforming reaction, is converted with water to additional hydrogen and CO_2. Therefore, the overall H_2 production is increased and toxic carbon monoxide is converted to nontoxic CO_2.[148]

$$\mathrm{CO} + \mathrm{H_2O} \rightleftharpoons \mathrm{H_2} + \mathrm{CO_2}\,. \qquad \text{(XIII)}$$

For the mentioned reasons, ceria supported Co particle catalysts are a promising candidate regarding the ethanol steam reforming reaction, combining low costs, high selectivities and high conversions.

4. Oxidation of Pt(111) at near-ambient pressures

4.1 General

Platinum – as a wide-spread catalyst – has been in the focus of research for many decades. Especially, its oxidation has received great attention, although the practical and theoretical investigation of the start of oxidation has been hampered by technical restrictions. Practically, XPS investigations have been limited to UHV pressures and DFT calculations were restricted to small system sizes and therefore to highly symmetric systems.[106, 149, 150] In this chapter, the formation of platinum phases at near-ambient pressures is described over time at different temperatures by NAP-XPS. This is an important step into the pressure gap, as no oxides are formed from molecular oxygen under UHV conditions, but under elevated pressures, underlining the need of *in situ* investigations in order to understand reaction mechanisms under realistic conditions. It was found that the time scale of the experiment is very crucial, as the growth was followed for at least 4 h until saturation in the O 1s XP intensity was observed. Complementary, the growth of platinum oxides under the same conditions was simulated using ReaxFF-GCMC by the work group of Prof. Dr. T. Jacob of the “Institut für Elektrochemie” at the University of Ulm, enabling the calculation of amorphous, highly disordered platinum oxide structures. The combination of both approaches, practical and theoretical, reveals the growth, coverages and structures of amorphous platinum oxides under these conditions. The experimental findings were rationalised by the simulations; therefore, the existence of the theoretically found phases was confirmed by the experiment. This is in contrast to previous findings, where only highly ordered oxides were conceived, which fail to explain the results obtained here by NAP-XPS.[106, 149] The results of this chapter have already been published and the text has been adapted from this publication:

“The growth of stable surface oxides on Pt(111) at near-ambient pressures”, Fantauzzi, D.*, Krick Calderón, S.*, Mueller, J.E., Jacob, T., Grabau, M., Papp, C., Steinrück, H.-P., Senftle, T., van Duin, A.C.T., *submitted*, **2016**, (*shared first authors).

Surface oxide formation presents a key challenge in understanding the catalytic properties of Pt surfaces, since many of the catalysed reactions are carried out in oxygen-rich environments. Indeed, surface oxidation is reported to alter the catalytic activity and selectivity of platinum [111, 151]. Experiments and theoretical calculations have both been used to study the oxidation of Pt(111). Several UHV experiments using different oxygen precursors (e.g. O_3, NO_2, atomic oxygen beam, etc.) show a stable p(2x2) oxygen overlayer with a coverage of

Θ_O = 0.25 ML as already reviewed in Chapter 3.1.2 [102, 152-154], whose stability has been verified using DFT [155-157]. For Θ_O > 0.25 ML Devarajan *et al.* [154] observed the appearance and growth of a zigzagged p(2x1) oxygen overlayer structure, which for Θ_O > 0.5 ML leads to one-dimensional Pt-oxide chains, modeled by Hawkins *et al*. [157]. For Θ_O = 1 ML, DFT calculations [150] comparing several proposed structures [106, 158] found a structure exhibiting subsurface oxygen to be most stable. This same theoretical study [150] features atomistic insights of Pt(111) surface oxidation for coverages up to $\Theta_O \leq 1$ ML, which compare favourably with and complement published STM and TPD experiments. Two important structural motifs, namely surface buckling and subsurface oxygen are identified and the kinetics of structure formation is discussed and shown to be possible at low temperatures. A recent study confirms these mechanistic findings and provides insights into the role of H_2O in Pt(111) surface oxide formation.[159] Starting already at 1.25 ML, experiments indicated the formation of “oxidic” oxygen on Pt(111), leading to the formation of PtO_x particles into a kinetically limited growth of a disordered oxide film with Θ_O = 2.4 ML [102] and Θ_O = 2.9 ML [153], respectively. DFT calculations have also been utilized to investigate highly symmetric surface oxide structures with up to Θ_O = 2 ML [160]. However, limitations in system size that can be reasonably investigated with DFT have thus far prohibited the consideration of amorphous structures as those observed experimentally.

Recent years have witnessed important and interesting extensions of surface science techniques such as XPS, conventionally limited to ultra-high vacuum (UHV) conditions, to systems applicable at near-ambient pressures (see also Chapter 2.1.2) [45, 56, 161]. Therefore, observation of adsorbates and oxidation states on the surface in a quantitative way is now possible even *in situ*, i.e. under elevated pressures and thus helps bridging the pressure gap between UHV and industrial conditions. Also, under such conditions, the surfaces of the catalysts themselves are often altered [70, 162]. Miller *et al*. used near-ambient pressure XPS (NAP-XPS) to study platinum surface oxides *in situ* [106], but did not discuss the temporal evolution of the surface.

To quantitatively investigate the growth and structure of high coverage oxygen surface phases on Pt(111), *in situ* NAP-XPS measurements were performed at O_2 partial pressures of 1 mbar and temperatures between 300 K and 700 K. In contrast to previous investigations, the time scale (t ≥ 4h) of the experiment was found to be crucial for the formation of platinum surface oxides. ReaxFF-GCMC calculations were used to rationalize the experimental findings and to identify and characterize the stabilities of amorphous surface oxide structures reflecting the experimentally observed surfaces.

4.2 Experimental aspects and methods

Acquisition times of the *in situ* spectra of the survey spectrum, O 1s and C 1s regions were 8, 9 and 10 min, respectively. For coverages beyond 1 ML, the O 1s signal of the underlying oxygen atoms are damped by the overlayers. Therefore, the coverages obtained were corrected for selfdamping with the calculated structure at 3.44 ML (see Fig. 4.7 (i)) assuming a thickness of 3.31 Å of one layer ($PtO_{1.15}$) and an inelastic mean free path of 10.3 Å calculated using the TPP-2M formula [163]. Thereby, one platinum oxide layer damps the intensity of the underlying layer by 27.5 %. The corrected coverages are used throughout this study. Details on the ReaxFF GCMC simulations are given in the Appendix 10.1.1.

4.3 NAP-XPS and ReaxFF GCMC results on the time-dependent growth of platinum oxides

In order to investigate the growth of platinum oxide, the O 1s and Pt 4f region were monitored *in situ* over several hours at 1 mbar O_2 and temperatures between 300 K and 700 K. The aim of these experiments was to elucidate the time dependent development of the different oxygen phases at different temperatures.

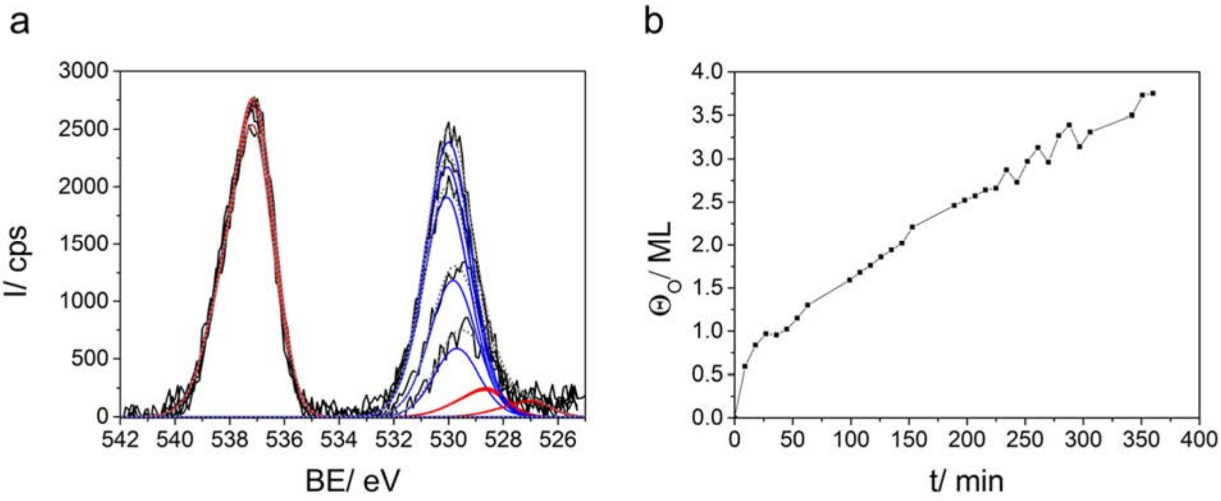

Figure 4.1: (a) Selected O 1s spectra for the growth at p(O_2) = 1 mbar and a sample temperature of 500 K; gas phase (red) and surface component (blue) and (b) the respective growth curve obtained by deconvolution of the surface signal.

Figure 4.1a shows selected *in situ* O 1s spectra during the oxidation of Pt(111) at a pressure of 1 mbar O_2 and a sample temperature of 500 K as an example of a typical experiment. The O_2 gas phase emerges at 537.2 eV with its x-ray satellites at 527.1 eV and

528.7 eV (red fit) and the surface species at 529.7 eV (blue fit). The quantitative analysis of this experiment is shown in Fig. 4.1b. Within the time resolution of the experiment, a coverage exceeding 0.5 ML is reached quickly followed by a continuous steady growth, which continues for at least the duration of the experiment (360 min).

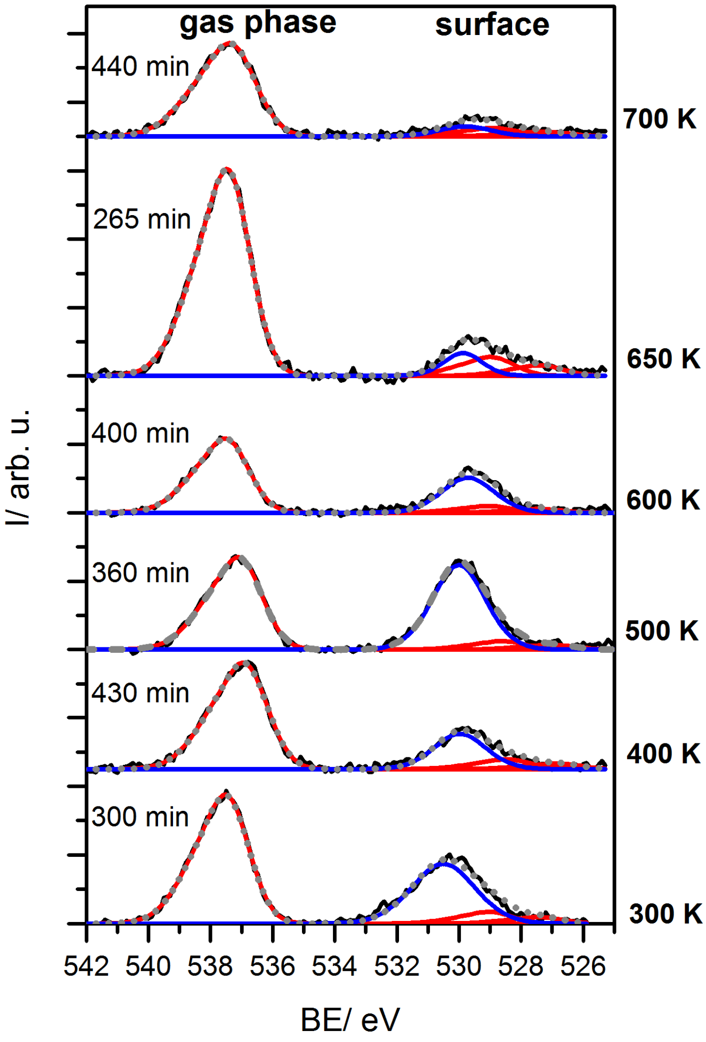

Figure 4.2: Last in situ O 1s spectrum and fits for all temperatures.

The O 1s spectra for similar experiments carried out at 300, 400, 600, 650 and 700 K are shown in Fig. 4.2. Here, the last *in situ* spectra with the respective growth times for all temperatures investigated in this study are shown. Again, the gas phase signals are observed at ~537.2 eV (red); gas phase signal satellites are again fitted (red) in order to extract the signals from the surface oxide species. Please note the strong differences in the gas phase intensity due to minor deviations in sample position (<< 1 mm). The binding energy shift of the gas phase is also explained by a different distance between sample and first aperture leading to the pumping stages (as explained in Chapter 2.1.2). The spectra are shown after subtracting a linear background, without scaling them; only an offset was used to plot the spectra.

At the end of the oxidation experiments platinum oxide coverages of 3.7 ML (300 K), 1.9 ML (400 K), 3.8 ML (500 K), 1.5 ML (600 K), 0.5 ML (650 K) and 0.3 ML (700 K) were obtained. Such oxidation experiments were found to be quite challenging as they are very sensitive to any impurities in the crystal (Si, Ca etc. [61, 164, 165]) and traces in the residual gas (CO, hydrocarbons etc.) that often poison the surface, making reproduction of exact coverages in the ambient pressure regime within defined time scales difficult. As the formed oxides are not stable in UHV at temperatures above 400 K, they were cooled down in 1 mbar O_2 ($T < 350$ K) before pump-down to UHV conditions (see also below for the computational results). For some experiments, after pump-down to UHV, the surface was checked by LEED. Besides the hexagonal diffraction pattern resulting from the Pt(111) crystal surface, no additional spots were found. For high coverages, solely a diffuse background was observed. This hints at an unordered nature of the found oxides.

In the following, the experiments at 300 and 500 K are discussed exemplarily in more detail. In Figure 4.3a and b, the Pt 4f and O 1s spectra after the oxidation experiment in UHV are shown, respectively. Besides the metallic Pt $4f_{7/2}$ and $4f_{5/2}$ contributions at 71.3 eV and 74.6 eV, the spectra taken after oxidation at 300 and 500 K show additional contributions at 73.7 and 77.0 eV (i.e. at 2.4 eV higher binding energy). These contributions are due to platinum oxide [106]. A closer inspection of the O 1s spectra points to differences in these two surface oxides, even though they both correspond to an oxygen coverage of ~3.7-3.8 ML. Whereas for 300 K the maximum is found at 529.7 eV, it is slightly shifted towards higher binding energies by 0.2 eV to 529.9 eV for 500 K and the peak is less asymmetric, indicating an additional oxygen species at 300 K. After heating the oxides to 1000 and 650 K (under UHV conditions), respectively, the surface is clean and Pt is in its metallic state, as can be seen in Fig. 4.3c and d. Note that the minor intensity in the O 1s region results from adsorption of residual gases. In contrast to previous investigations, where oxide formation was not detected below 400 K [49, 106], pronounced oxide growth was already observed at 300 K. The higher exposure times compared to earlier results [106, 111] are one possible explanation for this difference, and could indicate that the growth of platinum oxide, especially the formation of subsurface oxygen species, is diffusion limited, as also discussed as kinetic hindering earlier [153].

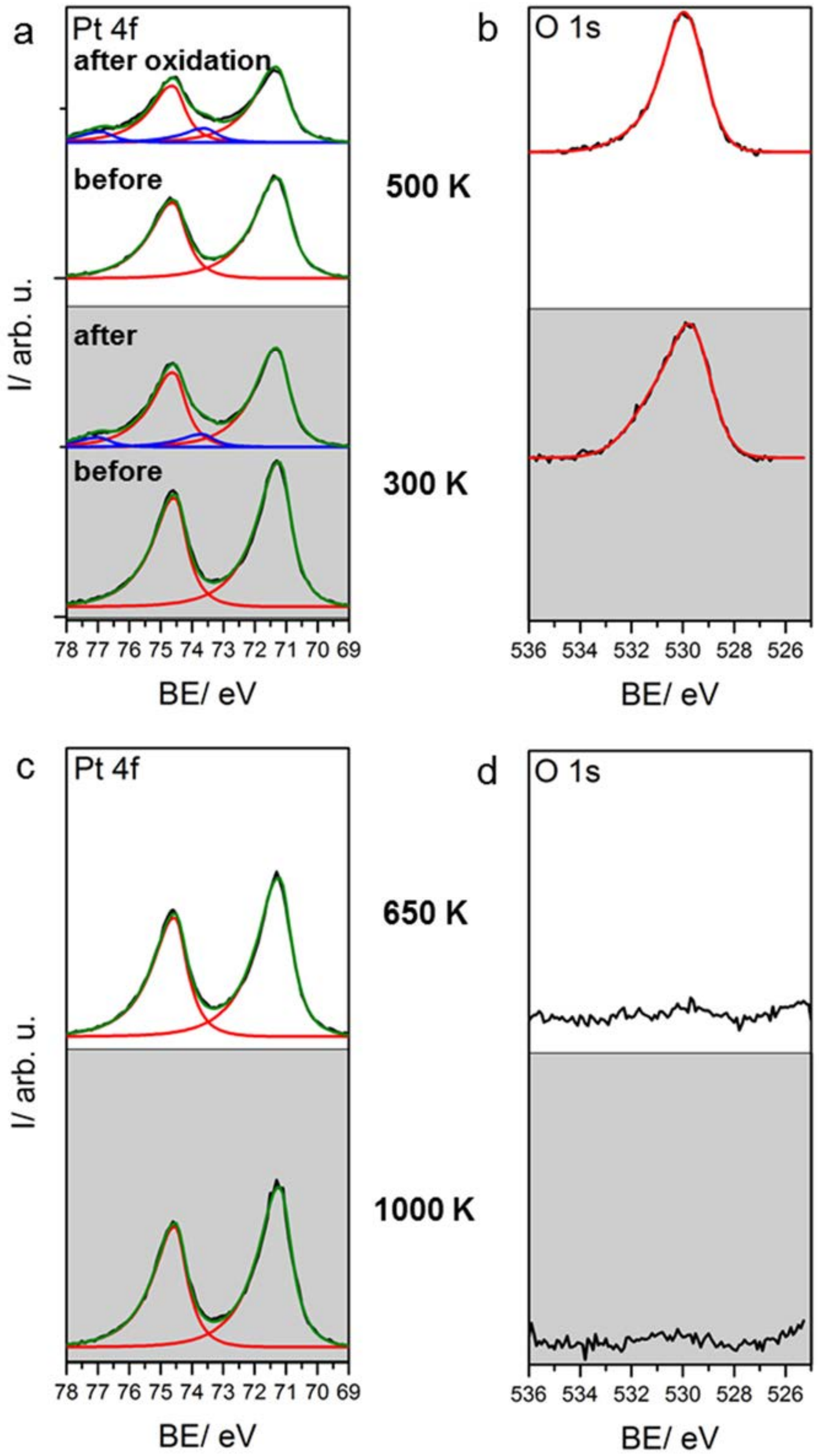

Figure 4.3: (a) Pt 4f spectra before (lower) and after (upper) an oxidation experiment $p(O_2)$ = 1 mbar and different sample temperatures (b) and the respective O 1s spectra after the experiments (c); Pt 4f spectra after heating the sample to 1000 and 650 K for the growth at 300 and 500 K, respectively and (d) the respective O 1s spectra.

Interestingly, oxygen adsorption at 600 K only yielded coverages below 1 ML, even for growth times exceeding 5.5 h. For this reason, an oxide of ~1.1 ML was grown at 300 K and subsequently, the crystal was heated to 600 K *in situ*, i.e. at 1 mbar O_2, and further oxidised up to 1.5 ML. Please note that the growth was not in saturation when the experiment was stopped; therefore, a higher saturation coverage has to be assumed. This hints at a slow growth at 600 K as will be further commented in Chapter 4.4. The respective growth curve is shown in Figure 4.4.

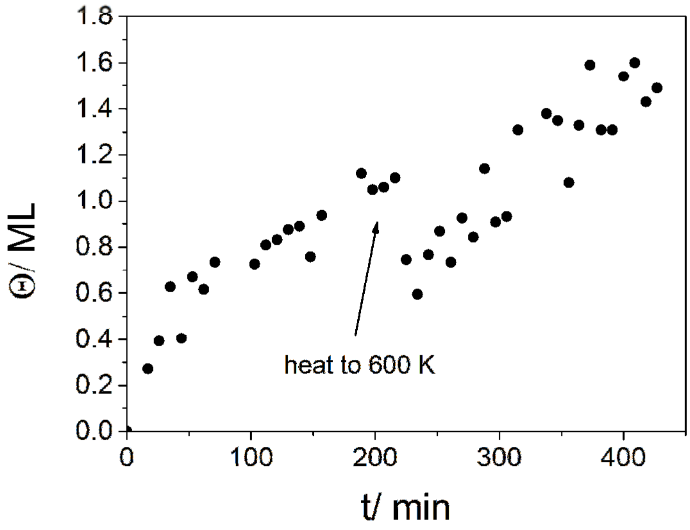

Figure 4.4: Platinum oxide growth at $p(O_2)$ = 1 mbar and 300 K for 225 min, then heated to 600 K in situ.

In order to exclude that the platinum oxide growth is favoured or induced by x-ray illumination, the beam damage during oxide growth was tested. For this reason, an oxide was grown at 300 K and 1 mbar O_2, and after pump-down to UHV, the sample was moved horizontally. As explained in Chapters 2.1.2 and 2.2.1, for NAP XPS investigations, the sample is put close (d ≈ 1 mm) to the first aperture with a diameter of 1.4 mm, which leads to the differential pumping stages up to the analyser. Therefore, as the sample is irradiated from one side by the x-ray gun, there should be a shadowing effect as the aperture is shielding the x-rays from the sample (d = 10 mm) as depicted in Figure 4.5c. Figure 4.5a and b show O 1s and Pt 4f spectra from different regions of the Pt(111) sample, where the blue spectrum represents the one which was taken from the “shadowed” area and the red one was taken from a region closer to the x-ray gun. The green spectrum was taken at the usual measurement position. As obviously no significant changes are observed, influence of the x-rays on the growth of the oxides is excluded.

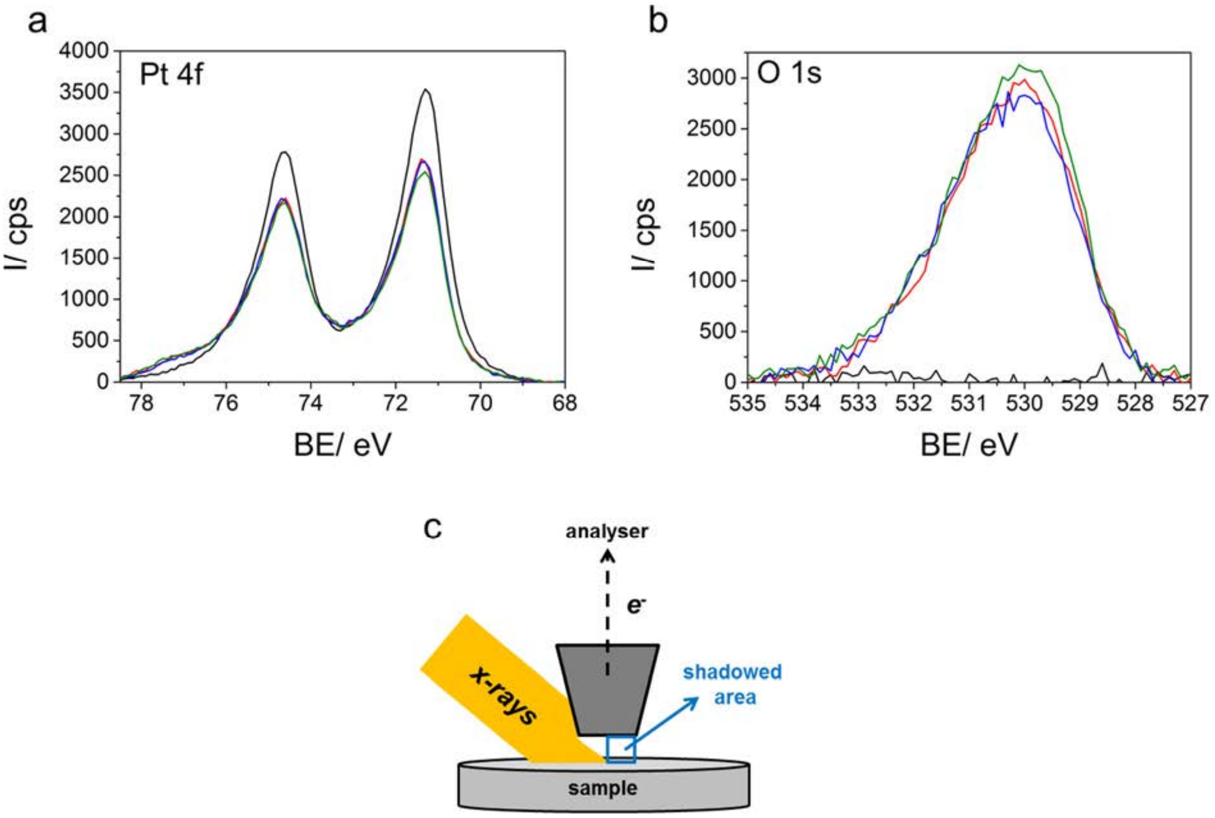

Figure 4.5: (a) Pt 4f and (b) O 1s UHV spectra of the platinum growth at 300 K before (black) and after oxidation at different sample positions (red, blue, green) and (c) schematic drawing of the shadowed area.

NAP-XPS provided time-dependent quantitative information on the chemical state of the surface, while theory offers the possibility to gain further insight to structural properties and a deeper understanding of the chemical processes occurring at this higher chemical potential. To enable a systematic theoretical investigation of the formation of such high-coverage surface oxide phases, ReaxFF-GCMC simulations were carried out at 7 different temperatures and an oxygen partial pressure of 1 mbar.

Each simulation started with a clean 9 layer Pt(111) slab, both sides of which were available for oxidation. Results from the ReaxFF-GCMC simulations at 600 K are shown in Fig. 4.6 as a representative example; the results at the remaining temperatures are provided in the Appendix 11.1.2. The oxygen coverage over the course of the simulation is shown in Fig. 4.6a. The coverage plateaus at ~1 ML following its initial climb, and then increases steadily in the final half of the simulation. The plateau corresponds to one monolayer adsorbed on each side of the slab, so that the uppermost layer of Pt on each side is oxidized. Further oxidation occurs with one complete Pt layer at a time, alternating between the top and bottom sides of the slab, as is reflected in the energy distributions in Fig. 4.6b and is confirmed by an examination of the corresponding structures.

A comparison of the coverages of the lowest energy structures and the coverages around which the simulation plateaus (even if only temporarily) suggests that there are notable metastable structures with approximate coverages of ~1 and ~3 ML. Similar results are obtained at 650 K except that oxidation beyond 1 ML is significantly slower, so that coverages greater than ~1.5 ML are not reached in the course of the simulation. At 700 K the GCMC simulations identify the p(2x2) 0.25 ML structure to be thermodynamically stable and at 800 K the clean Pt(111) slab, both in agreement with experiments [102, 152-154]. At temperatures below 600 K (see the simulations at 300, 400 and 500 K in Figures 11.1.1 and 11.1.2 of the Appendix) oxide growth does not saturate until the entire slab is oxidized into an amorphous Pt-oxide slab. This is explained by the high surface to bulk ratio in the simulation setup and is reflected in the sudden drop in the Gibbs energies of formation (see Fig. 10.1.1b, d and Fig. 10.1.2b of the Appendix) as soon as the coverage exceeds ~4.5 ML. Since the oxidation of the slab occurs from both sides of the slab, all platinum layers have been engulfed at these coverages and the surface oxides formed on each side of the slab reached each other.

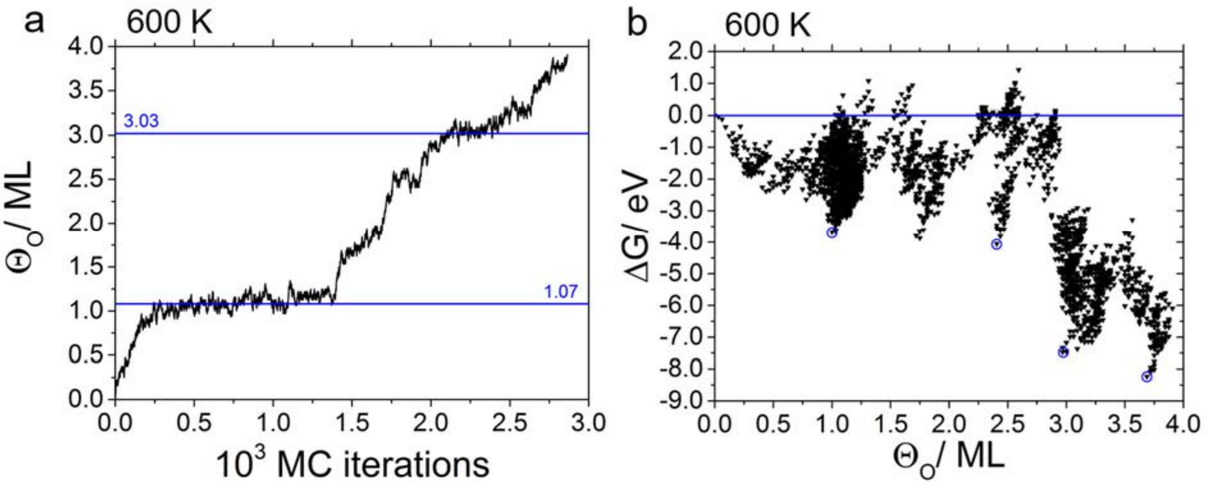

Figure 4.6: Results from GCMC simulations at 600 K and an oxygen partial pressure of 1 mbar, showing (a) the oxygen surface coverage as function of MC iterations and (b) the free energies of formation as functions of the oxygen surface coverage with respect to gas phase O_2 and a clean Pt(111) surface. The dashed blue lines in (a) show possible saturation coverages. The black line in (b) separates structures with negative free energies of formation from structures with positive free energies of formation. The blue circles highlight the structures used to draw the phase diagram in Fig. 4.7. The high densities of sampled structures at regular intervals of coverage (~0.5 ML) in (b) correspond to layer by layer oxidation. Results for other temperatures are shown in the Appendix.

However, since the interest of this work does not lie in the oxidation of the entire platinum slab and the surface oxide structures formed at temperatures below 600 K lie energetically well above surface oxide structures formed in the simulations at 600 and 650 K, (meta)stable surface oxide structures were only identified at these two simulation temperatures.

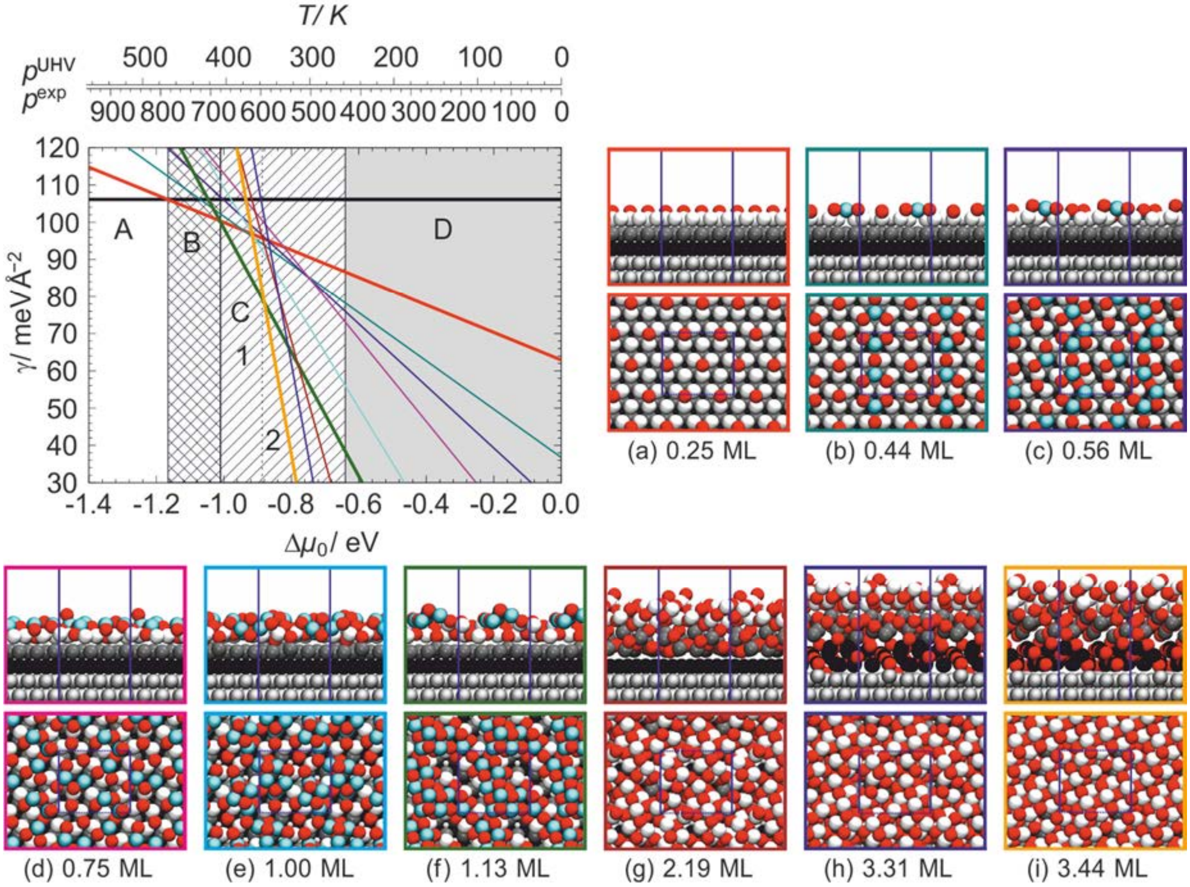

(a) 0.25 ML (b) 0.44 ML (c) 0.56 ML

(d) 0.75 ML (e) 1.00 ML (f) 1.13 ML (g) 2.19 ML (h) 3.31 ML (i) 3.44 ML

Figure 4.7: Phase diagram for Pt(111) surface oxidation derived from low-energy structures obtained in ReaxFF GCMC simulations at a MC temperature of 650 and 600 K. Temperature scales in degrees Kelvin for values of $\Delta\mu_O$ at oxygen partial pressures $p(O_2)$ corresponding to UHV (10^{-13} atm) and experimental (1 mbar) conditions are given at the very top. Side and top views of the most stable and metastable structures (a)-(i) with their respective surface unit cells (dashed blue lines) are shown. Oxygen atoms are red; platinum atoms are various shades of grey, depending on which layer they belong to in the initial structure or light blue when buckled (for $\Theta_O < 1.13$ ML). Subsurface oxygen is observed starting with the 0.75 ML structure. The phase diagram shows four thermodynamically stable regions: A clean Pt(111), B p(2 x 2) adsorbed atomic oxygen, C $PtO_{1.13}$ and $PtO_{1.15}$ surface oxides and D α-PtO_2 bulk oxide.

Thus, low energy structures (denoted with circles in Fig. 4.6b and Fig. 10.1.3b of the Appendix) were selected from these two simulations for further evaluation. For each of these structures the energy of formation of the oxide structure on each side of the slab was computed separately to identify only the lowest energy structures. Thus, the coverages of the most important structures presented in the phase diagram in Fig. 4.7 differ slightly from those highlighted in Fig. 4.6b and Fig. 10.1.3b.

This phase diagram includes amorphous surface oxide structures with oxygen coverages of 1.13 ($PtO_{1.13}$) and 3.44 ML ($PtO_{1.15}$). Thus, ReaxFF predicts the existence of stable surface oxides for oxygen chemical potentials in the range of -1.01 eV $\leq \Delta\mu_O \geq -0.64$ eV (corresponding to 430 K - 680 K in the experiment at 1 mbar O_2, area C in Fig. 4.7), and five stable surface phases for increasing oxygen chemical potential: A clean Pt(111), B p(2x2) adsorbed atomic oxygen, C low- and high-coverage surface oxide phases (1.13 ML and 3.44 ML) and D α-PtO_2 bulk oxide.

4.4 Comparison of experiment und theory

Figure 4.8 shows the experimental and theoretical growth curves obtained by NAP-XPS measurements and GCMC simulations, respectively. Note that GCMC does not provide real time units but MC iterations (Fig. 4.6 b) and therefore the growth curves cannot *per se* be compared in terms of time scales. However, a direct comparison of time scales between the experimental and theoretical growth curves is achieved via a calibration of the MC iterations at each simulation temperature to reflect the respective experimental growth curve.

Figure 4.8c enables an estimate on how the experimental growth curves might proceed beyond their actual range. Indeed, the theoretical growth curves at 400, 600 and 650 K predict an increase in surface coverage from ~1.5 to ~3.5 ML, ~1.1 to ~3.5 ML and ~0.5 to ~1.0 ML, respectively. Therefore, the growth curves at 600 and 650 K anticipate that the saturation coverages reached within the duration of the experiment represents intermediate coverages. In agreement with the steady growth observed in the experiment at a temperature of 400 K, the surface coverage is theoretically predicted to further increase from ~2 to ~3.5 ML. As no theoretical predictions on how the surface oxides grow for coverages > 3.5 ML can be made and the highest experimentally achieved coverages do not exceed ~3.8 ML, the duration of the bulk-oxidation, if kinetically accessible, remains unresolved. The coverages of the oxides grown at the different temperatures and 1 mbar O_2 obtained by NAP-XPS are summarized in Fig. 4.9 in conjunction with the theoretically predicted stability range of each phase as obtained from the phase diagram (see Fig. 4.7). Note that the coverages for the growth at 600, 650 and 700 K were determined from the last *in situ* spectra as the respective oxygen phases were not cooled down in oxygen and desorption set in during pump-down to UHV in case of the growth at 600 and 650 K, leading to an error of ~20 %. This observation is in agreement with theory as it predicts instability of oxides in UHV at temperatures exceeding 400 K (see Fig. 4.7).

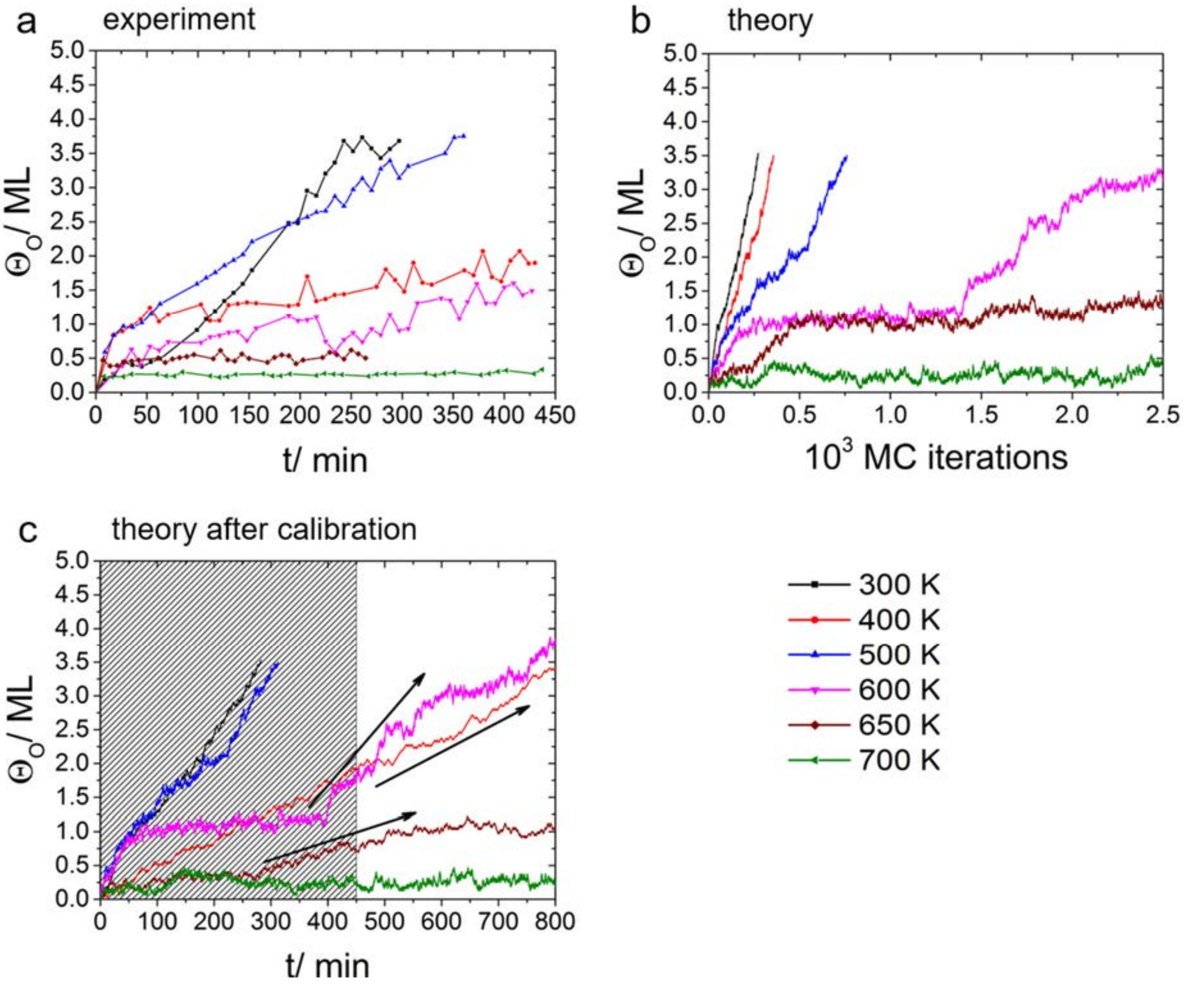

Figure 4.8: Results for platinum oxide growth at $p(O_2)$ = 1 mbar and different temperatures obtained from (a) experiments and ReaxFF GCMC simulations (b) before and (c) after calibration.

At 700 K, theory indicates oxygen adsorption with 0.25 ML (area B in Fig. 4.9) where 0.3 ML are obtained by XPS, being well in the margin of error of the XPS coverage determination. For 650 K, the simulations indicate that surface oxides with a coverage of 1.13 ML are stable (area C1). The lower coverage of 0.5 ML grown experimentally at 650 K might be due to an inadequate growth time (i.e., 265 min is too short), as theory predicts, meaning that the stable structure at 1.13 ML was not reached experimentally. For 600 K, a coverage of ~1.5 ML was obtained by NAP-XPS. The GCMC simulation shows a plateau ranging around 1 ML after which oxidation proceeds further until it reaches a second plateau at ~3.5 ML. Since no surface oxides grew in the experiment at 600 K, instead an oxide of ~1.1 ML was prepared at 300 K and subsequently the sample was heated to 600 K *in situ* for additional 200 min, leading to further oxide growth as already shown in Figure 4.4. This is consistent with theory, as also in the MC simulations a slow growth of the oxide observed at this temperature, i.e. the number of MC iterations when oxidation started was higher than in case of the other temperatures (please compare Figure 4.6 and 11.1.3 of the Appendix).

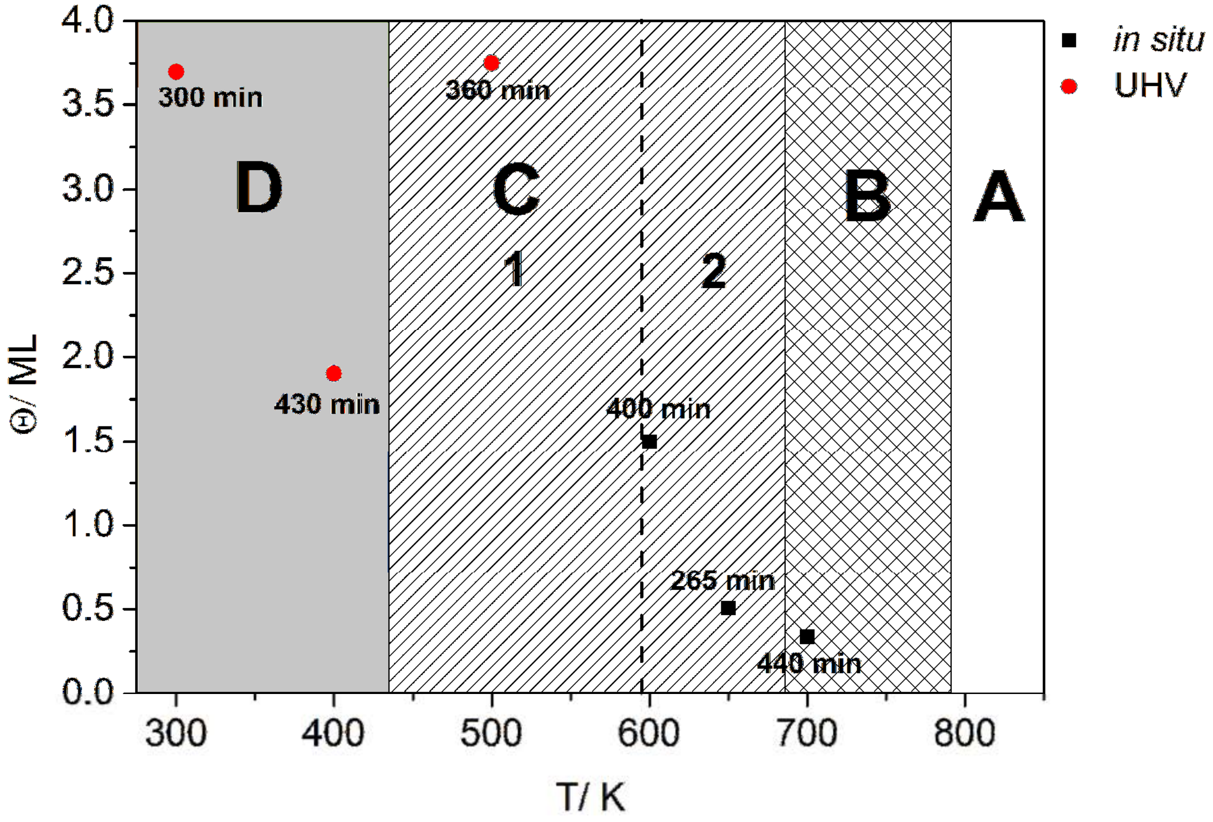

Figure 4.9: Experimental coverages of the platinum oxides grown at different temperatures and $p(O_2)$ = 1 mbar from in situ O 1s spectra (black squares) and UHV spectra after pump-down (red circles) are shown together with the theoretically predicted stability range of the different phases. The five thermodynamically stable phases are: A clean Pt(111), B p(2 × 2) adsorbed atomic oxygen, C $PtO_{1.13}$ and $PtO_{1.15}$ surface oxides (phase 1 and 2, respectively) and D PtO_2 bulk oxide.

In agreement to the GCMC simulations, the high-coverage surface oxide is not formed within the time scale of the experiment (400 min). Note that the growth at 600 K lies at the transition between the low-coverage (1.13 ML) and high-coverage (3.44 ML) surface oxide phases (area C1 and C2 in Fig. 4.9). Minor fluctuations in temperature within the experiment, beside the not negligible fact that already tiny differences in the calculated surface free energies of the phases can shift the phase-transition-temperature, are plausible explanations. For temperatures from 600 to 430 K, a surface oxide with a coverage of 3.44 ML (area C2 in Fig. 4.9) was the most stable structure found, which is metastable for T < 430 K (area D in Fig. 4.9). In line with this prediction, the highest coverages were obtained in the measurements at 300 and 500 K. For these measurements, additional features were observed in the Pt 4f core level at 2.4 eV higher binding energy that are consistent with the formation of platinum oxide, which is again in agreement with the GCMC simulations. The amorphous oxide formed with molecular oxygen described here might be similar to the ozone-derived oxide result obtained earlier [102]. At 500 K, oxidation is likely to be faster due to enhanced diffusion in the crystal than at 400 K. These results might also show the strong influence of minor, undetectable contaminations with e.g. hydrocarbons in the experimental set-up.

4.5 Conclusion

A combined NAP-XPS and ReaxFF-GCMC study was performed in order to investigate and elucidate the evolution of a Pt(111) surface in contact with an oxygen environment at 1 mbar oxygen partial pressure and temperatures ranging from 300 to 800 K. Theory predicts five different stable structures in this temperature window, namely clean Pt(111), chemisorbed oxygen, two different amorphous platinum surface oxides and platinum bulk oxide, depending on the growth temperature.

For temperatures below ~430 K, the simulations predict the formation of an α-PtO_2 bulk oxide. At 500 and 600 K, the simulations predict the formation of amorphous surface oxides with a coverage of 3.44 ML. This is in good agreement with the experiments where highest coverages were obtained for 300 and 500 K (3.7 and 3.8 ML, respectively). Further oxidation of the experimentally obtained surface oxides at 300 and 400 K appears to be kinetically hindered, which is in agreement to previous observations reported in the literature. At 600 K, coverages around 1.5 ML are found experimentally, which well exceed the typical coverage of 0.25 ML for the p(2×2) chemisorbed oxygen superstructure, and certainly correspond to surface oxides. The deviation from the theoretical value of 3.44 ML can be explained in so far as the saturation coverage was not reached within the time scales of the experiment (at least 4 h!). Indeed, the theoretical calculations predict a further growth of the surface oxide for $t \geq 600$ min at this temperature. The same explanation holds for the oxide growth at 650 K, where theoretical calculations predict a coverage of 1.13 ML ($t \geq 500$ min), which is not reached within the time scale of the experiment ($\Theta_O = 0.5$ ML; $t = 265$ min). At 700 K, a coverage of 0.3 ML was calculated from *in situ* measurements which is in good agreement with theory predicting 0.25 ML (chemisorbed oxygen). The clean Pt(111) surface is expected at temperatures above 800 K. Finally, no platinum phase was stable at temperatures exceeding 400 K in UHV, which is perfectly in line with theory.

In conclusion it was shown by NAP-XPS investigations that the time scale ($t \leq 4$h) of the experiment is very crucial for the formation of platinum oxide at near-ambient pressures.

Different results obtained previously are explained by their considerably shorter time scales [106]. From ReaxFF-GCMC simulations amorphous surface oxides were predicted at an oxygen partial pressure of 1 mbar temperatures in the range from 430 - 680 K as stable structures. These thermodynamically stable surface oxides might have some severe implications for the understanding of Pt in catalytic reactions, as their catalytic properties will certainly differ from those of bare platinum surfaces. The presented findings demonstrate the presence of a substantial pressure gap for this system which has to be considered for reactions in presence of O_2, as the active catalyst might change from metallic platinum to platinum oxides at a certain threshold pressure.

5. CO oxidation on Pt(111) at near-ambient pressures

5.1 General

In the previous chapter the formation of different platinum phases and surface oxides at near-ambient pressures was found for temperatures in between 300 and 700 K. In this chapter, CO oxidation on Pt(111) will be discussed. The insights gained in Chapter 4 will be used to evaluate whether the found oxides also exist under reaction conditions at 1 mbar total pressure. The results of this chapter have already been published and the text has been adapted from this publication:[74]

“CO oxidation on Pt(111) at near-ambient pressures”, Krick Calderón, S., Grabau, M., Óvári, L., Kress, B., Steinrück, H.-P., Papp, C., J. Chem. Phys., **2016**, *144*, 44706.

As discussed in Chapter 3.1, the CO oxidation reaction has received tremendous attention in surface science in the past. XPS stands out regarding the investigation of such surface reactions [11, 13, 166-168]. With the aim of surface science to provide a fundamental basis for the optimization of catalysts and a molecular understanding of the relevant reaction steps, the difference between these low pressures and the actual reaction conditions of real catalysts needs to be considered. The term “pressure gap” (Chapter 1.2) [15, 19, 45] describes the contrast between the pressure ranges used in real and model catalysis studies, and indicates that results obtained in surface science often cannot be simply extrapolated to higher pressures.[169] To narrow or even close this gap, different established surface science techniques such as XPS [45, 56, 161] and STM [44] have been refined towards the use at higher pressures, often denoted as near ambient pressure conditions. As this is a new and evolving field of surface science, there is the need to carefully probe even well-understood model reactions at these quite different conditions. Compared to a classical surface science experiment in UHV, entirely new effects have to be considered. One example is the occurrence of strong heat and mass transfer effects [18, 49, 170] that have been reported for reactions on transition metals, such that the reaction kinetics at elevated pressures are drastically influenced by the diffusion of reactants and products. These effects were, e.g., observed for CO oxidation on Pd and RuO_2 [18, 49], which are both well investigated and understood model reactions under surface science conditions.

As pointed out in Chapter 3.1, on Pt(111), CO oxidation under UHV conditions follows a Langmuir-Hinshelwood mechanism, that is, both reactants have to be adsorbed as next neighbours on the surface in order to react [88, 171]. The activation energy of this reaction strongly depends on the oxygen and carbon monoxide coverages: under CO rich conditions, the surface is poisoned as oxygen cannot adsorb and dissociate, which is required for the reaction to occur [5, 8, 23]. Interesting effects like an oscillatory behaviour [6] of this reaction have been reported to take place under UHV conditions [108, 172] and also at ambient pressures [109]. While the oscillations for Pt(100) observed in UHV [108, 172] are induced by surface phase transitions, at high pressures this behaviour was attributed to SiO_2 formation due to platinum bulk impurities [109]. In the last years, an intense debate arouse [17, 44, 71, 173] with respect to CO oxidation at higher pressures, especially concerning the state of the catalyst in the active range. Whereas Hendriksen *et al*. [21, 44, 70] suggested a Mars-van Krevelen oxidation-reduction mechanism for Pt(110) and also Pd(100), with the respective metal oxide as highly active species, other groups report a metallic state of the surface in the most active regime [17]. As techniques like STM, SFG and IR spectroscopy, which were used in other studies [21, 49, 174] lack direct chemical information on the oxidation state of the surface or the quantification of adsorbates, near ambient pressure XPS (NAP-XPS) could step in as a powerful quantitative tool. Indeed, the formation of platinum oxide above a certain oxygen pressure and at elevated temperatures has been reported before [49, 149], with these oxides being reducible by exposure to H_2 [106]. Additionally, new amorphous surface oxides were found in the investigations in Chapter 4 at 1 mbar O_2. These different platinum phases are found in NAP-XPS in the temperature window from 300 – 700 K, however, formation of platinum oxides in several cases took minutes to hours. Therefore, it has to be examined whether these phases exist under reaction conditions and are reactive towards CO, contributing to the discussion, whether metallic platinum or platinum oxide is the “better” catalyst in the CO oxidation reaction.

The reaction was investigated simultaneously by NAP-XPS and online gas analysis. Three different $CO:O_2$ reaction mixtures (2:1, 1:1 and 1:4) at total pressures of up to 1 mbar were used in continuous flow mode to obtain an understanding of the surface chemistry and the reactivity of the catalyst under different conditions. By temperature-programmed and by isothermal measurements the onset temperature of the reaction was determined for the different reactant mixtures. Highest turnover frequencies were found for the stoichiometric mixture. At elevated temperatures, it was found that the reaction becomes diffusion-limited in both temperature-programmed and isothermal measurements. In the highly active regime, no adsorbates were detected on the surface; it is therefore concluded that most of the catalyst surface is in a metallic state under the applied conditions and none of the platinum oxides investigated in Chapter 4 were found. Again, minor bulk impurities such as silicon were observed to influence the reaction up to total inhibition by formation of non-platinum oxides.

5.2 Experimental aspects

Region scans of the Pt 4f, O 1s and C 1s core levels as well as wide scans were taken to monitor the reaction *in situ* and also to describe the surface before and after the reaction. The acquisition time for the O 1s region during the CO oxidation reaction was ~5 min for the isothermal reactions, ~2 min for the heating ramps with 2 K/s and 1 K/s and ~8 min for the heating ramp with 2 K/min in the temperature programmed measurements. For further experimental details, please see Chapters 2.2.2, 2.3.2 and 2.5.1. Details on the fitting procedure are given in Table 11.2.1 of the Appendix. All coverages given were obtained with an accuracy of ~±0.15 ML.

5.3 Temperature programmed measurements

First the temperature programmed measurements are discussed, as they provide a good overview of the reaction and the occurring chemical species on the surface. The reaction was monitored by NAP-XPS and by online gas analysis using the quadrupole mass spectrometer (QMS), while exposing the Pt(111) sample to a defined mixture of CO:O_2, and subsequent heating with a defined heating ramp. Figure 5.1a shows the O 1s region for the 2:1 CO:O_2 mixture. The experiment started by admitting CO to the chamber with a pressure of 0.66 mbar and the sample at 300 K. This leads to a gas phase peak at 536.6 eV and to two peaks at ~532.8 and ~531.1 eV due to CO adsorbed in on-top sites (pink) and in bridge sites (purple) on the Pt(111) surface [23, 52, 53]. Please note that due to the limited resolution of the setup, these two peaks are not well resolved. In Figure 5.1b, exemplary fits are shown, where three successively measured O 1s spectra were added up in order to get a better signal-to-noise ratio. The respective temperature range of the averaged spectra is given on the right side.

At 540 s (XP spectrum 4), 0.33 mbar O_2 were added, with the sample still at 300 K, leading to an additional gas phase peak at 537.5 eV (see Figure 5.1b spectra 7-9), which consists of the two unresolved molecular O_2 gas phase signals [175]. As first CO was introduced to the chamber, the surface is blocked with CO and no adsorption of oxygen is found. At 300 K, no reaction occurs, as deduced from the lack of a CO_2 signal in the online gas analysis (Figure 5.2b) and the fact that no change of the adsorbate coverages is observed (Figure 5.1b) during CO and O_2 coexposure. The decrease of intensity of the adsorbed CO in the XP spectra by ~31% upon O_2 admission is due to increased damping by the gas phase, whereas the loss in signal intensity resulting from the gas phase is due to heating of the gas phase (especially observed in spectra 13-15) by the sample and to a minor degree from changes in the sample position relative to the analyser entrance, thereby reducing the gas amount sampled by XPS. Please note that in the analysis only relative amounts are used; therefore, this change in absolute intensity has no influence on the presented results.

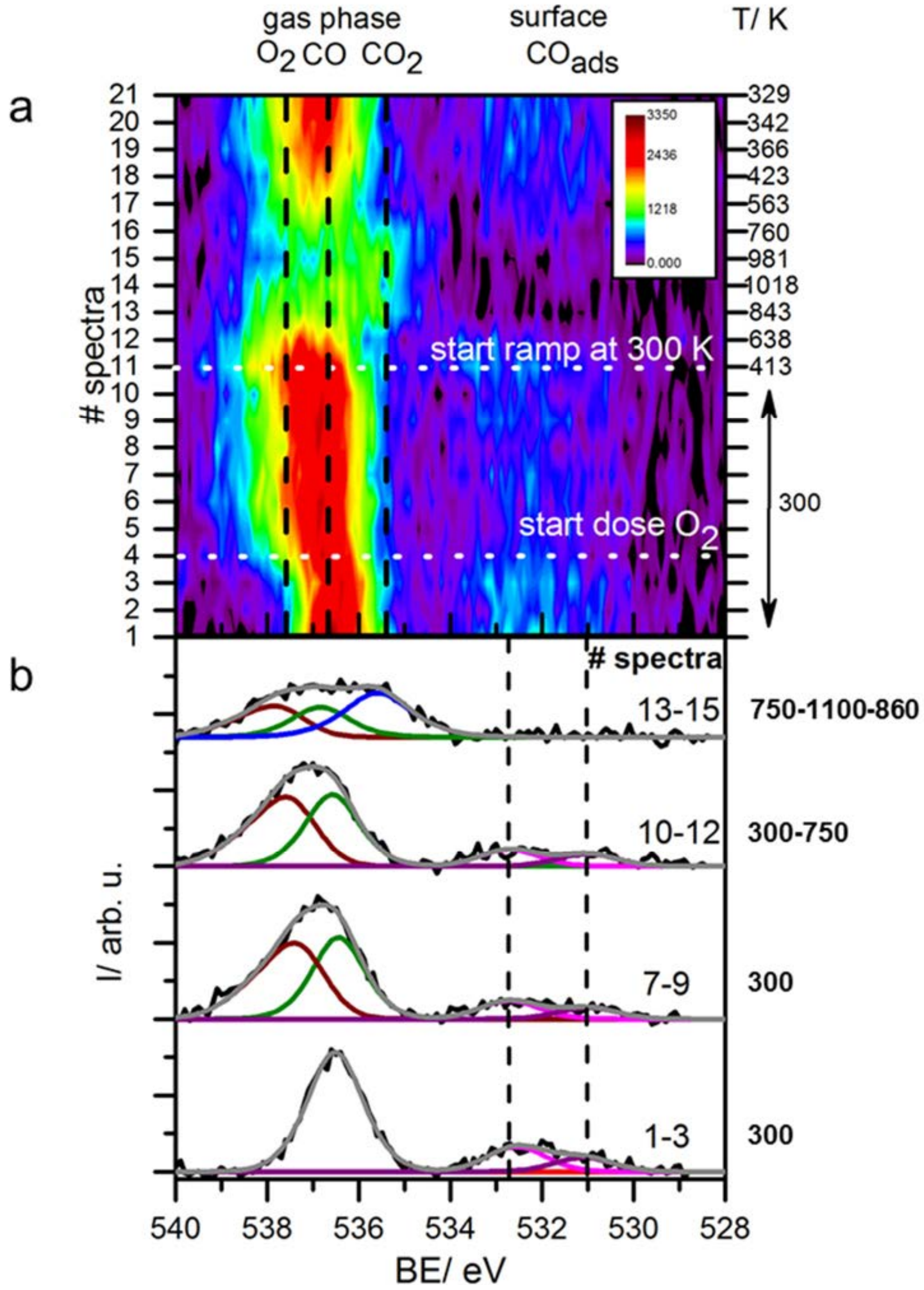

Figure 5.1: O 1s region of a TPXPS experiment of the reaction of a 2:1 CO:O$_2$ mixture with a heating ramp 300-1100-300 K with ß=2 K/s. (a) colour-coded density plot of the full experiment; for details see text; (b) selected XP spectra with the corresponding fits; note that the shown spectra are the sum of 3 neighbouring spectra to improve the signal-to-noise ratio.

In the quantitative analysis of the XP spectra, shown in Figure 5.2a, identical O 1s intensities of the gas phase for O_2 (brown squares) and CO (green circles) were used as constraint; this follows from the mixture of 0.66 mbar CO and 0.33 mbar O_2, and simplifies peak fitting. At 1250 s (XP spectrum 11), a heating ramp with 2 K/s was started, while XP spectra and the gas analysis were further recorded continuously. The temperature is shown as dashed line in Figure 5.2b, with the temperature scale at the right axis of the figure.

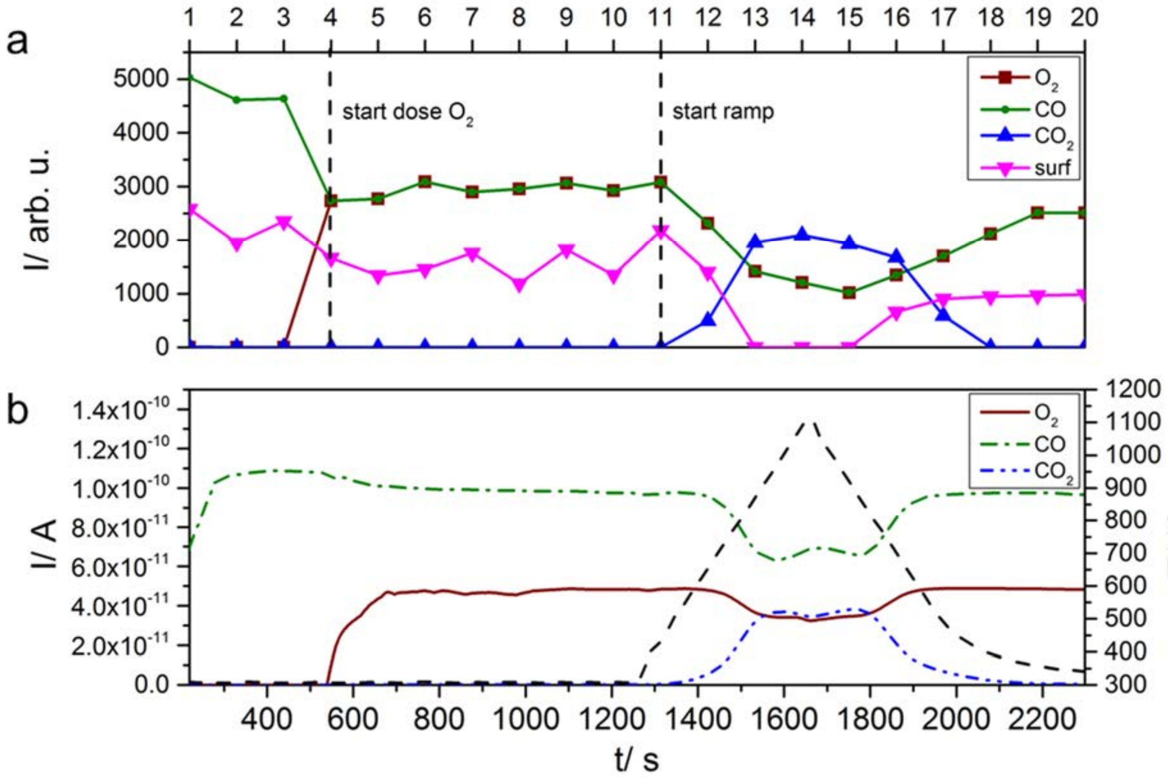

Figure 5.2: Comparison of TPXPS (a) and online gas analysis (b) of the 2:1 CO:O_2 mixture with a heating ramp of ß=2 K/s for the temperature range 300-1100-300 K.

At ~620 K, the onset of CO_2 production is observed by the emergence of the CO_2 signal (m/z=44) in the online gas analysis and the respective O 1s peak of gas phase CO_2 at 535.7 eV in the XP spectra. At the same time, also a decrease of the reactants CO and O_2 in the gas analysis and in the XP spectra is observed. The onset temperatures determined from XPS (Figure 5.2a) and online gas analysis (Figure 5.2b) are in a reasonably good agreement; one should note, however, that the temperature resolution of the online gas analysis is much higher than that of XPS: for the applied heating rate of 2 K/s the online gas analysis averages over 8 K (~4 sec per data point), whereas in XPS a temperature interval of ~240 K is averaged (~2 min per spectrum). Accordingly, in the following, the online gas analysis is used for the determination of the onset temperature, which here is defined as the temperature, at which

10% of the maximum CO_2 production is reached. The corresponding analysis of the data in Figure 5.2b yields 620 K. Interestingly, no adsorbed O-containing species are detected during reaction in the XP spectra; therefore, it is concluded that no (or only a minor amount of) oxide is present and that most of this reactive surface is in a metallic state. This is also observed in Fig 5.1b where the XP spectra 13-15 are added up: no surface species are observed in this very reactive region, whereas CO_2 production is observed in the fits of the gas phase signals and the gas analysis. After heating the surface to 1100 K, the heating ramp was reversed, and the sample was cooled with a rate of 2 K/s. The reaction persists down to temperatures of ~420 K (10 % of maximum CO_2 production). At this temperature, the O 1s peak of adsorbed CO grows again and the CO_2 gas phase signal decreases while the CO and O_2 signals rise. The same behaviour is also observed in the online gas analysis, which shows a decrease of CO_2 and an increase of CO and O_2 to the initial amounts. The observed reaction behaviour is explained by the Langmuir-Hinshelwood mechanism of the CO oxidation reaction: carbon monoxide and oxygen need to be adsorbed as next neighbours on the surface in order to react. As a CO precovered surface was chosen as starting point for the experiments, some CO first needs to desorb in order to allow oxygen to be adsorbed, which is required for the reaction. This saturated CO covered surface is well-known as CO poisoned surface in literature [8, 174], which inhibits the reaction. Note that no carbon impurities were found on the surface after the reaction.

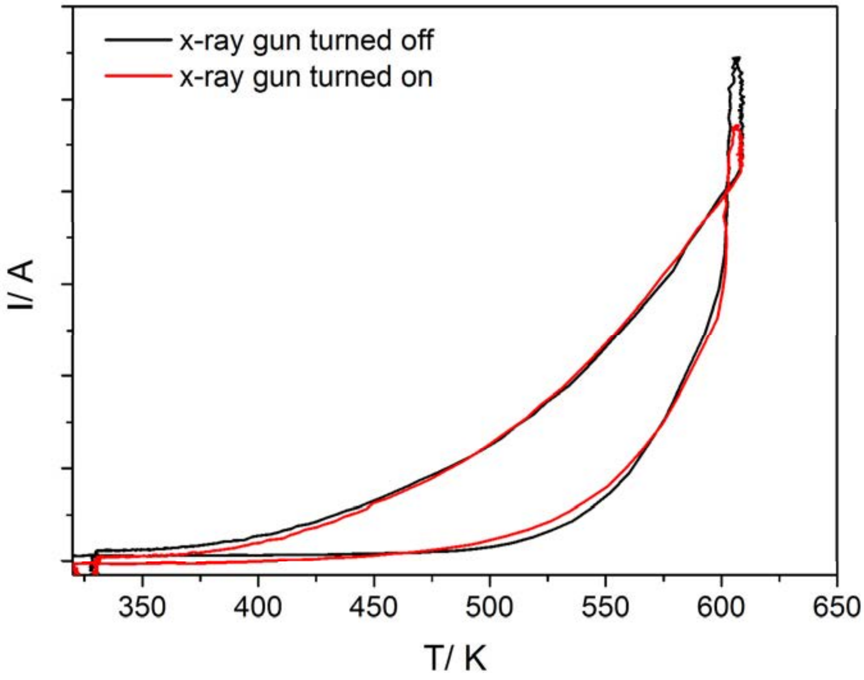

Figure 5.3: Comparison of the CO_2 signal of the online gas analysis of a 2:1 CO:O_2 mixture heated from 300 to 600 K with 2 K/s without (black) and under x-ray irradiation (red).

In order to exclude influence of the x-rays on the reaction, in Figure 5.3 an experiment without x-ray irradiation is compared to an experiment under x-ray irradiation. It shows the direct comparison of a 2:1 $CO:O_2$ mixture heated by a heating ramp from 300 to 600 K (β=2 K/s) without and under x-ray irradiation. Note that the slight changes at the beginning of the measurement are due to changes of the CO_2 background with time. No significant changes that are related to beam damage are observed, excluding influence of the x-ray irradiation.

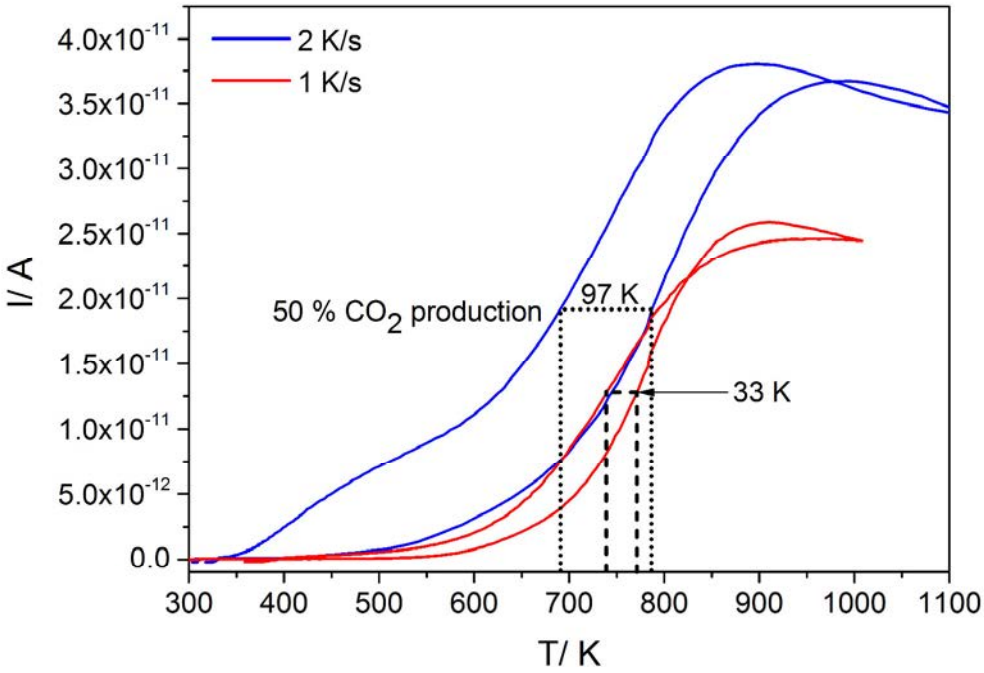

Figure 5.4: Intensity I vs temperature T of the CO_2 signals of the online gas analysis for a $CO:O_2$=2:1 mixture heated with 2 K/s (blue) and 1 K/s (red); hysteresis is shown at 50 % of the CO_2 production.

When analysing the reaction behaviour, a temperature difference was observed in the QMS data between the reaction onset during heating and the termination of the reaction during cooling as observed in Figure 5.4. This difference is much larger than expected from the different CO coverages on the surface that result from heating a saturated CO layer to a certain temperature or cooling the sample in a CO atmosphere to the same temperature. It is rather attributed to additional diffusion limitations (due to the finite pumping speeds) in the gas phase that are known for near ambient pressure systems: while the onset of CO_2 production is immediately monitored by XPS and online gas analysis (it occurs directly in the detection volume in front of the sample), at the end of the reaction CO_2 from the complete reaction chamber has to be pumped away, which proceeds at a much longer time constant. This interpretation is in line with the observation that the hysteresis of the CO_2 production is significantly reduced for a slower heating ramp (hysteresis of ~33 K at 50% of the CO_2 production for a heating ramp of 1 K/s compared to ~97 K at 2 K/s for the 2:1/CO:O_2 mixture).

To study the influence of the relative CO and oxygen pressures, the same type of experiment as in Figure 5.1 was performed for three different mixtures CO:O_2/ 1:1, 2:1 (stoichiometric) and 1:4, at a total pressure of 1 and 0.1 mbar. The temperature was ramped from 300 to 900 K with a heating rate of 1 K/s (averaging over 120 K in XPS). The onset temperatures are again derived from the more precise online gas analysis (10 % of maximum O_2 QMS signal). In Figures 5.5a and c, they are shown as function of the oxygen concentration in the reaction mixture for total pressures of 1 and 0.1 mbar.

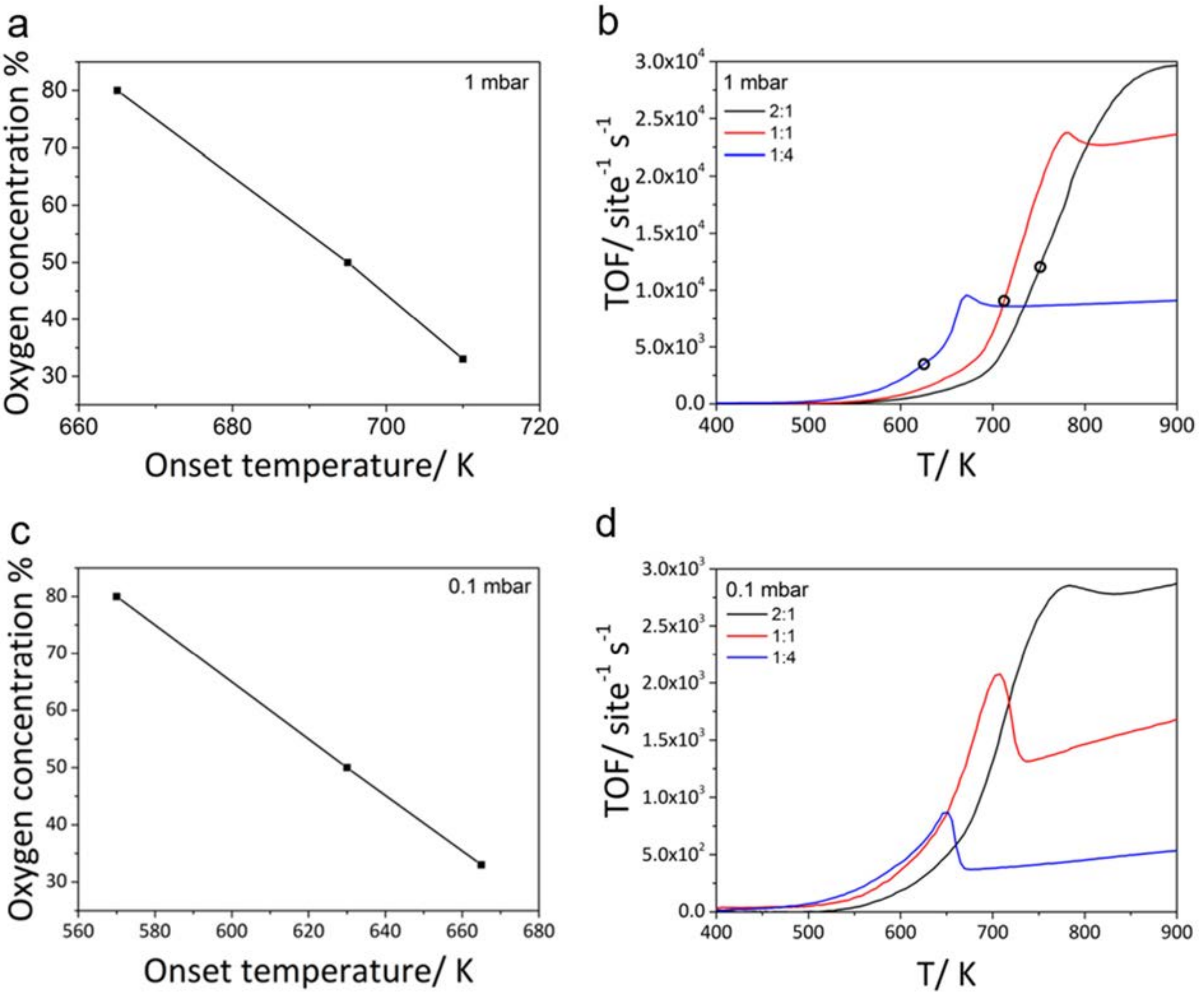

Figure 5.5: (a) Onset temperature for the reaction vs oxygen concentration in the gas mixture for the online gas analysis measurements; (b) TOFs for the different CO:O_2 gas mixtures with p_{tot} = 1 mbar; (c) onset temperatures and (d) TOFs with p_{tot} = 0.1 mbar. For further details see text.

A shift to lower onset temperatures with increasing oxygen concentration is found. This is attributed to the fact that the reaction only sets in when CO desorption from the CO poisoned surface takes place. The lower onset temperature for higher oxygen ratios at a given total pressure is due to the higher impingement and therefore adsorption rate of oxygen, which is in competition with (re-)adsorption of CO. At a total pressure of either 1 or 0.1 mbar, upon decreasing the CO partial pressure, the oxygen partial pressure is increased. Due to lower CO impingement rate, CO desorption sets in earlier and in addition the increased partial pressure of oxygen promotes oxygen adsorption. At 0.1 mbar reaction sets in at lower temperature than at 1 mbar, which is solely due to the lower CO partial pressure. Interestingly, no oxygen is found on the surface in the XP spectra during the reaction, thereby also ruling out the formation of a platinum oxide species. This leads to the conclusion that the reaction of adsorbed oxygen with CO as well as CO_2 desorption is fast, leading to an adsorbate free surface under the conditions investigated here.

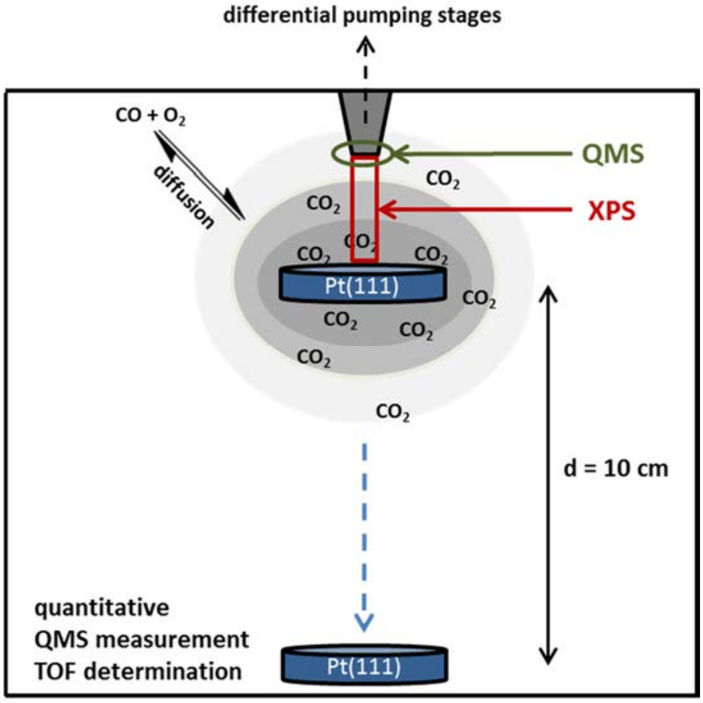

Figure 5.6: Schematic drawing of the measurement chamber and gas concentration above the surface.

Figures 5.5b and d show TOFs for the different mixtures as a function of temperature, as derived from the online gas analysis data. In general, the quantitative analysis from these data is, however, somewhat delicate as the results obtained from the gas analysis are strongly dependent on the sample position in front of the analyser entrance, due to the concentration gradient over the surface resulting from the mass transfer limitation (MTL) [18, 170, 176]; this is schematically illustrated in Figure 5.6. Therefore, for these measurements, the sample was moved to the bottom of the measurement chamber (d = 10 cm) where the influence of the pumping stages and the impact of an exact sample position is as low as possible (see Figure 5.6).

As a general trend, the temperature for reaching saturation decreases with oxygen content. Saturation indicates the point where the reaction is completely mass transfer controlled. In this regime, at a certain temperature CO oxidation is so fast, that the effective reaction rate and therefore activity is merely dependent on the diffusion of CO and O_2 to the catalyst surface; this behaviour results from the build-up of a concentration gradient due to insufficient mixing of the gas phase, as depicted in Figure 5.6. Diffusion-controlled reaction behaviour has been reported before for similar systems such as Pt(110)[17], RuO_2 [18] and Pd [170]. Unfortunately, this effect is influencing the reaction in such manner that a more detailed analysis of the reaction kinetics is not possible. The respective CO conversions are shown in Fig. 5.7. Here, as well, MTLs are observed. Interestingly, the CO conversions are higher for 0.1 mbar, which could be a result of higher diffusion limitations at the higher total pressure of 1 mbar.

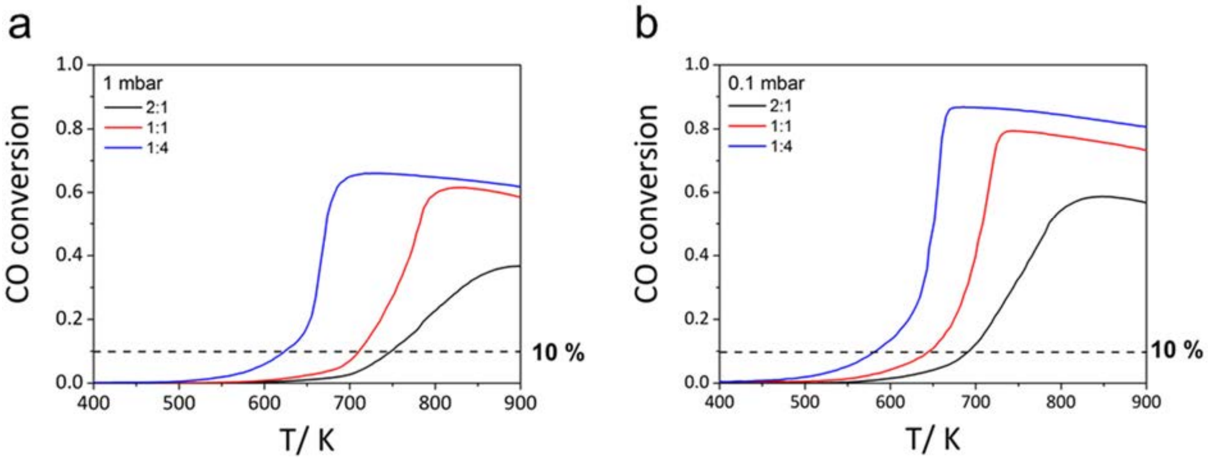

Figure 5.7: (a) CO conversion vs reaction temperature for the temperature programmed reactions for the 2:1 (black), 1:1 (red) and 1:4 (blue) CO: O_2 gas mixtures at 1 mbar and (b) at 0.1 mbar; the threshold of 10 % conversion is labelled.

The highest TOFs are observed for the 2:1 CO:O_2 mixture in Figure 5.5, whereas the lowest maximum TOF is found for a mixture of 1:4. The high values are in general explained by the CO_2 enrichment due to insufficient mixing. Comparing the calculated TOFs to literature [17, 67], TOFs in between 10^2-10^3 $s^{-1}site^{-1}$ are found under similar conditions for Pt and Rh; also in these cases MTLs determine the reaction and therefore the observed differences are explained by the different setups used. A maximum in TOF is observed before reaching the MTL regime for the oxidising mixtures only (1:1 and 1:4/ CO:O_2). The same behaviour was observed before, e.g. for Pt(110) and Rh(111), and was attributed to a sudden depletion of CO in the surface-near region; it was speculated that it is connected to the presence of chemisorbed oxygen on the surface for oxidising mixtures.[17, 48, 67] As no adsorbed species were observed at this point, in this case, latter assumption is not confirmed. The fact that the maximum was found for the oxidising mixtures exclusively, is explained by the excess of oxygen (CO/O_2 =1:4 and 1:1) for both oxidising mixtures in contrast to the stoichiometric mixture (2:1), where no such maximum occurs. Notably, in differential reactors the conversion is usually kept at 5-20 % in order to prevent changes in reactant ratios and hence to obtain differential rates. At higher conversions, concentration gradients are present, i.e. reactant concentrations are not uniform across the chamber.[177] For all investigated mixtures herein, CO conversion exceeds 10 % in the course of the heating ramp as illustrated in Figure 5.7a and b; for higher conversions, TOFs are effected to some extent by concentration gradients. TOFs up to conversions of 10 % are indicated by black circles in Figure 5.5b. For example, at 600 K TOFs of 420, 800 and 2100 CO_2 molecules site^{-1} s^{-1} are reached for 2:1, 1:1 and 1:4 CO:O_2, which are well in the order of TOFs observed in the mbar regime by other groups.[17, 49] Also at 0.1 mbar total pressure the reaction is suffering from MTLs as deduced from Figures 5.5d and 5.7b.

One point to be addressed is the fact that while the results derived from NAP-XPS and QMS measurements are in good qualitative agreement, they in some cases do show quantitative differences, that is, in some measurements higher values for conversion are observed by XPS than by the QMS analysis (see Figure 5.2 and Table 5.1). A possible reason for this is the setup of the chamber. While XPS averages the gradients in gas phase concentrations between the sample and the analyser, the QMS detects the gas composition at the entrance to the differential pumping stages (see Figure 5.6) and therefore detects less CO_2 and correspondingly more CO. This difference depends on the exact sample position, which can be reproduced only with a certain accuracy.

As there is an on-going debate about the nature of the oxidation state of platinum in the most active regime, also a temperature-programmed experiment in a highly oxidising CO:O_2 mixture of 1:10, at a total pressure p_{tot} = 1.1 mbar was performed. For Pt(110), it was claimed that platinum oxide is the most reactive species under highly oxidising conditions, leading to a steep increase in CO_2 production at 425 K and 1 bar [21, 44]. Therefore, here, a heating ramp of 2 K/min from 340 to 670 K was used; the respective online gas analysis of this experiment is shown in Figure 5.8.

Note that the short increase in CO signal at the time of admission of O_2 to the chamber is attributed to desorption from the chamber walls. Above 450 K, a significant increase in CO_2 production occurs. This increase dramatically accelerates at 563 K: within 1 K (i.e. 8 data points), there is an abrupt jump of ~50 % in CO_2 production (with 35 % occurring within 4 s, i.e. 1 data point). Thereafter, the signal stays nearly constant (with a small decrease) until 600 K, and subsequently starts to decline significantly. Note that the expected corresponding pressure drop in the O_2 signal (m/z = 32) of only a few percent cannot be unequivocally discerned at the given noise level of the O_2 data in Figure 5.8.

The O 1s XP spectra taken simultaneously were measured with 8 min per spectrum, i.e. a spectrum averages over a temperature range of ~17 K (the temperatures denoted in the following are the mean values). In Figure 5.9, selected spectra are shown; the denoted coverages were obtained from the total O 1s surface peak intensities. The spectra show the O 1s signals from the surface components, whereas the rise of signal intensity at the high binding energy side results from the gas phase signal.

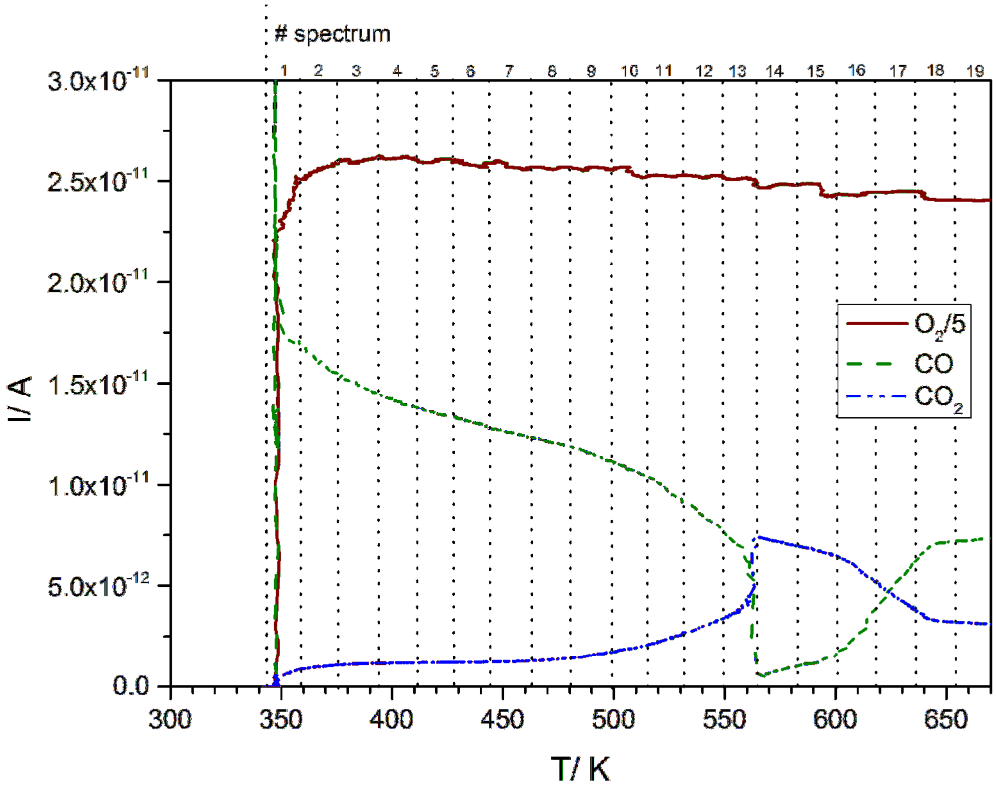

Figure 5.8: Online gas analysis of a 1:10 $CO:O_2$ mixture with a heating ramp 300-670 K with ß=2 K/min. Please note that the oxygen signal is divided by a factor of 5.

For the lowest temperature, the O 1s signal of adsorbed CO is observed (~368 K; spectrum 2; CO bridge (purple) and on-top (pink) were fitted to guide the eye), which strongly decreases upon heating (~488 K; spectrum 9, and also ~541 K; spectrum 12); in the last spectrum before the abrupt jump in CO_2 production at 563 K, no oxygen-containing species is observed (558 K; spectrum 13). Only in the spectrum taken after the jump (575 K, spectrum 14), an oxygen signal is observed again, which is attributed to oxide formation. Interestingly, with the onset of this oxide formation, the CO_2 production rate starts to decrease, indicating that the formed oxide increasingly inhibits the reaction. Note that the formed oxide is not a platinum oxide, but is identified as silicon oxide (see below). No oxidation of the platinum is observed in the Pt 4f region taken after the measurement in UHV, as shown in Figure 5.10.

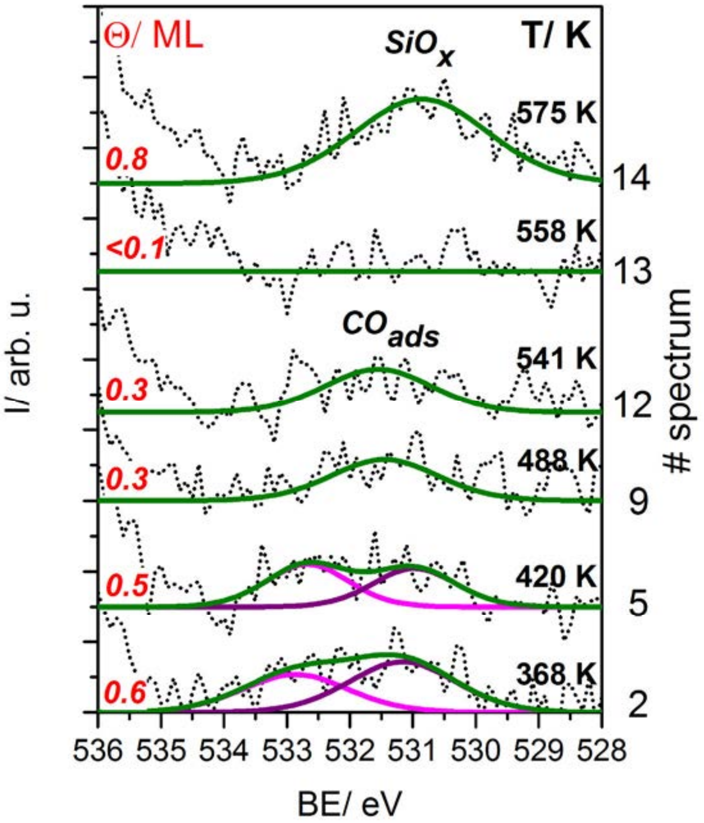

Figure 5.9: Selected XP spectra of the O 1s region of the surface species during the experiment in Figure 5.8 for the 1:10 CO:O_2 mixture with a heating ramp 300-670 K with ß=2 K/min; the surface coverages as determined from the total peaks areas are denoted. The temperatures of the XP spectra are given after half the spectrum was measured.

At this point, it has to be mentioned that although no O-containing species were detected in the highly active regime, one has to keep in mind, that a minority species with a coverage below the detection limit (here ~0.15 ML) could be responsible for the jump in activity at 563 K.

In other words, a jump from CO-covered to an adsorbate-“free” / clean surface occurs – which could be the jump already observed in literature when going from a carbon monoxide-covered to an oxygen-chemisorbed surface with a coverage below the detection limit.[17, 48, 178] In line with the interpretation of the *in situ* study that platinum oxide is not the active species, it was shown in an *ex-situ* experiment that α-platinum oxide is far less reactive towards CO than chemisorbed oxygen [111].

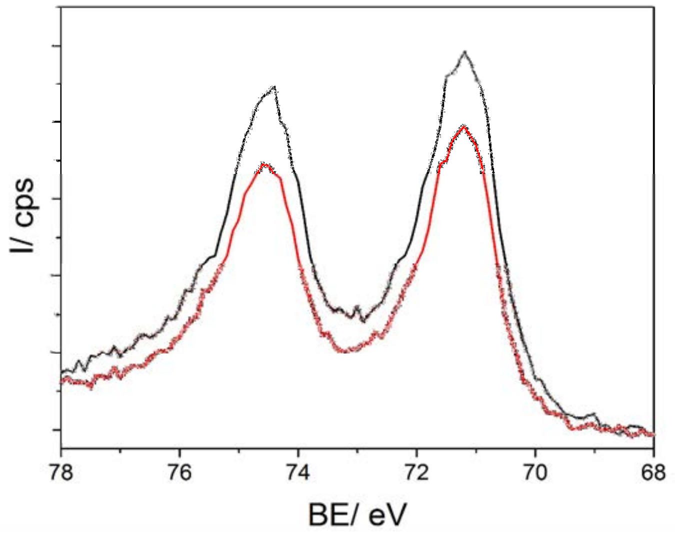

Figure 5.10: UHV Pt 4f XP spectra before (black) and after (red) the reaction for the 1:10 CO:O$_2$ mixture with a heating ramp 300-1100-300 K with ß=2 K/min; note that the damping of the signal results from the silicon oxide overlayer.

To summarize these results, the CO-inhibited regime at low temperatures and the role of the metallic, CO-free Pt surface (after CO desorption) as active phase with high activity for CO oxidation were discussed. Furthermore, a third regime was identified, where - in a very narrow temperature window - a dramatic increase of the CO$_2$ production occurs. It is likely that also in all other temperature-programmed experiments this sudden change in reaction takes place, but due to the limited time/temperature resolution and diffusion effects this effect is not sharp as observed signal increase in the online gas analysis.

5.4 Isothermal Reaction

As a second method to examine the interaction of CO and O$_2$ with the Pt(111) surface isothermal measurements were performed in order to gain information on the long term stability of the reaction. Again, the reaction was monitored simultaneously by NAP-XPS and QMS in a continuous flow mode.

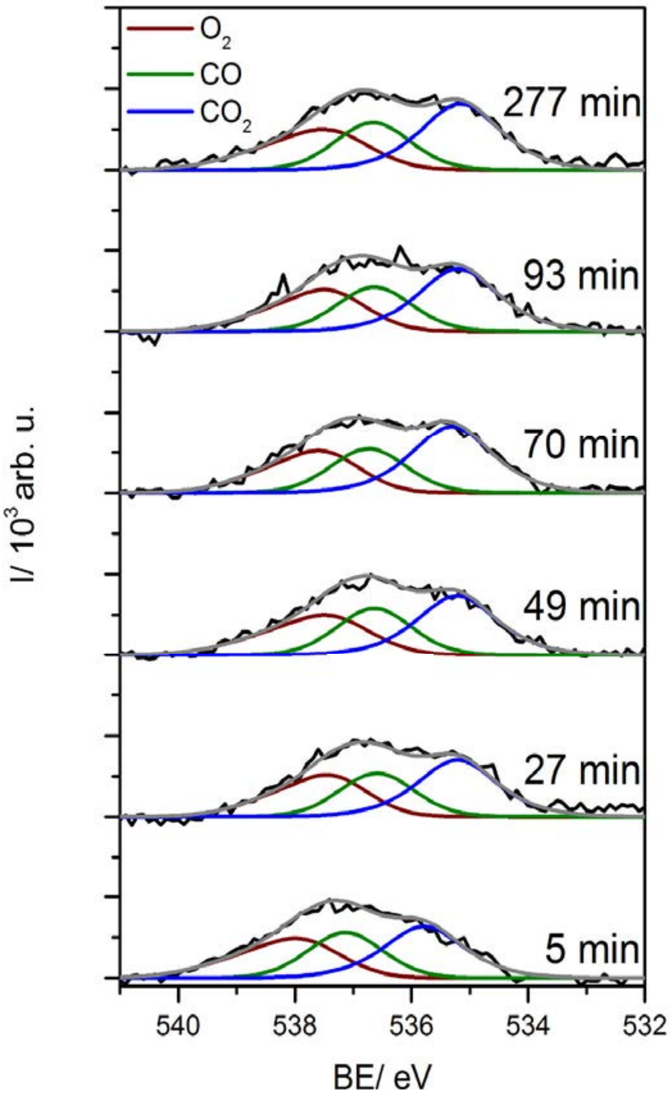

Figure 5.11: In situ O 1s spectra of the gas phase of a 2:1 CO:O_2 mixture at 750 K and respective fits for O_2 (red), CO (green), CO_2 (blue) and envelope (dark green).

First, the surface was exposed to CO and after establishing a stable background pressure, oxygen was added to yield CO:O_2 ratios of 2:1 (stoichiometric), 1:1 and 1:4, with p_{tot}=1 mbar. In all cases, the examination of the reaction over time did not show any significant changes of the activity during the isothermal experiments, which all took at least three hours. As a representative example, the gas phase O 1s spectra of the stoichiometric 2:1 mixture at 750 K are shown in Figure 5.11 as a function of reaction time. They consist of three signals belonging to O_2, CO and CO_2, whose ratios only change within the margin of error. Note that no O-containing surface species were detected during the reaction. The reaction of CO to CO_2 is evident from the CO_2 peak in the O 1s spectra in Figure 5.11, but also from the QMS measurements (data not shown). Table 5.1 summarizes the quantitative XPS and QMS analysis for the stoichiometric 2:1 mixture. At 650 K, only negligible reaction occurred, while at 750 K a significant reaction of CO is found (a conversion of 43 % deduced from XPS data, and 34 % from QMS; for an explanation of the larger value found in XPS see Chapter 5.3). Upon further increasing the temperature to 850 K, even higher conversion is observed, which then levels off at higher temperatures (see Table 5.1), due to mass transfer limitations.

Table 5.1: CO conversion in % for a 2:1 CO:O_2 mixture in an isothermal measurement; the XPS values in some cases are larger than the QMS values (see text); for the other studied gas mixtures a similar behaviour was found.

CO/O_2	**650 K**	**750 K**	**800 K**	**850 K**	**900 K**
XPS	5%	43 %	53 %	60 %	60 %
QMS	5 %	34 %	50 %	60 %	58 %

As for the temperature-programmed experiments, the isothermal reaction depends on the oxygen percentage in the mixture. This is evident from Figure 5.12a, where the TOFs and CO conversions for the different mixtures are plotted against reaction temperature, as derived from the O 1s NAP-XP spectra: for the 1:4 (CO:O_2) mixture, the reaction is very efficient already at 650 K, whereas for the stoichiometric (2:1) and for the slightly oxidising (1:1) gas compositions only at 750 K significant reaction was observed.

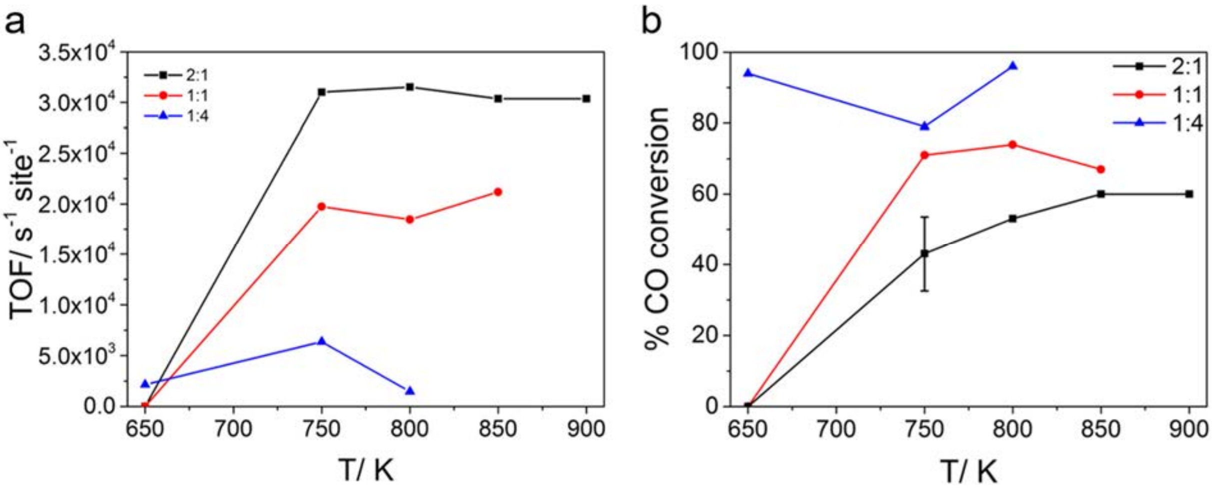

Figure 5.12: TOFs vs reaction temperature for the isothermal reactions for the 2:1 (black), 1:1 (red) and 1:4 (blue) gas mixtures.

The observed trend is in line with literature [175], were a lower onset in NAP-XP spectra was found at 535 K at a highly oxidising CO:O_2 ratio of 1:9, at a total pressure of 0.15 mbar. Again, no further increase in TOF is found from a certain temperature on, which is attributed to MTLs at the catalyst surface. The fact that MTLs start at lower temperatures for the 1:4 mixture indicates that CO is the limiting reactant. The MTLs are also reflected in the CO conversions shown in Figure 5.12b. Please note, that for TOF determination, the change in CO partial pressure due to build-up of a concentration gradient was considered; therefore, MTLs are observed in the TOF for the 2:1 mixture at 750 K already, while it is not clearly reflected in the CO conversion.

5.5 Growth and Poisoning with ”non-platinum”-oxides

In the course of the experiments, the development of an oxidic species at ~531.7 eV (slightly varying in binding energy) with time was detected in some of the O 1s region scans, especially at temperatures exceeding 600 K. A corresponding O 1s spectrum measured under UHV conditions after the growth of the respective oxide at 750 K is shown in Figure 5.13a.

For some experiments, the growth of the oxide led to a decrease in CO_2 production up to total inhibition of the reaction within minutes (Figure 5.13c), as observed in XPS and QMS. The formed oxide is stable towards heating up to 1100 K in UHV and also in a CO atmosphere of 1 mbar at 800 K. This stability is not in line with observations for platinum oxides in the literature [111] and discussed in Chapter 4 of this work, but has been observed for non-platinum oxides formed from minor bulk contamination of the Pt sample [61, 164, 165].

Indeed, the survey spectrum in Figure 5.13d shows the emergence of the Si 2s signal characteristic of Si oxides with roughly Si:O_2 stoichiometry; a blow-up of the Si 2s signal from a different experiment is also shown in the inset of Figure 5.13a. Note that the satellite of the Pt 4f signal overlaps with the Si 2p signals which are the strongest lines for silicon; therefore, only the weaker Si 2s signal is shown. The assignment is further supported by the absolute O 1s binding energy of 531.7 eV, which is typical for SiO_2, but much larger than the values of ~530 eV typically observed for platinum oxides [106, 111, 179]. Additionally, no changes were observed in the Pt 4f core level spectra taken before and after the oxidation experiment in UHV (see Figure 5.13b). The amount of silicon oxide increased with increasing oxygen partial pressure and/or temperature. By repeated oxidation/sputter cycles the silicon impurities could be removed. Interestingly, exposing the sample to ambient conditions leads again to an increased amount of silicon in the near surface region. Similar behaviour was also found during the platinum oxidation experiments shown in Chapter 4.

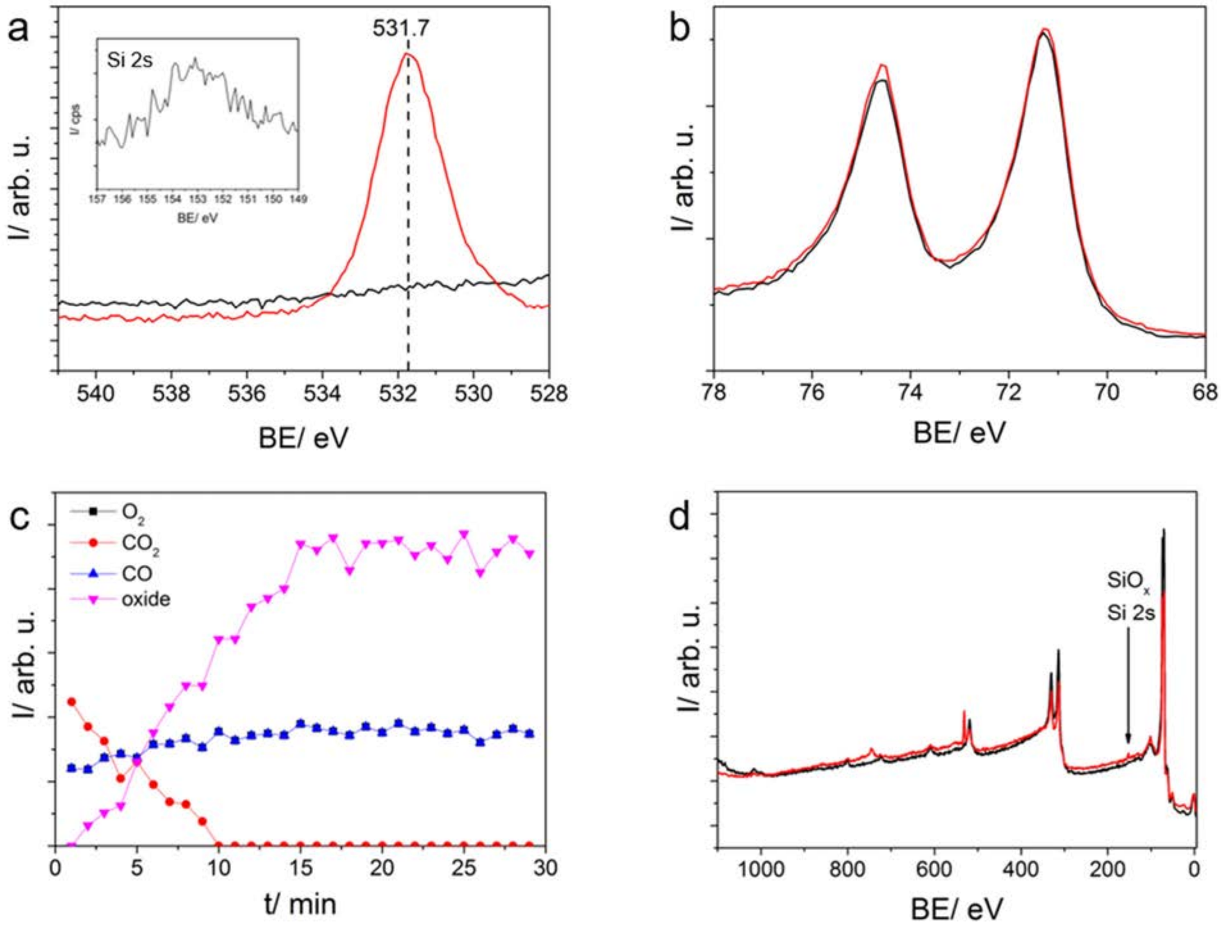

Figure 5.13: (a) O 1s spectrum before reaction (black) and after pump-down in UHV (red) of the reaction for a 2:1 CO:O_2 mixture at 750 K and in the inset the Si 2s signal from the survey, (b) the respective Pt 4f core level spectra before reaction (black) and after pump-down of the reaction (red) (c) integrated O 1s intensities (for the gas components O_2, CO, CO_2, and for surface oxide) vs time for the respective measurement and (d) survey spectrum before (black) and after (red) the oxidation experiment with the Si 2s signal at ~150 eV due to silicon oxide formation.

5.6 Conclusion

In this chapter isothermal as well as temperature-programmed reaction experiments of the CO oxidation reaction for three different mixtures of CO:O_2 (2:1, 1:1, 1:4) at total pressures up to 1 mbar monitored by NAP-XPS and online gas analysis were discussed. The reaction was followed by XPS via the clearly separated O 1s gas phase signals of O_2, CO and CO_2, and simultaneously by a QMS attached to the second differential pumping stage of the setup. With both techniques, the reaction was found to start at a certain onset temperature, which depends on the oxygen percentage of the mixture; the higher the relative oxygen content of the mixture, the lower the onset temperature. This behaviour is attributed to poisoning of the catalyst by CO and to a higher oxygen adsorption rate at higher oxygen content, due to the fact that adsorption of O_2 and (re-)adsorption of CO are competitive processes. At the investigated total pressures of 0.1 or 1 mbar for the different gas mixtures, the CO and O_2 partial pressures changed, influencing the ad- and desorption. The observations are in line with the literature, under the assumption of a Langmuir-Hinshelwood mechanism [8]. For both temperature-programmed and isothermal experiments, the highest TOFs were found for the stoichiometric mixtures. The TOFs increased with increasing temperature and stagnated at a particular temperature due to mass transfer limitations. While the results obtained from NAP-XPS and online gas analysis were qualitatively in good agreement, quantitative comparison showed that the QMS in some cases slightly underestimates the conversion, which is ascribed to different detection regions for the different methods. Concerning the reactive species in the active regime, no detectable amounts of oxygen-containing species were found on the surface in the temperature programmed investigations and therefore the surface is in a mostly metallic state. These findings are in line with the low stability and the slow growth observed for the platinum oxides investigated in Chapter 4 under similar conditions. Since the experiments were started out with a CO precovered catalyst surface, the reaction onset was determined by CO desorption. In an additional experiment using a highly oxidising mixture ($CO:O_2=1:10$; $p_{tot}=1.1$ mbar) in combination with a considerably slower heating rate three different regimes were observed: (I) CO-inhibited with negligible activity (II) partially CO-covered with moderate activity, and (III) adsorbate-free with high activity. Upon prolonged heating, in some cases the formation of SiO_2 was observed on the platinum surface; the growth of this oxide leads to a poisoning of the catalyst up to total inhibition of the reaction. This or similar “non-platinum” oxides result from minor Pt bulk impurities and hence similar effects should be considered also in heterogeneous catalysis.

This study revealed a metallic catalyst under reaction conditions at 1 mbar total pressure. Considering a high pressure-dependence of the Pt/O system, at higher pressures the platinum oxide growth might be considerably faster than at 1 mbar and compete with the CO oxidation reaction, i.e. change the oxidation state of the catalyst during the reaction and therefore also the mechanism. This underlines the importance of investigations within the pressure gap, as UHV results are not representative of the catalyst state under realistic conditions.

6. Reactivity of TiO_2 nanotube-supported Pt particles in the CO oxidation reaction

6.1 General

In a subsequent investigation, the reactivity of more complex catalyst/ support systems, that are TiO_2 nanotube arrays decorated with Pt particles, was tested in the CO oxidation reaction and compared to a TiO_2-supported nanostructured Pt film and a Pt(111) single crystal. The purpose was to introduce more complexity in a very controlled way, as the arrays consist of upright standing nanotubes of defined length (200 nm) and diameter (80 nm) and the Pt particles are spread uniformly across the tubes, while the size and location of the particles of different sizes have been specifically tuned. All nanotube-supported samples have been prepared in the work group of Prof. P. Schmuki at the Chair of Surface Science and Corrosion of the Department of Materials Science and Engineering of the University Erlangen-Nürnberg. These systems are used to mimic “real” catalysts, often containing porous oxidic supports with particles and therefore study the impact of effects like particle size with smaller particles exhibiting a higher step/defect density and pore diffusion. The results of this chapter have already been published and the text has been adapted from this publication:

“Reactivity of TiO_2 nanotube-supported Pt particles in the CO oxidation reaction”, Krick Calderón, S., Grabau, M., Yoo, J.E., Kilian, M.S., Schmuki, P., Steinrück, H.-P., Papp, C., ChemCatChem, *accepted,* **2016**.

In heterogeneous catalysis, oxide-supported metal particles are widely used due to their extraordinary activity in, amongst others, oxidation reactions. Titanium dioxide is one of the most prominent support materials in combination with transition metal particles.[25, 35, 180, 181] The reason for the high interest in this support material is its high chemical stability, non-toxic nature, the low production costs and its eco-friendliness.[182-184] Numerous model studies have been performed to further improve the fundamental understanding of the properties of TiO_2 and its role in surface reactions.[36, 180, 184-189] Although insights from model catalytic studies of the surface structure, adsorption behaviour, support-metal interaction and reactivity contribute to the understanding of more complex systems, there remains a materials gap between well-ordered systems like single crystals and “real” catalysts (see also Chapter 1.2).[4, 14, 15, 32, 190, 191] Therefore, more complex systems have to be investigated under realistic conditions in order to understand the reaction steps and as a result to improve catalytic reactions.

Additionally, the oxide supports are often porous materials with a high surface area, where a higher metal loading can be achieved compared to flat substrates. This in turn enhances the overall efficiency of a catalyst.[41, 42] New preparation methods in this field allow for nanostructuring of the catalyst to further enhance its performance. [192] Either the active catalyst particles or the support can be tuned, thereby opening a wide parameter space.[193-195] Nanostructuring can drastically change electronic as well as transport properties due to confinement effects and influence of reactant diffusion, leading to improved reactivity and selectivity for the targeted reactions.[43, 193] One example for a very well defined change of the catalyst support are TiO_2 nanotubes (NTs), as compared to titania powder or flat titania surfaces. They are produced by electrochemical anodization and their length and diameter can be tailored accurately.[183] This should allow for influencing parameters that are important for catalytic reactions such as pore diameter and specific surface area.[41, 42] The preparation of TiO_2 NT arrays, which are decorated with noble metals of controllable particle size, has been shown in previous work.[196-199]

The oxidation of CO over platinum was chosen as model reaction, because it is a well-studied model system in surface science to investigate changes in reactivity upon nanostructuring of the support and the catalyst particles. This reaction is particularly well suited as model reaction, because of its simplicity, that is, only one product, CO_2, is formed, as explained in Chapter 3.1.[47] Additionally, it has found high interest because of its importance in heterogeneous catalysis, where platinum group metals have been found to be very active in this reaction [46, 48] as was also shown in Chapter 5 on the Pt(111) single crystal.

Also already explained and shown in Chapter 5, the reaction was probed carefully in UHV studies [8, 17, 23, 46, 67, 89, 200, 201] and for platinum group metals it was found to follow a Langmuir-Hinshelwood mechanism.[8, 74, 88] It also is of high practical importance in the catalytic converters of cars, where the toxic CO is oxidized to CO_2.[84] Investigations in the mbar regime showed the reaction at the catalyst surface to be strongly mass-transfer limited at elevated temperatures (see also Chapter 5).[17, 18, 49, 67, 74] By using porous materials like NTs, in contrast to flat materials, it might be possible to additionally study transport effects like pore diffusion. In this case, the overall efficiency results from the combination of interphase diffusion to the catalyst surface and pore diffusion, which for real conditions often plays the major role.[4] Recently, TiO_2 NTs (similar to those investigated in this work) decorated with Pd particles were studied by *in situ* infrared reflection absorption spectroscopy (IRAS) in order to understand CO adsorption kinetics. It was found that the localization of the particles within the tubes strongly influences CO adsorption.[43] This could indicate that gas transport within the tubes indeed affects particle-catalysed reactions, depending on the localisation of the particles. This scenario is not desirable as the overall reaction rate is dependent on the diffusion of the reactants to the catalyst or within the pores and does not resemble the intrinsic rate of the catalyst, which reduces the efficiency.[4]

In this chapter, the CO oxidation reaction at total pressures up to 1 mbar was investigated by near-ambient pressure photoelectron spectroscopy (NAP-XPS) and simultaneous online gas analysis using a quadrupole mass spectrometer (QMS). In temperature-programmed experiments, the reactivity of different TiO_2 nanotube-supported samples, decorated with Pt particles of different sizes, was compared with that of nominally 5 nm Pt deposited on a $TiO_2(110)$ rutile single crystal, and with Pt(111). Catalyst and support were probed by NAP-XPS in temperature-programmed and isothermal experiments, and the species present on the surface were analysed. The impact of mass transport and ageing of the samples on the reaction was also discussed.

6.2 Experimental aspects

The acquisition time for the O 1s spectra was ~3 min for the temperature-programmed experiments. For the isothermal experiments, the acquisition times were ~60 min for the O 1s spectra, 90 to 180 min for the C 1s spectra, ~170 min for the Ti 2p spectra, ~140 min for the Pt 4f spectra, and ~15 min for the survey spectra. Binding energy shifts of the surface XP signals due to heating of the samples were compensated by shifting the TiO_2 lattice oxygen signal relative to the binding energy of the lattice oxygen peak without heating. Active Pt sites for all TiO_2-supported samples (Figure 6.2, Chapter 6.3) were titrated by CO. These values were used for turnover frequency (TOF) determination and *in situ* coverage determination on the particles. For the pristine TiO_2 NTs samples, that is, without deposited Pt, no CO_2 formation was observed under the reaction conditions applied when studying the Pt-loaded samples.

6.3 Investigated Pt/TiO_2NT samples and active sites determination

Three different types of Pt-decorated TiO_2 nanotube arrays were examined concerning their reactivity in the CO oxidation reaction. All consist of a support consisting of TiO_2NT arrays with upright standing tubes of 200 nm length and 80 nm diameter. To achieve different metal loadings and particle sizes, nominally 5 and 15 nm Pt were sputtered onto the NTs; in a dewetting process, particles of different sizes were formed, as can be seen in Figure 6.1a and b, respectively. The 15 nm Pt/TiO_2NT sample contains particles of ~40-80 nm on the rim of the tubes and smaller particles of ~10 nm inside the tubes. The 5 nm Pt/TiO_2NT sample contains particles of ~30-40 nm on the rim of the tubes and small particles of ~7 nm spread homogeneously at the rim, inside and at the bottom of the NTs.

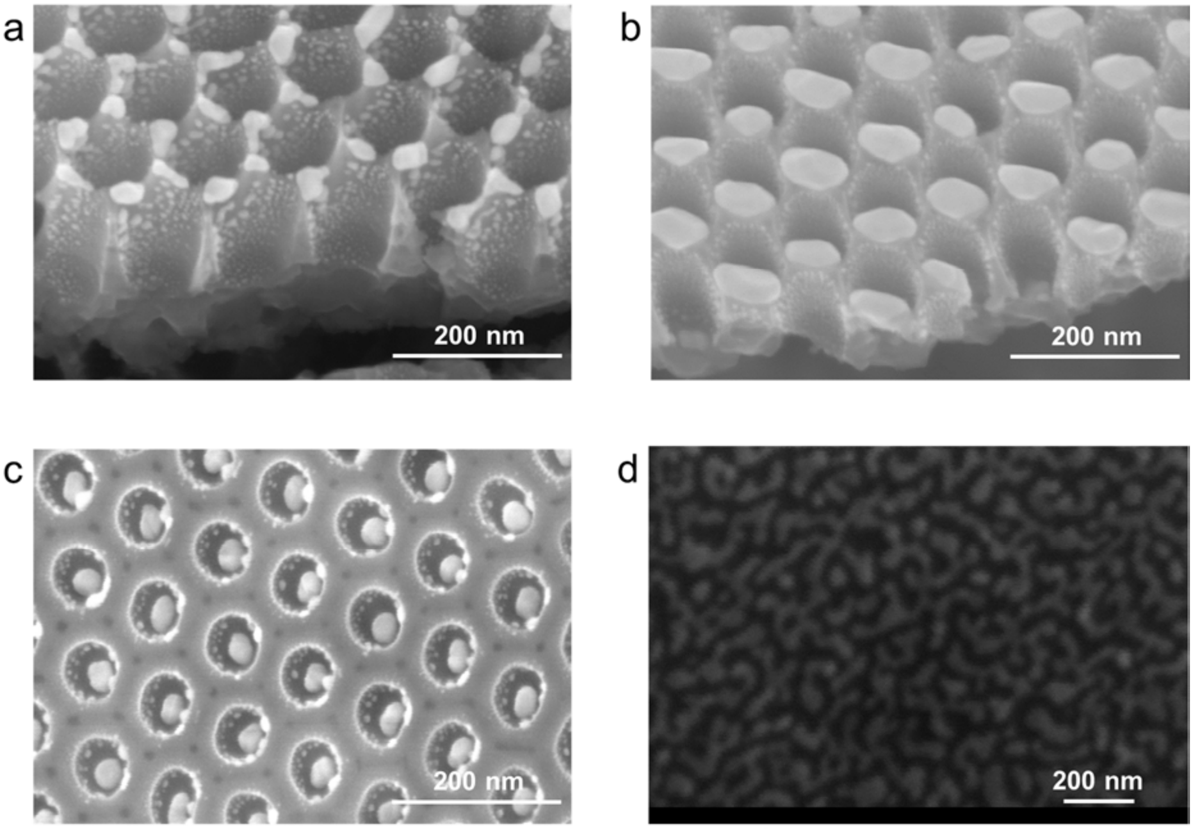

Figure 6.1: SE micrographs of (a) $Pt_{5nm}TiO_2NT$, (b) $Pt_{15nm}TiO_2NT$, (c) the $Pt_{ion\text{-}milled}TiO_2NT$, and (d) $Pt_{5nm}TiO_2(110)$, after preparation.

The third Pt/TiO_2NT sample was decorated with 15 nm Pt and subsequently ion-milled (sputtered) to remove the particles on the rim of the NTs. As evident from Figure 6.1c, this resulted in a single particle of ~40-60 nm on the bottom of the tube and smaller particles of ~10-20 nm diameter distributed on the nanotube walls. In the following, the samples will be referred to as $Pt_{5nm}TiO_2NT$, $Pt_{15nm}TiO_2NT$ and $Pt_{ion\text{-}milled}TiO_2NT$. Furthermore, the results from the NT samples are compared with measurements on a $TiO_2(110)$ rutile single crystal with a similar nominal Pt coverage (5 nm Pt, "$Pt_{5nm}TiO_2(110)$"), which forms a nanostructured film (Figure 6.1d), and with a Pt(111) single crystal.

Active sites in the CO oxidation reaction were determined from CO adsorption after exposure to CO in the mbar regime and pump down to UHV at 300 K. The signal intensities of CO adsorbed on platinum were compared to the c(2x4) CO superstructure on Pt(111) with a coverage of 0.5 ML (see Chapter 3.1.1) for site determination. Here, a saturation coverage of CO of 0.5 ML was assumed for all samples, while all surface sites were expected to be active in the CO oxidation reaction and therefore contribute to the number of active sites/cm^2 given on the right side of Figure 6.2. Please note, that possible desorption of CO molecules during pump down is neglected, although the error is within ± 0.1 ML. The respective C 1s spectra are shown in Figure 6.2 in combination with the C 1s spectra of the c(2x4) CO superstructure on Pt(111) and CO adsorbed on the TiO$_2$NT reference without Pt particles.

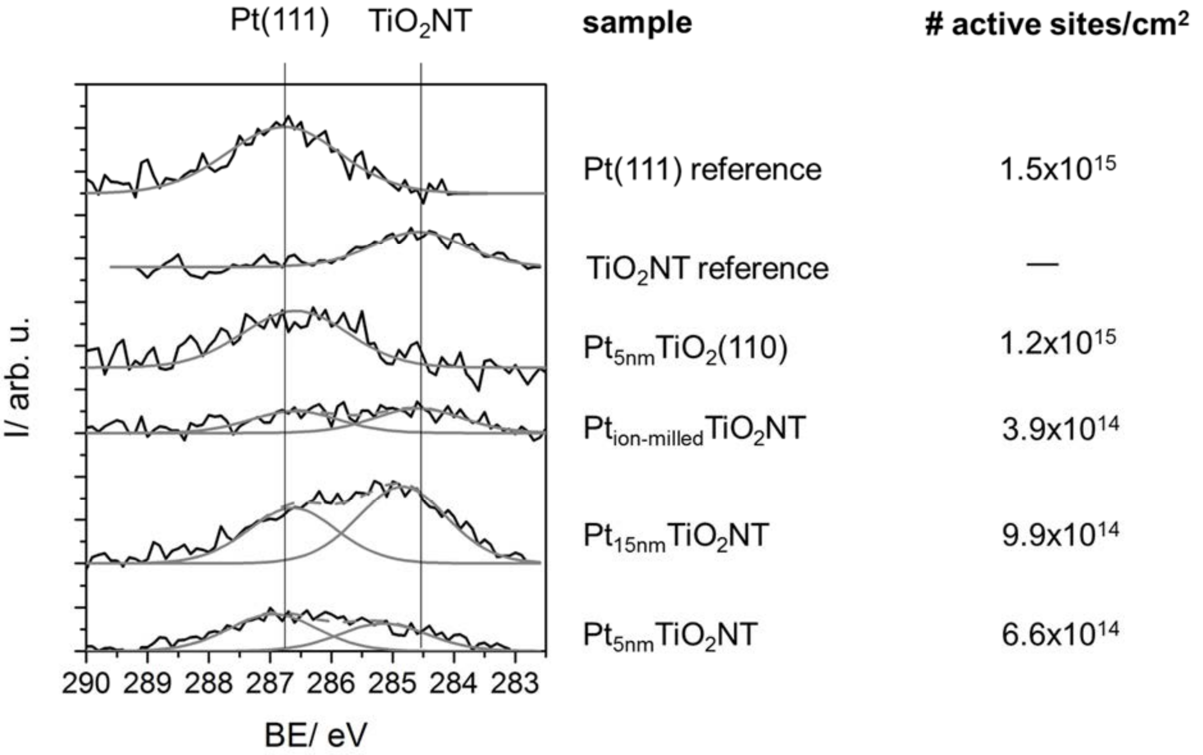

sample	**# active sites/cm^2**
Pt(111) reference	1.5x10^{15}
TiO$_2$NT reference	—
Pt$_{5nm}$TiO$_2$(110)	1.2x10^{15}
Pt$_{ion-milled}$TiO$_2$NT	3.9x10^{14}
Pt$_{15nm}$TiO$_2$NT	9.9x10^{14}
Pt$_{5nm}$TiO$_2$NT	6.6x10^{14}

Figure 6.2: C 1s region scans after CO adsorption in the mbar regime and determined active sites.

The upper C 1s spectra show CO adsorbed on a Pt(111) single crystal and on the pure TiO$_2$NT sample. The two signals are observed at 286.8 and 284.5 eV with a binding energy difference of 2.3 eV and therefore can be clearly separated. The C 1s region scans for the TiO$_2$NTs decorated with particles (Pt$_{5nm}$TiO$_2$NT, Pt$_{15nm}$TiO$_2$NT and Pt$_{ion-milled}$TiO$_2$NT), exhibit two separated peaks, respectively. Therefore, the peak at higher binding energy is attributed to CO adsorbed on the Pt particles and the peak at lower binding energies is attributed to CO adsorbed on the TiO_2NT support. In case of the $Pt_{5nm}TiO_2(110)$ sample, only one peak is observed, which is ascribed to CO adsorbed on the nano-structured platinum film; from the fact that the spectrum only shows one signal it is concluded, that the platinum film is closed and there is no interaction of CO with the TiO_2 support. Slight shifts in the position of the signal for CO/Pt are attributed to a changed bonding situation for the differently sized particles and the nanostructured film. Please note that a binding energy shift of ~0.9 eV in the signal of CO adsorbed on the TiO_2NT reference to lower binding energies was observed after pump-down to UHV (see Figure 6.3), which might also explain the slightly different binding energies of CO adsorbed on the NT supports found in Figure 6.2. The coverage of CO on the TiO_2NT reference sample is 0.26 ML compared to the 0.5 ML c(2x4)-CO superstructure on Pt(111).

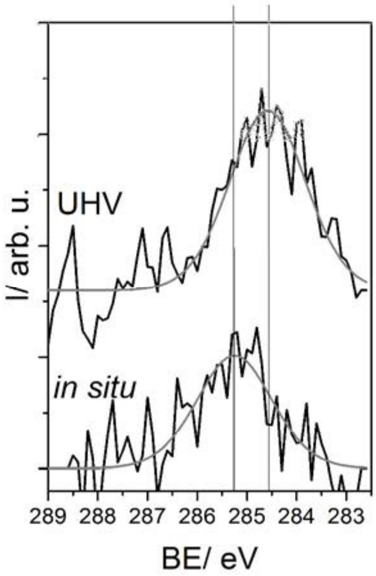

Figure 6.3: C 1s region scans of the TiO_2NT reference sample at 1 mbar CO (in situ; lower spectrum) and after pump-down to UHV after CO adsorption (upper spectrum).

6.4 Reactivity of different Pt-containing samples

The CO oxidation reaction was carried out with an oxygen-rich gas mixture, that is a CO to O_2 ratio of 1:4, to prevent CO poisoning of the Pt. The samples were heated from 300 to at least 600 K with a heating rate of 10 K/min at a total pressure of 1 mbar. During the reaction, the surface was monitored via NAP-XP spectra of the O 1s region, and the gas phase was analysed by a quadrupole mass spectrometer (QMS).

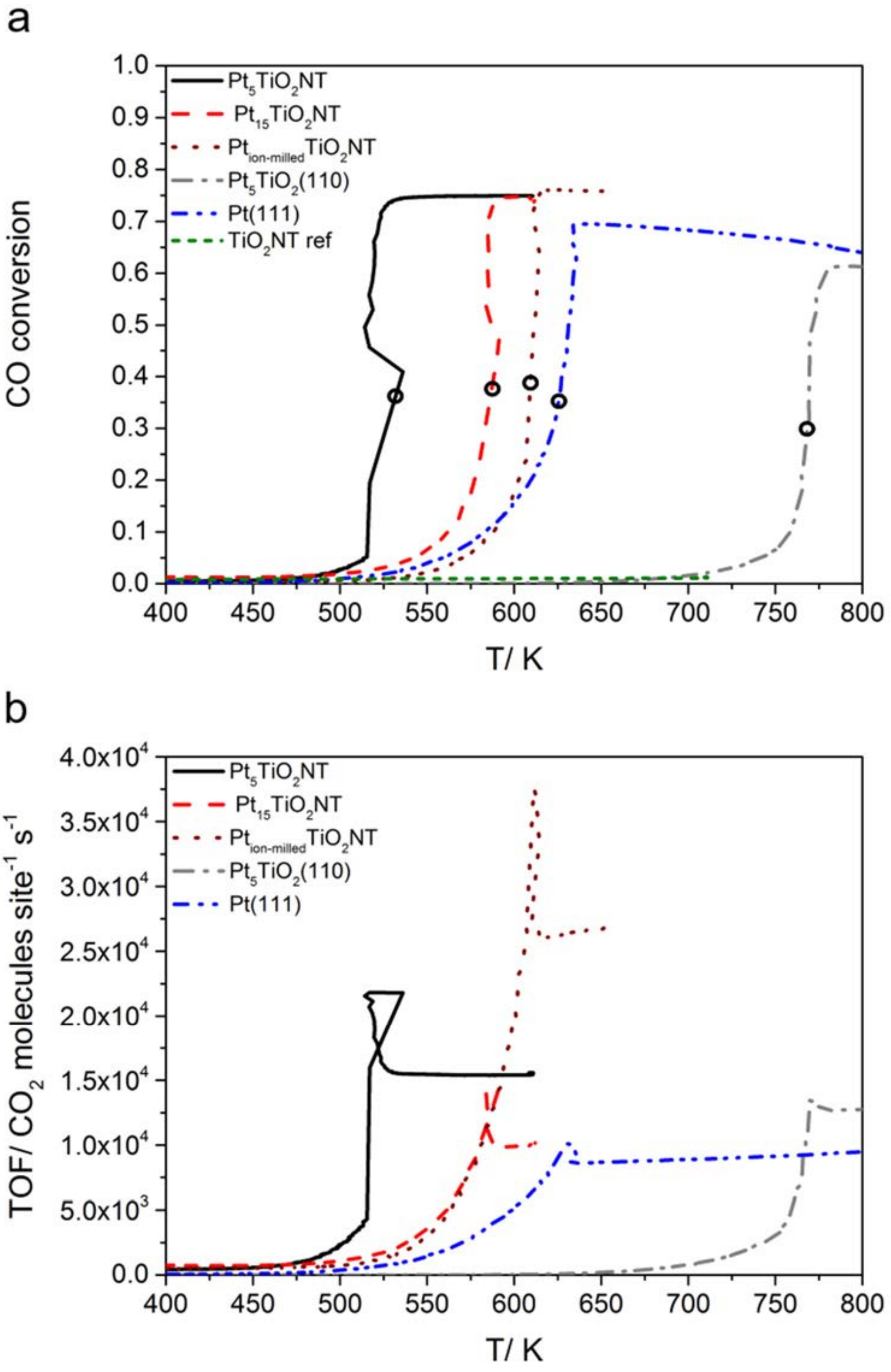

Figure 6.4: (a) CO conversions derived from the online gas analysis taken during the heating ramp from 300 to 600 (650, 800) K in a mixture of 1:4 CO/O_2 at p_{tot}=1.0 mbar on the $Pt_{5nm}TiO_2NT$ sample (black solid line), the $Pt_{15nm}TiO_2NT$ sample (red dashed line), ion-milled sample (brown dotted line), $Pt_{5nm}TiO_2(110)$ (grey dashed-dotted line), a Pt single crystal (blue dashed-dotted line) and the TiO_2NT reference (green dashed line) and (b) respective TOFs.

The CO conversion on the different samples as deduced from the online gas analysis is shown in Figure 6.4a, including the reference experiment on the pristine TiO_2NTs, where no conversion was observed; the respective turnover frequencies (TOFs) are shown in Figure 6.4b.

Please note, that for all samples conversions exceeding 10 % are obtained and therefore concentration gradients are present. This is also reflected in the very high TOFs shown in Figure 6.4b. For example, for the $Pt_{5nm}TiO_2NT$ sample we obtain a TOF of ~4200 molecules site^{-1} s^{-1} and for the Pt(111) single crystal a TOF of ~1900 molecules site^{-1} s^{-1} at 5 % conversion which is close to reported values under similar conditions.[17, 67, 74]

For all samples, first no conversion is observed. This is a result of adsorbed CO on the surface, because gas dosage was started at 300 K. Therefore, the catalyst is initially saturated with CO. Since CO oxidation follows a Langmuir-Hinshelwood mechanism[8], adsorbed oxygen is required for the reaction to occur. To enable adsorption of oxygen, CO first needs to desorb and then CO oxidation can start. In all cases, CO_2 production increases upon heating; however, the behaviour for the different samples is quite different: for the $Pt_{5nm}TiO_2NT$ sample, after a slow exponential increase at ~450 K, a dramatic increase is observed at ~515 K, by a factor of 4 between two data points, which means within 4 seconds.

In contrast, on the Pt(111) crystal only the same smooth increase is found in the beginning, which continues to proceed at higher temperatures, but no rapid increase is observed. Notably, in a more oxidizing mixture, that is, at a CO to O_2 ratio of 1:10, a sharp increase in the reactivity was also found for Pt(111).[74] The non-linear temperature behaviour for the $Pt_{5nm}TiO_2NT$ sample is due to the exothermic nature of the CO oxidation reaction: the strong increase in CO_2 production in a very short time leads to an increase in temperature that cannot be compensated fast enough by the temperature control unit. For the pristine TiO_2 NTs reference sample, that is, without deposited Pt, no CO_2 formation and therefore no increase in CO conversion observed in Figure 6.4a (green dashed line) under reaction conditions.

In order to compare the behaviour of the different samples, the temperature $T_{1/2}$ is defined, which denotes the temperature, where the CO conversion has reached half of its maximum value; maximum conversion is reached, when the reaction enters the mass transfer-limited regime (see below). The $Pt_{5nm}TiO_2NT$ sample shows the lowest $T_{1/2}$ value with ~530 K, followed by $Pt_{15nm}TiO_2NT$ with ~585 K, $Pt_{ion\text{-}milled}TiO_2NT$ with ~610 K, Pt(111) with ~625 K, and finally $Pt_{5nm}TiO_2(110)$ with ~770 K. The lowest $T_{1/2}$ value for the $Pt_{5nm}TiO_2NT$ sample is attributed to the higher step/defect density of the highly dispersed small Pt particles, as apart from the different particle diameters, the TiO_2NT-supported samples are identical (see Fig. 6.1). Please note that strong particle size effects are well-known for supported particles with diameters of 10 nm and smaller, one reason being an increasing amount of step, kink and defect sites with decreasing particle diameter, which changes the adsorption strength of the reactants.[25] The higher $T_{1/2}$ value for the $Pt_{15nm}TiO_2NT$ sample is probably also related to the location of the particles: the bigger particles on the rims of the tubes seem to have a higher impact than the smaller particles within the tubes, which might be related to a diffusion limitation of the gases to and from the inside of the NTs. The comparably high $T_{1/2}$ value for the $Pt_{ion\text{-}milled}TiO_2NT$ sample indicates that the big particles on the bottom seem to play the major role. The most surprising behaviour is observed for the $Pt_{5nm}TiO_2(110)$ sample, which consists of a nano-structured film (see Figure 6.1c). For this film with a high step/defect density one would expect a rather low $T_{1/2}$ value, certainly lower than that of Pt(111). Nevertheless, reaction sets in only at ~770 K, which is ~145 K higher than found for Pt(111). Like all particle samples, this sample was also heated in O_2, but up to 600 K, in order to remove carbon impurities; in addition it was heated to 980 K in UHV in contrast to the NT-supported samples, which were not heated to such high temperatures. During this procedure and the CO oxidation experiments, the overall XP signal from the Pt particles decreased, whereas the support signals increased, which is shown in Figure 11.3.2 of the Appendix as a comparison of the respective core levels before and after the temperature programmed experiment shown in Figure 6.4a and b. This clearly shows that the catalyst/support system changed, which is attributed to particle sintering and/or strong metal support interaction (SMSI) effects. The latter effect is known for Pt/TiO_2 [37, 202, 203] and is known to change the electronic structure of the platinum system or TiO_2 might even "creep" onto the catalyst material and thereby, for example, change CO adsorption[36]. This goes along with a change in the film morphology, as smaller aggregates are observed on parts of the sample after the experiments compared to the nanostructures found before the reaction (compare Figures 1d and 11.3.3b). The fact, that no such changes (as observed in Fig. 11.3.2) were observed in the core levels of the nanotube-supported samples, shows that these sample exhibit not such strong sintering/SMSI effects. In the course of prolonged heating experiments, that is, for ~8 h at temperatures up to 615 K, we did not find an indication of ageing effects for the $Pt_{15nm}TiO_2NT$ sample (a second sample showed the same $T_{1/2}$ value and an unchanged activity even after ~24 h of isothermal experiments). Only for the $Pt_{5nm}TiO_2NT$ sample, in contrast, the CO conversion decayed more rapidly and after 16 h only a conversion of ~4% remained even at a temperature of 610 K; this ageing indicates a lower stability of the sample with the small clusters, which is also seen as partial decomposition of the sample in the SE micrograph after the reaction experiments (c.f. Figure 6.1a and 11.3.3a), and also effected the isothermal measurements described below.

At a sample-specific temperature, a region of (more or less) constant CO conversion is reached, corresponding to the MTL regime. In the MTL regime, the consumption of the reactants CO and O_2 is so fast that it cannot be replenished fast enough and consequently a concentration gradient results in close vicinity to the sample; due to this concentration gradient, that is, a lack of reactants at the catalyst, the reaction is determined by the diffusion of the reactants to the catalyst and not its catalytic activity as already discussed in Chapter 5 for the Pt(111) single crystal. The analysis of the TOFs in Figure 6.4b shows that for all particle samples higher values are reached than for the Pt(111). The very high TOF for the ion-milled sample is ascribed to a possible underestimation of the number of active sites of the particles on the bottom of the tube.

6.5 Oxidation states and surface species

To understand the steep increase in CO_2 production, the oxidation states of catalyst and support as well as the presence and nature of adsorbates was investigated. Figure 6.5a and b show XP spectra of the O 1s region for the $Pt_{5nm}TiO_2NT$ and the $Pt_{15nm}TiO_2NT$ sample taken during the heating ramps shown in Figure 6.4.

The waterfall plots show the data from lower to higher temperatures, with the average temperatures indicated on the right side. Note that one spectrum averages over a temperature range of ~25 K.

For the experiment on the $Pt_{5nm}TiO_2NT$ sample shown in Figure 6.5a, in the spectra at 312 and 390 K, that is, before the strong increase in reactivity, the largest peak at 530.6 eV is assigned to the lattice oxygen peak of the TiO_2 support. The high binding energy shoulder at 532.5 eV is attributed to CO adsorbed on Pt. On Pt(111), usually bridge and on-top sites are populated with binding energies of 531.0 and 532.7 eV, respectively.[53]. These contributions are not resolved, but due to the experimental procedure, i.e. the exposure of the surface to CO, an assignment to CO appears plausible. For NAP-XPS, always unintended adsorbates like CO_2 or hydroxyl species are found on the surface, which are a result of ppm impurities in the gases. The signals of these contaminants are found at very similar binding energies reported for $TiO_2(110)$ and thus their presence cannot be excluded.[204] The gas phase signals of oxygen and CO are detected at 536.7 and 537.7 eV, respectively.

In the online gas analysis for the $Pt_{5nm}TiO_2NT$ sample shown in Figure 6.4, first a smooth reaction onset related to the onset of CO desorption was found, followed by a strong increase of CO_2 production at 515 K. Please note that time resolution in the online gas analysis is much more precise, because it averages over ~0.6 K per data point while XPS averages over ~25 K per spectrum. Taking this into account, the loss of the adsorbate signal at 532.5 eV in the XP spectrum at 520 K coincides with this strong increase. At higher temperatures, the system is in the MTL regime. Here, no adsorbates are found on the surface. At 546 K, a small, but significant signal due to gaseous CO_2 appears at 534.7 eV; at higher temperatures, no further changes are observed. The Pt 4f and Ti 2p XP spectra taken before and after the reaction in UHV are shown in Figure 6.6. No significant changes are observed, that is, Pt still is in the metallic state, while the TiO_2 NT support still is in the oxidised state (Ti^{4+}) (≥96 %).

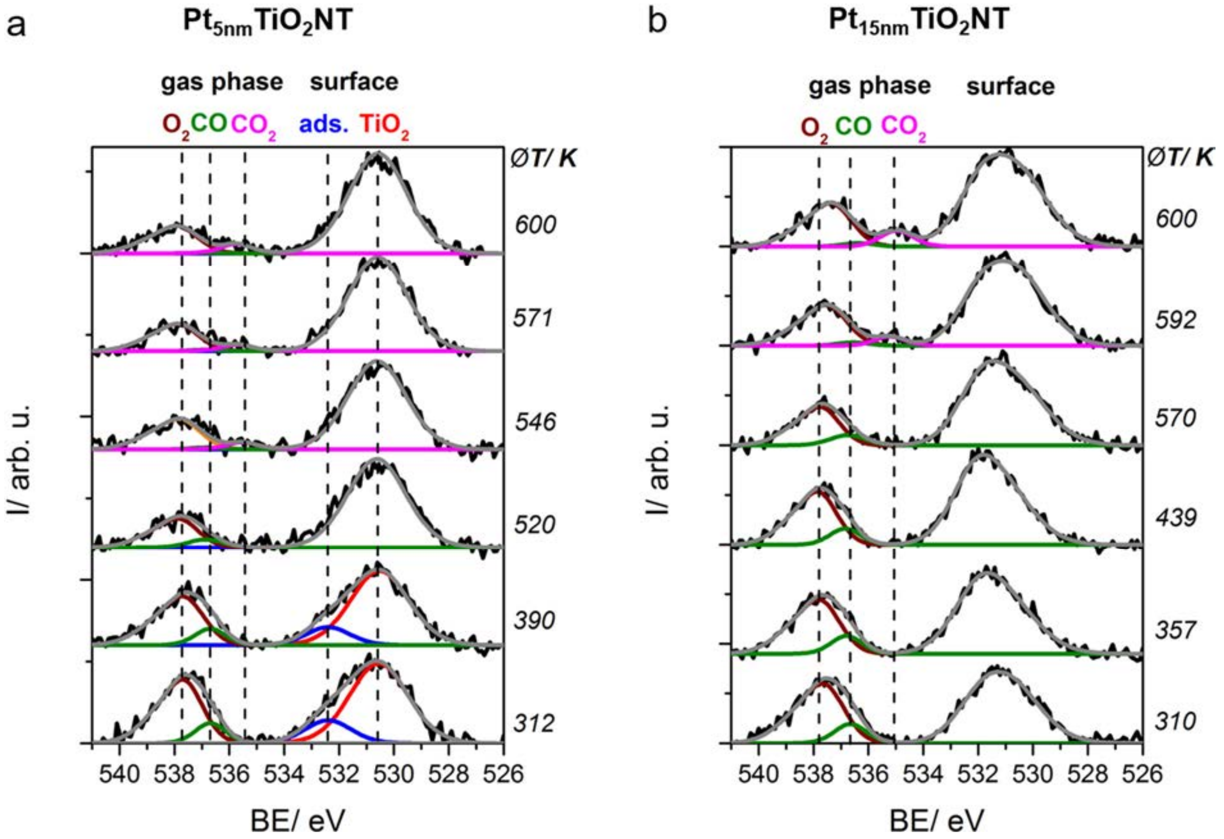

Figure 6.5: In situ XP spectra taken during the experiments shown in Figure 6.4, i.e. the heating ramp from 300 to 600 K in a mixture of 1:4 CO/O_2 at p_{tot}=1.0 mbar (a) on the $Pt_{5nm}TiO_2NT$ sample and (b) on the $Pt_{15nm}TiO_2NT$ sample.

Overall, the measurements for the $Pt_{15nm}TiO_2NT$ (Fig. 6.5b) show a similar behaviour, albeit with the onset of CO_2 signal in the O 1s XP spectrum shifted to higher temperatures (between 590 and 600 K), which is in line with Figure 6.4. In this case, the surface signals were not fitted as the changes in peak shape are not easily understood and additional effects like sintering or changes in particle-support interaction might be occurring.

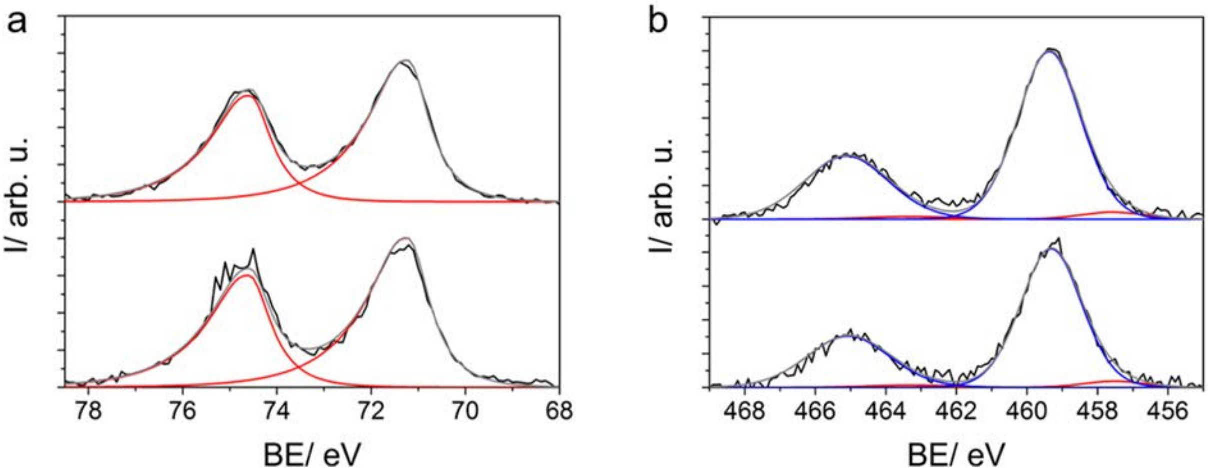

Figure 6.6: Pt 4f and Ti 2p region before and after the reaction ramp on the Pt$_{5nm}$*TiO*$_2$*NT sample.*

As the *ex situ* characterization (before and after the heating ramp) of the oxidation states of catalyst and support might not reveal the active state during reaction, *in situ* spectra during the isothermal experiments on the Pt$_{15nm}$TiO$_2$NT sample were measured, at the same total pressure and gas composition of p_{tot}=1 mbar and CO:O$_2$=1:4. The temperatures were chosen such that the state of the surface was examined below, close to and above $T_{1/2}$ where the strong increase in reactivity occurred, that is, at 565, 575 and 590 K, respectively. The respective XP spectra are shown in Figure 6.7a and the online gas analysis for the isothermal experiment is shown in Figure 6.7b, which is used to correlate the CO$_2$ production to the species present on the surface.

In the following, the results found for the TiO$_2$ support and the Pt catalyst are shortly discussed. In general, the TiO$_2$ NT support was found to be stable during our isothermal experiments at the three temperatures chosen. In the Ti 2p$_{3/2}$ region, fully oxidized Ti^{4+} is found at 459.0 eV; the shoulder at 457.2 eV indicates the presence of a small amount (~7%) of Ti^{3+}. For all samples, the amount of reduced Ti in UHV and for the *in situ* measurements was 5±3 %, without noticeable trend. The Pt 4f$_{7/2}$ and 4f$_{5/2}$ signals in Figure 6.7a at 71.1 and 74.4 eV, respectively, are due to metallic platinum. Notably, for the corresponding measurements for the Pt$_{5nm}$TiO$_2$NT sample, the Pt 4f signals are found at +0.2 eV higher binding energies, which is attributed to different final state screening for small particles (see Figure 6.8a and Figure 6.7a).[205]

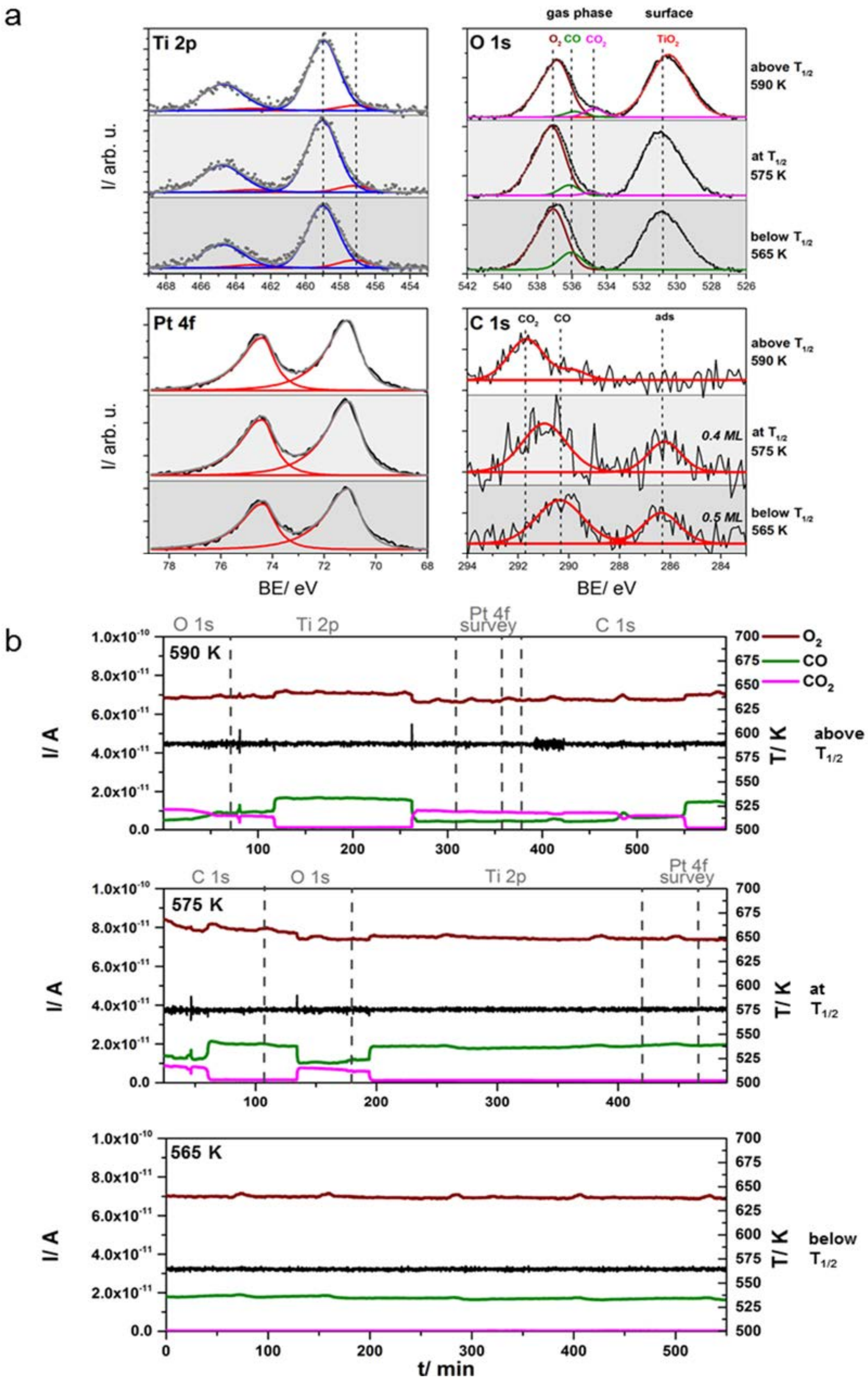

Figure 6.7: (a) In situ XP spectra for the reaction of a 1:4 CO/O_2 mixture at p_{tot}=1.0 mbar on the $Pt_{15nm}TiO_2NT$ sample at sample temperatures of T_s = 565, 575 and 590 K; (b) corresponding online gas analysis.

Since no significant changes of the support or the particles are observed in the *in situ* measurement, it is concluded that metallic platinum is the active catalyst, which has also been found for Pt(111).[74] The results also indicate that the TiO_2 is either not involved in the reaction or only takes part in fast process, such as oxidation/reduction reactions or spillover effects that cannot be resolved.

In the online gas analysis measurements at 565 K, that is below $T_{1/2}$ (Figure 6.7b, bottom panel), a very low conversion of only ~4 % is observed. The CO coverage on the Pt particles is determined to be 0.5 ML, as derived from the corresponding C 1s in Figure 6.7a. This coverage is very close to the CO saturation coverage of 0.6 ML on Pt(111) at 0.1 mbar.[74] For the measurement at 575 K a smaller CO coverage of 0.4 ML is observed in the C 1s spectrum (Figure 6.7 a, middle panel). In the corresponding online gas analysis, the reaction rate is not stable (Figure 6.7b, middle panel), as it switches from high CO conversion of ~50 % to regions of low conversion of ~8 %. The comparably large CO coverage of 0.4 ML is attributed to the fact that the C 1s spectrum averages over both states, that is, low conversion, where a high CO coverage is expected and high conversion in the MTL regime, where the CO coverage should be low. Notably, the O 1s spectra cannot be used for this analysis, since they also contain unresolved adsorbed molecular species such as hydroxyl [187, 204] on the TiO_2 NT support. For the $Pt_{15nm}TiO_2NT$ sample at 590 K, in the regime of high reactivity in (or very close to) the MTL regime, again fluctuations in CO_2 production are observed with time (Figure 6.7b, top panel). Here, even three different regions are observed, with high (~60 %), intermediate (~40 %) and low (~8 %) conversion. In the corresponding XP spectra in Figure 6.7a no adsorbate signals are observed in the C 1s and also the O 1s region. This suggests that at this temperature CO on Pt and also other adsorbates ("impurities") on the TiO_2 support have desorbed.

A series of isothermal experiments was also carried out for the $Pt_{5nm}TiO_2NT$ sample (see Figure 6.8 and 6.9), yielding overall similar results, that is, adsorbed CO below and close to the $T_{1/2}$ value and no adsorbed CO above, as expected in the MTL regime. Note that the reaction on the small particles was even less stable and the reaction stopped after a few minutes after the start of the experiment at $T_{1/2,}$ which is attributed to rapid ageing of the small catalyst particles. Therefore, the temperature for the measurement in the MTL regime was chosen as 595 K, significantly above the $T_{1/2}$ of 530 K value derived from Figure 6.4.

At 595 K, CO conversions close to unity were observed and the reaction started to oscillate, as is evident from the online gas analysis in Figure 6.9a. These rate oscillations are attributed to oscillations of the temperature: at such high rates more heat is generated by the exothermic reaction than can be transported away from the sample (cf. non-linear temperature increase in Figure 6.4; explained above); as a result, the sample instantaneously heats up. The temperature control unit compensates this increase by decreasing the heating power; since the reaction is extremely sensitive to this, it immediately falls into a state of lower production, which again is compensated by a heat increase of the temperature controller and so forth. When heating the sample manually at the same temperature, no oscillations were observed, but a heat-up of the sample occurred after some time and consequently, the heating power had to be regulated to lower values, as shown in Figure 6.9b. The red arrows in Figure 6.9b indicate the times (~207 and 227 min), where the temperature lowered manually. Interestingly, the sample is first heating up again slowly and at a certain “threshold” temperature, suddenly extensive reaction sets in and the temperature has to be lowered again (at ~203 and 212 min).

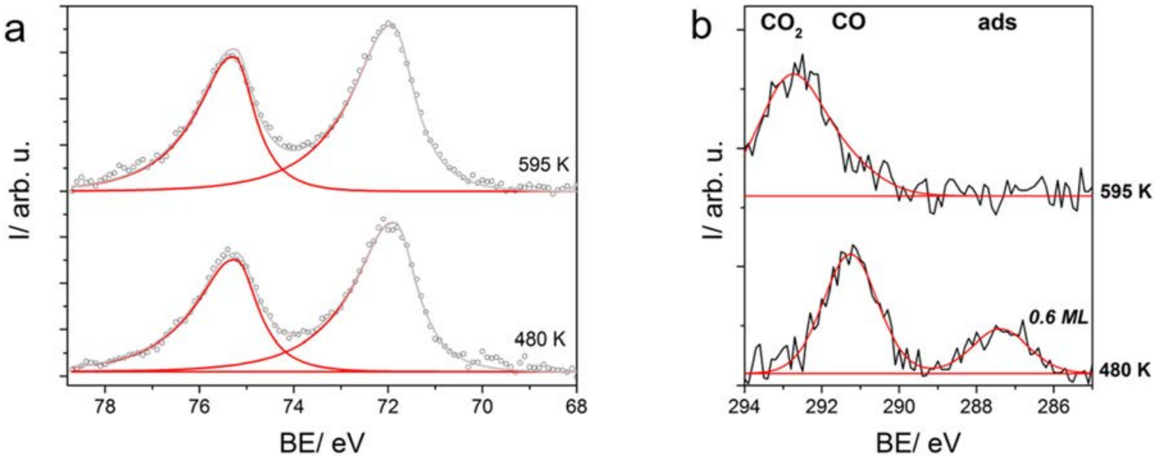

Figure 6.8: (a) In situ Pt4f XP spectra at sample temperatures of 570 and 595 K and (b) in situ Pt4f XP spectra at sample temperatures of 570 and 595 K for the reaction of a 1:4 CO/O_2 mixture at p_{tot}=1.0 mbar on the $Pt_{5nm}TiO_2NT$.

Similar oscillations as in Figure 6.9a were observed for supported Pt particles before, where the oscillations were traced back to Pt oxidation-reduction cycles or refacetting of the NPs.[30, 72, 110] In this study, the platinum particles were fully reduced at 480 K, and also at 595 K no oxidation is observed in the Pt 4f spectra within a detection limit of 4% (Figure 6.8a). Also, the TiO_2 NT support was in the same state for the both temperatures, where ~3 % were reduced.

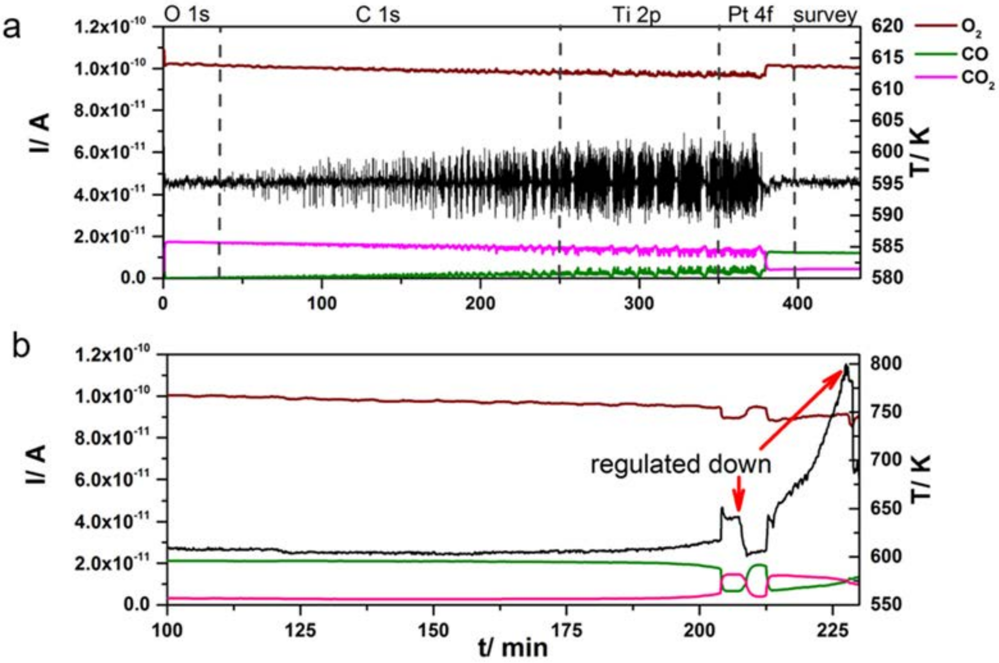

Figure 6.9: (a) Online gas analysis at a sample temperature of 595 K for the reaction of a 1:4 CO/O_2 mixture at p_{tot}=1.0 mbar on the $Pt_{5nm}TiO_2NT$ regulated by a temperature control unit and (b) reaction under identical conditions regulated manually.

6.6 Diffusion and mass transfer limitations

As already explained in Chapter 6.4, MTLs were observed for all samples at a total pressure of 1 mbar in the temperature-programmed reaction. In order to investigate this behaviour and also if pore diffusion plays a role, the CO oxidation was examined at total pressures in the range between 1 mbar and 10^{-3} mbar ($CO:O_2$=1:4) from 400 to 650 K on the $Pt_{ion\text{-}milled}TiO_2NT$ sample. For this sample no particles are localised on the rim of the NTs and hence pore diffusion might influence the reaction. The CO conversions of these experiments are shown in Figure 6.10a. For 0.1 and 0.01 mbar, conversions close to unity are reached, whereas for 1 mbar the CO conversion drops to ~75 % (see also Figure 6.4).

In all cases, a maximum in conversion is reached, which stays constant when going to higher temperatures; this behaviour clearly indicates that the MTL regime is reached at the higher total pressures. The explanation for the MTLs lies in the depletion of CO in the surface-near region, which is shown in Figure 6.10b as the change in CO pressure with respect to the CO pressure at 400 K. The reason for the shift of $T_{1/2}$ to higher temperature with higher p_{tot} is that CO partial pressure within the gas mixture increases with the total pressure. Adsorbed CO “poisons” the Pt particles, and CO desorption is shifted to higher temperatures at higher partial pressures. For 0.1 and 0.01 mbar, CO nearly completely depletes within the detection area of the QMS, which is schematically shown in the inset of Figure 6.10b. Therefore, the QMS mainly detects CO_2, which results in the high CO conversions. Surprisingly, the depletion is smaller for 1 mbar; the possible reasons for this are manifold. For example, reactions in the mbar regime are influenced by strong heating effects, which could also play a role in our case [18], and at 1 mbar diffusion might by limited by the increased total pressure as compared to 0.1 mbar. The same behaviour was observed for Pt(111) in Chapter 5.

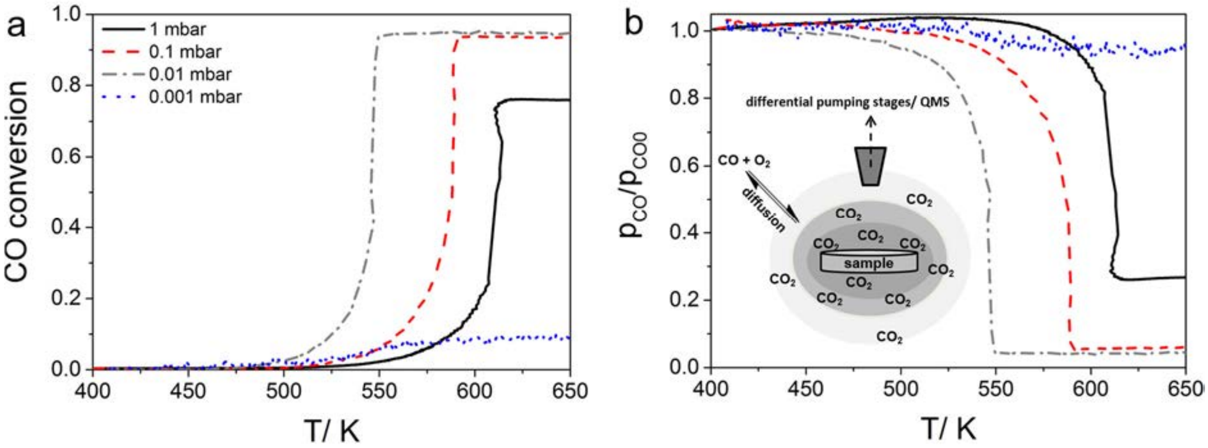

Figure 6.10: (a) CO conversion from 400 to 650 K on the ion-milled $Pt_{ion\text{-}milled}TiO_2$ NT sample for different total pressures; (b) relative CO pressure with respect to the CO pressure at 400 K during the heating ramps.

Interestingly, at 10^{-3} mbar, a CO depletion of less than 10 % is found in Figure 6.10b. The CO oxidation reaction on Pt group metals was reported to be mass transfer-limited at this pressure rather than collision-limited.[17, 67] In Figure 6.10a, correspondingly, no increase in CO_2 production is observed as for the higher pressure, but CO conversion stagnates at ~600 K. This stagnation is not attributed to MTLs or pore diffusion but rather reflects that at this pressure the reaction is still collision-limited. For all other total pressures, this phenomenon is not observed as the reaction immediately jumps into the MTL regime and pore diffusion cannot be discriminated from this effect. The reaction is so efficient that CO is depleted over the surface-near region to such an extent that pore diffusion does not play a role and gas diffusion to the sample is the rate limiting step.

6.7 Conclusion

Three different types of TiO_2 NT-supported samples decorated with Pt particles ($Pt_{5nm}TiO_2NT$, $Pt_{15nm}TiO_2NT$, $Pt_{ion\text{-}milled}TiO_2NT$) were investigated concerning their reactivity in the CO oxidation reaction, and compared to a rutile sample covered with a nanostructured Pt film and a Pt(111) single crystal. The samples differed with respect to the size and localization of the particles on the NTs. The oxidation states of catalyst and support as well as surface species were probed *in situ* by NAP-XPS, and simultaneous online gas analysis using a QMS was used to evaluate conversions and TOFs.

In a temperature-programmed reaction in a mixture of $CO:O_2=1:4$ at $p_{tot}=1$ mbar with a heating ramp of $\beta=10$ K/min starting at 400 K, the reactivity of the samples was compared. The maximum temperature of the heating ramp was chosen between 620 and 800 K, until the maximum conversion and TOF were reached. All NT-supported samples showed a sharp increase in CO conversion at a defined temperature, in contrast to a smooth increase found for the Pt(111) single crystal. The order of the characteristic temperature $T_{1/2}$, where 50 % conversion was reached, is $Pt_{5nm}TiO_2NT < Pt_{15nm}TiO_2NT < Pt_{ion\text{-}milled}TiO_2NT < Pt(111) < Pt_{5nm}TiO_2(110)$. Therefore, all NT-supported samples outperformed the single crystal in terms of reactivity at lower temperatures. The differences for the NT-supported samples were attributed to different particle sizes, with smaller particles exhibiting a lower $T_{1/2}$. The surprisingly high temperature for the rutile-supported sample with respect to Pt(111) may result from effects like strong metal support interactions. While the $Pt_{15nm}TiO_2NT$ samples were stable for many hours, the $Pt_{5nm}TiO_2NT$ and also the $Pt_{5nm}TiO_2(110)$ samples degraded with time, resulting in changes of onset temperatures and activity, which could be due to SMSI or other aging effects.

All samples reached the MTL regime at higher temperatures due to depletion of CO in the surface-near region which corresponds to the detection volume of the QMS. For the $Pt_{ion\text{-}milled}TiO_2NT$ sample, pressure-dependent measurements were performed from $p_{tot} = 0.001$ to 1 mbar; at high temperatures the diffusion to the sample (interphase diffusion) was identified as the rate-limiting step and the influence of pore diffusion was not evident. The comparably high $T_{1/2}$ value for the $Pt_{15nm}TiO_2NT$ indicates that the big particles at the bottom of the NT dominate the reaction compared to the small particles distributed across the tubes.

Isothermal experiments were performed in order to evaluate the oxidation states of catalyst and support as well as CO coverages on the sample under reaction conditions. Three different temperatures were chosen: below, at and above $T_{1/2}$ as deduced from the temperature-programmed experiments. No change in oxidation state for catalyst and support were found. Pt was in a metallic state, the TiO_2 NT support was found to be 5±3 % reduced in all cases, most likely not taking part in the reaction. Therefore a Mars-van Krevelen reduction-oxidation mechanism can be discarded, which is in line with literature and also the results of Chapter 5, where the Langmuir-Hinshelwood mechanism was found for CO oxidation on Pt.[8, 88] Simultaneous online gas analysis showed a stable low conversion of ~4 % below $T_{1/2}$. At and above $T_{1/2,}$ the reaction was not stable but changed in between different conversion regimes.

7. Intercalation of CO and O_2 at the graphene/Rh(111) interface

7.1 General

In Chapter 6, the influence of nanostructuring of the support and Pt particles size on the CO oxidation reaction was investigated. It was found that the reaction onset and the activity are highly influenced by the particle size, i.e. the step/defect density of the catalyst, which is most likely a result of the different adsorption strength of the reactants on the different particles.

Another way, as already mentioned in Chapter 3.2, to influence the adsorption strength and therefore reaction behaviour, is the use of so-called “2D nanoreactors”. As previously shown [130, 135], 2D systems such as graphene grown on a transition metal substrate may act as a nanoreactor, confining the reaction at the graphene - metal interface to two dimensions. In these studies, the intercalation and reaction of CO and O_2 underneath the graphene layer was experimentally followed by LEEM, PM-IRRAS and NAP-XPS. Enhanced activity in terms of lower onset temperature in the CO oxidation reaction was assumed to be a result of lower adsorption energy of intercalated CO underneath the graphene cover, which interacts with the CO molecule. This explanation was concluded from TPD experiments, where a shift of the CO desorption to lower temperatures compared to the desorption from the bare Pt(111) surface was observed. Additionally, this assumption was supported by DFT calculations, where the electronic interaction between graphene and CO was found to lower the electron density in the bond between CO and the substrate. Due to this interaction, a decrease of the adsorption energy of CO on the surface by 0.4 eV was determined from DFT.[130, 135] The reason for the lowered adsorption energy therefore is attributed to the energy penalty that emerges by lifting up of the graphene layer in order to intercalate CO.[135] This is well in agreement with the NAP XPS observations as explained in the following: Usually, graphene/Pt(111) shows a single peak at ~284.2 eV. When CO intercalation takes place, the peak is shifted by -0.2 eV to ~284 eV on account of a decoupling of the graphene layer from the Pt(111) substrate. Therefore, the lower binding energy more reflects the binding energy of free-standing graphene. The changes in the C 1s were accompanied by the emergence of the signals of CO in on-top and bridge sites in the O 1s at ~0.013 mbar CO partial pressure. In case of Pt(111), the interaction of graphene and the substrate surface is rather low [122, 123]; therefore, after growth of the graphene layer on the surface, in the Pt 4f core level, still, the surface core level component is observed. When intercalating CO, this signal is strongly decreased, which confirms the bonding of CO to the surface and therefore intercalation between the graphene sheet and Pt(111). Importantly, the graphene layer was stable during CO and O_2 intercalation, i.e. it was not oxidised and still intact after CO oxidation experiments as concluded from AES measurements.[135]

Intercalation of gases like CO and O_2 has also been observed between graphene and other transition metal surfaces like Ru(0001) [127, 129], Ir(111) [131, 134], Cu(111) [133] and Ni(111) [132, 133]. From these measurements, a general trend was found that the required partial pressure of the intercalant is dependent on the graphene-metal interaction strength. For CO intercalation the order of the required partial pressure was Ru > Ni > Ir > Pt and for oxygen Ru > Cu > Ir > Pt, where in case of Ru the substrate has to be heated in order to enable intercalation; at room temperature no intercalation of O_2 is observed.[127-135] As a consequence, the shift in the C 1s core level upon intercalation gives insight into the strength of the interaction between graphene and metal substrate.

So far, no intercalation of small molecules like CO and O_2 has been reported for graphene/Rh(111). From the reported interaction strength, the threshold pressure for intercalation of both gases should lie in between Ru(0001) and Ir(111), where the interaction between Ru(0001) and graphene is the strongest of the mentioned metal surfaces. Indeed, in this chapter, the intercalation of CO and O_2 under a closed layer of graphene/Rh(111) at partial pressures of 1 mbar will be discussed. The intercalation was observed using NAP-XPS and the desorption behaviour was investigated by TPD.

7.2 Experimental aspects

Acquisition of the *in situ* XP spectra at 1 mbar took ~ 5 - 6 h for a whole data set including a survey, a Rh 3d region, a C 1s region and an O 1s region scan. For the TPD experiments, a linear heating ramp from 300 to 720 K (CO)/ 1015 K (O_2) with a heating rate of β = 2 K/s was used.

7.3 Growth of graphene on Rh(111)

Graphene was grown on Rh(111) in a CVD process using propene as precursor at a sample temperature of 920 K and a propene pressure of ~8×10^{-9} mbar (increasing to ~5×10^{-8} mbar during growth), which has been previously reported to be the optimum conditions in order to obtain a graphene layer with a low defect density and large, single crystalline domains.[66] During the growth, the C 1s region was monitored and the growth was stopped, when saturation of the C 1s signal was reached, which took several hours. A C 1s spectrum of a graphene layer grown under these conditions is exemplarily shown in Figure 7.1a. The peak with the maximum at 284.9 eV is composed of two unresolved contributions due to the corrugation of the graphene layer [66, 206], as was reported in synchrotron work and are fitted according to the peak splitting of 0.7 eV found in Ref [66]. The blue fit at lower binding energy at 284.2 eV ("C2") is attributed to carbon atoms, that are in larger distance to the Rh(111) surface [206], and accordingly, the red fit at 284.9 eV ("C1") belongs to carbon atoms above bridge positions in closer vicinity to the surface, i.e. atoms that are more strongly bound to the surface. In Ref [66] the ratio of C1/C2 was found to be 1.4 after preparation, being reasonably close to the ratio of 1.6 found in Figure 7.1a.

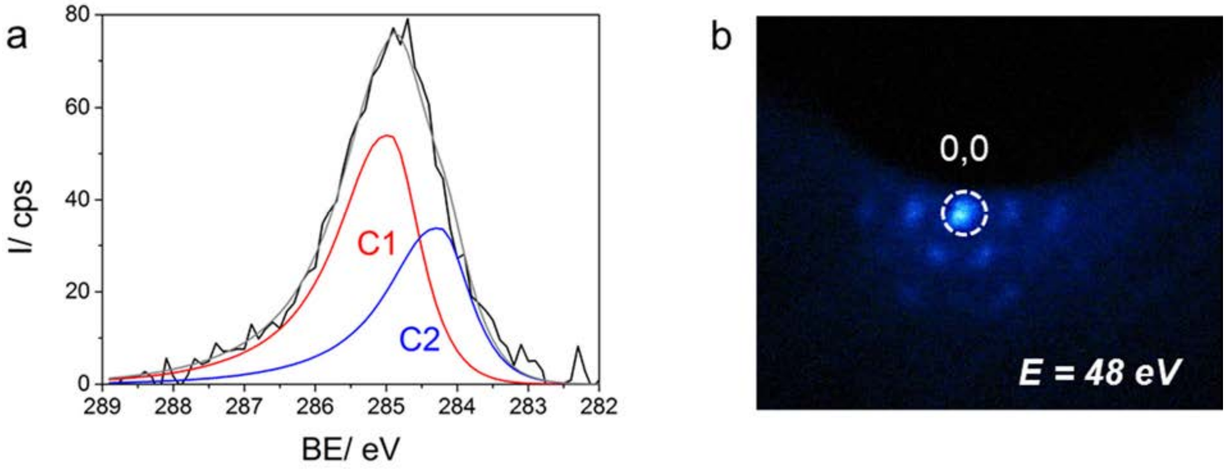

Figure 7.1: (a) C1s spectra after graphene growth and (b) LEED image of the 0,0 spot after graphene growth.

Figure 7.1b shows a LEED image at a beam energy of 48 eV after the graphene growth under the same conditions. In the centre of the picture, the (0,0) spot of the hexagonal Rh(111) surface is observed; additional spots arranged hexagonally around this spot are observed, which belong to the Moiré diffraction pattern of the corrugated graphene layer. Please note that the upper half of the diffraction pattern is shadowed by the sample holder. The emergence of this Moiré pattern is an indicator for a graphene layer of good quality, that is, large single crystalline domains and a low defect density.[66, 123]

The Rh 3d core level spectra before and after growth of graphene are shown in Figure 7.2. The spin-orbit split signals of Rh $3d_{5/2}$ and Rh $3d_{3/2}$ are observed at 307.3 and 312.0 eV, respectively. Except for a damping of the signal by ~9% due to the graphene overlayer, no changes are observed in this region.

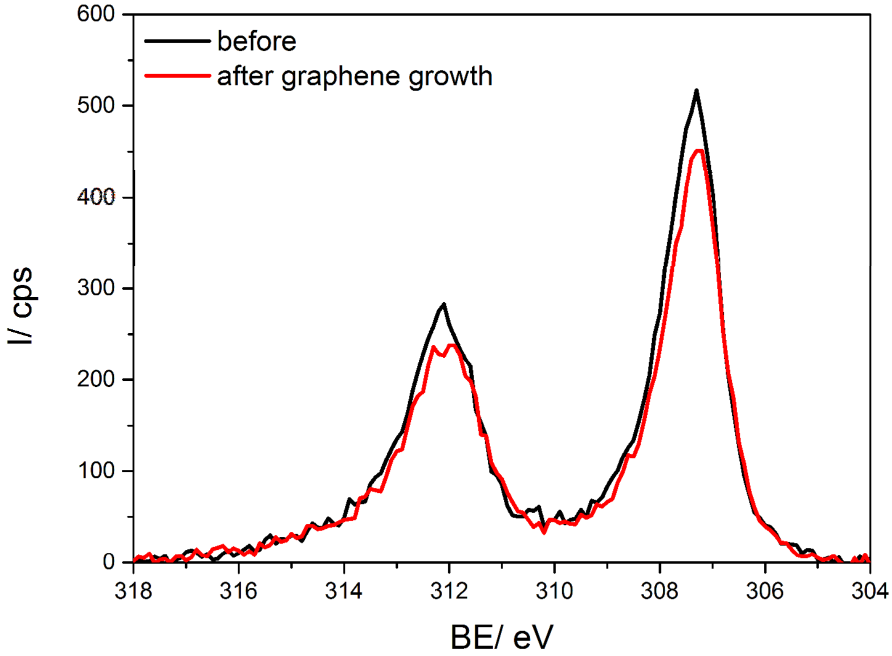

Figure 7.2: Rh 3d core level spectrum before (black) and after (red) the growth of a closed graphene layer.

7.4 Intercalation of CO

The intercalation of CO under the closed graphene layer was followed by NAP-XPS via the C 1s, O 1s and Rh 3d regions. The graphene layer was prepared as described in Chapter 7.3 and CO was intercalated at 1 mbar of CO and 300 K after the sample was stored in UHV overnight; as the threshold pressure to intercalate gases is expected to be in the mbar range, graphene acts as a protecting layer and prevents adsorption of residual gases on the Rh(111) surface. This is additionally a sign for a closed layer of graphene on Rh(111) as no adsorption was found even after several hours in a pressure of ~10^{-9} mbar. Figure 7.3a and b show the O 1s and C 1s spectra before (lowest spectrum), during (lower middle spectrum) and after (upper middle spectrum) CO intercalation at 1 mbar in combination with the respective spectra of the (2x2)-3CO superstructure of CO on Rh(111) with a coverage of 0.75 ML.[62, 65] In Figure 7.3a, the emergence of different features is observed due to exposure of the sample to CO, which will be discussed in the following.

As expected, before the intercalation, no oxygen containing species are found on the surface. During exposure to 1 mbar of CO, an intensity at high binding energies (above 535 eV) that is due to the CO gas phase above the sample is found. As a result of the unchromatized excitation source, there are satellites of this gas phase peak emerging at low binding energies (528.3 and 526.2 eV; grey fits), which have to be subtracted in order to deconvolute the signal of intercalated CO molecules.

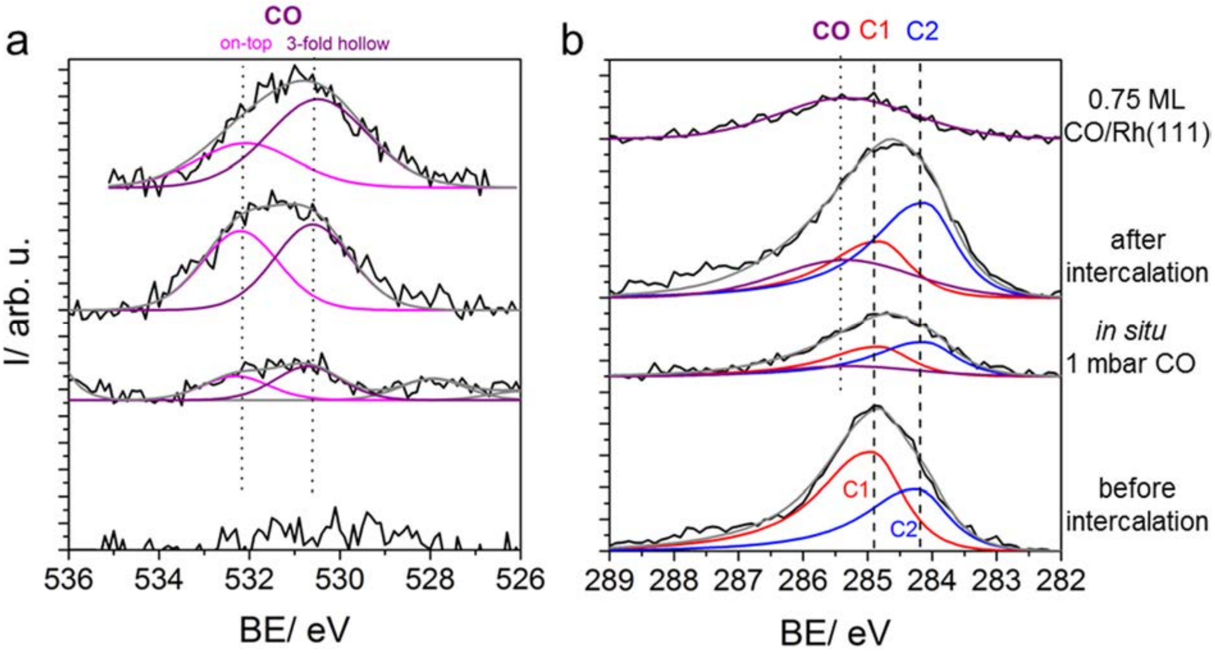

Figure 7.3: (a) O 1s region scan and (b) C 1s region scan for the CO intercalation experiment at 1 mbar CO and 300 K.

This signal due to intercalated CO is found as a broad peak at ~531.4 eV, and is composed of two different contributions. As reported for CO/Rh(111), CO molecules can adsorb in two different surface sites, namely on-top and three-fold hollow sites, see upper spectrum in Fig. 7.3.a. For the (2x2)-3CO superstructure of CO on Rh(111) it was found that two CO molecules are adsorbed in three-fold hollow sites and one in an on-top site within in the unit cell. The O 1s spectrum of this superstructure is shown in the upper spectrum, where both contributions are fitted in an area ratio of 2:1. The signal belonging to CO in three-fold hollow sites ("$CO_{3\text{-fold-hollow}}$") is observed at ~530.4 eV and the signal of CO in on-top sites ("$CO_{\text{on-top}}$") is found at ~532.0 eV, which is in good agreement with the literature.[62, 63]

When comparing the *in situ* spectrum obtained during exposure of the sample to CO to this reference spectrum, the same contributions can be identified and therefore the signals are attributed to $CO_{\text{on-top}}$ and $CO_{3\text{-fold-hollow}}$. Interestingly, the ratio of $CO_{3\text{-fold-hollow}}/CO_{\text{on-top}}$ is changed to ~1.4:1 instead of 2:1 for the superstructure on the bare Rh(111) surface. This indicates that adsorption of CO in three-fold hollow sites is hindered by the graphene overlayer and in turn on-top sites are more favoured, which is surprising, since the adsorption at on-top sites is sterically hindered underneath the graphene cover on a Pt(111) surface.[130] A possible explanation for this difference is that, in case of graphene on Pt(111), the graphene is a rather flat-lying layer without strong interaction with the substrate, i.e. no pronounced corrugation.[122] In case of graphene on Rh(111), it was found that carbon atoms in on-top ("atop") configuration define higher-lying regions above Rh(111) with d = 3.15 Å in contrast to atoms in bridge configuration, which form the lowest topographic area with d = 2.08 Å as deduced from STM and DFT calculations.[206] Please note, that in the on-top configuration, no carbon atom is directly located above the rhodium atom. Accordingly, there is more "space" for intercalated atoms at on-top sites, or in other words, there is less energy needed to intercalate compared to other configurations, which are in closer vicinity to the substrate surface and block three-fold hollow sites. For a detailed picture of the crystallographic structure of graphene on Rh(111), please see Ref. [206]. When comparing to the area ratio in the spectrum obtained after pump-down to UHV, a further decrease to ~1.1:1 is observed. Surprisingly, by estimation of the coverage of CO by comparison to the (2x2)-3CO superstructure, neglecting the damping of the graphene overlayer, ~0.75 ML of CO have intercalated graphene after exposure to 1 mbar for ~5 h, which would indicate that a saturated CO layer is formed and a complete intercalation occurred.

Further prove for the intercalation of CO is obtained from the C 1s region scans shown in Fig. 7.3b. When comparing the spectra taken before and after exposure to CO, a broadening and increase in total signal intensity is observed. The latter observation indicates that CO is adsorbed – the broadening of the peak is attributed to the intercalation of CO between graphene and the Rh(111) surface as explained in the following. The signal of the (2x2)-3CO superstructure is found at ~285.3 eV, which is again shown in the topmost spectrum. When using the binding energy and fitting parameters of this signal as a template, the broadening of the C 1s peak after CO exposure can be rationalised by fitting an additional contribution due to CO adsorption on the Rh(111) substrate. A further indication that the CO molecules are intercalated, is the ratio of the C1/C2 contributions of the graphene sheet. For the as-prepared graphene a ratio of 1.6:1 was found, as discussed in Chapter 7.3. Upon CO exposure, the ratio changes to 0.9:1 in the *in situ* spectrum and even 0.6:1 in the spectrum after pump-down to UHV. The even lower ratio found after the intercalation in UHV can be explained by a kinetic limitation of CO intercalation, which was also observed on other supports for a closed graphene layer.[130, 135] As the C 1s spectrum was taken as the first *in situ* spectrum but CO exposure was continued during acquisition of the O 1s, Rh 3d and survey spectrum, consequently, more

CO might have intercalated the graphene sheet after pump-down from defects or domain boundaries, which was found to be the limiting step for Pt(111).[130, 135] As explained in Section 7.3, the C1 signal is due to carbon atoms in closer vicinity to the surface; for CO intercalation a lift-up of the graphene sheet is required, which explains the relative loss in C1 contribution and the increase of the C2 contribution, which is due to carbon atoms in larger distance to the Rh surface. Please note that it is expected that the intercalation should lead to only one graphene signal at lower binding energy related to "quasi-freestanding" graphene as observed for example for graphene on Pt(111) and Ru(0001) for intercalation of CO. In case of a Pt(111) substrate, a shift of -0.2 eV towards lower binding energies was observed upon intercalation at ~0.7 mbar, which was attributed to a decoupling of the graphene sheet from the surface. Note that on Pt(111), the graphene layer is interacting only weakly with the substrate and therefore only one signal is observed, which completely shifts due to intercalation. Interestingly, this shift can be reversed by heating the sample to 633 K in UHV, indicating full desorption of CO from the interface.[135] On Ru(0001), also two signal are observed for the pure graphene layer due to carbon atoms that are coupled with different strength to the substrate. When exposing the sample to ~13 mbar CO, both signals decrease on account of a new peak emerging at lower binding energies; this observation again was interpreted as a complete decoupling of the graphene layer from the surface.[129] In case of Rh(111) now, no new feature is observed for CO intercalation. As explained in Chapter 3.2, the corrugation of the graphene sheet is a result of the interaction strength between graphene and substrate, which decreases in the order Ru(0001) > Rh(111) > Pt(111). Therefore, Rh(111) is an intermediate case, where the carbon atoms that are in higher distance to the surface already are in a very similar state like carbon atoms in quasi free-standing graphene, which is also reflected in the similar binding energy.[66, 123] This is the reason why there is no shift in both signals, C1 and C2, but the C1 component is shifted to the binding energy of C2, i.e. all carbon atoms are in the same distance, which is resembled by the binding energy of C2 (~284.2 eV). The fact, that both contributions, i.e. C1 and C2, are still observed after intercalation in Figure 7.3b, although a coverage of 0.75 ML was achieved, which is the saturation coverage on the bare Rh(111) surface, has to be further evaluated. In case of a complete intercalation one would expect a flat, non-corrugated layer and therefore only one C 1s contribution, namely C2.

In order to investigate the desorption behaviour of the intercalated CO, TPD experiments were conducted, followed at m/z = 28. CO was intercalated at 1 mbar CO at 300 K for 5 min in the measurement chamber (Chapter 2.2); subsequently, the chamber was evacuated to UHV and the sample was transferred to the preparation chamber for the TPD experiment. After stabilisation of the background pressure, a TPD experiment with a linear heating ramp of 2 K/s from ~300 to ~720 K was conducted. The respective TPD spectrum is shown in Figure 7.4 together with a TPD spectrum of the (2x2)-3CO superstructure of CO on the bare Rh(111) surface. The TPD spectrum of CO/Rh(111) in Figure 7.4 (red line) shows a desorption feature at ~485 K and a broadening towards lower temperatures, which is in line with the literature for the(2x2)-3CO superstructure, where a feature at ~490 K and a shoulder at ~415 K was observed. This shoulder is not resolved here due to a slower heating rate of 2 K/s instead of 5 K/s in literature.[65, 207] For high coverages (close to the saturation coverage of 0.75 ML), from high-resolution XPS work is was concluded that on-top and three-fold hollow sites are populated [208], and in combination with RAIRS, TPD and DFT calculations it was concluded that the main peak is mainly due to desorption from on-top sites and the shoulder at lower temperatures is attributed to desorption from three-fold hollow sites.[65, 209]

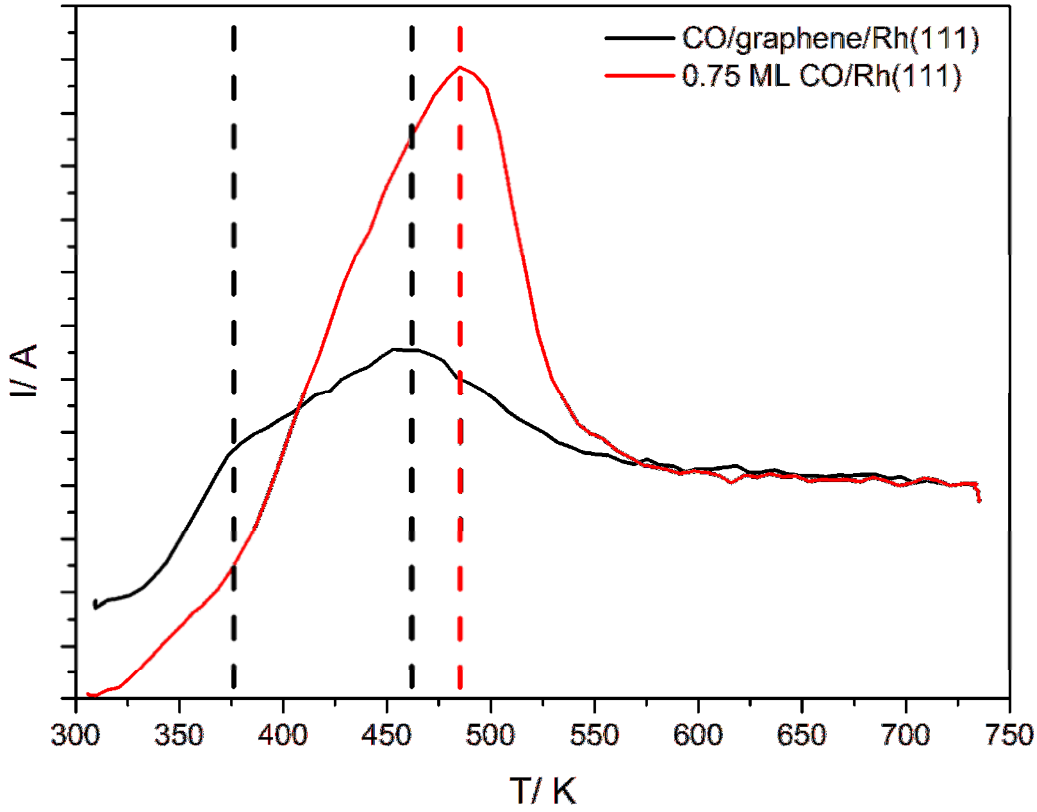

Figure 7.4: TPD spectra of CO intercalated between graphene/Rh(111) (black line) and the (2x2)-3CO superstructure on Rh(111) (red line); please note that the black spectrum was multiplied by a factor of 1.24.

The TPD spectrum of CO intercalated at the interface of graphene/Rh(111) is also shown in Figure 7.4 (black line). Please note that this spectrum was multiplied by a factor of 1.24 in order adjust the CO background to the level of the reference spectrum at high temperatures;

the unprocessed (raw) spectra are shown in Figure 11.4.1 of the Appendix. Please note that XPS shows for both samples, CO on Rh(111) and CO under graphene on Rh(111) the same CO amount. This condition is better reflected in the normalized spectra. In contrast to the reference spectrum of CO/Rh(111), two well-resolved features are observed at ~460 and ~375 K. The signal at higher temperatures is again attributed to CO molecules in on-top sites according to the CO/Rh(111) reference, and exhibits a shift of ~25 K to lower temperatures. For CO/graphene/Pt(111), a sharpening of the signal at low temperatures was observed compared to CO on bare Pt(111). This effect was, in combination with PM-IRRAS measurements and DFT calculations, explained by a weakening of the CO-substrate interaction by an interaction of the graphene sheet with the CO molecules (see also Chapter 3.2). In case of CO/graphene/Rh(111), the shift to lower temperatures compared to the reference might also be a result of a similar interaction of the graphene layer with the CO molecules, weakening the CO-substrate interaction, resulting in desorption at lower temperatures. Additionally, the shoulder signal is well-resolved and also shifted to lower temperatures. The shift in temperature leads to the same conclusion as for the main peak, namely a weakened CO-substrate interaction. Taking into account the high rise in background CO during the TPD experiment, the found ratio of 1:1.1 of $CO_{3\text{-fold-hollow}}/CO_{\text{on-top}}$ after CO intercalation found in XPS seems conceivable for the TPD peaks. Besides, the fact that the CO that is bound to threefold-hollow sites shows a stronger shift to lower temperatures and therefore seems to be destabilized is in line with XPS, where more on-top sites are populated compared to the graphene free surface. Nevertheless, the ratio might not be exactly the same on account to the considerably different intercalation times (XPS: ~5 h, TPD: 5 min), assuming the intercalation is limited to defects and domain boundaries and a saturation coverage was not yet reached. Please note that no deviation within ± 10 % in intensity was observed in the C 1s region before and after the TPD experiment, i.e. the graphene layer is stable and CO intercalation is reversible.

7.5 Intercalation of O_2

The intercalation of O_2 at 1 mbar and 300 K was followed by NAP-XPS, like in the case of CO. The respective O 1s and C 1s spectra are shown in Figure 7.5a and b. Upon O_2 exposure, a feature at ~530.6 eV is observed in the *in situ* O 1s (middle spectrum), which is shifted +1.2 eV to higher binding energies compared to the signal at 529.4 eV of chemisorbed oxygen adsorbed in three-fold hollow sites on Rh(111).[62] Again, the intensity at high binding energies in the *in situ* spectrum is due to the O_2 gas phase and additionally, the gas phase satellites are fitted at low binding energies in order to deconvolute the signal due to adsorbed oxygen.

When examining the C 1s region shown in Figure 7.5b, remarkable changes are observed between the spectrum acquired before and during/after intercalation of oxygen. Like in case of CO intercalation, a decrease in the C1 component belonging to more strongly bound carbon atoms is observed. However, apart from a relative decrease of the ratio of C1/C2 contribution from ~1.6:1 before intercalation to 0.7:1 for the *in situ* spectrum, a new feature is observed at ~283.7 eV ("C3", green fit). This observation is different to the CO intercalation, where merely a decrease in the C1/C2 ratio was observed, but is in line with the changes observed in the C 1s core level observed for intercalation of CO and O_2 between a full layer of graphene and Ru(0001).[128, 129] In these cases, the new feature was assigned to a strong decoupling of the graphene layer from the surface due to intercalation, and therefore, it is concluded, that this effect also takes place for intercalation of O_2 at the graphene/Rh(111) interface. This observation also suggests a stronger change in the interaction of graphene with the Rh(111) substrate due to intercalated oxygen than in case of intercalated CO, where this feature was not observed. Please note, that in the spectrum after pump-down the fit suggests an increase in the C1 component, which could indicate loss of a part of intercalated oxygen.

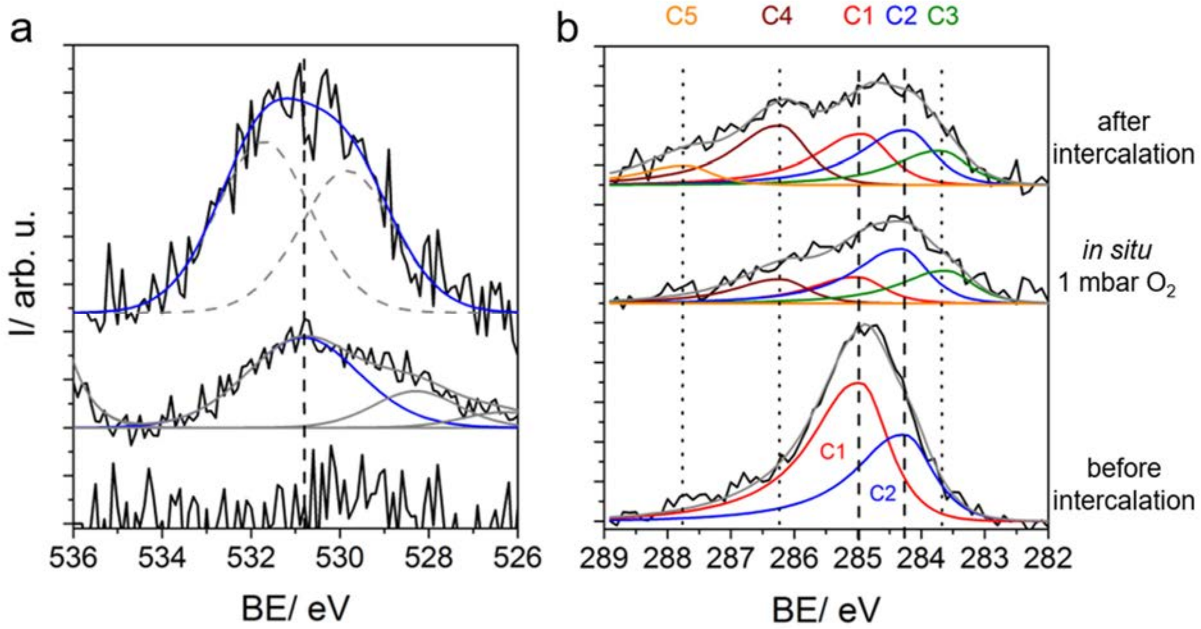

Figure 7.5: (a) O 1s region scan and (b) C 1s region scan for the O_2 intercalation experiment at 1 mbar CO and 300 K.

Furthermore, new C 1s signals are observed at higher binding energies. More precisely, in the *in situ* spectrum (middle spectrum) a new signal is observed at ~286.2 eV ("C4", purple fit) and in the spectrum after intercalation in UHV even two additional signals are observed at ~286.2 and ~287.8 eV ("C4" and "C5", purple and orange fits). These additional features at high binding energies were not observed in case of graphene/Ru(0001), however, signals at higher binding energies were observed on graphene on Ir(111) as a result of atomic oxygen adsorption. The authors concluded oxidation of the graphene layer to graphene oxide mostly leading to the formation of epoxide, which leads to additional features at high binding energies in the C 1s and O 1s region. To be exact, a new signal at 286.2 eV was observed in the C 1s, whereas in the O 1s, a signal at 531.1 eV was found.[210] Therefore, the new signal C4 at 286.2 eV observed in the *in situ* C 1s spectrum of Figure 7.5b is attributed to partial oxidation of the graphene layer, resulting in formation of epoxy species. According to literature, the signal C5 at 287.8 eV found in the C 1s spectrum after O_2 exposure (upmost spectrum) is attributed to carbonyl groups as for example present in esters [210-212], which is explained by a further oxidation of the graphene layer for higher exposure times. This also explains a coverage of ~1.6 ML deduced from the O 1s (neglected any damping through the graphene layer), as both, intercalated oxygen and oxygen species on the graphene sheet contribute to that signal.

The conclusions drawn from the C 1s spectra in Figure 7.5b suggest the presence of different O 1s species, which are not resolved. As a first-order approximation, two different features are used for the O 1s spectrum after pump-down to UHV (upper spectrum) that are attributed to intercalated oxygen and graphene oxide, albeit the fit is not unambiguous and it is not clear, whether more than two components may be present in the O 1s spectrum. Please note, that the change in total C 1s area before and after oxygen exposure was less than 5 %, i.e. the full graphene layer is still present, with ~56 % of the layer being oxidised according to fitting of the C 1s region. The sample was left in UHV overnight and changes in the C 1s and O 1s spectra were recorded for ~17 h. The first and last O 1s and C 1s spectrum are shown in Figures 7.6a and b, respectively. A loss of ~46 % in O 1s intensity is observed in Figure 7.6a, which goes along with considerable changes in the C 1s in Figure 7.6b. Here, a decrease of the C4 and C5 components is found, while the C1 component again increased, yielding a C1/C2 ratio of 1.5:1, which is very close to the ratio of 1.6:1 initially found after preparation of the graphene layer. This behaviour indicates that the partial oxidation of the graphene layer is, at least partly, reversible, while the C3 component, attributed to intercalated oxygen is stable at 300 K. Again, the overall C 1s intensity was not decreased during these measurements, i.e. the graphene layer was not decomposed, which suggests desorption of oxygen from the (partly oxidised) graphene layer. During and after the oxygen exposure, no changes in the Rh 3d region are found as compared to the graphene / Rh(111) situation.

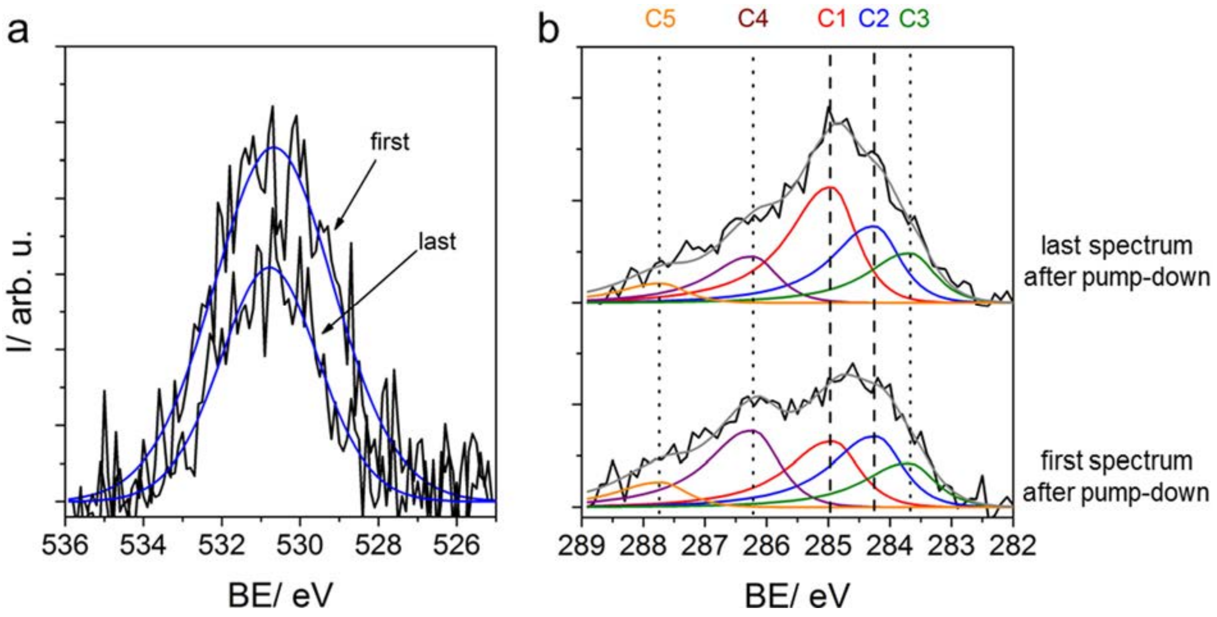

Figure 7.6: (a) O 1s region scan and (b) C 1s region scan after pump-down to UHV and after ~17 h in UHV.

In order to investigate, whether the oxidation/intercalation of oxygen is fully reversible, also for O_2, TPD experiments were conducted in order to investigate the desorption behaviour. Before heating the sample with a linear heating ramp of 2 K/s from ~300 – 1015 K, the sample was exposed to 1 mbar O_2 for 5 min before pump-down to UHV and transfer to the preparation chamber. Figure 7.7a and b show the TPD spectra for molecular O_2 (m/z=32), and CO (m/z=28), atomic O (m/z=16) and CO_2 (m/z=44).

Examining the TPD spectrum of molecular oxygen in Figure 7.7a, surprisingly, only very weak signal intensity is observed, more precisely, a signal at ~415 K and an increase in intensity at ~900 K. The signal at low temperatures is in line with desorption from e.g. epoxy groups (present in high coverages) from an oxidised graphene layer on Ir(111), which was observed in between 350 and 550 K.[212] The rise in intensity of desorbing O_2 at high temperatures might be understood as desorption of oxygen from the Rh(111) surface, i.e. of intercalated oxygen. On bare Rh(111), the desorption temperature of oxygen takes place at temperatures up to 1400 K.[213] This might explain the low intensity of the signal, as maybe full desorption of intercalated oxygen takes place at temperatures above 1015 K, which has to be clarified in an additional TPD experiment, including experiments going to higher temperatures. The low temperature desorption feature of O_2 from the oxidised graphene layer might be understood, when observing the signal of the masses belonging to CO, CO_2 and atomic oxygen shown in Figure 7.7b.

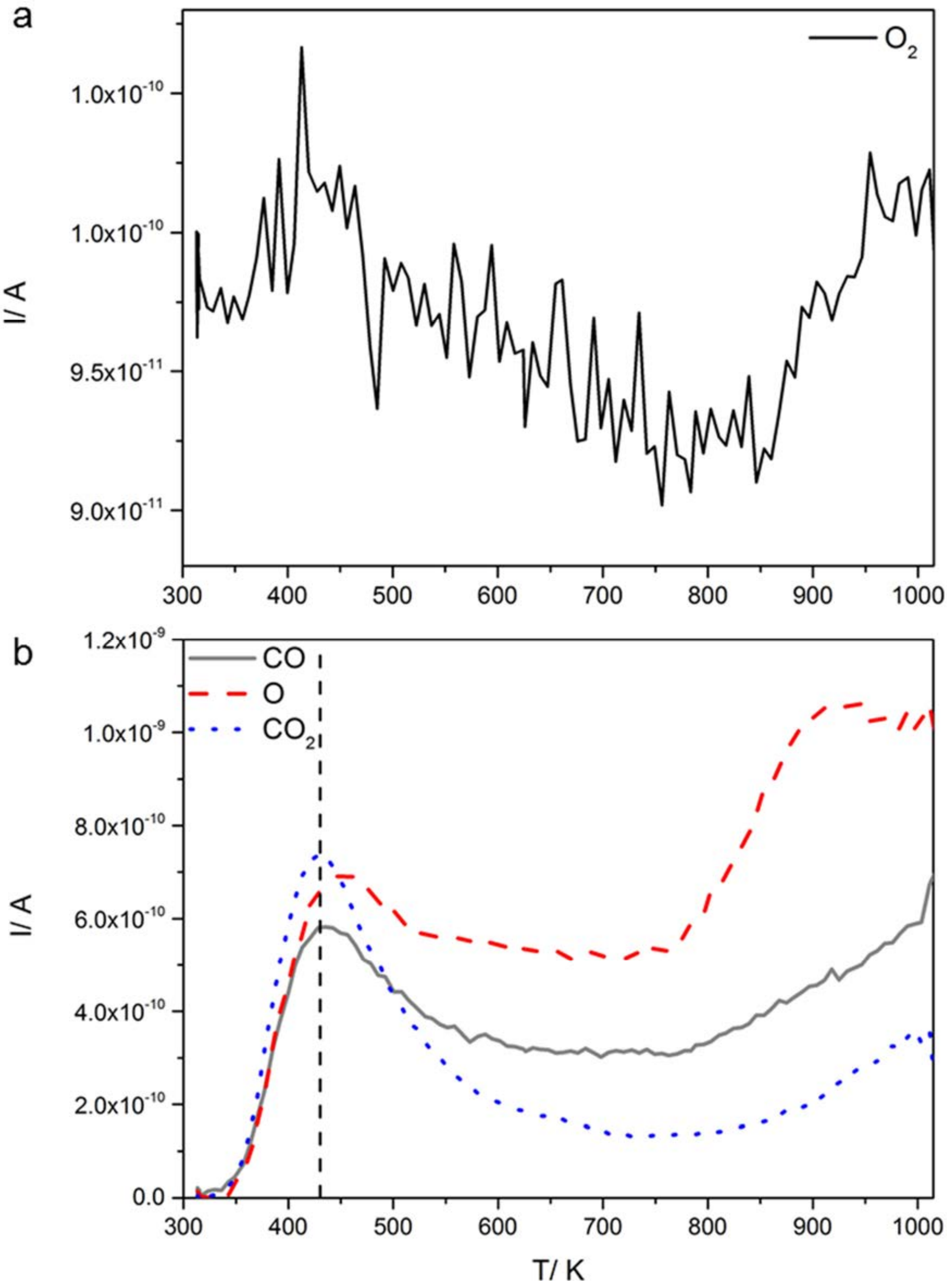

Figure 7.7: TPD spectrum of (a) molecular oxygen and (b) CO (grey line), atomic oxygen (red dashed line) and CO_2 (blue dotted line) after exposure to 1 mbar O_2 for 5 min.

Much higher ion currents are observed for these signals, suggesting reaction of adsorbed oxygen and the graphene layer at ~415 K. When comparing the areas of the CO desorption signal shown in Figure 7.7 with the signal from the (2x2)-3CO superstructure shown in Figure 7.4, it can be estimated that the formation of CO from reaction of graphene and oxygen results in a slight decomposition of the graphene which is within 10-15 % of the intact layer. The deviations in the C 1s and Rh 3d core levels before and after the TPD experiments are within the same magnitude. In order to finally evaluate the desorption behaviour, further desorption experiments have to be performed, e.g. up to higher temperatures.

7.6 Conclusions

Intercalation of CO and O_2 at 1 mbar partial pressure and 300 K between graphene and a Rh(111) substrate was investigated by NAP-XPS and TPD. Prior to exposure, a graphene layer was grown on the substrate by a CVD process using propene at 920 K according to Ref. [66] and the quality of the film was checked by LEED. According to this reference, the C 1s spectra were deconvoluted, resulting in two contributions, namely C1 and C2, ascribed to carbon atoms in closer and larger distance to the substrate surface.

For CO, the intercalation was observed by the emergence of signal intensity in the O 1s region, which was attributed to CO adsorbed in on-top and three-fold hollow sites, respectively. Interestingly, the ratio of $CO_{3\text{-fold-hollow}}/CO_{\text{on-top}}$ deviated substantially from the ratio found for the (2x2)-3CO superstructure of CO on the bare Rh(111) surface of 2:1 and was found to be 1.1:1 after pump-down to UHV after intercalation for ~5 h. This finding is surprising, as $CO_{\text{on-top}}$ was proposed to be sterically hindered underneath the graphene layer compared to $CO_{3\text{-fold-hollow}}$ in the case of Pt(111). This indicates a significantly different graphene / substrate interaction for graphene on Rh(111) that leads to a destabilization in this particular case for threefold-hollow bound CO. The intercalation of CO was also observed in the C 1s through a broadening of the C 1s peak, due to the signal of CO adsorbed on the Rh(111) substrate surface. Additional prove for the intercalation was obtained by a decrease in C1/C2 component ratio, which is interpreted as a lift-up of carbon atoms in closer vicinity to the substrate surface upon intercalation. From TPD experiments it was found that the desorption was facilitated, resulting in a shift of ~25 K to lower temperatures compared to desorption from the bare Rh(111), which was attributed to electronic interaction between the graphene and the intercalated CO molecules, resulting in a decrease in adsorption strength similar to the findings for graphene on Pt(111).[130, 135]

In case of O_2 intercalation, the evolution of an O 1s signal was observed, found at ~530.6 eV. Taking into consideration the C 1s region, where in total three new signals were observed due to O_2 exposure, it was concluded that this signal is composed of different contributions that are not resolved: Firstly, an additional feature (C3) shifted 0.5 eV to lower binding energies compared to C2, was attributed to carbon atoms in even higher distance to the surface than atoms contributing to C2. This indicates a higher impact of O_2 intercalation on the morphology of the graphene layer than for CO intercalation, where no such signal was observed. Additionally, again a decrease in C1/C2 ratio was observed. The new features arising at higher binding energies at ~286.2 and ~287.8 eV were ascribed to partial oxidation of the graphene layer, forming epoxy- and carbonyl groups. These groups were found to partly decompose in UHV in the course of ~17 h.

TPD experiments on the intercalation of O_2 did so far not completely explain the processes taking place during desorption. Whereas the signal for molecular oxygen was surprisingly small, high intensities for CO, CO_2 and atomic oxygen were observed. In order to obtain further understanding, TPD experiments to higher temperatures and after higher exposure times should be conducted.

Concluding, the obtained results may be used to understand the CO oxidation reaction confined under the graphene layer, which should be possible at 1 mbar partial pressure of the reactants, as intercalation occurred at this pressure. Changes in the reactivity are expected, as it was shown that the adsorption strength of CO is considerably influenced by the graphene overlayer. Before going to coexposure experiments, the threshold pressures for CO and O_2 intercalation should be determined, as they might be lower than 1 mbar.

8. Near ambient pressure XPS investigation of the interaction of ethanol with Co/CeO_2(111)

8.1 General

In the previous chapters, the main focus was kept on platinum and rhodium as widely used catalysts in heterogeneous catalysis. As a first reaction, the CO oxidation was chosen, which is a typical test reaction in surface science, besides its technical importance. Platinum is applicable in many reactions, but exhibits one major draw-back, which is the low availability and therefore high cost, inducing the need of replacement by cheaper metals.

In this chapter, cobalt was chosen as the active catalyst, being a less expensive metal in combination with a commonly used support, which is ceria. This model system was studied during ethanol adsorption and reaction. First, the interaction of ethanol with a well-ordered CeO_2(111) layer grown on a Cu(111) surface was investigated and in a second step, Co particles were deposited on this surface and included into the investigations. Ethanol adsorption is a key step in the steam reforming reaction as discussed in Chapter 3.2, as it is part of the first step and therefore already may determine the reaction progress. The results of this chapter have already been published and the text has been adapted from this publication:[214]

"Near ambient pressure XPS investigation of the interaction of ethanol with Co/CeO_2(111)", Óvári, L.*, Krick Calderon, S.*, Lykhach, Y., Libuda, J., Erdőhelyi, A., Papp, C., Kiss, J., Steinrück, H.-P., J. Catal, **2013**, *307*, 132, (*shared first authors).

The steam reforming of ethanol (SRE), alongside the partial oxidation of ethanol (POX), and the oxidative steam reforming (OSR) are currently in the focus of catalytic research as potential candidates for H_2 production [215]. One advantage of bio-derived ethanol is its low sulfur content, reducing the poisoning of catalysts, and its low toxicity as compared to methanol. Furthermore, ethanol from bio sources contains water and thus is particularly well-suited for steam reforming, since the distillation step to produce pure ethanol can be omitted.

During the steam reforming of ethanol, acidic supports like Al_2O_3 favour dehydration and thereby increase the tendency for coke formation due to the polymerization of ethylene [147]. However, on ceria (CeO_2), which is considered to be a basic support, dehydration is limited and its redox properties hinder coke formation. Additionally, ceria promotes the water–gas-shift (WGS) reaction (Equation XIII in Chapter 3.3) [216, 217].

Noble metals, especially Rh and Pt, proved to be excellent catalysts for the reaction, but their price is prohibitively high. As an alternative to expensive transition metals, Co is considered a promising catalyst for the reaction [144, 217, 218]. Co achieves a high ethanol conversion and selectivities of over 90 % for H_2 and CO_2 on CeO_2 and also on other supports, even at relatively low temperatures (~723 K) [145, 146]. Supported Co catalysts break the C–C bond in adsorbed ethanol [219]. It was found that addition of a CeO_2 promoter to the unsupported Co powder catalyst stabilizes the more active hcp structure of Co and hinders sintering during SRE [220]. Depending on the particular metal, dehydrogenation and C–C bond scission lead to the formation of alkoxide, oxametallacycle, aldehyde, acyl, and coke on the surface and mostly H_2, CH_4, CO, and aldehyde in the gas phase.[221] The rupture of the C–C bond generally requires higher activation energy than the scission of C–H and O–H bonds. C–O bond breakage was not observed in the majority of cases. On metallic Co, decarbonylation was dominant. However, CoOx surfaces, exposing Co^{2+} as majority cobalt sites, were selective toward dehydrogenation to produce acetaldehyde and smaller by-products. On the Co_3O_4 surface, total oxidation prevailed. The authors suggested that Co^{2+} sites are the active centres in SRE, and Co^0 sites are responsible for coke formation. Though the initial oxidation state of cobalt was analysed by XPS, the surface was not monitored during or after ethanol decomposition in this study. Thus, the role of Co^{2+} and Co^0 in SRE is still a subject of debate [144, 222, 223]. A high-resolution photoemission study performed during ethanol adsorption on Co(0001) [224] at 160 K showed that O–H bond scission led to the formation of ethoxide. In contrast to many other low index Group VIIIB surfaces, it was found that ethoxide on Co(0001) mostly decomposed into ethylene/acetylene and atomic O via C–O bond scission, presumably through an acetaldehyde intermediate.

In order to elucidate the role of Co in SRE, the reactivity of metallic and oxidized Co foils towards ethanol was investigated by temperature-programmed desorption.[222] On high surface area CeO_2, the adsorption and decomposition of ethanol were investigated by TPD and infrared spectroscopy (IR) [225, 226]. Literature agrees that there is ethanol, ethoxide, and acetate species on the surface, but concerning the formation of acetyl no agreement exists. In TPD experiments, mostly ethanol and acetaldehyde were desorbing. Reduced ceria was more reactive towards ethanol decomposition, resulting in less molecular ethanol desorption, with acetaldehyde again being the product with the highest yield. Ethoxide fragments were stable against annealing up to 623 K in vacuum. The changes in IR spectra observed at 623–673 K were assigned to the transformation of acetate groups to carbonates. The importance of the metal-support perimeter in SRE is frequently emphasized [215]. Surface OH groups can facilitate the transformation of ethoxide to acetate [147, 215]. The presence of steam contributes to the demethanation of acetate groups to produce carbonate leading to CO_2 and CH_4, which is participating in a later SR reaction [215].

Since real catalysts are often structurally very complex, for the better understanding of surface reactions, it is helpful to investigate simplified, but well-controlled model catalyst systems, like metal nanoparticles on supported single crystalline oxide surfaces [227, 228]. With relevance to ceria, the formation of CeO_2(111) films was characterized on Cu(111) [80-83, 229, 230] and on other supports [31,32]. Evaporation of Ce onto Cu(111) at $T = 520$ K substrate temperature in an O_2 atmosphere resulted in the formation of nearly stoichiometric CeO_2 films with a (1.5x1.5) unit cell of CeO_2(111)/Cu(111) [82]. From low energy electron diffraction (LEED), it was concluded that the films are indeed closed layers [81, 231].

In this chapter NAP-XPS was used to study interactions between ethanol and Co/CeO_2(111) *in situ* under more realistic conditions, i.e. up to pressures of 1 mbar. The aim was to get closer to the real catalytic conditions and to determine not only the transient intermediates but especially the oxidation states of active components during the reaction. The investigation of the model catalyst under near ambient conditions allows bridging the pressure gap between the surface science and realistic conditions.

8.2 Experimental aspects

The acquisition of the spectra took ~2 hours, with the exception of the 1 mbar pressure, when ~6 hours were required for a complete data set of all relevant regions.

8.3 XPS characterization of CeO_2(111) on Cu(111)

After the preparation of the CeO_2(111) film on the Cu(111) surface, it was characterized by XPS. The Ce 3d spectrum shown in Fig. 8.1a (“clean”) is composed of three doublets, (u''', v'''), (u'', v'') and (u, v) corresponding to the emission from the spin-orbit split $3d_{3/2}$ and $3d_{5/2}$ core levels [232-235]. The three doublets are assigned to different final states of tetravalent Ce (Ce^{4+} ions) in Ce compounds: u''' (916.6 eV) and v''' (898.2 eV) are due to a Ce $3d^9 4f^0$ O $2p^6$ final state, u'' (907.5 eV) and v'' (888.8 eV) to a Ce $3d^9 4f^1$ O $2p^5$ final state, and u (900.7 eV) and v (882.3 eV) to a Ce $3d^9 4f^2$ O $2p^4$ final state.

For a more detailed picture, which might allow a deeper understanding of the core levels and the properties of Ce in these spectra, the reader is referred to [236]. Note that especially the well separated u''' peak at 916.6 eV is characteristic for the presence of Ce^{4+} [233].

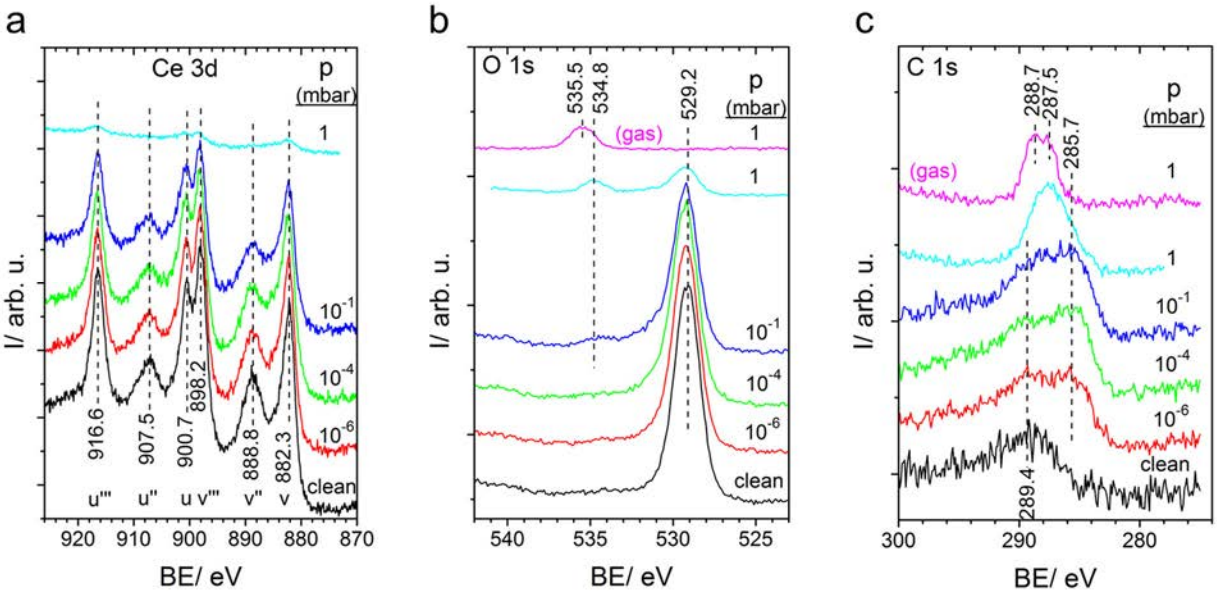

Figure 8.1: XP spectra of the $CeO_2(111)$ surface collected at 300 K in the presence of ethanol at increasing pressures. For comparison, spectra of the clean ceria surface and spectra of gas phase ethanol (1 mbar) are also displayed. Before exposure to ethanol at 300 K at each pressure, the surface was reoxidized in 10^{-6} mbar of O_2 at 623 K.

Indeed, after evaporating a 0.3 nm Ce layer onto the $CeO_2(111)$ film at 523 K, the intensity of the u''' peak at 916.6 eV significantly decreased (Fig. 8.2), and four new features developed in the Ce 3d region: they are assigned to two spin-orbit split doublets, (u', v') and (u_0, v_0), resulting from two different final states of Ce^{3+}. These Ce^{3+} cations are formed by the reaction of Ce metal with CeO_2. According to literature, u' (903.8 eV) and v' (885.2 eV) are assigned to a Ce $3d^9 4f^1$ O $2p^6$ final state, and u_0 (899.3 eV) and v_0 (~880.7 eV) to a Ce $3d^9 4f^2$ O $2p^5$ final state [233]. Interestingly, upon heating to 600 K for 10 min, the six-peak structure of Ce^{4+}, characteristic of the oxidized surface, was largely recovered (Fig. 8.2). This shows an increased exchange between sub-surface and surface oxygen vacancies on $CeO_2(111)$ upon heating [237]. To summarize, in XPS the Ce^{3+} and Ce^{4+} species are differentiated with distinct line shapes corresponding to their various final states. Note that also the freshly prepared $CeO_2(111)$ film showed a small degree of reduction as demonstrated by the deconvolution of the Ce 3d region (Fig. 8.3a, bottom spectrum). Additional information on the quality of the $CeO_2(111)$ film is obtained from the O 1s spectrum in Fig. 8.1b (clean), which shows the signal of lattice oxygen at 529.2 eV. The C 1s region in Fig. 8.1c (clean) exhibits a peak at 289.4 eV that is not resulting from carbon impurities, but from the Ce 4s core level. Overall, one can state the spectra of the obtained $CeO_2(111)$ film resemble literature spectra very well [233], confirming the quality of the preparation.

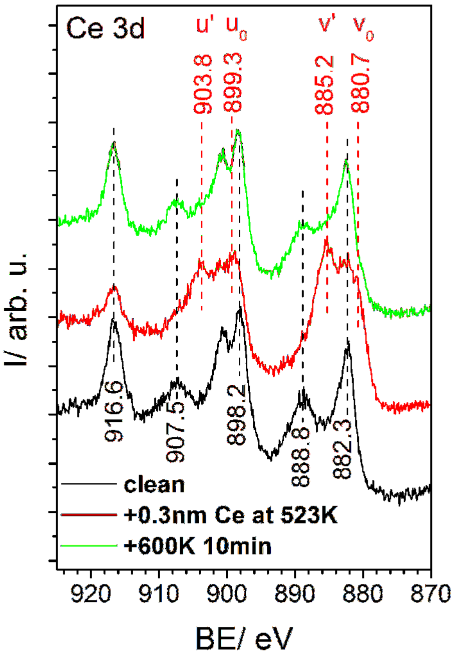

Figure 8.2: Ce 3d spectrum of the clean $CeO_2(111)$ surface, after deposition of (nominal) 0.3 nm of metallic Ce at 523 K, and after subsequent annealing at 600 K.

8.4 Adsorption and decomposition of ethanol on $CeO_2(111)$ at different pressures at 300 K

As a reference, first XP spectra of vapour phase ethanol (CH_3CH_2OH) were measured at 1 mbar. The corresponding C 1s and O 1s spectra are displayed in Figure 8.1b and Figure 8.1c as topmost spectra. The O 1s region displays one peak at 535.5 eV, and in the C 1s region two peaks at 287.5 and 288.7 eV are observed, in agreement with literature data [238]. The two C 1s peaks are assigned to methyl carbon and alkoxy carbon, respectively.

The adsorption of ethanol on $CeO_2(111)$ at 300 K was investigated by recording spectra at 10^{-6}, 10^{-4}, 10^{-2}, 10^{-1} and 1 mbar. Prior to each experiment, the sample was oxidized at 623 K, to ensure identical conditions. The evolution of Ce 3d spectra is shown in Figure 8.1a. The increase of ethanol pressure resulted in attenuation of the intensity of the Ce 3d spectrum. Simultaneously, a relative increase of the intensity in the valleys between v and v”, and u and u" was noted. This indicates the emergence of v' (~885.2 eV) and u' (903.8 eV) peaks from Ce^{3+}, due to mild reduction of ceria under increasing ethanol pressure at 300 K. The peak fitting of selected Ce 3d spectra shown in Figure 8.3a confirms this trend. To quantify the amount of Ce^{3+}, the ratio of the integrated intensities of Ce^{3+} spectral contribution to the total Ce 3d spectrum, i.e., $Ce^{3+}/(Ce^{3+} + Ce^{4+})$, is plotted in Figure 8.4a as a function of ethanol pressure. The plot shows that the reduction of $CeO_2(111)$ increases up to 10^{-4} mbar, and levels off thereafter. This behaviour suggests that at pressures of 10^{-4} mbar or higher the further reduction is hindered, due to a reduced mobility of either oxygen or Ce^{3+} centers at 300 K.

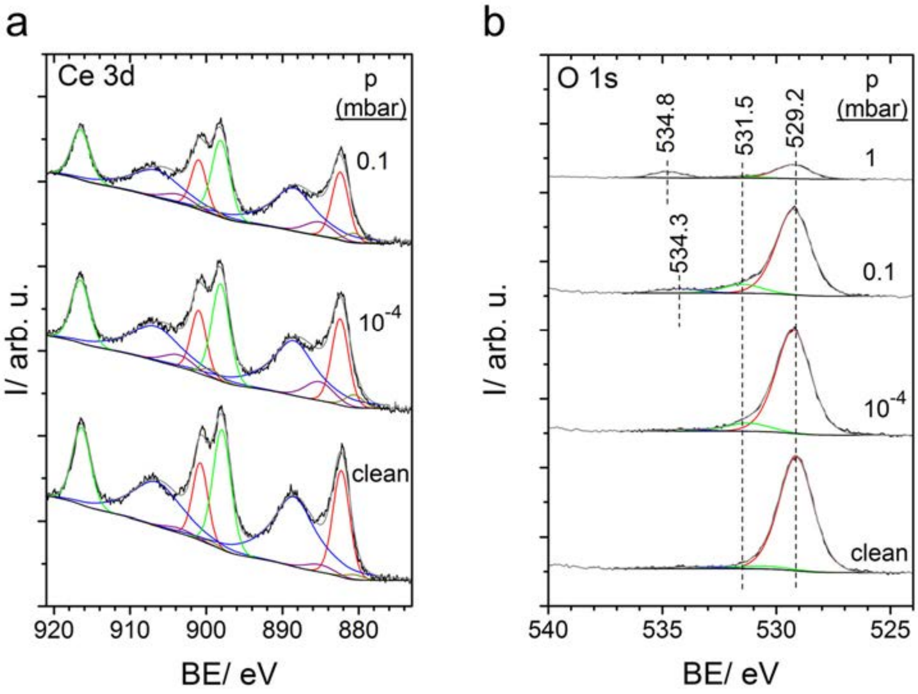

Figure 8.3: Peak fitting for selected curves of Fig. 8.1. For the assignment of the Peaks in a and b please refer to the text.

To reveal, if the reduction is due to the high exposure dose (time x pressure) or due to the high pressure, the effect of time in this reaction was investigated, see Figure 8.4. The $CeO_2(111)$ surface was in contact with 1×10^{-5} mbar of ethanol for 69 hours at 300 K (exposure: $\sim1.9\times10^{6}$ L). Thereafter, the spectra were taken in 10^{-5} mbar ethanol (b) and after 15 min of pump-down (c), with these two spectra showing only minor differences. In a separate experiment, a spectrum was taken in 10^{-1} mbar ethanol (d) after ~1 hour at this pressure, yielding a much higher exposure of $\sim2.8\times10^{8}$ L (see also Figure 8.1a): The analysis shows that the extent of reduction is higher for the lower total exposure, i.e., at lower pressure but higher exposure time, with a $Ce^{3+}/(Ce^{3+} + Ce^{4+})$ ratio of 0.22, as compared to the value of 0.10 at

10^{-1} mbar. Note that this effect is not attributed to the exposure of ceria to vacuum, since for CeO_2 none or only slight reduction is observed [230, 239]. It is rather attributed to diffusion of oxygen or Ce^{3+} centres through the reduced surface layer as the rate-limiting step, as also suggested at the end of last paragraph.

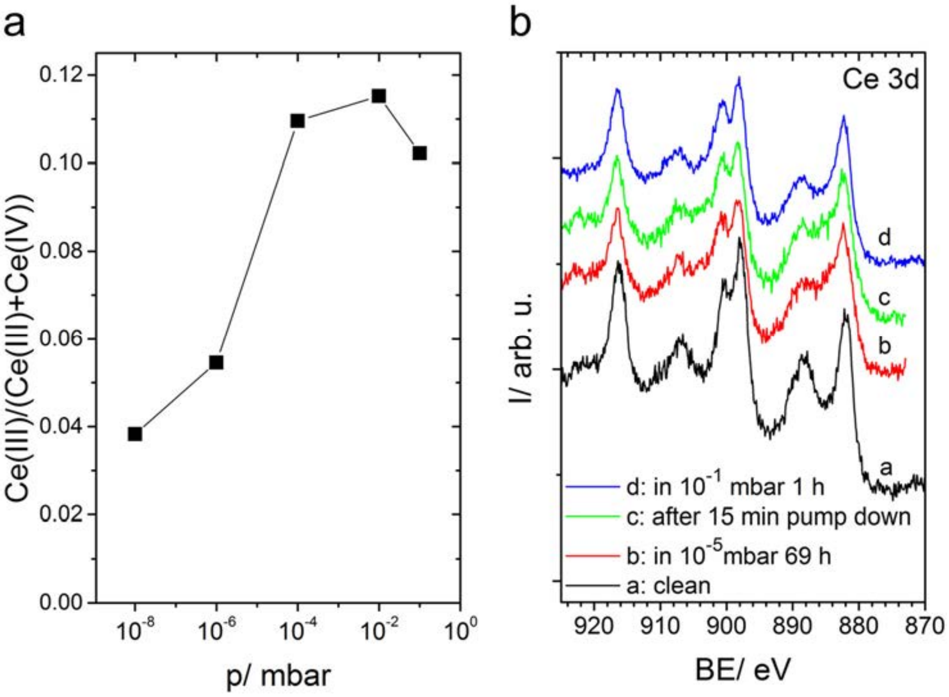

Figure 8.4: (a) Reduction of ceria at 300 K, calculated from peak fitting of the Ce 3d region; (b) Ce 3d spectra of clean $CeO_2(111)$ (a), after exposure to ethanol at 10^{-5} mbar for 69 h (b), followed by 15-min evacuation at 300 K (c), and after exposure to ethanol at 10^{-1} mbar for 1 h (d).

During ethanol adsorption at 300 K, the O 1s peak at 529.2 eV for lattice oxygen develops a shoulder at the high binding energy side at 531.5 eV (see Figure 8.3b). This value would be in line with the formation of OH groups, which were observed after exposure to H_2O [240, 241] or CH_3OH [242]. This assignment is however equivocal, as the O 1s peaks of ethoxide and acetaldehyde surface species are also expected at this binding energy. Especially, ethoxide formation is likely as proposed in literature [215, 225, 243]. At higher pressures, an additional contribution from weakly held, molecularly adsorbed ethanol should also be considered. Matolín *et al*. found the O 1s peak of a methanol multilayer on $CeO_2(111)$ at 534 eV [242], and the corresponding O 1s peak for physisorbed ethanol is expected to occur at a similar position. Indeed, the inspection of the O 1s spectra in Figure 8.1b and the fits in Figure 8.3b reveal a weak peak at 534.3 eV, which becomes observable at 10^{-1} mbar (note that the comparably large peak at 534.8 eV at 1 mbar is due to the ethanol gas phase). The negligible intensity of the peak due to molecular ethanol adsorption below 10^{-1} mbar suggests that dissociative adsorption of ethanol prevails at 300 K. At 0.1 and 1 mbar, however, the presence of molecularly adsorbed ethanol cannot be excluded. The gas phase spectrum of ethanol with the sample not present (topmost spectrum in Figure 8.1b) displays a somewhat higher binding energy (535.5 eV) than with the sample present, due to the differences in the work functions of the sample and the spectrometer (please see Chapter 2.1.2) [57].

The C 1s region at different ethanol pressures at 300 K is shown in Figure 8.1c. As mentioned above, the broad peak centered at 289.4 eV originates from the Ce 4s level. Upon exposure to ethanol at 300 K, a very broad C 1s feature is observed at ~285.9 eV. Its assignment is challenging because of the possible presence of various surface species (mostly ethoxide, acetaldehyde and acetate groups), giving multiple overlapping peaks in that energy range. The adsorption of ethanol [244] and acetaldehyde [137] was previously studied by Mullins and coworkers on $CeO_2(111)$, and by other authors on polycrystalline samples [245, 246]. Formation of alkoxy species was detected by XPS on oxidized $CeO_2(111)$ after adsorption of alcohols at 300 K [244]. The two non-equivalent C 1s levels of the ethoxide species were located at ~285.9 eV and at ~286.9 eV [244]. Acetaldehyde did not decompose on the stoichiometric $CeO_2(111)$ surface and desorbed below room temperature. On reduced $CeO_x(111)$ chemisorbed acetaldehyde was more stable, characterized at room temperature by C 1s peak positions at 286.9 and 289.5 eV and assigned to non-dissociated acetaldehyde as majority species. The C 1s binding energy of the carboxylic carbon atom in acetate was observed at 290 eV [244]. Since both for acetate and for acetaldehyde one of the C 1s peaks was found in the literature at ~289.5-290.0 eV and only a slight increase in that region upon ethanol adsorption is observed, it is concluded that these species can only be minorities here and the dominating surface fragment is ethoxide up to 10^{-1} mbar, formed by reaction (1):

$$CH_3CH_2OH + O_s \rightarrow CH_3CH_2O_a + OH_a \qquad \text{(XIV)}$$

$$OH_a + OH_a \rightarrow H_2O_g + O_s + V_o \qquad \text{(XV)}$$

Reaction (XV) may lead to the formation of water, lattice oxygen and oxygen vacancies (V_o) and finally to the reduction of ceria. Indeed, water production was observed during adsorption of ethanol on CeO_2 at low temperatures (~200 K) [244]. At 1 mbar the C 1s region is dominated by gas phase ethanol (Fig. 8.1c). A clear distinction of surface species was not possible due to the small intensity of the surface species.

8.5 Reactions of 0.1 mbar C_2H_5OH on $CeO_2(111)$ film at different temperatures

Next, the interaction of 0.1 mbar of ethanol with $CeO_2(111)$ was investigated at different temperatures up to 600 K. The corresponding spectra are shown in Figure 8.5. In the Ce 3d region pronounced changes are observed, which become most striking starting at 500 K. While the u'-peak (903.8 eV) and the v'-peak (885.2 eV) due to Ce^{3+} markedly increase in Intensity, the u'''-peak (916.6 eV) characteristic for Ce^{4+} significantly decreases in Figure 8.5a; the corresponding peak fitting for selected Ce 3d spectra is shown in Figure 8.6a. These changes indicate a strong reduction in the surface layer. To quantify the changes, the ratio of $Ce^{3+}/(Ce^{3+} + Ce^{4+})$ was plotted in Figure 8.6b for increasing temperatures; this plot shows an almost linear dependence on temperature to ~0.5 at 600 K. From this large value it is concluded that an in-depth reduction of the ceria film occurred at this temperature. This is not surprising in the light of Figure 8.2, which suggests that diffusion of ions within the ceria film is more pronounced at elevated temperatures.

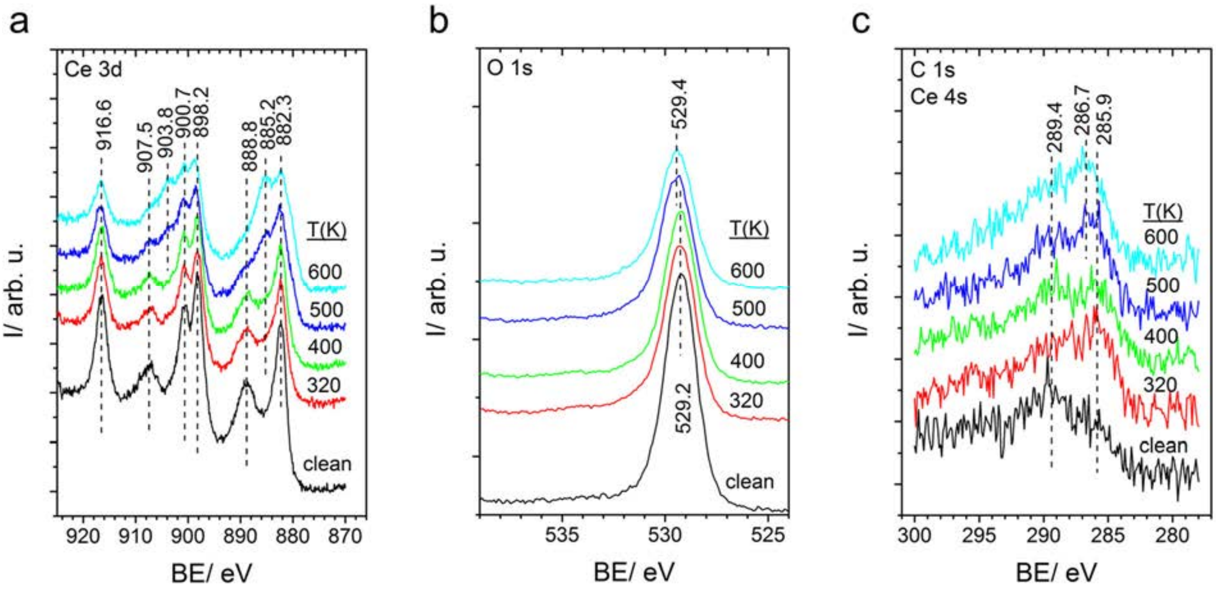

Figure 8.5: XP spectra collected from CeO_2 in 0.1 mbar of ethanol at temperatures of up to 600 K. The “clean” spectrum was recorded before ethanol exposure.

With increasing temperature, the O 1s peak in Figure 8.5b decreases significantly, in accordance with the reduction of CeO_2 observed in the Ce 3d region. In the C 1s region, shown in Figure 8.5c, again a broad feature with maxima at 285.9, 286.7 and 289.4 eV is observed, with their relative intensities changing with temperature. For the qualitative interpretation of the spectral changes during heat treatment the literature results for $CeO_x(111)$ thin films [137, 244, 245, 247] are considered. The peak assigned to ethoxide (285.7 eV) is found at all temperatures, in agreement with literature; its shift to higher binding energies at 600 K is attributed to the different bonding situation of ethoxide on the reduced ceria surface.[244] Please note that identification of the surface species is rather challenging, due to the overlap of the signals and the low intensity in the C 1s region.

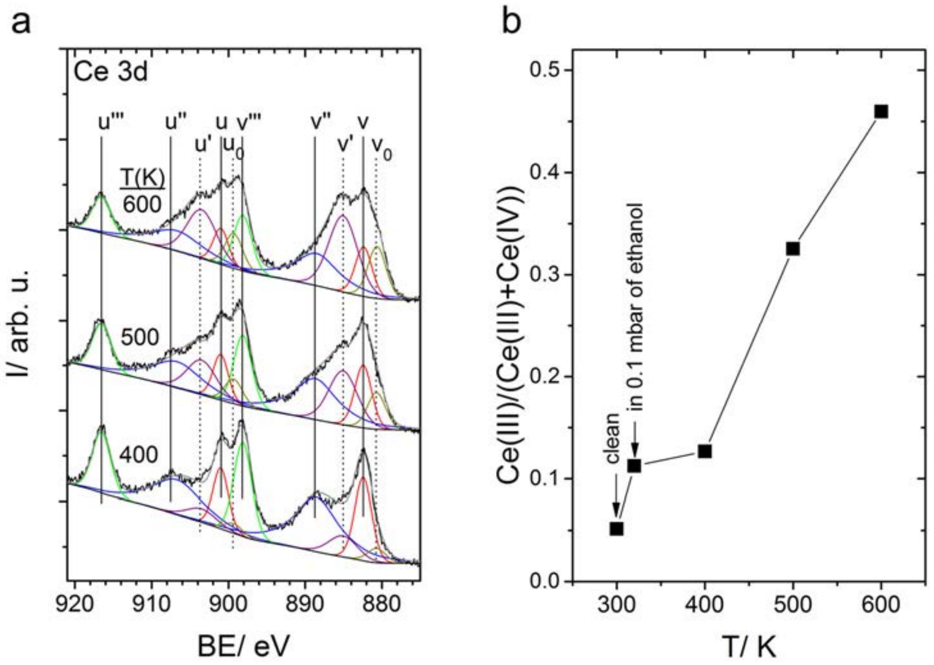

Figure 8.6: (a) Peak fitting for selected curves of Figure 8.5; (b) $Ce^{3+}/(Ce^{3+} + Ce^{4+})$ ratio as a measure for the reduction of ceria at temperatures of up to 600 K during exposure to 0.1 mbar of ethanol; calculated from the peak fitting of the Ce 3d region shown in (a).

8.6 Interaction of C_2H_5OH with $Co/CeO_2(111)$

The growth of Co on $CeO_2(111)$ was briefly studied previously using XPS [247]. Based on the linear dependence of the Ce 3d/Co 2p intensity ratio vs. cobalt coverage, two-dimensional growth of Co was proposed up to 1 ML. From the Co 2p peak shape, the resulting surface species were identified as Co^0 and Co^{2+}. Furthermore, reduction of Ce was observed upon Co deposition, due to the reaction of Co with CeO_2. In the literature data, for metallic cobalt (Co^0) an asymmetric Co $2p_{3/2}$ peak is observed at 778.0-778.5 eV. Co^{2+} is characterized by a Co $2p_{3/2}$ peak at 780-781 eV, with a strong satellite at 786-787 eV. The signature of Co^{3+} is a Co $2p_{3/2}$ peak at 780-781 eV with no satellite [222, 247-249].

To study the reaction of ethanol on Co-covered ceria, 0.7 ML of Co were deposited at 300 K. The Co coverage was kept below 1 ML to prevent a closed Co layer. Upon Co deposition, similar to the previous findings [247], an increase of Ce^{3+} is found; this is evident from the comparison of the bottom curves of Fig. 8.1a and 8.7a, and from the increase of the $Ce^{3+}/(Ce^{3+} + Ce^{4+})$ ratio from 0.04 ± 0.01 in Figure 8.4a to 0.11 ± 0.02 in Fig. 8.7f.

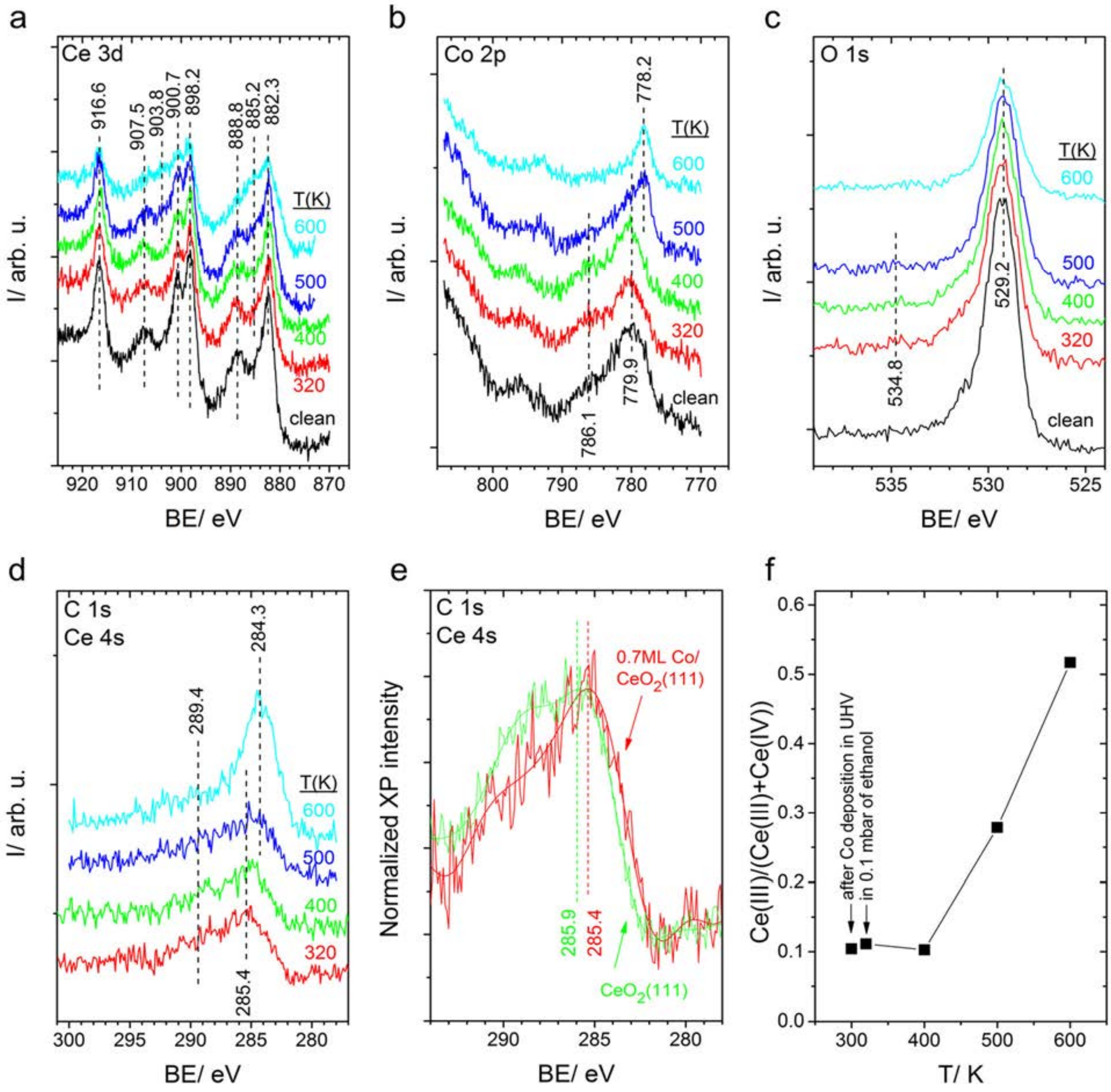

Figure 8.7: (a-d) XP spectra recorded after deposition of 0.7 ML of Co on the $CeO_2(111)$ surface at 320 K ("clean"), followed by admission of 0.1 mbar of ethanol at 320 K and annealing the surface in ethanol at higher temperatures. Spectra were collected in 0.1 mbar ethanol at the given temperatures. (e) Normalized XP spectra of the C 1s/Ce 4s region of the $CeO_2(111)$ and 0.7 ML Co/$CeO_2(111)$ surfaces collected in 0.1 mbar of ethanol at 320 K. Spectra are displayed also after heavy smoothing to guide the eye. (f) Reduction of ceria in the presence cobalt during exposure to ethanol at temperatures of up to 600 K.

The Co $2p_{3/2}$ region, shown in Fig. 8.7b, is dominated by a rather broad peak at 779.9 eV with a weaker satellite at 786.1 eV, indicative of Co^{2+}; for details see also Figure 8.8. The large width of the main peak suggests the coexistence of several oxidation states, predominantly Co^{2+} and some Co^0. Since the reaction of Co and CeO_2 and the resulting Co^{2+} formation is expected to proceed mainly at the ceria support/metal cluster interface, the small amounts of unreacted Co^0 species are presumably located mainly on top of the cobalt clusters (i.e. away from the interface) and hence should be available for interaction with ethanol.

The O 1s peak after Co deposition was found to be slightly more asymmetric towards higher binding energies compared to the clean $CeO_2(111)$ surface (see Figures 8.1, 8.3, 8.5 and 8.7). This is most likely due to the O 1s contribution from CoO [222, 249] with a binding energy of 529.2-530.4 eV, but might partly also result from some ethanol, CO or H_2O adsorption from the background.

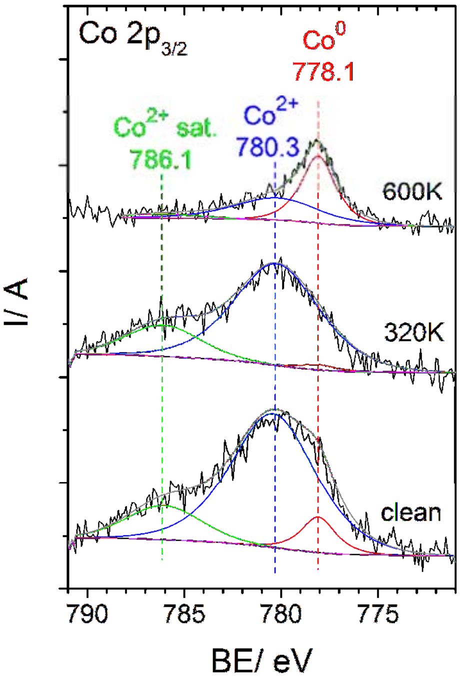

Figure 8.8: Peak fitting of the Co $2p_{3/2}$ region for selected curves of Fig. 8.7b: after the deposition of 0.7 ML of Co in UHV ("clean"), followed by exposure to ethanol at 320 K, and stepwise annealing up to 600 K.

Next, the $Co/CeO_2(111)$ was exposed to 0.1 mbar of ethanol at temperatures up to 600 K; at each temperature a set of XP spectra was collected under the ethanol pressure. At 320 K, 0.1 mbar of ethanol led to no change in the shape of the Ce 3d spectra in Figure 8.7a, i.e. to no further reduction of the CeO_2 surface, in contrast to the situation for Co-free ceria; this is evident from Figure 8.7f, where the first two data points corresponding to the situation prior and after exposure to ethanol are identical within the margin of error. As 0.7 ML CoO/Co is not sufficient to fully cover the substrate, it is concluded that by deposition of this amount of Co the ceria surface is reduced to the approximately same level, i.e. a $Ce^{3+}/(Ce^{3+} + Ce^{4+})$ ratio of 0.11, which was achieved by ethanol on the Co-free ceria surface (see Figure 8.4a), and thus a further reduction does not occur. Apart from that, a decrease of the Co^0 intensity at 778.1 eV in Figs. 8.7b and 8.8 is found. This is probably due to a C-O bond scission, or the presence of ethoxide, the latter coordinating to the cobalt surface via the electronegative O atom. Indications for ethoxide and/ or OH are also seen in the O 1s region, where the high binding energy shoulder (531.5 eV) has increased relative to the main ceria O 1s peak. Please note that the presence of CO cannot be ruled out as was proposed in earlier studies [221, 224]. The C 1s feature in Figure 8.7d is rather broad, containing a peak at 289.4 eV (mostly Ce 4s contribution) in addition to the dominant broad peak at 285.4 eV. In Fig. 8.7e, the C 1s spectra obtained at 320 K in 0.1 mbar of ethanol on $Co/CeO_2(111)$ and on $CeO_2(111)$ are compared after intensity normalization. The comparison clearly shows that the low binding energy edge of the C 1s region is shifted down by ca. 0.5 eV in the presence of cobalt. Due to the overlap of the signals of different species one can only speculate on possible reasons for this difference, e.g. C-O or C-C bond breaking leading to C_xH_y fragments, or different surface potentials for Co/CoO and ceria. The presence of acetyl groups cannot be excluded either, as such species were proposed on Pt(111) [250] and on Pd(111) [251], but is unlikely, as it was not observed on Co(0001) [224].

Heating of $Co/CeO_2(111)$ in ethanol at 400 K induced only minor changes in the spectra in Figure 8.7. However, annealing at 500 K led to a significant reduction of Co, accompanied by a shift of the C 1s feature towards smaller binding energies, and some further reduction of ceria ($Ce^{3+}/(Ce^{3+} + Ce^{4+})$ ratio is ~0.3). At 600 K, significant further reduction of Ce and Co is found leading to a $Ce^{3+}/(Ce^{3+} + Ce^{4+})$ ratio of ~0.5 ± 0.05. In the Co 2p region in Figure 8.7b, a narrow peak is observed at 778.2 eV, i.e. the position of metallic Co known from literature [222, 247-249]. By fitting the peaks (Figure 8.8), it is deduced that ~55-65 % of the total Co area originates from Co^0. In the C 1s region (Figure 8.7d) the overall intensity strongly increased with the peak maximum at 284.3 eV, which is very probably due to the formation of carbonaceous species. Surface carbon is a known reaction product in the decomposition of ethanol on metal surfaces [221].

The reduction of Ce and Co can proceed in a variety of ways, e.g. by the recombination of OH groups possibly formed as ethanol or the $C_xH_yO_z$ surface fragments lose H, or by the reaction of surface C with O producing CO, etc. Oxygen-containing gas phase products originating from the substrate might be CO, CO_2, acetaldehyde [225] and H_2O. After the partially contrasting results related to ethanol decomposition on a Co foil [222], and on Co(0001) [224], the role of a transient oxametallacycle on metallic Co sites cannot be completely excluded. Presumably, the ceria support, acting as an oxygen “reservoir” at low temperatures, hinders reduction of Co and also the formation of coke by O (reverse) spillover, but after the reduction of ceria at 500-600 K this oxygen buffer is exhausted. Note that coke formation was not observed on pure ceria (Figure 8.5c). The accumulation of carbon certainly contributed to the severe intensity loss in the Co 2p region (Figures 8.7b and 8.8), together with a sintering of Co nanoparticles. Sintering of Co particles could also contribute to the downward shift of Co $2p_{3/2}$ binding energy, as was previously observed for metal clusters on oxide supports [227, 252, 253]. In this study, however, the presence of the satellite feature of Co^{2+} at 786.6 eV at low temperatures and its strong attenuation upon annealing in ethanol is a strong indication of the change in the oxidation state itself. Moreover, the binding energy shifts due to cluster size effects are typically in the range of 0.5-1 eV, while in Figure 8.7b a shift of 1.7 eV is observed. The sintering of cobalt and the increased oxygen mobility facilitates the access of ethanol to surface CeO_2, which is subsequently reduced. Please note that the use of pure ethanol gives different results than using ethanol/water mixtures over oxidized Co/CeO_2 polycrystalline catalyst, where the reduction of Co, but not that of ceria was observed [144, 223].

8.7 Conclusions

Concluding this chapter, NAP-XPS was applied to study the interaction of ethanol with a well-ordered $CeO_2(111)$ film prepared on Cu(111) and with a $Co/CeO_2(111)$ model catalyst, with respect to the oxidation state of the surface and to the chemical nature of reaction intermediates. At 300 K, the oxidation state of ceria decreased gradually with increasing ethanol pressure, presumably through H_2O desorption involving lattice O. The transformation of Ce^{4+} to Ce^{3+} increased significantly upon increasing the temperature from 320 to 600 K at 0.1 mbar. The primary intermediate, ethoxide, was formed by dissociative adsorption of ethanol at room temperature. No coke formation was observed up to 600 K. On the Co/CeO_2 model catalyst it was found that a significant part of metallic Co reacted with ceria upon deposition, leading to the formation of Co^{2+} sites and to some reduction of ceria. During the interaction of 0.1 mbar ethanol with a 0.7 ML $Co/CeO_2(111)$ model catalyst the amount of Co^{2+} decreased with increasing temperature, and at 600 K the majority of Co was metallic, accompanied by a severe reduction of Ce. At 600 K, significant amounts of carbon formed on Co/CeO$_2$(111).

This study contributes to the understanding of a fundamental reaction step of the ethanol steam reforming reaction, which is ethanol adsorption. In order to elucidate the whole process, however, as a subsequent step, the co-adsorption of ethanol and water should be considered, taken place during this reaction. This could for example have a strong impact on the oxidation state of the support – and influence carbon formation as observed at 600 K on the Co/CeO$_2$(111) system in this study.

9. Summary and Outlook

This thesis is focused on the influence of the pressure and materials gap on prototypical systems studied in surface science. These gaps are a result of the different conditions applied in surface science and industrial catalysis. While many catalytic systems have been thoroughly investigated in surface science studies under defined and very controlled conditions, i.e. at UHV pressures, the transfer and extrapolation of the obtained results to realistic conditions used in heterogeneously catalysed processes still poses challenges in many cases. Throughout this work, NAP-XPS has been used for taking a step into the pressure gap; in contrast to conventional XPS, measurements at pressures up to 1 mbar were performed. For reaction experiments, online gas analysis was applied using a QMS in order to simultaneously monitor the gas composition. Complementarily, the materials gap was approached by extension of the investigations on a single crystalline surface to a particle/support model catalyst and further to nanotube-supported particles. Therefore, catalyst complexity was introduced in order to mimick porous catalysts often found in industrial processes.

After the introduction and experimental section, the growth of platinum oxides at 1 mbar O_2 and temperatures between 300 and 700 K was investigated on a Pt(111) single crystal. The aim was to understand the effect of an oxygen partial pressure of up to 1 mbar on a well-defined surface, before advancing to more complex systems. Different oxide phases were found in the temperature range from 300 to 700 K. The highest platinum oxide coverages obtained at 300, 400 and 500 K were 3.7, 1.9 and 3.8 ML and lower coverages of 1.5, 0.5 and 0.25 ML were found at 600, 650 and 700 K, respectively. Notably, the time scale of the experiment is crucial, as the growth times were exceeding 4 h before reaching a saturation, which might explain that no oxide growth was found at 300 K in literature under similar conditions [49, 106]. These findings were combined with ReaxFF GCMC simulations performed in the work group of Prof. Dr. Timo Jacob of the “Institut für Elektrochemie” at the University of Ulm, which predicted five stable surface phases for increasing oxygen chemical potential (i.e. as a function of decreasing temperature at 1 mbar O_2): a clean Pt slab (800 K), p(2x2) adsorbed atomic oxygen (700 K), low- and high coverage amorphous surface oxides (1.13 and 3.44 ML, 650, 600 and 500 K) and α-PtO_2 (300 and 400 K). These time-dependent simulations were in line with the experiment and therefore were able to elucidate the structure and especially amorphous nature of the surface oxides. Deviations in absolute coverages for these amorphous oxides are traced to insufficient experimental growth times and kinetic limitations for the growth at 300 and 400 K. In general, these oxides were not stable in UHV at 400 K and temperatures above, which is confirmed by theory.

In Chapter 5, in order to find out whether these oxides exist and actively take part in the CO oxidation reaction and, hence, if metallic or oxidic platinum is the active catalyst, the reaction was performed at total pressures up to 1.1 mbar with different gas mixtures ($CO:O_2$ = 2:1, 1:1, 1:4, 1:10) in isothermal as well as temperature-programmed measurements in the temperature range from 300 to 900 K and 300 to 1100 K, respectively. This investigation takes up the discussion among the scientific community whether the reaction follows a Langmuir-Hinshelwood mechanism (as found in UHV) or if a Mars-van-Krevelen mechanism takes place at elevated pressures.[17, 44] No oxide formation was found under these conditions – in all cases the reaction was mass-transfer limited at high temperatures and no adsorbates were found on the metallic catalyst surface. In particular, three different reaction regimes were observed in the temperature-programmed reaction experiments: (I) CO-inhibited with negligible conversion, (II) partially CO-covered with moderate activity, and (III) adsorbate-free with high activity (MTL regime). Reaction onset was found to be dependent on the O_2 partial pressure within the mixture and was lower at higher O_2 content. As the catalyst is saturated with CO at 300 K, CO (re)adsorption and oxygen adsorption are competitive processes. If the O_2 partial pressure in the mixture is increased, CO desorption sets in at lower temperatures due to its lower partial pressure, enabling oxygen adsorption and as a result reaction of the adsorbates.

As a follow-up, the materials gap was addressed in Chapter 6 by using a porous support in combination with platinum particles in the CO oxidation reaction. More precisely, three different TiO_2 nanotube arrays which were decorated with platinum particles of different sizes spread homogeneously across tubes with a length of 200 nm and a diameter of 80 nm were investigated: 1. “$Pt_{5nm}TiO_2NT$” with smaller particles of ~30-40 at the rim and ~7 nm on the nanotube walls and 2. “$Pt_{15nm}TiO_2NT$” with bigger particles of ~40-80 at the rim and ~10 nm on the nanotube walls. A third sample containing a big particle of 40-60 nm at the bottom of the tubes and smaller particles of ~10-20 nm diameter distributed on the nanotube walls was ion-milled to remove particles sitting at the rim of the tubes in order to investigate if pore diffusion influences adsorption and reaction. All samples were tested in the CO oxidation reaction at total pressure up to 1 mbar and a ratio of 1:4 of $CO:O_2$ from 300 to at least 600 K and compared in terms of reactivity to a flat $TiO_2(110)$ rutile single crystal with a nanostructured Pt film (“$Pt_{5nm}TiO_2(110)$”) and the Pt(111) single crystal. All particle samples out-performed the $TiO_2(110)$-supported sample and the single crystal in terms of lower reaction temperatures $T_{1/2}$, which is defined as the temperature where the CO conversion has reached half of its maximum value. The order of the $T_{1/2}$ values was: $Pt_{5nm}TiO_2NT < Pt_{15nm}TiO_2NT < Pt_{ion\text{-}milled}TiO_2NT <$ Pt(111) $< Pt_{5nm}TiO_2(110)$. The higher reactivity for smaller particles was attributed to a higher step/defect density at the particle surface. Again, all samples showed MTLs at high temperatures explained by a depletion of CO in the surface-near region. For the ion-milled sample, it was found that interphase diffusion is the rate-limiting step for 1 – 0.01 mbar. In isothermal reaction experiments performed on the $Pt_{15nm}TiO_2NT$ sample, it was observed that no change in oxidation state occurs for the catalyst which is in a metallic state. The support is reduced 5±3 % for all measurements, that is, in UHV and under elevated pressures. Adsorbed CO was found on the platinum particles below (low conversion of ~ 4 %) and close to $T_{1/2}$ (conversion of up to 50 %) with coverages up to 0.5 ML. Above $T_{1/2}$, no adsorbed CO was found with conversion up to 60 %. Similar observations were made for the $Pt_{5nm}TiO_2NT$ sample; in general, the conversions were not stable and switched in between regimes of low and high conversions at $T_{1/2}$ and above. For the $Pt_{15nm}TiO_2NT$, the $Pt_{5nm}TiO_2NT$ and the $Pt_{5nm}TiO_2(110)$ sample, ageing was observed.

In Chapter 7, the intercalation of CO and O_2 under a closed graphene layer grown on Rh(111) was investigated by NAP-XPS. Intercalation of both gases was observed at 1 mbar at room temperature. In case of CO, the graphene layer was lifted upon intercalation as concluded from a ratio of the components C1 and C2, which are attributed to carbon atoms in closer vicinity and larger distance to the substrate, respectively. Both, O 1s and C 1s region showed clear evidence for the adsorption of CO on the Rh(111) substrate, exhibiting new features upon CO exposure. From TPD experiments, it was concluded, that the adsorption strength of CO on the substrate is influenced in such way, that desorption occurs at ~25 K lower temperature compared to the bare Rh(111) surface. Also for O_2 intercalation a lift-up of the graphene sheet was concluded from the NAP-XP spectra; here, a completely new feature at lower binding energies was observed in the C 1s spectrum. New signals at higher binding energies in the C 1s were traced to partial oxidation of the graphene layer forming epoxides and carbonyl groups, which partly desorbed in UHV within 17 h. The TPD experiments on the O_2 intercalation did so far not explain the mechanism of oxygen desorption, as only a very weak O_2 desorption signal was obtained up to 1015 K.

In the last experimental chapter of this thesis, the steam reforming of ethanol was in the focus of the investigations. A Co/CeO_2 model catalyst was chosen, where in a first step CeO_2 was deposited on a Cu(111) single crystal and in a subsequent step 0.7 ML Co were deposited on the prepared CeO_2 surface. The aim of this investigation was to examine the interaction of ethanol with Co/CeO_2 at pressures up to 0.1 mbar, which is part of a step taking place in the steam reforming of ethanol. First, the interaction of ethanol with the pure support was tested; it was found that at 300 K the ceria surface is successively reduced by ethanol adsorption with increasing ethanol pressure but stops at a certain point due to kinetic limitations. The reduction can be enhanced by heating the film and the primary reaction intermediate is ethoxide formed by dissociative adsorption of ethanol, forming OH groups from lattice O. For the Co/CeO_2 model catalyst some reduction of ceria and partly oxidation of the cobalt forming Co^{2+} was observed upon metal deposition. When exposing the model catalyst to 0.1 mbar ethanol with increasing temperatures up to 600 K, the Co^{2+} sites were completely reduced and also for the CeO_2 support a strong reduction was observed. At 600 K, coke formation occured, in contrast to the pure support, where no coke was observed.

In conclusion, this thesis offers fundamental insights into the impact of increased pressure and catalyst complexity even on well-understood processes under model conditions (i.e. in UHV) like oxygen adsorption on Pt(111) or the CO oxidation reaction on platinum. Due to the higher oxygen partial pressure, the chemical potential is changed in such way that completely new phases are found on the Pt(111) single crystal, including amorphous surface oxides. CO oxidation reaction experiments revealed that these oxides found under equilibrium conditions and pure O_2 atmosphere do not necessarily exist in gas mixtures and under reaction conditions. This underlines the importance of *in situ* investigations and the need to probe even well-understood, “simple” reactions at elevated pressures. Higher reactivity was found for Pt particles as compared to a nanostructured film and the Pt(111) single crystal, showing the importance of using *real* catalysts. New effects like mass transfer limitations due to very high conversions and also heat transfer limitations resulting in temporary sample heat-up were observed to highly influence the reaction, pointing out the complexity of reactions at high pressures.

Taking into consideration these findings, in a last step, “real” catalysts, as for instance found in catalytic converters of cars, should be tested in the CO oxidation reaction. These may consist out of porous supports (e.g. Al_2O_3) and bimetallic particles (e.g. RhPt) [84] and are not as highly ordered as the model systems used in this thesis. As now the influence of higher pressure and controlled introduction of catalyst complexity on the reaction is understood, this comprehension may help to interpret results obtained for real catalysts. Following the investigations of the CO oxidation as a typical test reaction, also more complex reactions should be faced. In this respect, the effect of an ethanol-water mixture should be investigated on the Co/CeO_2 model catalyst, hence the steam reforming reaction itself. Complementarily, imaging techniques such as TEM (Transmission Electron Microscopy) and high-pressure STM (Scanning Tunneling Microscopy), which are able to capture dynamic effects like refacetting of particles and SMSI, could help to resolve fast processes that cannot be observed using XPS. Additionally, these techniques are able to visualize different areas of the samples and hence differentiate whether the phases found in XPS are of homogeneous nature or if different phases coexist, as this is not evident from XPS.

10. Zusammenfassung und Ausblick

Im Mittelpunkt dieser Arbeit steht der Einfluss von erhöhtem Druck und erhöhter Komplexität von Katalysatoren auf klassische Modellsysteme, die in der „Surface Science“ (Oberflächenwissenschaften) untersucht werden. Die enormen Unterschiede in Druck und Katalysatorkomplexität in der industriellen Katalyse und der Surface Science werden als „Pressure Gap“ und „Materials Gap“ („Druck- und Materiallücke“) bezeichnet. Während viele Katalysatoren sorgfältig unter definierten Bedingungen im UHV untersucht wurden, stellen der Transfer und die Extrapolation der erhaltenen Ergebnisse auf die Bedingungen der angewandten heterogenen Katalyse in vielen Fällen immer noch eine Herausforderung dar. In dieser Arbeit wurde NAP-XPS genutzt, um diese Lücke zu schließen und es wurde, im Gegensatz zu konventionellen XPS-Arbeiten, bei Drücken bis 1 mbar gemessen. Gleichzeitig wurde ein Massenspektrometer verwendet, um während Reaktionsexperimenten die Gasphasenzusammensetzung über der Probe zu messen.

Zunächst wurde ein Einkristall mit einer sehr definierten Oberfläche untersucht, bevor die Untersuchungen auf Katalysatorpartikel, welche auf flachen Substraten, sowie auf Nanoröhren aufgebracht wurden, erweitert wurden. Dadurch wurde die Komplexität der Katalysatoren sukzessive erhöht, um industrielle Katalysatoren nachzuahmen, die oft aus Partikeln auf porösen Substraten bestehen.

In Kapitel 4 dieser Arbeit wurde das Wachstum von Platinoxiden bei 1 mbar O_2 und Temperaturen zwischen 300 und 700 K auf einem Pt(111) Einkristall untersucht. Ziel war es, den Effekt von erhöhtem Sauerstoffpartialdruck auf eine klar definierte Oberfläche zu verstehen, bevor komplexere Systeme betrachtet werden sollten. Daher wurde untersucht, ob und in welchem Zeitrahmen Oxide wachsen. Es wurden unterschiedliche Oxidphasen gefunden, wobei die höchsten Bedeckungen von 3,7, 1,9 und 3,8 ML bei 300, 400 und 500 K und geringere Bedeckungen von 1,5, 0,5 und 0,25 ML bei 600, 650 und 700 K beobachtet wurden. Bemerkenswerterweise waren Wachstumszeiten von mehr als 4 h nötig, um eine Sättigung im O 1s Signal zu beobachten. Dies könnte erklären, dass in der Literatur [49, 106] kein Oxidwachstum bei 300 K unter ähnlichen Druckbedingungen gefunden wurde. Die experimentellen Ergebnisse wurden mit ReaxFF GCMC Simulationen kombiniert, welche in der Arbeitsgruppe von Prof. Dr. Timo Jacob des Instituts für Elektrochemie der Universität Ulm durchgeführt wurden. Es wurden fünf stabile Oberflächenphasen mit steigendem chemischen Potential von Sauerstoff (also als Funktion sinkender Temperatur bei 1 mbar O_2) in den Simulationen gefunden: ein sauberer Pt(111) Slab (800 K), in der p(2x2) Überstruktur adsorbierter, atomarer Sauerstoff (700 K), amorphe Oberflächenoxide (1,13 und 3,44 ML bei

650, 600 und 500 K) und α-PtO_2 (300 und 400 K). Die experimentellen Ergebnisse konnten durch zeitabhängige Simulationen korrekt beschrieben werden und zusätzlich konnte die amorphe Struktur der Oberflächenoxide aufgeklärt werden. Abweichungen in den absoluten Bedeckungen dieser amorphen Oxide wurden auf nicht ausreichende Wachstumszeiten im Experiment und kinetische Limitierung des Wachstums bei 300 und 400 K zurückgeführt. Generell waren diese Oxide im UHV bei 400 K und Temperaturen darüber nicht stabil, was durch die Theorie bestätigt wurde.

Nachfolgend sollte untersucht werden, ob diese Platinoxide auch unter den Reaktionsbedingungen der CO Oxidation existieren und aktiv an dieser Reaktion teilnehmen, folglich ob metallisches oder oxidiertes Platin der aktive Katalysator ist. Hierfür wurde diese Reaktion bei Gesamtdrücken bis 1.1 mbar und verschiedenen Gasgemischen (CO:O_2 = 2:1, 1:1, 1:4, 1:10) in isothermen und temperaturprogrammierten Messungen im Temperaturbereich von 300 bis 1100 K untersucht. Diese Untersuchung greift die Diskussion innerhalb der wissenschaftlichen Welt auf, ob die Reaktion (wie im UHV) einem Langmuir-Hinshelwood Mechanismus folgt oder ob die Reaktion bei erhöhten Drücken nach einem Mars-van-Krevelen Mechanismus verläuft.[17, 44] Es wurden keine Platinoxide unter Reaktionsbedingungen beobachtet, sondern der Katalysator war metallisch. Bei hohen Temperaturen war die Platinoberfläche adsorbatfrei und die Reaktion wurde durch den Stofftransport in der Gasphase limitiert (mass-transfer limited („MTL“) Regime). Im Einzelnen wurden drei verschiedene Regimes beobachtet: (I) CO inhibiert, mit vernachlässigbarem Umsatz, (II) teils CO bedeckt, mit moderater Aktivität und (III) adsorbatfrei, mit hoher Aktivität (MTL Regime). Beim Vergleich der Reaktion in den verschiedenen Mischungen wurde gefunden, dass das Eintreten der Reaktion vom O_2 Partialdruck innerhalb der Mischung abhängt und die Reaktion bei höherem O_2 Gehalt bei niedrigerer Temperatur eintritt. Dieses Verhalten kann mit einer höheren Adsorptionsrate von Sauerstoff bei höherem Sauerstoffpartialdruck erklärt werden, da der Katalysator bei 300 K mit CO saturiert ist, und die CO Adsorption und Sauerstoffadsorption konkurrierende Prozesse sind. Bei konstantem Gesamtdruck wird durch eine Erhöhung des Sauerstoffpartialdrucks automatisch der CO Partialdruck gesenkt, was die CO Desorption bei niedrigeren Temperaturen, und somit auch eine frühere Reaktion, ermöglicht.

Weiterführend wurde die Komplexität des Katalysators erhöht, um die Vergleichbarkeit mit industriellen Katalysatoren zu steigern. Anstelle von einem flachen Einkristall wurde die CO Oxidationsreaktion auf Platinpartikeln, welche auf TiO_2 Nanoröhren der Länge 200 nm und eines Durchmessers von 80 nm aufgebracht wurden, durchgeführt und dadurch poröse Systeme, die oft in der Industrie verwendet werden, nachgeahmt. Im Speziellen wurden drei verschiedene Systeme untersucht, welche mit Platinpartikeln verschiedener Größen dekoriert wurden: 1. „$Pt_{5nm}TiO_2$“ mit kleineren Partikeln von ~30-40 nm auf den Rändern und ~7 nm Durchmesser an den Wänden der Nanoröhren, 2. „$Pt_{15nm}TiO_2$“ mit größeren Partikeln von ~40-80 nm auf den Rändern und ~10 nm Durchmesser an den Wänden der Nanoröhren und 3. „$Pt_{ion\text{-}milled}TiO_2NT$“ mit einem großen Partikel von ~40-60 nm am unteren Ende der Nanoröhre und kleineren Partikel von 10-20 nm an den Wänden der Röhren. Die $Pt_{ion\text{-}milled}TiO_2NT$-Probe wurde mit Ionen beschossen, um die Partikel am Rand der Röhre zu entfernen und dadurch Untersuchungen zur Beeinflussung der Adsorption und Reaktion durch Porendiffusion zu erlauben. Alle Proben wurden in der CO Oxidation bei Totaldrücken bis 1 mbar getestet und in Bezug auf Reaktivität zusätzlich mit einem flachen $TiO_2(110)$ Rutil Einkristall mit einem nanostrukturierten Pt Film („$Pt_{5nm}TiO_2(110)$“) und dem Pt(111) Einkristall verglichen. Alle Partikelproben übertrafen die $Pt_{5nm}TiO_2(110)$-Probe und den Einkristall in ihrer Reaktivität, was sich in der Reihenfolge der Reaktionstemperaturen $T_{1/2}$, widerspiegelt. Hierbei ist $T_{1/2}$ als die Temperatur definiert, bei welcher der Umsatz die Hälfte seines Maximalwertes erreicht hat. Die Reihenfolge der $T_{1/2}$–Werte war: $Pt_{5nm}TiO_2NT < Pt_{15nm}TiO_2NT < Pt_{ion\text{-}milled}TiO_2NT < Pt(111) < Pt_{5nm}TiO_2(110)$. Die beobachtete höhere Reaktivität der kleineren Partikel wurde auf eine höhere Stufen-/ Defektdichte auf der Partikeloberfläche zurückgeführt. Auch in dieser Untersuchung wiesen alle Proben MTLs bei höheren Temperaturen auf, was durch eine Verarmung von CO in der oberflächennahen Umgebung erklärt wird. Es wurde gezeigt, dass im Fall der $Pt_{ion\text{-}milled}TiO_2NT$-Probe Interphasendiffusion der geschwindigkeitsbestimmende Schritt für 1 – 0.01 mbar ist. In isothermen Reaktionsexperimenten bei drei verschiedenen Temperaturen (unterhalb, nahe und oberhalb von $T_{1/2}$) wurde keine Änderung in der Oxidationsstufe des Katalysators beobachtet, welcher in allen Fällen metallisch war. Das Trägermaterial war in allen Messungen, d.h. im UHV sowohl als auch bei erhöhtem Druck, um 5±3 % reduziert. Unterhalb von $T_{1/2}$ (geringer Umsatz von ~4 %) und nahe an $T_{1/2}$ (Umsätze bis zu 50 %) wurde adsorbiertes CO mit Bedeckungen bis zu 0,5 ML auf den Platinpartikeln gefunden. Oberhalb von $T_{1/2}$ wurde kein adsorbiertes CO gefunden und der Umsatz betrug bis zu 60 %. Ähnliche Beobachtungen wurden für die $Pt_{5nm}TiO_2NT$ Probe gemacht, wobei generell für beide Proben die Umsätze nicht stabil waren und zwischen Regionen geringen und hohen Umsatzes nahe an $T_{1/2}$ und darüber wechselten. Für die $Pt_{15nm}TiO_2NT$-, die $Pt_{5nm}TiO_2NT$- und die $Pt_{15nm}TiO_2(110)$-Proben wurden Alterungsprozesse beobachtet, welche sich in Änderungen von $T_{1/2}$ und Umsätzen zeigten.

In Kapital 7 wurde die Interkalation von CO und O_2 unter einem geschlossenen Graphenfilm, welcher auf einem Rh(111)-Substrat gewachsen wurde, mit NAP-XPS untersucht. Für beide wurde die Interkalation bei 1 mbar und Raumtemperatur beobachtet. Im Fall von CO wurde der Graphenfilm von der Oberfläche „angehoben“, was aus dem Verhältnis von C1 und C2 Komponente des C 1s Spektrums abgeleitet wurde. Hierbei wird die C1

Komponente auf Kohlenstoffatome, welche näher an die Oberfläche gebunden sind, und die C2 Komponente auf Kohlenstoffatome in weiterem Abstand zur Probe, zurückgeführt. Im C 1s und auch im O 1s Spektrum traten neue Signale auf, die auf die Adsorption auf dem Rh(111)-Substrat zurückzuführen waren. Aus TPD Experimenten wurde geschlossen, dass die Adsorptionsstärke von CO auf Rh(111) durch die darüber liegende Graphenschicht geschwächt wird, was sich in einer Verschiebung der Desorptionstemperatur um ~25 K zu niedrigeren Temperaturen, verglichen mit der reinen Rh(111) Oberfläche, zeigte. Auch für die O_2 Interkalation wurde aus den NAP-XPS Spektren gefolgert, dass die Graphenschicht von dem Substrat „angehoben“ wird; der Effekt war hier jedoch noch deutlicher, was aus einem neuen Signal bei niedrigeren Bindungsenergien im C 1s geschlossen wurde. Zwei zusätzliche Signale bei höheren Bindungsenergien wurden mit einer partiellen Oxidation des Films unter Bildung von Epoxid- und Carbonylgruppen erklärt, welche teilweise innerhalb von ~17 h im UHV desorbierten. TPD Experimente der O_2 Interkalation konnten bisher nicht den Mechanismus der Sauerstoffdesorption klären, da ein nur sehr schwaches O_2 Signal bei Temperaturen bis 1015 K detektiert wurde.

Im letzten Teil dieser Arbeit wurde die Dampfreformierung von Ethanol in den Fokus der Untersuchungen gerückt. Als Katalysator-Trägersystem wurde ein Co/CeO_2 Modellkatalysator gewählt, wobei in einem ersten Schritt CeO_2 auf einem Cu(111) Einkristall abgeschieden wurde und in einem Folgeschritt 0.7 ML Co auf die präparierte CeO_2 Oberfläche aufgedampft wurden. Ziel dieser Untersuchung war es, die Wechselwirkung von Ethanol mit Co/CeO_2 bei Drücken bis 0.1 mbar zu erforschen, welche ein Teil des ersten Schrittes der Dampfreformierung von Ethanol ist. Zunächst wurde die Wechselwirkung von Ethanol mit dem reinen Träger getestet, wobei die CeO_2 Oberfläche bei 300 K mit steigendem Ethanoldruck nach und nach durch Ethanoladsorption reduziert wurde, die Reduktion jedoch an einem bestimmten Punkt durch kinetische Limitierungen stoppte. Der Reduktionsgrad konnte durch Heizen des Films weiter erhöht werden. Das Hauptreaktionsintermediat war Ethoxid, das durch dissoziative Adsorption von Ethanol, welche die Bildung von OH Gruppen aus Gittersauerstoff beinhaltet, gebildet wurde. Durch das Aufdampfen von Co wurde eine Reduktion des Ceroxids und partielle Oxidation von Co zu Co^{2+} für den Co/CeO_2 Modellkatalysator beobachtet. Durch Exposition des Modellkatalysators mit 0.1 mbar Ethanol bei steigenden Temperaturen bis zu 600 K wurden die Co^{2+} Plätze vollständig reduziert und auch für den CeO_2-Träger wurde eine starke Reduktion beobachtet. Die starke Reduktion bei 600 K wurde, im Gegensatz zu dem reinen Ceroxidsystem, von Verkokung begleitet.

Zusammenfassend bietet diese Arbeit fundamentale Erkenntnisse zu den Auswirkungen von erhöhtem Druck und Katalysatorkomplexität selbst auf im UHV vollständig verstandene Prozesse wie Adsorption von Sauerstoff auf Pt(111) oder der CO Oxidation auf Platin. Es wurde gezeigt, dass durch den erhöhten Sauerstoffpartialdruck das chemische Potential so verändert wird, dass völlig neue Phasen auf dem Pt(111) Einkristall gefunden werden, darunter amorphe Oberflächenoxide. CO Oxidationsexperimente zeigten, dass diese Oxide, welche unter Gleichgewichtsbedingungen und reiner O_2 Atmosphäre gefunden wurden, nicht zwingend in Gasmischungen und unter Reaktionsbedingungen existieren. Dies unterstreicht die Bedeutung von *in situ* Untersuchungen und die Notwendigkeit selbst vollständig verstandene, „einfache“ Reaktionen bei hohem Druck zu erforschen. Des Weiteren wurde eine erhöhte Reaktivität für Pt Partikel, verglichen mit einem nanostruktiertem Film und dem flachen Pt(111) Einkristall, gefunden, was wiederum die Wichtigkeit betont, *reelle* Katalysatoren anstatt von Modellkatalysatorproben zu untersuchen. Neue Effekte wie Limitierungen des Stofftransports aufgrund sehr hoher Umsätze und auch Wärmetransferlimitierungen, welche sich in temporärem Aufheizen der Probe zeigten, wurden beobachtet, was die Komplexität von Reaktionen bei hohen Drücken aufzeigt. Weiterführend sollten, unter Berücksichtigung dieser Ergebnisse, *reelle* Katalysatoren, wie sie etwa im Abgaskatalysator der Automobilindustrie gefunden werden, in der CO Oxidation untersucht werden. Diese können aus porösen Trägern (z.B. Al_2O_3) und bimetallischen Partikeln (z.B. RhPt)[84] bestehen und weisen eine geringere Ordnung auf, als die in dieser Arbeit betrachteten Modellkatalysatoren. Da nun die Auswirkungen von erhöhtem Druck und kontrollierter Einführung von Katalysatorkomplexität auf die Reaktion verstanden sind, kann dieses Verständnis genutzt werden, um Ergebnisse, welche für *reelle* Katalysatoren erhalten werden, nachzuvollziehen. Den Untersuchungen der CO Oxidation als eine typische Testreaktion folgend, sollte das für die simpleren Systeme gesammelte Wissen auch auf komplexere Reaktionen angewandt werden. In dieser Hinsicht sollte beispielsweise der Effekt eines Ethanol-Wasser-Gemisches auf den Co/CeO_2 Katalysator untersucht werden, somit die eigentliche Dampfreformierung selbst. Ergänzend könnten bildgebende Techniken wie TEM (Transmissionselektronenmikroskopie) und Hochdruck STM (Rastertunnelmikroskopie), welche im Stande sind, dynamische Prozesse, wie Refacettierung von Partikeln und SMSI, zu erfassen, helfen, schnelle Prozesse, welche nicht mittels XPS untersucht werden können, aufzulösen. Zusätzlich ermöglichen es diese Techniken, verschiedene Regionen der Probe zu visualisieren und können daher unterscheiden, ob die unterschiedlichen Phasen, die im XPS gefunden werden, von homogener Natur sind oder ob verschiedene Phasen koexistieren, was aus XPS nicht ersichtlich ist.

11. Appendix

11.1 Appendix to Chapter 4

11.1.1 Details on the ReaxFF GCMC simulations

The GCMC simulations make use of the Pt/O force field developed recently [254] and the hybrid grand canonical Monte Carlo/molecular dynamics (GC-MC/MD) method implemented in ReaxFF [255]. By definition (within the $TV\mu_{O2}N_{Pt}$ ensemble) the system temperature (T), volume (V), oxygen chemical potential (μ_{O2}) and number of Pt atoms (N_{Pt}) are fixed throughout the simulation. The following Monte Carlo (MC) trial moves are available during the simulation: (1) addition of oxygen, (2) deletion of oxygen, and (3) translation of oxygen. MC moves are executed on an off-grid basis, as there are no pre-defined oxygen-insertion sites. Prior to applying acceptance criteria, the GC-MC/MD method algorithm performs a conjugate gradient (CG) structural optimization step allowing the Pt lattice to restructure upon oxygen addition. The CG relaxation is required to reach equilibrium, as insertion moves without structural relaxation of the Pt lattice would result in high system energies leading to high MC rejection rates. The CG relaxation step employed here uses a convergence criterion of 0.5 kcal mol^{-1} Å^{-1} for the root mean square of the gradient of the energy, which is sufficient to allow the Pt lattice to locally restructure to accommodate inserted O atoms as oxide phases are formed. After applying the CG relaxation of forces, the resulting system energy is applied in the usual Metropolis acceptance criteria [256, 257]:

$$P_{insert}^{accept} = min\left\{1, \frac{V}{\lambda^3(\mathrm{N}+1)} \exp[-\beta(E_2 - E_1 - \mu_O)]\right\} \qquad \text{(XVI)}$$

$$P_{delete}^{accept} = min\left\{1, \frac{N\,\lambda^3}{V} \exp[-\beta(E_2 - E_1 + \mu_O)]\right\} \qquad \text{(XVII)}$$

$$P_{displace}^{accept} = min\,\{1, \exp[-\beta(E_2 - E_1)]\} \qquad \text{(XVIII)}$$

where N is the number of oxygen atoms, λ is the thermal de Broglie wavelength of oxygen, β is defined by temperature and the Boltzmann constant: $\beta = (k_B\,T^{-1})$, E_1 and E_2 are the system energy before and after the MC move, and μ_O is the oxygen chemical potential. The chemical potential of oxygen is calculated from standard statistical mechanical formulations:

$$\mu_O(\mathrm{T,P}) = \frac{1}{2}\left[\mu_{O2}(\mathrm{T}, \mathrm{p}^0) + \mathrm{k_B}Tln\left(\frac{p}{\mathrm{p}^0}\right) - (E_\mathrm{d} + E_\mathrm{zpe})\right] \qquad \text{(XIX)}$$

where $\mu_{O2}(T, p^0)$ is the chemical potential of O_2 at T and p^0 available in standard thermodynamic tables [258], E_d is the bond dissociation energy of O_2 and E_{ZPE} the zero-point-energy correction. Further details regarding the implementation of the GC-MC/MD method for ReaxFF are available in previous publications [255, 259, 260].

11.1.2 GCMC simulations

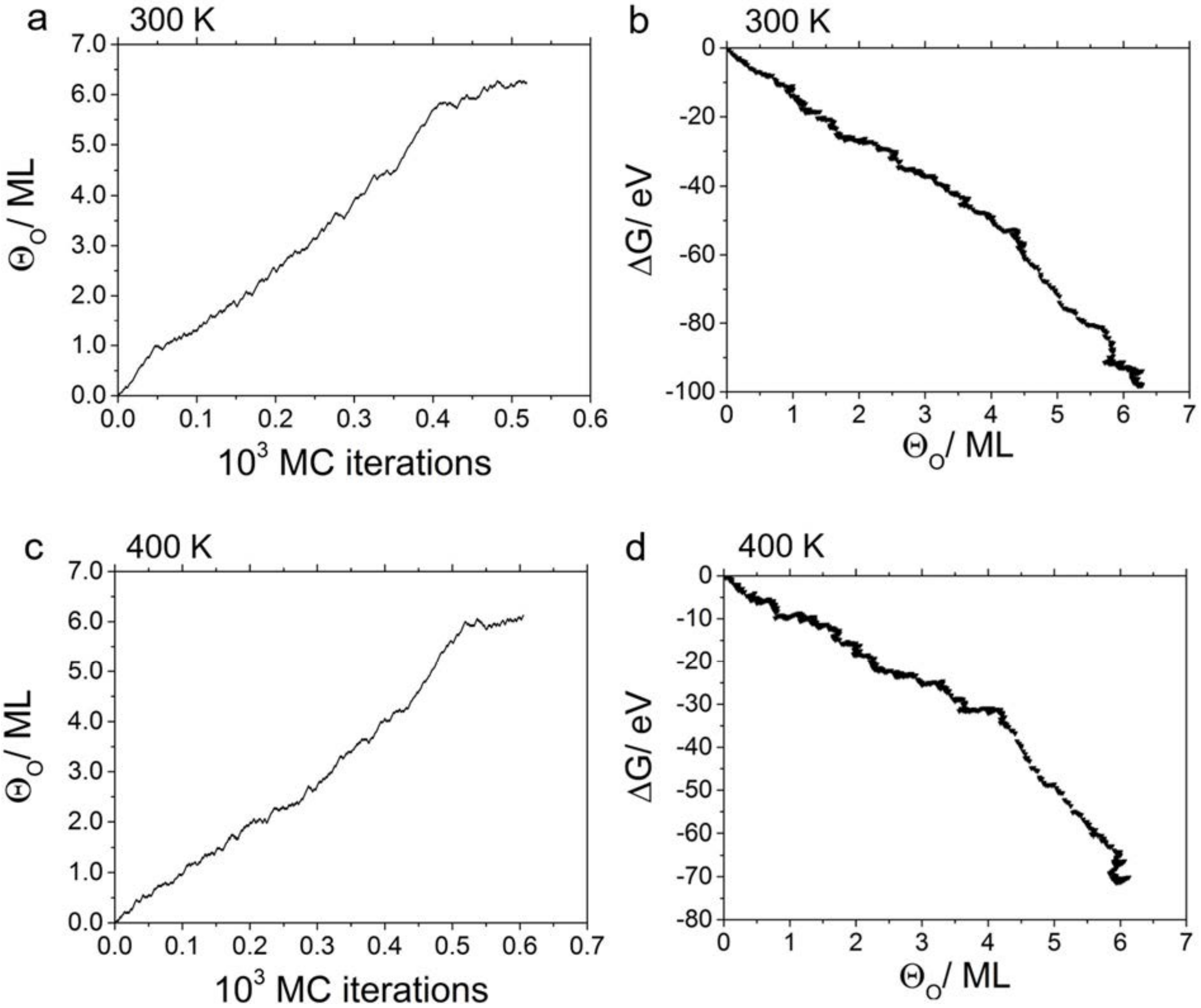

Figure 11.1.1: Results from GCMC simulations at 300 and 400 K and an oxygen partial pressure of 1 mbar, showing in (a) and (c) the oxygen surface coverage as function of MC iterations and in (b) and (d) the free energies of formation as functions of the oxygen surface coverage with respect to gas phase O_2 and a clean Pt(111) surface. Both types of plots show the constant driving force towards bulk oxidation. Furthermore all structures in (b) and (d) have negative free energies of formation showing that the addition of oxygen is always energetically favourable. This behaviour is not surprising, since the employed temperatures at an oxygen partial pressure of 1 mbar correspond to oxygen chemical potentials where the α-PtO_2 bulk oxide is the thermodynamically most stable phase.

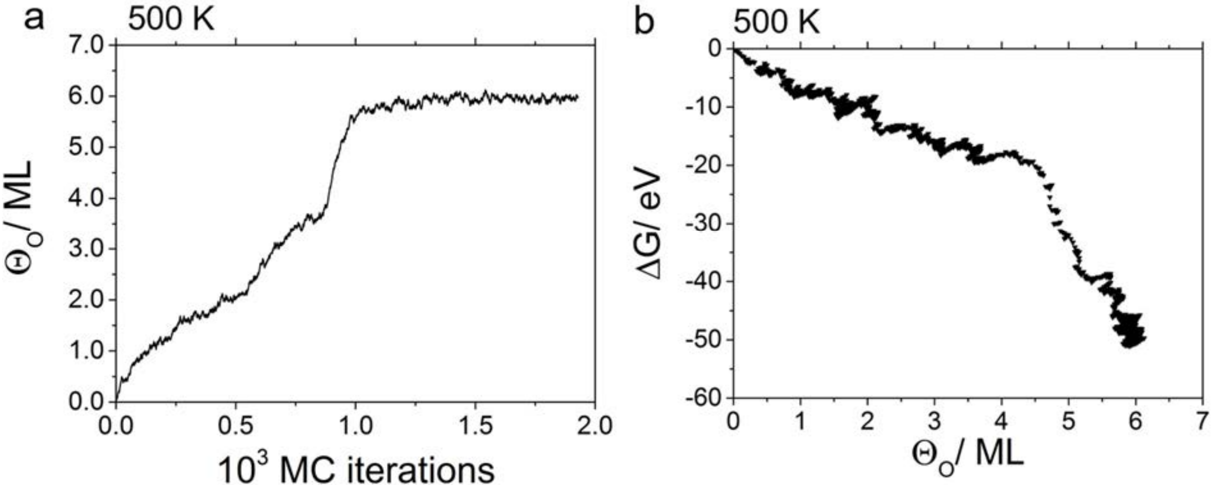

Figure 11.1.2: Results from GCMC simulations at 500 K and an oxygen partial pressure of 1 mbar, showing in (a) the oxygen surface coverage as function of MC iterations and in (b) the free energies of formation as functions of the oxygen surface coverage with respect to gas phase O_2 and a clean Pt(111) surface. All structures in (b) have negative free energies of formation.

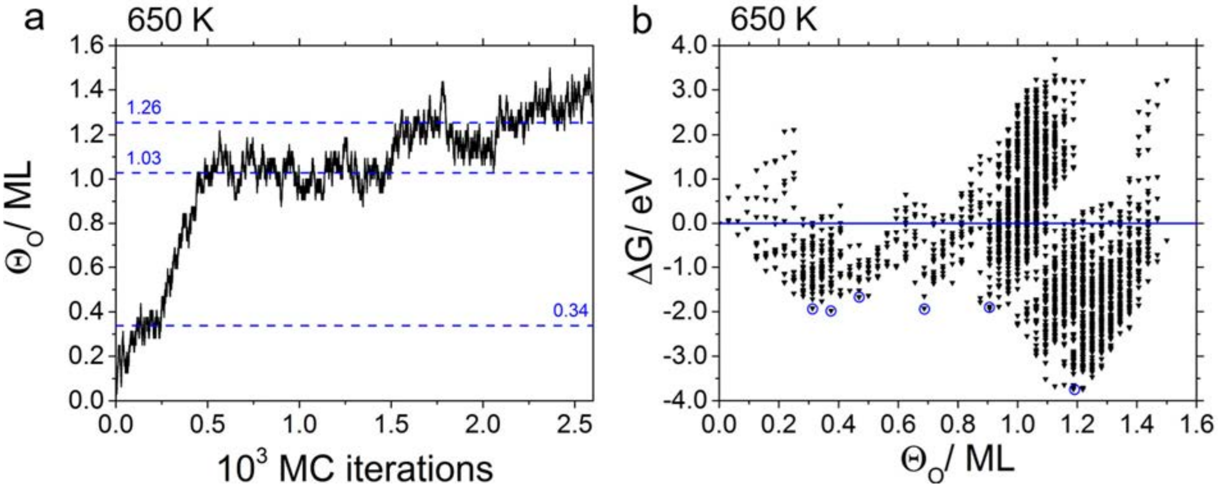

Figure 11.1.3: Results from GCMC simulations at 650 K and an oxygen partial pressure of 1 mbar, showing (a) the oxygen surface coverage as function of MC iterations and (b) the free energies of formation as functions of the oxygen surface coverage with respect to gas phase O_2 and a clean Pt(111) surface. The dashed blue lines in (a) show possible saturation coverages. The black line in (b) separates structures with negative free energies of formation from structures with positive free energies of formation. The blue circles highlight the structures used to draw the phase diagram in Fig. 4.7.

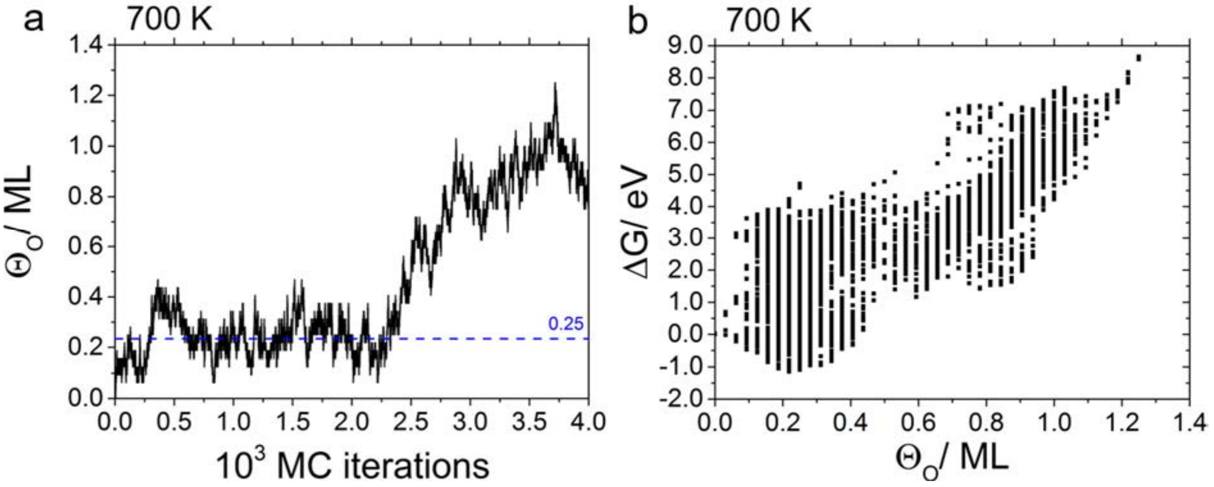

Figure 11.1.4: Results from GCMC simulations at 700 K and an oxygen partial pressure of 1 mbar, showing (a) the oxygen surface coverage as function of MC iterations and (b) the free energies of formation as functions of the oxygen surface coverage with respect to gas phase O_2 and a clean Pt(111) surface. The dashed blue line in (a) shows a possible saturation coverage of ~0.25 ML. The black line in (b) separates structures with negative free energies of formation from structures with positive free energies of formation (0 ML < Θ_O < 0.5 ML).

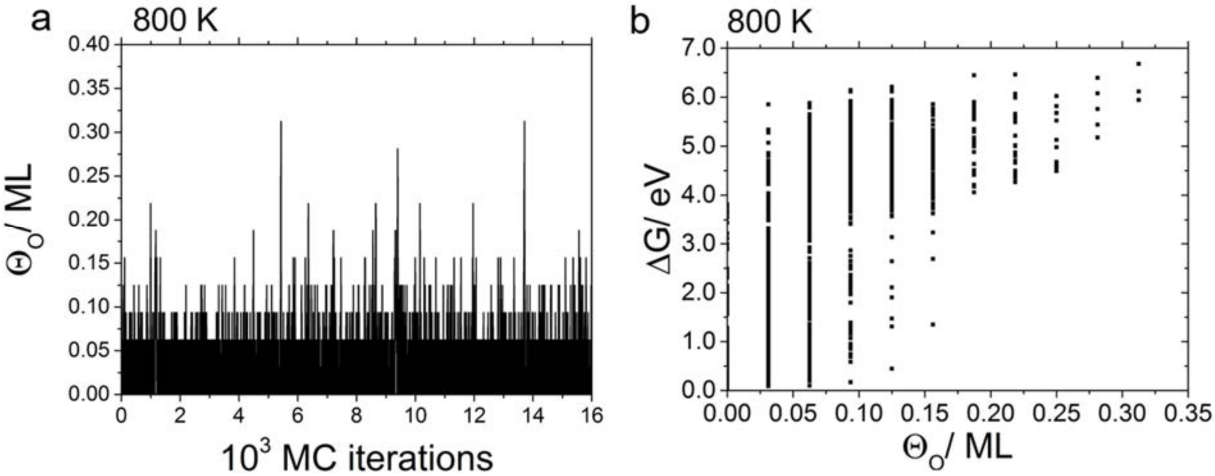

Figure 11.1.5: Results from GCMC simulations at 800 K and an oxygen partial pressure of 1 mbar, showing (a) the oxygen surface coverage as function of MC iterations and (b) the free energies of formation as functions of the oxygen surface coverage with respect to gas phase O_2 and a clean Pt(111) surface. Oxygen surface coverage fluctuates around the clean surface (a). All structures in (b) have positive free energies of formation.

11.2 Appendix to Chapter 5

11.2.1 Fitting procedure

A linear background was subtracted from all spectra prior to fitting. For the O 1s surface components a symmetric function (product of a Gaussian and Lorentzian) was used, which reproduces the data well. The gas phase peaks in the presence of the sample were fitted with line shapes that were determined from reference measurements of the respective gas, obtained in absence of a sample. The O_2 gas phase was fitted with an asymmetric line shape, whereas the CO and CO_2 gas phase signals were fitted with symmetric functions. For details of the fitting parameters for the respective signals see Table 8.2.1.

Table 11.2.1: Binding energies, full width at half maximum and line shapes of the fits for the different O 1s signals.

component	Binding Energy/ eV	FWHM/ eV	line shape
O_2 gas phase	537.5	1.5	asymmetric pseudo-Voigt
CO gas phase	536.6	1.3	symmetric pseudo-Voigt
CO_2 gas phase	535.7	1.7	symmetric pseudo-Voigt
CO on-top	532.8	1.5	symmetric pseudo-Voigt
CO bridge	531.1	1.5	symmetric pseudo-Voigt
SiO_x	531.7	-	-

11.3 Appendix to Chapter 6

11.3.1 LEED picture of the 1x1 reconstruction of TiO_2(110)

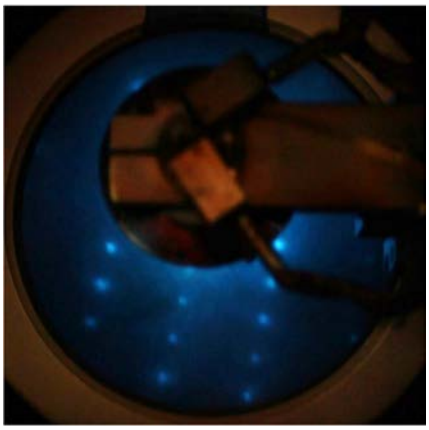

Figure 11.3.1: LEED picture of the 1x1 reconstruction of the TiO_2(110) surface.

11.3.2 Changes in the film for the $Pt_{5nm}TiO_2$(110) sample before and after the reaction ramp

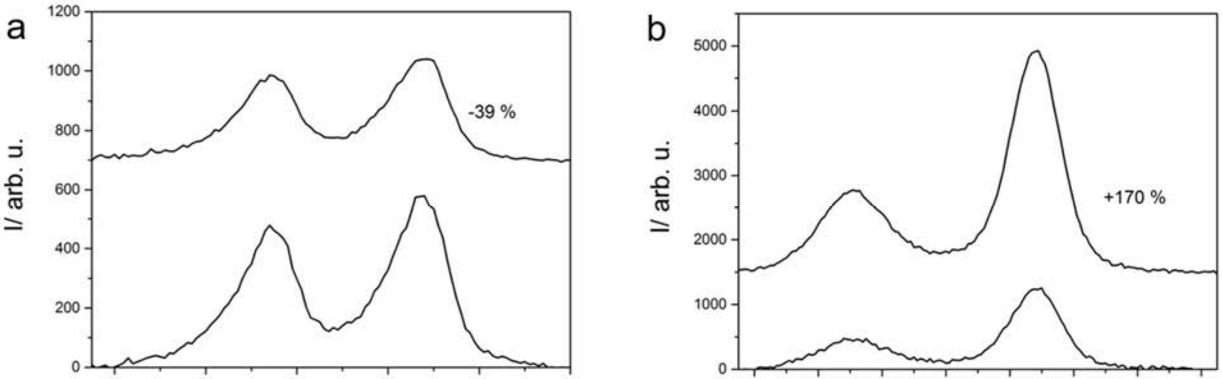

Figure 11.3.2: (a) Pt 4f and (b) Ti 2p core level spectra before (lower) and after (upper) the temperature-programmed reaction experiment shown in Figure 6.4 for the $Pt_{5nm}TiO_2NT$ sample.

Figure 11.3.2a and b shows the Pt 4f and Ti 2p core level spectra taken before (lower) and after (upper) the reaction experiment shown in Figure 6.4 for the $Pt_{5nm}TiO_2$NT sample. Clearly a decrease in signal intensity in the Pt 4f core level and an increase in the Ti 2p core level is observed. This effect is attributed to the SMSI effect and/or particle sintering.

11.3.3 SE micrographs of the $Pt_{5nm}TiO_2NT$ and the $Pt_{5nm}TiO_2(110)$ samples after use in reaction experiments

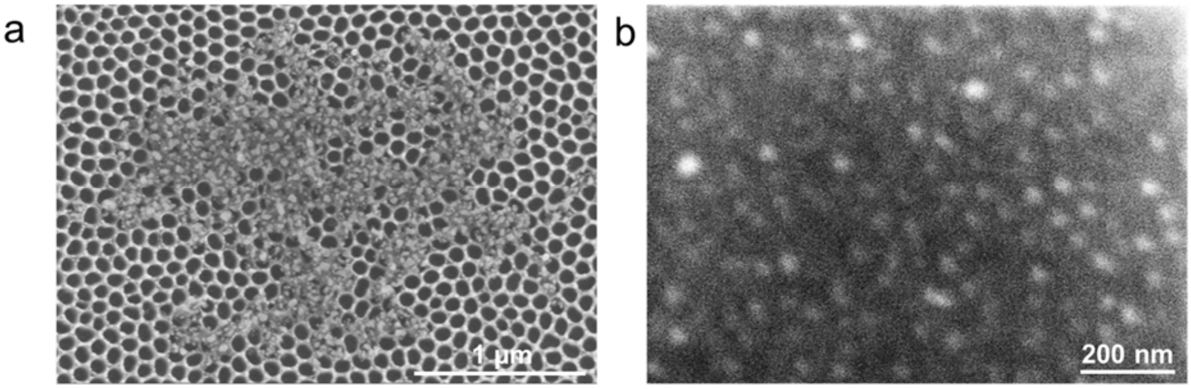

Figure 11.3.3: (a) SE micrograph of the $Pt_{5nm}TiO_2NT$ *and (b) the* $Pt_{5nm}TiO_2(110)$ *sample after the reaction experiments.*

11.4 Appendix to Chapter 7

11.4.1 Unprocessed TPD spectra for CO intercalation

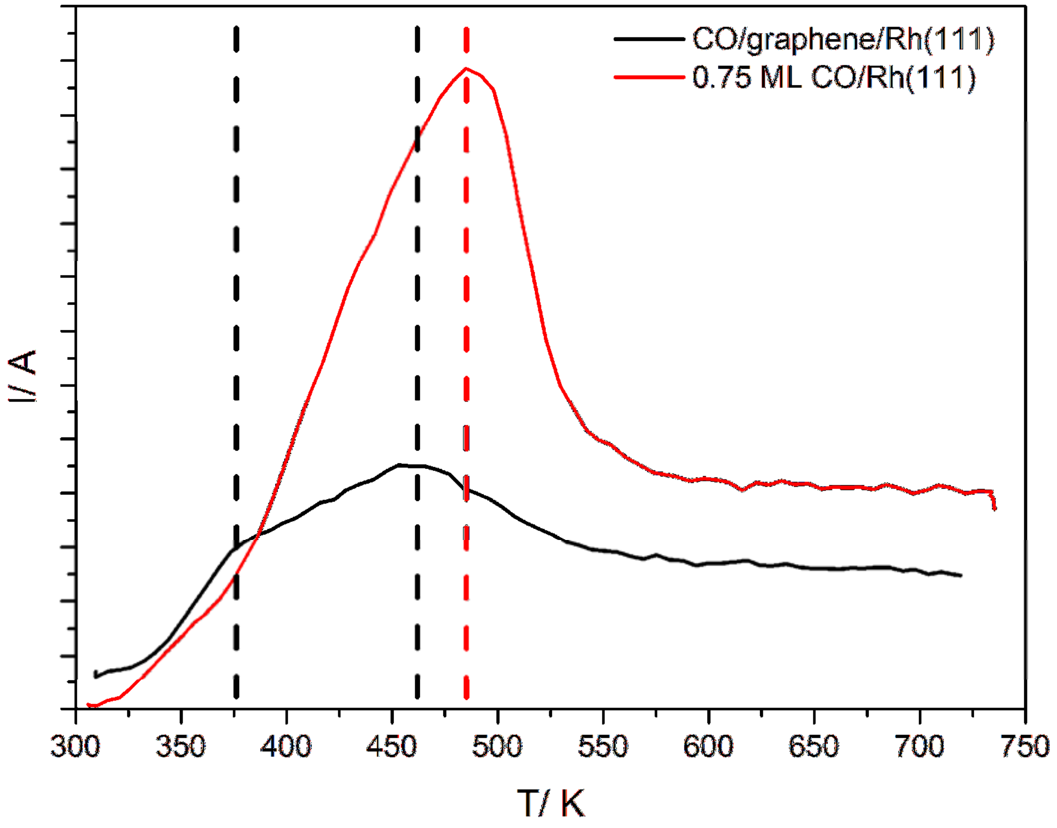

Figure 11.4.1: Unprocessed TPD spectra of CO intercalated between graphene/Rh(111) (black line) and the (2x2)-3CO superstructure on Rh(111).

12. Literature

1. Robertson, A.J.B., Platin. Met. Rev., **1975**, *19*, 64.
2. Hagen, J., *Industrial Catalysis*, WILEY-VCH Verlag GmbH & Co. KGaA (2006).
3. Lindström, B., Pettersson, L.J., CATTECH, **2003**, *7*, 130.
4. Ertl, G., Knözinger, H., Weitkamp, J., *Handbook of Heterogeneous Catalysis*, VCH Verlagsgesellschaft mbH (1997).
5. Ertl, G., Angew. Chem. Int. Ed. Engl., **2008**, *47*, 3524.
6. Ertl, G., Science, **1991**, *254*, 6.
7. Zambelli, T., Barth, J.V., Wintterlin, J., Ertl, G., Nature, **1997**, *390*, 495.
8. Campbell, C.T., Ertl, G., Kuipers, H., Segner, J., J. Chem. Phys., **1980**, *73*, 5862.
9. King, D.A., Top. Catal., **1994**, *1*, 315.
10. Woodruff, D.P., Delchar, T.A., *Modern Techniques of Surface Science*, Cambridge University Press (1994).
11. Papp, C., Steinrück, H.-P., Surf. Sci. Rep., **2013**, *68*, 446.
12. Kolasinski, K.W., *Surface Science: Foundation of Catalysis and Nanoscience*, John Wiley & Sons, Ltd (2012).
13. Hüfner, S., *Photoelectron Spectroscopy: Principles and Applications*, Springer (2003).
14. Imbihl, R., Behm, R.J., Schlögl, R., Phys. Chem. Chem. Phys., **2007**, *9*, 3459.
15. Bron, M., Teschner, D., Knopgericke, A., Steinhauer, B., Scheybal, A., Hävecker, M., Wang, D., Fodisch, R., Honicke, D., Wootsch, A., J. Catal., **2005**, *234*, 37.
16. Brodkey, R.S., Hershey, H.C., *Transport Phenomena: A Unified Approach*, Brodkey Publishing (1988).
17. Gao, F., Wang, Y., Cai, Y., Goodman, D.W., J. Phys. Chem. C., **2009**, *113*, 174.
18. Matera, S., Reuter, K., Catal. Lett., **2009**, *133*, 156.
19. Over, H., Kim, Y.D., Seitsonen, A.P., Wendt, S., Lundgren, E., Schmid, M., Varga, P., Morgante, A., Ertl, G., Science, **2000**, *287*, 3.
20. Gao, F., Wang, Y., Goodman, D.W., J. Phys. Chem. C., **2010**, *114*, 6874.
21. Hendriksen, B.L.M., Frenken, J.W.M., Phys. Rev. Lett., **2002**, *89*, 46101.
22. Bandlow, J., Kaghazchi, P., Jacob, T., Papp, C., Tränkenschuh, B., Streber, R., Lorenz, M.P.A., Fuhrmann, T., Denecke, R., Steinrück, H. P., Phys. Rev. B, **2011**, *83*, 174107.
23. Kinne, M., Fuhrmann, T., Zhu, J.F., Whelan, C.M., Denecke, R., Steinrück, H.-P., J. Chem. Phys., **2004**, *120*, 7113.
24. Herring, C., Phys. Rev., **1951**, *82*, 87.
25. Schauermann, S., Nilius, N., Shaikutdinov, S., Freund, H.-J., Acc. Chem. Res., **2013**, *46*, 1673.
26. Hendriksen, B.L.M., Ackermann, M.D., van Rijn, R., Stoltz, D., Popa, I., Balmes, O., Resta, A., Wermeille, D., Felici, R., Ferrer, S., Frenken, J.W., Nat. Chem., **2010**, *2*, 730.
27. Vang, R.T., Honkala, K., Dahl, S., Vestergaard, E.K., Schnadt, J., Laegsgaard, E., Clausen, B.S., Norskov, J.K., Besenbacher, F., Nat. Mater., **2005**, *4*, 160.
28. Li, Y., Zakharov, D., Zhao, S., Tappero, R., Jung, U., Elsen, A., Baumann, P., Nuzzo, R.G., Stach, E.A., Frenkel, A.I., Nat. Commun., **2015**, *6*, 7583.
29. Tao, F., Grass, M.E., Zhang, Y., Butcher, D.R., Renzas, J.R., Liu, Z., Chung, J.Y., Mun, B.S., Salmeron, M., Somorjai, G.A., Science, **2008**, *322*, 932.
30. Vendelbo, S.B., Elkjaer, C.F., Falsig, H., Puspitasari, I., Dona, P., Mele, L., Morana, B., Nelissen, B.J., van Rijn, R., Creemer, J.F., Kooyman, P.J., Helveg, S., Nat. Mater., **2014**, *13*, 884.
31. Hansen, T.W., Delariva, A.T., Challa, S.R., Datye, A.K., Acc. Chem. Res., **2012**, *46*, 1720.
32. Freund, H.-J., Kuhlenbeck, H., Libuda, J., Rupprechter, G., Bäumer, M., Hamann, H., Top. Catal., **2001**, *15*, 201.

33. Schubert, M.M., Hackenberg, S., van Veen, A.C., Muhler, M., Plzak, V., Behm, R.J., J. Catal., **2001**, *197*, 113.
34. Yang, M., Liu, J., Lee, S., Zugic, B., Huang, J., Allard, L.F., Flytzani-Stephanopoulos, M., J. Am. Chem. Soc., **2015**, *137*, 3470.
35. Bonanni, S., Ait-Mansour, K., Harbich, W., Brune, H., J. Am. Chem. Soc., **2012**, *134*, 3445.
36. Bonanni, S., Ait-Mansour, K., Brune, H., Harbich, W., ACS Catal., **2011**, *1*, 385.
37. Dulub, O., Hebenstreit, W., Diebold, U., Phys. Rev. Lett., **1999**, *84*, 3646.
38. Xu, J., Harmer, J., Li, G., Chapman, T., Collier, P., Longworth, S., Tsang, S.C., Chem. Commun., **2010**, *46*, 1887.
39. Melchionna, M., Fornasiero, P., Mater. Today, **2014**, *17*, 349.
40. Vayssilov, G.N., Lykhach, Y., Migani, A., Staudt, T., Petrova, G.P., Tsud, N., Skála, T., Bruix, A., Illas, F., Prince, K.C., Matolín, V., Neyman, K.M., Libuda, J., Nat. Mat., **2011**, *10*, 310.
41. Perego, C., Millini, R., Chem. Soc. Rev., **2013**, *42*, 3956.
42. Parlett, C.M., Wilson, K., Lee, A.F., Chem. Soc. Rev., **2013**, *42*, 3876.
43. Honciuc, A., Laurin, M., Albu, S., Sobota, M., Schmuki, P., Libuda, J., Langmuir, **2010**, *26*, 14014.
44. Hendriksen, B.L.M., Bobaru, S.C., Frenken, J.W.M., Top. Catal., **2005**, *36*, 43.
45. Salmeron, M., Schlögl, R., Surf. Sci. Rep., **2008**, *63*, 169.
46. Santra, A.K., Goodman, D.W., Electrochim. Acta, **2002**, *47*, 3595.
47. Freund, H.-J., Meijer, G., Scheffler, M., Schlögl, R., Wolf, M., Angew. Chem. Int. Ed. Engl., **2011**, *50*, 10064.
48. Chen, M.S., Cai, Y., Yan, Z., Gath, K.K., Axnanda, S., Goodman, D. W., Surf. Sci., **2007**, *601*, 5326.
49. Farkas, A., Zalewska-Wierzbicka, K., Bachmann, C., Goritzka, J., Langsdorf, D., Balmes, O., Janek, J., Over, H., J. Phys. Chem. C., **2013**, *117*, 9932.
50. Hertz, H., Ann. Phys., **1887**, *267*, 983.
51. Einstein, A., Ann. Phys., **1905**, *322*, 132.
52. Kinne, M., Fuhrmann, T., Zhu, J.F., Tränkenschuh, B., Denecke, R., Steinrück, H.-P., Langmuir, **2004**, *20*, 7.
53. Kinne, M., Fuhrmann, T., Whelan, C. M., Zhu, J. F., Pantförder, J., Probst, M., Held, G., Denecke, R., Steinrück, H.-P., J. Chem. Phys., **2002**, *117*, 10852.
54. Axnanda, S., Scheele, M., Crumlin, E., Mao, B., Chang, R., Rani, S., Faiz, M., Wang, S., Alivisatos, A.P., Liu, Z., Nano Lett., **2013**, *13*, 6176.
55. Wilson, K., Lee, A.F., *Heterogeneous Catalysts for Clean Technology*, Wiley-VCH Verlag GmbH & Co. KGaA (2014).
56. Bluhm, H., Hävecker, M., Knop-Gericke, A., Kiskinova, M., Schlögl, R., Salmeron, M., MRS Bull., **2007**, *32*, 1022.
57. Pantförder, J., Pöllmann, S., Zhu, J. F., Borgmann, D., Denecke, R., Steinrück, H.-P., Rev. Sci. Instrum., **2005**, *76*, 014102.
58. Pantförder, J., Phd Thesis at Physikalische Chemie II, (FAU, Erlangen, 2004).
59. Siegbahn, H., J. Phys. Chem., **1985**, *89*, 897.
60. Siegbahn, H., Lundholm, M., J. Electron Spectrosc. Relat. Phenom., **1982**, *28*, 135.
61. Salmeron, M., Brewer, L., Somorjai, G.A., Surf. Sci., **1981**, *112*, 207.
62. Jaworowski, A.J., , Beutler, A., Strisland, F., Nyholm, R., Setlik, B., Heskett, D., Andersen, J.N., Surf. Sci., **1999**, *431*, 33.
63. Beutler, A., Lundgren, E., Nyholm, R., Andersen, J.N., Setlik, B.J., Heskett, D., Surf. Sci., **1998**, *396*, 117.
64. Ertl, G., Neumann, M., Streit, K. M., Surf. Sci., **1977**, *64*, 393.
65. Linke, R., Curulla, D., Hopstaken, M.J.P., Niemantsverdriet, J.W., J. Chem. Phys., **2001**, *115*, 8209.
66. Gotterbarm, K., Zhao, W., Hofert, O., Gleichweit, C., Papp, C., Steinrück, H.-P., Phys. Chem. Chem. Phys., **2013**, *15*, 19625.

67. Gao, F., Cai, Y., Gath, K.K., Wang, Y., Chen, M.S., Guo, Q.L., Goodman, D.W., J. Phys. Chem. C, **2009**, *113*, 182.
68. Redhead, P.A., Vacuum, **1962**, *12*, 203.
69. Eley, D.D., Pines, H., Weisz, P.B., *Advances in Catalysis*, Academic Press, Inc. (1989).
70. Ackermann, M., Pedersen, T., Hendriksen, B.L.M., Robach, O., Bobaru, S.C., Popa, I., Quiros, C., Kim, H., Hammer, B., Ferrer, S., Frenken, J.W.M., Phys. Rev. Lett., **2005**, *95*, 255505.
71. Gao, F., Goodman, D.W., Langmuir, **2010**, *26*, 16540.
72. Jensen, R., Andersen, T., Nierhoff, A., Pedersen, T., Hansen, O., Dahl, S., Chorkendorff, I., Phys. Chem. Chem. Phys., **2013**, *15*, 2698.
73. van Spronsen, M.A., van Baarle, G.J.C., Herbschleb, C.T., Frenken, J.W.M., Groot, I.M.N., Catal. Today, **2015**, *244*, 85.
74. Krick Calderón, S., Grabau, M., Óvári, L., Kress, B., Steinrück, H.-P., Papp, C., J. Chem. Phys., **2016**, *144*, 44706.
75. Held, G., Bunsen-Magazin, **2010**, *12*, 124.
76. Henzler, M., Göpel, W., *Oberflächenphysik des Festkörpers*, B.G. Teubner (1994).
77. VanHove, M.A., Weinberg, W.H., Chan, C.-M., *Low-Energy Electron Diffraction*, Springer Verlag (1996).
78. Yoo, J.E., Altomare, M., Mokhtar, M., Alshehri, A., Al-Thabaiti, S.A., Mazare, A., Schmuki, P., J. Phys. Chem. C, **2016**, *120*, 15884.
79. Onishi, H., Iwasawa, Y., Surf. Sci., **1994**, *313*, 783.
80. Staudt, T., Lykhach, Y., Hammer, L., Schneider, M.A., Matolín, V., Libuda, J., Surf. Sci., **2009**, *603*, 3382.
81. Šutara, F., Cabala, M., Sedláček, L., Skála, T., Škoda, M., Matolín, V., Prince, K.C., Cháb, V., Thin Solid Films, **2008**, *516*, 6120.
82. Matolin, V., Sedlacek, L., Matolinova, I., Sutara, F., Skala, T., Smid, B., Libra, J., Nehasil, V., Prince, K.C., J. Phys. Chem. C, **2008**, *112*, 3751.
83. Dvořák, F., Stetsovych, O., Steger, M., Cherradi, E., Matolínová, I., Tsud, N., Škoda, M., Skála, T., Mysliveček, J., Matolín, V., J. Phys. Chem. C, **2011**, *115*, 7496.
84. Twigg, M.V., Catal. Today, **2011**, *163*, 33.
85. Paul, J., Hoffmann, F.M., Robbins, J.L., J. Phys. Chem., **1988**, *92*, 6967.
86. Fielicke, A., Gruene, P., Meijer, G., Rayner, D.M., Surf. Sci., **2009**, *603*, 1427.
87. Kamath, P.V., Sarma, D.D., Rao, C.N.R, Proc. Indian Acad. Sci., **1984**, *93*, 335.
88. Langmuir, I., J. Chem. Soc. Faraday Trans., **1922**, *17*, 607.
89. Gland, J.L., Kollin, E.B., J. Chem. Phys., **1983**, *78*, 963.
90. Blyholder, H., J. Phys. Chem., **1964**, *68*, 2772.
91. Chou, K.C., Westerberg, S., Shen, Y.R., Ross, P.N., Somorjai, G.A., Phys. Rev. B, **2004**, *69*, 153413.
92. Christmann, K., *Introduction to Surface Physical Chemistry*, Dr. Steinkopff Verlag GmbH & Co. KG (1991).
93. McEwen, J.S., Payne, S.H., Kreuzer, H.J., Kinne, M., Denecke, R., Steinrück, H.P., Surf. Sci., **2003**, *545*, 47.
94. Steininger, H., Lehwald, S., Ibach, H., Surf. Sci., **1982**, *123*, 264.
95. Gotterbarm, K., Späth, F., Bauer, U., Bronnbauer, C., Steinrück, H.-P., Papp, C., ACS Catal., **2015**, 2397.
96. Scott, R.A., Lukehart, C.M., *Application of Physical Methods to Inorganic and Bioinorganic Chemistry*, John Wiley & Sons Ltd. (2007).
97. Gland, J.L., Surf. Sci., **1980**, *93*, 487.
98. Campbell, C.T., Ertl, G., Kuipers, H., Segner, J., Surf. Sci., **1981**, *107*, 220.
99. Steininger, H., Lehwald, S., Ibach, H., Surf. Sci., **1982**, *123*, 1.
100. Miller, S.D., Pushkarev, V.V., Gellman, A.J., Kitchin, J.R., Topics in Catalysis, **2014**, *57*, 106.
101. Segner, J., Vielhaber, W., Ertl, G., Isreal J. Chem., **1982**, *22*, 375.

---

102. Saliba, N.A., Tsai, Y.-L., Panja, C., Koel, B.E., Surf. Sci., **1999**, *419*, 79.
103. Parkinson, C.R., Walker, M., McConville, C.F., Surf. Sci., **2003**, *545*, 19.
104. Krasnikov, S.A., Murphy, S., Berdunov, N., McCoy, A.P., Radican, K., Shvets, I.V., Nanotechnology, **2010**, *21*, 1.
105. G. Lindauer, P.L., P., Maire, G., Surf. Sci., **1983**, *126*, 301.
106. Miller, D.J., Öberg, H., Kaya, S., Sanchez Casalongue, H., Friebel, D., Anniyev, T., Ogasawara, H., Bluhm, H., Pettersson, L.G.M., Nilsson, A., Phys. Rev. Lett., **2011**, *107*, 195502.
107. Gland, J.L., Kollin, E.B., Surf. Sci., **1985**, *151*, 260.
108. Ertl, G., Norton, P., Rüstig, J., Phys. Rev. Lett., **1982**, *49*, 177.
109. Yeates, R.C., Turner, J.E., Gellman, A.J., Somorjai, G.A., Surf. Sci., **1985**, *149*, 16.
110. Boubnov, A., Gänzler, A., Conrad, S., Casapu, M., Grunwaldt, J.-D., Top. Catal., **2013**, *56*, 333.
111. Miller, D.J., Sanchez Casalongue, H. Bluhm, Ogasawara, H., Nilsson, A., Kaya, S., J. Am. Chem. Soc., **2014**, *136*, 6340.
112. Kao, C.-L., Carlsson, A., Madix, R.J., Surf. Sci., **2002**, *497*, 356.
113. Freund, H.-J., Roberts, M.W., Surf. Sci. Rep., **1996**, *25*, 225.
114. Liu, Z.M., Zhou, Y., Solymosi, White, J.M., J. Phys. Chem., **1989**, *93*, 4383.
115. Castro Neto, A.H., Guinea, F., Peres, N.M.R., Novoselov, K.S., Geim, A.K., Rev. Mod. Phys., **2009**, *81*, 109.
116. Novoselov, K.S., Fal'ko, V.I., Colombo, L., Gellert, P.R., Schwab, M.G., Kim, K., Nature, **2012**, *490*, 192.
117. Bonaccorso, F., Lombardo, A., Hasan, T., Sun, Z., Colombo, L., Ferrari, A.C., Mater. Today, **2012**, *15*, 564.
118. Geim, A.K., Novoselov K.S., Nat. Mat., **2007**, *6*, 183.
119. Singh, V., Joung, D., Zhai, L., Das, S., Khondaker, S.I., Seal, S., Prog. Matter. Sci., **2011**, *56*, 1178.
120. Perreault, F., Fonseca de Faria, A., Elimelech, M., Chem. Soc. Rev., **2015**, *44*, 5861.
121. Batzill, M., Surf. Sci. Rep., **2012**, *67*, 83.
122. Wintterlin, J., Bocquet, M.L., Surf. Sci., **2009**, *603*, 1841.
123. Preobrajenski, A.B., Ng, M.L., Vinogradov, A.S., Mårtensson, N., Phys. Rev. B: Condens. Matter. Mat. Phys., **2008**, *78*, 073401.
124. Gall, N.R., Rut'kov, E.V., Tontegode, A.Y., Usufov, M.M., Tech. Phys., **1999**, *44*, 1066.
125. Huang, L., Pan, Y., Pan, L., Gao, M., Xu, W., Que, Y., Zhou, H., Wang, Y., Du, S., Gao, H.J., Appl. Phys. Lett., **2011**, *99*, 163107.
126. Sicot, M., Leicht, P., Zusan, A., Bouvron, S.,Zander, O., Weser, M., Dedkov, Y.S., Horn, K., Fonin, M., ACS Nano, **2012**, *6*, 151.
127. Zhang, H., Fu, Q., Cui, Y., Tan, D., Bao, X., J. Phys. Chem. C, **2009**, *113*, 8296.
128. Dong, A., Fu, Q., Wei, M., Liu, Y., Ning, Y., Yang, F., Bluhm, H., Bao, X., Surf. Sci., **2015**, *634*, 37.
129. Jin, L., Fu, Q., Dong, A., Ning, Y., Wang, Z., Bluhm, H., Bao, X., J. Phys. Chem. C, **2014**, *118*, 12391.
130. Mu, R., Fu, Q., Jin, L., Yu, L., Fang, G., Tan, D., Bao, X., Angew. Chem. Int. Ed., **2012**, *51*, 4856.
131. Grånäs, E., Knudsen, J., Schröder, U.A., Gerber, T., Busse, C., Arman, M.A., Schulte, K., Andersen, J.N., Thomas Michely, T., ACS Nano, **2012**, *6*, 9951.
132. Wei, M., Fu, Q., Yang, Y., Wei, W., Crumlin, E., Bluhm, H., Bao, X., J. Phys. Chem. C, **2015**, *119*, 13590.
133. Ma, L., Zeng, X.C., Wang, J., J. Phys. Chem. Lett., **2015**, *6*, 4099.
134. Grånäs, E., Andersen, M., Arman, M.A., Gerber, T., Hammer, B., Schnadt, J., Andersen, J.N., Michely, T., Knudsen, J., J. Phys. Chem. C, **2013**, *117*, 16438.
135. Yao, Y., Fu, Q., Zhang, Y. Y., Weng, X., Li, H., Chen, M., Jin, L., Dong, A., Mu, R. Jiang, P., Liu, L., Bluhm, H., Liu, Z., Zhang, S. B., Bao, X., Proc. Natl. Acad. Sci. U.S.A., **2014**, *111*, 17023.
136. Politano, A., Cattelan, M., Boukhvalov, D.W., Campi, D., Cupolillo, A., Agnoli, S., Apostol, N.G., Lacovig, P., Lizzit, S., Farias, D., Chiarello, G., Granozzi, G., Larciprete, R., ACS Nano, **2016**, *10*, 4543.

137. Chen, T.-L., Mullins, D.R., J. Phys. Chem. C, **2011**, *115*, 3385.
138. Ng, M.L., Shavorskiy, A., Rameshan, C., Mikkelsen, A., Lundgren, E., Preobrajenski, A., Bluhm, H., Chemphyschem, **2015**, *16*, 923.
139. Yang, Y., Fu, Q., Wei, M., Bluhm, H., Bao, X., Nano Res., **2014**, *8*, 227.
140. Kirubakaran, A., Jain, S., Nema, R.K., Renew. Sust. Energ. Rev., **2009**, *13*, 2430.
141. Bshish, A., Yaakob, Z., Narayanan, B., Ramakrishnan, R., Ebshish, A., Chem. Pap., **2011**, *65*, 65.
142. Benito, M., Sanz, J.L., Isabel, R., Padilla, R., Arjona, R., Daza, L., J. Power Sources, **2005**, *151*, 11.
143. Brown, L.F., Int. J. Hydrogen Energy, **2001**, *26*, 381.
144. Bayram, B., Soykal, I.I., von Deak, D., Miller, J.T., Ozkan, U.S., J. Catal., **2011**, *284*, 77.
145. Llorca, J., Homs, N., Sales, J., de la Piscina, P.R., J. Catal., **2002**, *209*, 306.
146. Lin, S.S.-Y., Kim, D.H., Ha, S.Y., Catal. Lett., **2008**, *122*, 295.
147. Erdőhelyi, A., Raskó, J., Kecskés, T., Tóth, M., Dömök, M., Baán, K., Catal. Today, **2006**, *116*, 367.
148. Hilaire, S., Wang, X., Luo, T., Gorte, R.J., Wagner, J., Appl. Catal., A, **2001**, *215*, 271.
149. Ellinger, C., Stierle, A., Robinson, I.K., Nefedov, A., Dosch, H., J. Phys.: Condens. Matter, **2008**, *20*, 184013.
150. Fantauzzi, D., Mueller, J.E., Sabo, L., van Duin, A.C., Jacob, T., Chemphyschem, **2015**, *16*, 2797.
151. Smith, C.E., Bihehian, J.P., Somorjai, G.A., J. Catal., **1979**, *57*, 426.
152. Norton, P.R., Davies, J.A., Jackman, T.E., Surf. Sci., **1982**, *122*, L593.
153. Weaver, J.F., Chen, J.-J., Gerrard, A.L., Surf. Sci., **2005**, *592*, 83.
154. Devarajan, S.P., Hinojosa, J.A., Weaver, J.F., Surf. Sci., **2008**, *602*, 3116.
155. Tang, H., Van der Ven, A., Trout, B.L., Phys. Rev. B, **2004**, *70*, 045420.
156. Getman, R.B., Xu, Y., Schneider, W.F., J. Phys. Chem. C, **2008**, *112*, 9559.
157. Hawkins, J.M., Weaver, J.F., Asthagiri, A., Phys. Rev. B, **2009**, *79*, 125434.
158. Holby, E.F., Greeley, J., Morgan, D., J. Phys. Chem. C, **2012**, *116*, 9942.
159. Eslamibidgoli, M.J., Eikerling, M.H., Electrocatalysis, **2016**, *7*, 345.
160. Seriani , N., Pompe , W., Ciacchi, L.C., J. Phys. Chem. B, **2006**, *110*, 14860.
161. Starr, D.E., Liu, Z., Hävecker, M., Knop-Gericke, A., Bluhm, H., Chem. Soc. Rev., **2013**, *42*, 5833.
162. Tao, F., Dag, S., Wang, L.-W., Liu, Z.,Butcher, D. R., Bluhm, H., Salmeron, M., Somorjai, G. A., Science, **2010**, *327*, 850.
163. Tanuma, S., Powell, C.J., Penn, D.R., Surf. Interface Anal., **2003**, *35*, 268.
164. Niehus, H., Comsa, G., Surf. Sci., **1981**, *102*, L14.
165. Bonzel, H.P., Franken, A.M., Pirug, G., Surf. Sci., **1981**, *104*, 625.
166. Baraldi, A., Comelli, G., Lizzit, S., Kiskinova, M., Paolucci, G., Surf. Sci. Rep., **2003**, *49*, 169.
167. Niedermaier, I., Taccardi, N., Wasserscheid, P., Maier, F., Steinrück, H.-P., Angew. Chem. Int. Ed. Engl., **2013**, *52*, 8904.
168. Denecke, R., Appl. Phys. A, **2005**, *88*, 977.
169. Stampfl, C., Ganduglia-Pirovano, M.V., Reuter, K., Scheffler, M., Surf. Sci., **2002**, *500*, 368.
170. Blomberg, S., Hoffmann, M., Gustafson, J., Martin, N., Fernandes, V., Borg, A., Liu, Z., Chang, R., Matera, S., Reuter, K., Lundgren, E., Phys. Rev. Lett., **2013**, *110*, 117601.
171. Palmer, R.L., J. Chem. Phys., **1974**, *60*, 1453.
172. Cox, M.P., Ertl, G., Imbihl, R., Rüstig, J., Surf. Sci., **1983**, *134*, 517.
173. van Rijn, R., Balmes, O., Felici, R., Gustafson, J., Wermeille, D., Westerström, R., Lundgren, E., Frenken, J.W.M., J. Phys. Chem. B, **2010**, 6875.
174. Su, X., Cremer, P.S., Shen, Y.R., Somorjai, G.A., J. Am. Chem. Soc, **1997**, *119*, 3994.
175. Schnadt, J., Knudsen, J., Andersen, J. N., Siegbahn, H., Pietzsch, A., Hennies, F., Johansson, N., Martensson, N., Ohrwall, G., Bahr, S., Mahl, S., Schaff, O., J. Synchrotron. Radiat., **2012**, *19*, 701.

176. Zetterberg, J., Blomberg, S., Gustafson, J., Sun, Z. W., Li, Z. S., Lundgren, E., Alden, M., Rev. Sci. Instrum., **2012**, *83*, 53104.
177. Harriott, P., *Chemical Reactor Design*, Marcel Denker, Inc. (2003).
178. Gao, F., McClure, S., Chen, M., Goodman, D.W., J. Phys. Chem. C., **2010**, *114*, 22369.
179. Rocha, T.C., Oestereich, A., Demidov, D.V., Hävecker, M., Zafeiratos, S., Weinberg, G., Bukhtiyarov, V.I., Knop-Gericke, A., Schlögl, R., Phys. Chem. Chem. Phys., **2012**, *14*, 4554.
180. Bagheri, S., Julkapli, N.M., Hamid, S.B.A., Scientific World J., **2014**, *2014*, 1.
181. Freund, H.-J., Angew. Chem. Int. Ed. Engl., **1997**, *36*, 452.
182. Matos, J., Garcia, A., Cordero, T., Chovelon, J.-M., Ferronato, C., Catal. Lett., **2009**, *130*, 568.
183. Roy, P., Berger, S., Schmuki, P., Angew. Chem. Int. Ed. Engl., **2011**, *50*, 2904.
184. Diebold, U., Surf. Sci. Rep., **2003**, *48*, 53.
185. Dumbuya, K., Cabailh, G., Lazzari, R., Jupille, J., Ringel, L., Pistor, M., Lytken, O., Steinrück, H. P., Gottfried, J. M., Catal. Today, **2012**, *181*, 20.
186. Haubrich, J., Quiller, R.G., Benz, L., Liu, Z., Friend, C.M., Langmuir, **2010**, *26*, 2445.
187. Wang, L.-Q., Baer, D.R., Engelhard, M.H., Shultz, A.N., Surf. Sci., **1995**, *344*, 237.
188. Schierbaum, K.D., Fischer, S., Torquemada, M.C., de Segovia, J.L., Rom, E., Martin-Gago, J.A., Surf. Sci., **1996**, *345*, 261.
189. Pan, J.S., Tao, J.G., Huan, C.H.A., Chiam, S.Y., Zhang, Z., Li, D.T.H., Sun, Y., Chai, J.W., Wang, S.J., Sun, C.Q., Surf. Interface Anal., **2010**, *42*, 878.
190. Baerns, M., Imbihl, R., Kondratenko, V., Kraehnert, R., Offermans, W., Vansanten, R., Scheibe, A., J. Catal., **2005**, *232*, 226.
191. Reuter, K., Oil Gas Sci. Technol., **2006**, *61*, 471.
192. Zaera, F., Chem. Soc. Rev., **2013**, *42*, 2746.
193. Chen, X., Mao, S.S., Chem. Rev., **2007**, *107*, 2891.
194. Zhang, G.-R., Zhao, D., Feng, Y.-Y., Zhang, B., Su, D.S., Liu, G., Xu. B.-Q., ACS Nano, **2012**, *6*, 2226.
195. Lim, B., Jiang, M., Camargo, P.H.C., Cho, E.C.,Tao, J., Lu, X., Zhu, Y., Xia, Y., Science, **2009**, *324*, 1302.
196. Honciuc, A., Laurin, Albu, M.S., Amende, M., Sobota, M., Lynch, R., Schmuki, P., Libuda, J., J. Phys. Chem. C, **2010**, *114*, 8.
197. Basahel, S.N., Lee, K., Hahn, R., Schmuki, P., Bawaked, S.M., Al-Thabaiti, S.A., Chem. Commun., **2014**, *50*, 6123.
198. Song, Y.-Y., Gao, Z.-D., Schmuki, P., Electrochem. Commun., **2011**, *13*, 290.
199. Cha, G., Lee, K., Yoo, J.E., Killian, M.S., Schmuki, P., Electrochimica Acta, **2015**, *179*, 423.
200. Li, W.-X., J. Phys.: Condens. Matter, **2008**, *20*, 184022.
201. Razon, L.-F., Schmitz, R.A., Catal. Rev. - Sci. Eng., **1986**, *28*, 89.
202. Spencer, M.S., J. Catal., **1985**, *93*, 216.
203. Ocal, C., Ferrer, S., J. Chem. Phys., **1986**, *84*, 6474.
204. Ketteler, G., Yamamoto, S., Bluhm, Andersson,H.K., Starr,D.E., Ogletree, D.F., Ogasawara, H., Nilsson, A., Salmeron, M., J. Phys. Chem. C, **2007**, *111*, 8278.
205. Bagus, P.S., Ilton, E.S., Nelin, C.J., Surf. Sci. Rep., **2013**, *68*, 273.
206. Voloshina, E.N., Dedkov, Y.S., Torbrügge, S., Thissen, A., Fonin, M., Appl. Phys. Lett., **2012**, *100*, 241606.
207. Thiel, P.A., ED. Williams, E.D., Yates, J.T.,Weinberg, W.H., Surf. Sci., **1979**, *84*, 54.
208. Smedh, M., Beutler, A., Ramsvik, T., Nyholm, R., Borg, M., Andersen, J.N., Duschek, R., Sock, M., Netzer, F.P., Ramsey, M.G., Surf. Sci., **2001**, *491*, 99.
209. Krenn, G., Bako, I., Schennach, R., J. Chem. Phys., **2006**, *124*, 144703.
210. Vinogradov, N.A., Schulte, K., Ng, M.L., Mikkelsen, A., Lundgren, E., Mårtensson, N., Preobrajenski, A.B., J. Phys. Chem. C, **2011**, *115*, 9568.
211. Larciprete, R., Gardonio, S., Petaccia, L., Lizzit, S., Carbon, **2009**, *47*, 2579.
212. Larciprete, R., Fabris, S., Sun, T., Lacovig, P., Baraldi, A., Lizzit, S., JACS, **2011**, *133*, 17315.
213. Root, T.W., Schmidt, L.D., Surf. Sci., **1983**, *134*, 30.

214. Óvári, L., Krick Calderon, S., Lykhach, Y., Libuda, J., Erdőhelyi, A., Papp, C., Kiss, J., Steinrück, H. P., J. Catal., **2013**, *307*, 132.
215. Mattos, L.V., Jacobs, G., Davis, B.H., Noronha, F.B., Chem. Rev., **2012**, *112*, 4094.
216. Vaidya, P.D., Rodrigues, A.E., Chem. Eng. J., **2006**, *117*, 39.
217. Song, H., Ozkan, U., J. Catal., **2009**, *261*, 66.
218. Song, H., Mirkelamoglu, B., Ozkan, U.S., Appl. Cat. A: General, **2010**, *382*, 58.
219. Llorca, J., Homs, N., Ramirez de la Piscina, P., J. Catal., **2004**, *227*, 556.
220. Lin, S.S.-Y., Kim, D.H., Ha, S.Y., Appl. Cat. A: General, **2009**, *355*, 69.
221. Mavrikakis, M., Barteau, M.A., J. Mol. Catal. A: Chemical, **1998**, *131*, 135.
222. Hyman, M.P., Vohs, J.M., Surf. Sci., **2011**, *605*, 383.
223. Llorca, J.D., J.-A., Ramírez de la Piscina, P., Homs, N., Appl. Cat. A: General, **2003**, *243*, 261.
224. Weststrate, C.J., Gericke, H.J., Verhoeven, M.W.G.M., Ciobîc, I.M., Saib, A.M., Niemantsverdriet, J.W., J. Phys. Chem. Lett., **2010**, *1*, 1767.
225. Yee, A., Morrison, S.J., Idriss, H., J. Catal., **1999**, *186*, 279.
226. de Lima, S.M.d.S., A.M., da Costa, L.O.O., Graham, U.M., Jacobs, G., Davis, B.H., Mattos, L.V. Noronha, F.B., J. Catal., **2009**, *268*, 268.
227. Fu, Q., Wagner, T., Surf. Sci. Rep., **2007**, *62*, 431.
228. Libuda, J., Freund, H. J., Surf. Sci. Rep., **2005**, *57*, 157.
229. Rodriguez, J.A., Graciani, J., Evans, J., Park, J.B., Yang, F., Stacchiola, D., Senanayake, S.D., Ma, S., Perez, M., Liu, P., Danz, J.F., Hrbek, J., Angew. Chem. Int. Ed. Engl., **2009**, *48*, 8047.
230. Matolín, V., Libra, J., Matolínová, I., Nehasil, V., Sedláček, L., Šutara, F., Appl. Surf. Sci., **2007**, *254*, 153.
231. Grinter, D.C., Ithnin, R., Pang, C.L., Thornton, G., J. Phys. Chem. C, **2010**, *114*, 17036.
232. Burroughs, P., Hamnett, A., Orchard, A.F., Thorton, G., J. Chem. Soc. Dalton Trans., **1976**, *17*, 1686.
233. Pfau, A., Schierbaum, K.D., Surf. Sci., **1994**, *321*, 71.
234. Fujimori, A., Phys. Rev. B, **1983**, *28*, 4489.
235. Mullins, D.R., Overbury, S.H., Huntley, D.R., Surf. Sci., **1998**, *409*, 307.
236. Nelin, C.J., Bagus, P.S., Ilton, E.S., Chambers, S.A., Kuhlenbeck, H., Freund, H.-J., Int. J. Quant. Chem., **2010**, *110*, 2752.
237. Li, H.Y., Wang, H.F., Guo, Y.L., Lu, G.Z., Hu, P., Chem. Commun., **2011**, *47*, 6105.
238. Abu-Samha, M., Borve, K.J., Saethre, L.J., Thomas, T.D., Phys. Rev. Lett., **2005**, *95*, 103002.
239. Henderson, M.A., Perkins, C.L., Engelhard, M.H., Thevuthasan, S., Peden, C.H.F., Surf. Sci., **2003**, *526*, 1.
240. Matolín, V., Matolínová, I., Dvořák, F., Johánek, V., Mysliveček, J., Prince, K.C., Skála, T., Stetsovych, O., Tsud, N., Václavů, M., Šmíd, B., Catal. Today, **2012**, *181*, 124.
241. Lykhach, Y., Johánek, V., Aleksandrov, H.A., Kozlov, S.M., Happel, M., Skála, T., Petkov, P.S., Tsud, N., Vayssilov, G.N., Prince, K.C., Neyman, K.M., Matolín, V., Libuda, J., J. Phys. Chem. C, **2012**, *116*, 12103.
242. Matolín, V., Libra, J., Škoda, M., Tsud, N., Prince, K.C., Skála, T., Surf. Sci., **2009**, *603*, 1087.
243. Raskó, J., Dömök, M., Baán, K., Erdőhelyi, A., Appl. Cat. A: General, **2006**, *299*, 202.
244. Mullins, D.R., Senanayake, S.D., Chen, T.-L., J. Phys. Chem. C, **2010**, *114*, 17112.
245. Idriss, H., Diagne, C., Hindermann, J.P., Kiennemann, A., Barteau, M.A., J. Catal., **1995**, *155*, 219.
246. Raskó, J., Kiss, J., Appl. Cat. A: General, **2005**, *287*, 252.
247. Martono, E., Vohs, J.M., J. Catal., **2012**, *291*, 79.
248. Lin, S.S.-Y., Kim, D.H., Engelhard, M.H., Ha, S.Y., J. Catal., **2010**, *273*, 229.
249. Wagner, C.D., Riggs, W.M., Davis, L.E., Moulder, J.F., Muilenberg, G.E., *Handbook of X-ray Photoelectron Spectroscopy*, Perkin-Elmer Corp. (1979).
250. Lee, A.F., Gawthrope, D.E., Hart, N.J., Wilson, K., Surf. Sci., **2004**, *548*, 200.
251. Davis, J.L., Barteau, M.A. Surf. Sci. 1990, 235, 235., Surf. Sci., **1990**, *235*, 235.

252. Steinrück, H.-P., Pesty, F., Zhang, L., Madey, T.E., Phys. Rev. B, **1995**, *51*, 2427.
253. Óvári, L., Kiss, J., Appl. Surf. Sci., **2006**, *252*, 8624.
254. Fantauzzi, D., Bandlow, J., Sabo, L., Mueller, J.E., van Duin, A.C., Jacob, T., PhysChemChemPhys, **2014**, *16*, 23118.
255. Senftle, T.P., Meyer, R.J., Janik, M.J., van Duin, A.C., J. Chem. Phys., **2013**, *139*, 044109.
256. Metropolis, N., Rosenbluth, A.W., Rosenbluth, M.N., Teller, A.H., Teller, E., J. Chem. Phys., **1953**, *21*, 1087.
257. Frenkel, D., Smit, B., *Understanding molecular simulations*, Academic Press (2002).
258. NIST, *Thermochemical Tables*, NIST-JANAF (1998).
259. Senftle, T.P., Janik, M.J., van Duin, A.C.T., J. Phys. Chem. C, **2014**, *118*, 4967.
260. Senftle, T.P., van Duin, A.C.T., Janik, M.J., Catal. Commun., **2014**, *52*, 72.

13. Acknowledgements

I would like and certainly have to express my gratitude and appreciation to a lot of people who supported and helped me throughout my PhD time.

In particular, I would like to thank my first supervisor Prof. Hans-Peter Steinrück for his understanding and open ear for all “challenges” one may face during a PhD work. I also appreciate his patience throughout long discussions, ideas and answers “as a last resort”. Thank you for providing such a calm and inspiring atmosphere in your work group.

In line with this, I would especially thank Dr. Christian Papp for his supervision and support. His encouragement for trying out things and discussions helped me a lot during my PhD work, not to forget his view at things from a different perspective.

Thanks also to Mathias Grabau for the uncomplicated sharing of the GAP and the help with all the things that need to be done in a surface science lab (repairing, bake-out, bake-out and bake-out…). Also thank you for the nice atmosphere and often funny times in the office – of course also to Michael Röckert.

I am very grateful to Bernd Kress and Hans-Peter Bäumler, firstly for their technical support and help – but importantly also for their encouraging words and support far beyond “work”. In this context also the technical work shop is acknowledged for their help and excellent work.

Apart the whole PC II work group I would to thank some special people for the pleasant time and friendship: thank you Inga, Michi, Andre, Flo and who else might be missing here!

Of course I would like to acknowledge also Prof. Georg Held from the University of Reading who gave me the opportunity to work in his group at the Diamond Light Source. I really enjoyed the stay and appreciate the opportunity to gain insights into synchrotron work. A big thank also to Dr. Rosa Arrigo, Dr. Pilar Ferrer, Dr. Federica Venturini and Christopher Stephens for welcoming me in Didcot.

I would also like to acknowledge Prof. Timo Jacob and Dr. Donato Fantauzzi for the ReaxFF GCMC calculations. Also, I would like to thank JeongEun, Manuela Killian and Prof. Patrik Schmuki for the TiO_2NT samples and cooperation. Additionally, Lázló Óvári, Markus Licklederer, Christine Weichselbaum and Stephen Massicot are thanked for their scientific contributions.

Last but not least I would like to deeply thank my parents Willy and Krystyna, my brother Rafael, and my partner Stephan who always supported and encouraged me.

14. Curriculum Vitae

Personal

Name: Sandra Christina Krick Calderón

Born: 19/07/1988 in Erlangen, Germany

Citizenship: German

Education

1994-1998	Elementary School in Röttenbach (Germany)
1998-2007	Ohm-Gymnasium in Erlangen (Germany)
06/2007	Abitur (university entrance diploma)
2007-2010	Bachelor Studies in Chemistry at the Friedrich-Alexander-University Erlangen-Nürnberg Bachelor Thesis at the Chair of Physical Chemistry I (Prof. D. Guldi): “Photophysical Characterisation of a new supramolecular tetra(ruthenium phtalocynine) perylenediimide complex”
11/2010	Degree in Bachelor of Science
2010-2012	Master Studies in Molecular Science at the Friedrich-Alexander-University Erlangen-Nürnberg Master Thesis at the Chair of Physical Chemistry II (Prof. H.-P. Steinrück): “Synthesis and ARXPS investigations of new nitrile-functionalized ionic liquids” 3-month stay at the University of Nottingham (Prof. P. Licence) for the synthesis of the ionic liquids
03/2012	Degree in Master of Science
since *06/2012*	PhD Thesis at at the Chair of Physical Chemistry II (Prof. H.-P. Steinrück) of the Friedrich-Alexander-University Erlangen-Nürnberg

15. List of Publications

(1) A.J. Jiménez, B. Grimm, V.L. Gunderson, M.T. Vagnini, **S. Krick Calderón**, M.S. Rodríguez-Morgade, M.R. Wasielewski, D.M. Guldi, T. Torres, “Synthesis, Characterization, and Photoinduced Energy and Electron Transfer in a Supramolecular Tetrakis (Ruthenium(II) Phthalocyanine) Perylenediimide Pentad”, *Chem. Eur. J.*, 2011, *17*, 5024.

(2) T. Cremer, L. Wibmer, **S. Krick Calderón**, A. Deyko, F. Maier, H.-P. Steinrück, “Interfaces of ionic liquids and transition metal surfaces -adsorption, growth, and thermal reactions of ultrathin [C_1C_1Im][Tf_2N] films on metallic and oxidised Ni(111) surfaces”, *Phys. Chem. Chem. Phys.*, 2012, *14*, 5153.

(3) L. Óvári, **S. Krick Calderón**, Y. Lykhach, J. Libuda, A. Erdöhelyi, C. Papp, H.-P. Steinrück, “Near ambient pressure investigation of ethanol with Co/CeO_2(111)”, *J. Catal.*, 2013, *307*, 132.

(4) I. Niedermaier, M. Bahlmann, C. Papp, C. Kolbeck, W. Wei, **S. Krick Calderón**, M. Grabau, P. Schulz, P. Wasserscheid, H.-P. Steinrück, F. Maier, "Carbon Dioxide Capture by an Amine Functionalized Ionic Liquid: Fundamental Differences of Surface and Bulk Behavior", *JACS*, 2014, *136*, 436.

(5) M. Ledendecker, **S. Krick Calderón**, C. Papp, H.-P. Steinrück, M. Antontietti, M. Shalom, „The Synthesis of Nanostructured Ni_5P_4 Films and their Use as a Non-Noble Bifunctional Electrocatalyst for Full Water Splitting”, *Angew. Chem.*, 2015, *54*, 12361.

(6) **S. Krick Calderón**, M. Grabau, L. Óvári, B. Kress, C. Papp, H.-P. Steinrück, „CO oxidation on Pt(111) at near ambient pressures“, *J. Chem. Phys.*, 2016, *144*, 44706.

(7) M. Grabau, **S. Krick Calderón**, F. Rietzler, I. Niedermaier, N. Taccardi, P. Wasserscheid, F. Maier, H.-P. Steinrück, C. Papp, „Surface enrichment of Pt in Ga_2O_3 films grown on liquid Pt/Ga alloys”, *Surf. Sci.*, 2016, *651*, 16.

(8) A. Späth, F. Tu, F. Vollnhals, M. Drost, **S. Krick Calderón**, B. Watts, R.H. Fink, H. Marbach, “Energy-selective Additive Fabrication of Nanostructures with Focused Soft X-Rays”, *submitted,* 2016.

(9) **S. Krick Calderón**, M. Grabau, J.E. Yoo, M. Kilian, P. Schmuki, H.-P. Steinrück, C. Papp, “Reactivity of TiO_2 nanotube-supported Pt particles in the CO oxidation reaction”, ChemCatChem*, accepted*, 2016.

(10)D. Fantauzzi, **S. Krick Calderón**, J.E. Mueller, T., Jacob, M. Grabau, C. Papp, H.-P. Steinrück, T. Senftle, A.C.T van Duin, “The growth of stable surface oxides on Pt(111) at near-ambient pressures”, *submitted*, 2016.